Luis Evelio Garcia Acevedo

ANÁLISE E DESENVOLVIMENTO DE MODELO DE TRANSPORTE DE MASSA VISANDO A APLICAÇÃO EM CÉLULAS A COMBUSTÍVEL TIPO PEM

Tese submetida ao Programa de Programa de Pós-Graduação em Engenharia Mecânica da Universidade Federal de Santa Catarina para a obtenção do Grau de Doutor em Engenharia Mecânica.
Orientador: Prof. Amir Antônio Martins de Oliveira Jr., Ph.D.

Florianópolis
2012

Ficha de identificação da obra elaborada pelo autor,
através do Programa de Geração Automática da Biblioteca Universitária da UFSC.

Garcia-Acevedo, Luis Evelio
Análise e desenvolvimento de modelo de transporte de massa visando a aplicação em células a combustível tipo PEM [tese] / Luis Evelio Garcia-Acevedo ; orientador, Amir Antônio Martins de Oliveira Jr. - Florianópolis, SC, 2012.
323 p. ; 21cm

Tese (doutorado) - Universidade Federal de Santa Catarina, Centro Tecnológico. Programa de Pós-Graduação em Engenharia Mecânica.

Inclui referências

1. Engenharia Mecânica. 2. Células a combustível. 3. Transporte de massa. 4. Maxwell-Stefan. 5. Eletroquímica Conversão de energia. I. Oliveira Jr., Amir Antônio Martins de. II. Universidade Federal de Santa Catarina. Programa de Pós-Graduação em Engenharia Mecânica. III. Título.

Luis Evelio Garcia Acevedo

ANÁLISE E DESENVOLVIMENTO DE MODELO DE TRANSPORTE DE MASSA VISANDO A APLICAÇÃO EM CÉLULAS A COMBUSTÍVEL TIPO PEM

Esta Tese foi julgada adequada para obtenção do Título de "Doutor em Engenharia Mecânica", e aprovada em sua forma final pelo Programa de Programa de Pós-Graduação em Engenharia Mecânica

Florianópolis, 29 de Junho de 2012

_____
Prof. Júlio César Passos, Dr.
Coordenador do Curso

Banca Examinadora:

_____
Prof. Amir Antônio Martins de Oliveira Jr. Ph. D
Orientador
EMC - UFSC

_____
Prof. Paulo Smith Schneider Dr.
UFRGS (Relator)

_____
Prof. Ernesto Rafael Gonzalez Dr.
IQSC-USP

_____
Prof. Paulo César Philippi, Dr
EMC - UFSC

_____
Prof. Edson Bazzo, Dr.Eng
EMC - UFSC

_____
Prof. Jader Riso Barbosa Junior, Ph.D
EMC - UFSC

A Kamila e Carmen.
Como reconhecimento a *la juventud académica de Toledo, Chinácota y Labatéca, en especial a la escuela rural Santa Ana y al colegio Nacional San Luis Gonzag*a.

AGRADECIMENTOS

Agradeço a Deus pela vida, pelo amor e por esta existência plena de felicidade. A minha amada esposa Kamila pelo seu amoroso e comprometido companheirismo no esforçado caminhar destes anos. Agradeço a minha mãe Carmen e minha irmã Dorena que desde criança e até agora me fizeram sentir no seio da família, amando, a pesar do tempo e distancia. A minha família neotrentina, Trainotti e Butichevistz, pelo amor que me fortalece e guia, pelo constante e incondicional apoio. Aos grandes amigos que sempre souberam estar ai, Lucila, Joanna e Simone, Lara, Maycon. Agradeço em forma especial ao meu orientador Amir, pela orientação, carinho e por me ensinado coragem e atitude positiva diante da vida. Aos diferentes e em todo tempo bem qualificados professores, que no percurso da minha formação de mestrado colaboraram para a obtenção deste título; Aos membros da banca, por sua valiosa contribuição. Aos colegas, docentes e corpo técnico e administrativo do LabCET pela colaboração e vida de partilhada nestes longo anos. Aos conterrâneos de tantas alegrias e angustias que sempre me fizeram lembrar minha origem e preencheram a "saudade da terra", em especial aqueles mas próximos que no dia a dia sempre demonstraram sua desinteressada amigada. A igreja católica e sua doutrina que dão sentido ao meu existir através do constante ensinamento da Palavra e exercício do Amor. As instituições que fizeram possível o desenvolvimento deste trabalho, Laboratório de Combustão e Engenharia de Sistemas Térmicos - LabCET, a Pós-graduação em Engenharia Mecânica Pós-MEC, a Universidade Federal de Santa Catarina UFSC – a CAPES e seu programa PEC PG pela bolsa, a CNPq pelos recursos de projeto. Agradeço e parabenizo ao governo do Brasil e aos brasileiros por estas oportunidades que fazem todos nós melhores, e contribuem concreta e definitivamente com o tão sonhado desenvolvimento latino-americano uno.

E ainda que tivesse o dom de profecia, e conhecesse todos os mistérios e toda a ciência, e ainda que tivesse toda fé, de maneira tal que transportasse os montes, e não tivesse amor, nada seria.

1 Coríntios 13:2

RESUMO

O atual cenário mundial na área de energia demanda o desenvolvimento tecnológico de alternativas sustentáveis, e de menor impacto ambiental. O uso eficiente de fontes de energia renováveis para a produção de energia elétrica em sistemas descentralizados e isolados, bem como para o setor de mobilidade, destaca-se como um ingrediente capaz de mitigar a agressão ambiental dos sistemas de energia. A célula a combustível é um dispositivo eletroquímico que converte diretamente a energia interna de ligação química de combustíveis em energia elétrica e calor com alta eficiência global, ausência de ruído e emissões. O elevado custo de desenvolvimento destes sistemas sugere que estratégias que combinem medições e previsões teóricas apresentem a maior chance de atingir os desenvolvimentos necessários. O principal objetivo da presente tese é desenvolver uma teoria para o transporte de massa em uma célula a combustível tipo PEM a partir de uma análise fenomenológica com base nos fundamentos do transporte de massa multicomponente, multifásico em meios porosos. O modelo tem por objetivo prever o comportamento do transporte elétrico e de massa com uma formulação adequada. Para este fim, foram revisadas as escalas de comprimento característicos dos diferentes componentes e fenómenos dentro da célula a combustível visando determinar as relações entre os processos termodinâmicos, eléctricos e eletroquímicos em uma célula de combustível tipo PEM. Foi revisada a grande quantidade de informações sobre teoria, modelagem e simulação da célula a combustível tipo PEM, a fim de classificar os diferentes modelos, ressaltar sua aplicabilidade e definir as necessidades de melhoria. A curva de polarização de um sistema de célula de combustível foi medida com o objetivo de identificar os fenómenos que controlam o transporte e a fenomenologia química, avaliar a aplicabilidade dos modelos globais disponíveis e determinar a ordem de grandeza dos parâmetros característicos globais da operação da célula de combustível. Então, foram revisadas as teorias fundamentais de transporte de massa e carga em duas fases, em fluxo multicomponente em meios porosos, focando na base do continuo e da termodinâmica para o tratamento de Maxwell-Stefan do transporte de massa. Finalmente, foi proposto um modelo fenomenológico geral para transferência de massa e carga aplicável às células a combustível tipo PEM. O modelo foi comparado com outros modelos da literatura e alguns problemas mais simples fundamentais foram resolvidos.

Palavras-chave: Células a combustível, transporte de massa, Maxwell-Stefan, Eletroquímica, Conversão de energia.

ABSTRACT

The present world energy scenario requires the development of alternative and sustainable energy sources and conversion systems that also result in an overall smaller impact in the environment. The efficient use of renewable energy sources for the production of electrical power in decentralized and isolated systems, as well as for the mobility sector, stands out as a possible ingredient to mitigate the environmental aggression from energy systems. Fuel cells are electrochemical devices that convert internal energy of chemical bond in electricity and heat power in an efficient, noiseless and lower emissions form. The relative high cost of system development suggests that a combined measurement, theoretical and simulation effort is the way to achieve the required breakthroughs. The main objective of the present thesis is to develop a theory for mass transport in a PEM fuel cell from a phenomenological analysis based on the fundamentals of the multicomponent, multiphase mass transport in porous media. The model aims at predicting the electric and mass transport behaviors with a formulation suitable for solution with current computational resources. To this end, the characteristic length scales of the different components and phenomena within the fuel cell were revised aiming at determining the relations between thermodynamic, electric and electrochemical processes in a PEM fuel cell. The vast amount of information on PEM fuel cell theory, modeling and simulation was reviewed with a view to classify the different models, point out their applicability and define the needs for further improvements. The polarization curve for a fuel cell system was measured with the purpose of identifying the controlling transport and chemical phenomena, assess the applicability of the available lumped models and to determine the orders of magnitude of global parameters characteristic of the fuel cell operation. Then, the fundamental theories of mass and charge transport in two-phase, multicomponent flow in porous media were reviewed, focusing on the continuum and thermodynamic basis for the Maxwell-Stefan treatment of mass transport. Finally, a general phenomenological model for mass and charge transfer applicable to PEM fuel cells was proposed, compared to other models from the literature and a few simpler fundamental problems were solved.

Keywords: PEM fuel cells, mass transport, Maxwell-Stefan, Electrochemistry, Energy conversion.

LISTA DE FIGURAS

Figure 1 -A schematic description of the components of a PEM fuel cell. 46
Figure 2 – Rendering of the different fluxes in an operating fuel cell. 47
Figure 3 - Zoom representation of the different layers forming the fuel cell. A detailed rendering of the transport of participating species and the boundaries between adjacent layers is also presented..... 50
Figure 4 - End plate localization inside the fuel cell (KIM, 2008). 51
Figure 5 - Flow field designs. a) Pin-type, b) straight and parallel channel, c) single serpentine, d) interdigitated (LI and SABIR, 2005)..... 54
Figure 6 - Representation of the molecular unit of the Nafion® chain. (MAURITZ AND MOORE, 2004)..... 57
Figure 7 - Characterization of a Nafion® membrane at progressively smaller scales using various techniques. (From: DIAT and GEBEL, 2008)..... 59
Figure 8 -Parallel water channel model of Nafion® . (SCHMIDT-ROHR AND CHEN, 2008a) 61
Figure 9 - Two-stage Nafion swelling: (RUBATAT et al., 2004) 62
Figure 10 - Micrographs of gas diffusing media substrates for fuel cell. 65
Figure 11 – Rendering representing (b) the platinum crystallites covering the carbon particles. 68
Figure 12 - Rendering of the platinum crystallites attached to a carbon particle. 68
Figure 13 - Work made on an electrical charge in presence of an electrical field. 74
Figure 14 - Sketch of an electrochemical cell. Positive charges are cations and negative charges are electrons 76
Figure 15 – Rendering showing the relation between reaction Gibbs energy and electrical potential. 79
Figure 16 - The variation of the cell potential with the value of the reaction 81
Figure 17 – Rendering of the molecular structure of the double layer. 86
Figure 18 - Variation of potential with distance from a metallic electrode:. 88

Figure 19 – Rendering of the electrical potentials in the electrode-electrolyte interface: 89
Figure 20 - Pathway of a general electrode reaction 95
Figure 21 - A reaction profile and activated complex 97
Figure 22 - Electrode reaction Gibbs energy profile for a reversible process. 102
Figure 23 - Reaction profiles for the oxidation reduction reaction. 104
Figure 24 Rendering of a typical potential surface in a fuel cell as a function of the extent of reaction and the current density, the **EpErCd** curve. 110
Figure 25 - Relation among fuel cell potential E (V), extent of reaction and current density i(A/cm2). 111
Figure 26 - Tafel plots for slow and fast electrochemical reaction 113
Figure 27 – Typical curves of cell voltage against current density. 114
Figure 28 - Linear variation in concentration on the model of the Nernst diffusion layer. 118
Figure 29 - Typical polarization curve for a PEM fuel cell..... 121
Figure 30 - Sketch of the polarization curve with the electrical power density curve. 125
Figure 31 - Sketch of the classification according to the complexity level. 129
Figure 32 - Key features of fuel cell models according to Haraldsson (2004). 134
Figure 33 - Overview of the fuel cell models available in literature and commercially according to Haraldsson (2004). . 136
Figure 34 - Gas distribution and control network 158
Figure 35 - Gas control measure and humidification system ... 159
Figure 36 - Fuel cell stack electrical performance system 159
Figure 37 - 200W PEM Fuel cell stack bench at LabCET 160
Figure 38 - Gas humidifier and thermal control 161
Figure 39 -Average curves of (a) polarization and (b) electrical power for the four temperatures in the first group of tests 164
Figure 40 – Polarization curve for the 200W PEM fuel cell operating in the base conditions (at 70^{o}C)..... 165
Figure 41 – Control volume used for analysis including channel, GDL and Catalyst layer. 169

Figure 42 – Comparison of concentration overpotential losses between reference model (Kim et al.1995) and both a) model 1 and b) model 2. 177
Figure 43 - – Comparison of polarization curve between reference model (Kim et al.1995) and both a) model 1 and b) model 2 179
Figure 44 - Comparison of polarization curve between reference model (Kim et al.1995) and both a) model 1 and b) model 2 at 70°C 180
Figure 45 -Polarization curve of the model for temperatures of a) 50°C, b) 60°C, c) 70°C and d) 80°C 187
Figure 46 - Comparison of the result of the Maxwell-Stefan equations (Krishna and Wesselingh, 1997) with the experiments of Duncan and Toor (1962). 285

LISTA DE TABELAS

Table 1 - A few fuel cells classified by the electrolyte material. 43
Table 2 - Characteristic length scales of fuel cell components... 49
Table 3 - Characteristic MEA components and their roles (Source: HOOGERS, 2003). 55
Table 4 - Standard reaction Gibbs energy and standard cell potential for different temperatures. 112
Table 5 - Exchange current and transfer coefficients at 298K (ATKINS, 1998). 115
Table 6 - Values for the semi- empirical cell potential equation. 124
Table 7 – Some researches groups on fuel cell..... 138
Table 8 - Fuel cell pioneer model in literature 154
Table 9 - Characteristics of the standard T type cylinder for gas storage 157
Table 10 - Measurement uncertainties of the measurement systems. 162
Table 11- Parameters obtained using the first mass transfer model (constant c_s). 181
Table 12 - Parameters obtained using the second mass transfer model (variable c_s). 181
Table 13 - Exchange current densities (in A/cm2) from Table 4 and from the curve-fitted model for io (parameters k1, k2 and γ), using both mass transfer models..... 185
Table 14 - Regression parameters for exchange current density 185
Table 15 - Fitting Parameters of the model to the measured polarization assuming a constant membrane water saturation.. 185
Table 16 - Summary of the different concentration measures. The summations refer to all species, from 1 to N_c 195
Table 17 - Different forms of expressing the conservation of species *i* and mixture momentum, and the corresponding stress-relations. 206
Table 18 - Comparison of Curtiss and Bird (1996) definitions and the ones used here..... 207
Table 19 - Comparison of Whitaker (1999) definitions and the ones used here..... 207

LISTA DE ABREVIATURAS E SIGLAS

A	Helmholtz energy (kJ/kmol), área (m^2)
a_a	Anode/cathode water activity (-)
A_E	Pre-exponential coefficient for the empirical equation of the concentration overpotential (V)
b	Body force (N/m^3)
B_i	Exponential coefficient for the empirical equation of the concentration overpotential (cm^2/mA)
$C^{\mp}$	Activated complex (mol)
c	Bulk concentration (mol)
c'	Ion concentration a the OHP (mol)
D_{im}	Mass diffusivity of the specie i in the gas mixture (m^2/s)
e	Electron charge (C)
E	cell potential (V)
E_{el}	Electrode potential
E_{ref}	Reference electrode potential(V)
E^o	Standard cell potential (V)
E^0	Formal cell potential (V)
E	Theoretical cell potential (V)
E'	Theoretical cell potential at the local OHP ions concentration (V)
E_c	Cell potential (V)
f	Fugacity (Pa)
F	Faraday constant (96485 C/mol)
g	Standard acceleration of gravity (9.81 m^2/s)
G	Gibbs energy (kJ)
$\overline{G}$	Gibbs energy in presence of a electrical field (kJ)
$G^{\neq}$	Gibbs energy of activation (kJ/kmol)
h	Molar enthalpy (kJ/kmol)
h_i	Local molar enthalpy of species *i* (kJ/kmol*i*)
$h_{f,i}$	Standard enthalpy of formation of species *i* (kJ/kmol*i*)
h_{ch}	Channel height (m)
h_p	Plank Constant (6.6261×10^{-34} J.s)
H	Enthalpy (kJ/kmol)
$\overline{H}$	Average curvature of the liquid/gas meniscus (1/m)
i	Current density (A/cm^2)

i_o	Exchange current density (A/cm^2)
$\vec{j}_i$	Diffusion mass flux vector of species *i* (mol/m^2-s)
J_i	Diffusion molar flux of species *i* (mol/m^2-s)
k	Rate constant ()
k_e	Electric conductivity (1/Ohm-cm)
k_{ox}	Pseudo rate constant of the oxidation reaction in the redox ()
k_{red}	Pseudo rate constant of the reduction reaction in the redox ()
$k_{o,A}$	Pre-exponential constant of the current density for the anode ()
$k_{o,Ct}$	Pre-exponential constant of the current density for de cathode ()
$k^{\mp}$	Unimolecular rate constant for transition reaction ()
$\mathbb{k}$	Boltzmann constant (1.3806504×10^{-23} J/K)
K	Thermodynamic equilibrium constant ()
$\overline{K}$	Thermodynamic pseudo-equilibrium constant
K_p	Thermodynamic equilibrium constant as a function of pressures
$K_{r,p}$	Reaction quotient a function of pressures at no-equilibrium state
K_r	Reaction quotient a function of activities at no-equilibrium state
$K^{\mp}$	Proportionally constant
K^P	Permeability (m^2)
K_{rg}^P	Non-wetting phase relative permeability
K_{rl}^P	Wetting phase relative permeability
l_G	GDL thickness (m)
l_c	Catalyst layer thickness (m)
l_m	Membrane thickness (m)
n	Number of moles (mol)
$n_{d,i}$	Electro-osmotic drag coefficient (kmol/s-A)
$\dot{n}_H$	Proton flux through the membrane, (kmol/s)
N_A	Avogadro constant (6.02214199×10^{23} particles/mol)
N_i	Total molar flux of species *i* (mol/m^2-s)
Ox	Oxidant (mol)
p	Pressure (Pa)
P	Products (mol)
q	Electric charge (C)

$\vec{q}$	Heat flux (kJ/(m^{2}s))
q_c	Partition function
$\overline{q}_c$	Molar partition function
q_c^o	Standard partition function
Q	Net exchanged heat form the surrounding to the system (kJ)
r	Radius (m)
$\vec{r}$	Position vector(m)
R	Universal gas constant (8.314472 J/mol-K)
R_{cell}	Total resistance of the fuel cell (Ohm)
Red	Reductant (mol)
S	Entropy (kJ/K), active site.
$\mathbb{S}$	liquid saturation (-)
S_W	Wetting fluid saturation
S_{NW}	Non-wetting fluid saturation
s_W^{eff}	Effective saturation (-)
S_{NWr}	Residual saturation of the non-wetting fluids
S_{Wr}	Residual saturation of the wetting fluids
t	Time (s)
T	Temperature (K)
u	x-component of velocity (m/s)
U	Internal energy (kJ/mol)
v	y-component of velocity (m/s)
v	Reaction rate for activated complex (mol/(s.m^3))
ν	Vibration frequency
v_{red}	rate of oxidation (mol/(s.m^2)
V	Volume (m^3)
W	Total work performed on the system (kJ)
W_e	Extra-non-expansion work (or electric) (kJ)
$\dot{w}_{r,i,g}$	Volumetric mass generation of the specie i in gaseous phase (mol/m^3-s)
$\dot{w}_{r,i,l}$	Volumetric mass generation of the specie i in liquid phase (mol/m^3-s)
$\dot{w}_{r,T,g}$	Volumetric heat generation in the gaseous phase (mol/m^3-s)
x	Axial coordinate (m)
X_i	Molar fraction of the species i (-)

Y_i	Mass fraction of species *i* (-)
z	Number of electrons
Z	Compression factor
$\overline{Z}$	Correction factor to account for the change in contact angle due to roughness

Greek symbols

α	Transfer coefficient
α_G	Slip coefficient
β	Water content in the membrane
χ	Surface potential (V)
δ	Nernst diffusion layer thickness (m)
Δ_r	Derivative (of reaction)
ε	Porosity
σ_m	Local membrane protonic conductivity (S)
ϕ	Galvanic potential or electrical potential (V)
ϕ_e	Potential in the polymer electrolyte (V)
$\Gamma(s_W^{eff})$	Function of the effective saturation of the wetting fluid.
η_{th}	Thermal efficiency
η_{2nd}	Second law efficiency
η	Global overpotential (V)
η^a	Activation overpotential (V)
η^o	Ohmic overpotential (V)
η^c	Concentration overpotential (V)
κ	Transmission coefficient
λ	Thermal conductivity (W/m-K)
μ	Chemical potential (kJ/mol)
$\overline{\mu}$	Electrochemical potential (kJ/mol)
θ_{cW}	Intrinsic contact angle of the wetting fluid to the solid (rad)
ρ	Density (kg/m^3)
σ	Surface tension (N/m)

υ_i	Difference of the stoichiometric coefficients between products and reactants
$\upsilon_i^{'}$	Stoichiometric coefficients for specie *i* as a reactants.
$\upsilon_i^{''}$	Stoichiometric coefficients for specie *i* as a products
ξ	Extern of reaction (moles)
ψ	Volta potential (V)
ς	Dimensionless fugacity coefficient
Π	Product operator
Θ	Electrical field (V/m)

Subscripts

A	Anode
ads	adsorved
aq	Aqueous
c	Catalyst
ch	Channel
Ct	Cathode
d	drag
e	Extra, electron
el	Electrode
f	Formation
g	Gas
G	GDL
i	Chemical species
im	Specie *i* in the gas mixture
l	Liquid
m	Membrane
M	Metallic
Max	maximum
n_i	At constant composition of the other components
ox	Oxidant (mol)
o	Exchange state
p	At constant pressure
pol	Polymer
r	Reaction
r	Relative
rev	Reversible

ref	Reference
red	Reductant (mol)
S	Solution; at constant entropy
sd	Solid
T	At constant temperature
th	Thermal
V	At constant volume
w	Water
W	Wall
+	Corresponding to the hydronium ion
-	Corresponding to the sulfonic site in the hydrophilic region of the Nafion®

Superscripts

a	Activation
c	Concentration
eff	Effective
o	Standard state
o	Ohmic
0	Formal
p	Relative to the permeability
Sat	Saturation
-	Negative charge

Acronyms

ANL	Argonne National Laboratory
ANN	Artificial Neural Network
AFC	Alkaline Fuel Cell
ATC	Activated Complex Theory
CFCD	Computational fuel cell dynamics
CFD	Computational Fluid Dynamic.
CHP	Combined heat and power
DMFC	Direct Methanol Fuel Cell
DOE	US Department of Energy
EW	Equivalent weight
EMF	Electromotive force.
GDL	Gas Diffusion Layer
HHV	Higher Heating Value
IHP	Inner Helmholtz Plane
KTH	Royal Institute of Technology (Sweden)
LHV	Lower Heating Value

MCFC	Molten Carbonate Fuel Cell
MD	Molecular dynamics
MEA	Membrane Electrode Assembly
Mtoe	Million Tonnes of Oil Equivalent
NASA	National Aeronautics and Space Agency of the United States
NETL	National Energy Technology Laboratory
OECD	Organization for Economic Co-operation and Development
OHP	Outer Helmholtz Plane
OCV	Open circuit voltages
PAFC	Phosphoric Acid Fuel Cell
PEMFC	Proton Exchange Membrane Fuel Cell
PTFE	Polymerized TetraFluoroEthylene
SEM	Scanning electron microscopy
SOFC	Solid Oxide Fuel Cell
SPFC	Solid polymer fuel cell
STP	Standard Temperature and Pressure
TOCV	Theoretical open circuit voltage

Summary

1 Introduction 35
2 Fundamentals of PEM fuel cells 43
2.1 Description and function of components 45
2.1.1 End plates 51
2.1.2 Bipolar plates 52
2.1.3 Membrane Electrode Assembly (MEA) 55
2.1.4 Other peripheral devices 69
2.2 Basic theory of processes occurring in fuel cells 70
2.2.1 Thermodynamics 71
2.2.2 Electrode potential and interfacial phenomena 84
2.2.3 Kinetics of electrochemical reactions 93
2.2.4 Overpotential and polarization curve 109
2.2.5 A Simple Mathematical Expression for the Polarization Curve 122
2.3 Review of the models for PEM fuel cells 126
2.3.1 General Classifications of the Fuel Cell Models 126
2.3.2 Level of Complexity of the Model 128
2.3.3 Other Classifications 133
2.3.4 Review of Theoretical Fundamental Works 135
3 Measurement of the polarization curve 157
3.1 Materials and apparatus 157
3.2 Methodology 161
3.3 Results 162
4 Zero dimensional modeling and empirical parameters 167
4.1 Model validation 173
4.1.1 Results of the validation 175
4.1.2 Discussion of the validation 182
4.2 Results and analysis 186
4.3 Conclusion 187
5 Modeling flow with multicomponent diffusion 191
5.1 Basic definitions 192
5.2 Gibbs-Duhem relation 195
5.3 Basic conservation equations for multicomponent fluids 198
5.3.1 Conservation of mass 198
5.3.2 Conservation of linear momentum 201
5.3.3 Conservation of energy 208
5.3.4 Entropy balance 211
5.3.5 Constitutive relation for mass diffusion 213
5.3.6 Maxwell-Stefan equations 220

6 Analysis of the classic formulations for the driving force for diffusion 227
6.1 Analysis of the formulation from the species momentum equation 227
6.1.1 Reduction to Lam. 227
6.1.2 Reduction to Whitaker 230
6.1.3 Critique to the partial viscosity concept 231
6.2 Analysis of the formulation from the dissipation function. 233
6.3 Comparison of DF to SLM 236
6.4 Development and analysis of a formulation valid for general mechanical non equilibrium 237
6.4.1 Formulation for general mechanical non-equilibrium 237
6.4.2 Development by Kherkof and Geboers (2005) 240
6.4.3 Whitaker's equation for the diffusion velocity 242
6.5 Discussion on the extensions to creeping flow and summary 244
7 Modeling of transport in porous media 249
7.1 Volume –average models 249
7.1.1 Single-phase, multicomponent flow 252
7.1.2 Two-phase, immiscible, single component flow 256
7.1.3 Two-phase, miscible, multi-component flow 261
7.2 Maxwell-Stefan Models 263
7.2.1 Lightfoot's model 264
7.2.2 Dusty-gas model 264
7.2.3 Binary friction model 267
7.2.4 Analysis 268
8 Development of a general one component model for multiphase, multicomponent mixture 271
8.1 Conservation of mass of species i 273
8.1.1 Maxwell-Stefan formulation 274
8.1.2 Frame of reference 278
8.2 Phase momentum equations 279
8.3 Reduction to the binary friction model 280
8.4 Formulation of simple mass diffusion problems 283
8.4.1 Constant pressure, zero convective flow mass diffusion 284
8.4.2 Constant pressure, prescribed convective flow mass diffusion 287
8.4.3 Variable pressure, prescribed convective flow mass diffusion 290
9 Conclusion 295

References 301

1 INTRODUCTION

Control of energy sources has been one of the most important drives of civilization. Over the years, humanity has developed different alternatives for transport, storage and utilization of energy. Initially, wood and coal were used as energy sources. The advances in the natural sciences in the late 17th century allowed the design and construction of steam machines by Papin (1647-1712) and Savery (1650 - 1715). In the 18th century the industrial revolution provided a sudden impulse in the energy evolution with significant social consequences. But it was only in the late 19th century that the great age of energy development occurred with the wide control of the petroleum and electrical energy industries. In spite of the relatively short period of time (last 60 years approximately) in which petroleum and its derivate have been the main fuel source, a critical point in environment, energy delivery and social context has been reached. In the environmental scenario, continuous and massive emission of pollutants to the atmosphere has changed the delicate natural equilibrium with potential devastating consequences for life around the world. In the energy area, it is very likely that petroleum has reached its peak of production around 2005. The remaining petroleum reserves are harder to reach, the total reserves are declining fast, new discoveries have diminished and, in the long run, there is a clear tendency of scarcity of sources and elevation of prices. The political and economic issues that have followed the petroleum peak production have sparked the newest and intensive large scale research in alternative energies. The developments in alternative energy sources, mostly in the OECD nations, have increase vastly during the last years stimulated mainly by economic and strategic interests, i.e., nations seeking energy independency and intending to become major players in the technological markets, and, to a lesser extent, by the official environmental constraints imposed internally by the environmental agencies of individual nations.

The Brazilian energy scenario, as it stands in 2012, has some particular features when compared to the OCDE nations. The first is the relatively high participation of renewables, mostly in the electrical energy and industrial sectors. Second, there is a relatively high amount of electrical energy losses. The following data was extracted from the Brazilian National Energy Assessment (BEN, 2012) and from the Global Energy Statistical Yearbook (ENERDATA, 2012).

The Brazilian total energy consumption for the year 2011 was 272.2 Mtoe, corresponding to 2.06% of the world energy consumption. The participation of energy from renewable sources in the energy matrix in Brazil stands among the highest in the world. While the world average participation of renewables in the energy mix was 13% in 2011, in Brazil it reached 44%, which included hydropower (14.7%), sugarcane biomass (15.7%), other biomass (9.7 %) and other renewable sources (4.1%). When observing the consumer side, the industries account for 35.9% (of this total, 20.1% are in the form of renewable energy and 15.8% as non-renewable energy), transport for 30.1% (5.1% renewable), residential for 9.5% (6.5% renewable), the energy sector for 8.9%, the agricultural sector for 4.0%, and the services sector for 4.4%. Noteworthy is the fact that electricity has a participation of 18.1%, while the remaining 81.9% is used as thermal energy.

The total electricity supply (both domestic and imported) for 2011 was 568.8 TWh. Consumption accounted for 481.3 TWh, while the remaining 15.4% of losses are attributed to business and technical factors. This electrical energy supply is mostly renewable. While the global average of the participation of renewable sources in the electrical energy matrix was 20.1% in 2011, the Brazilian average stood at 88.8%, with an increase of 2.5% when compared to 2010. This participation originates mainly from two sources, the hydroelectricity (467.0 TWh) and the sugarcane biomass (37.2 TWh). Other renewable sources have a smaller contribution, but have experienced a fast growth. As an example, the electricity from wind presented a 75.8% growth between 2009 and 2010, reaching 928 MW of installed capacity producing 2176.6 GWh. Because of the large distances and the different regional needs in Brazil, diversification and decentralization of the energy matrix are strategic goals to be pursued in the next years.

From the alternative energy sources and conversion devices, fuel cells appear as a promising long term option. The principle of operation was described in 1839 and the first fuel cell was developed in 1845. However, the research in fuel cell technology only begun in the second half of the last century by the aeronautics and space agency of the United States (NASA). Then, other institutes continued this line of research mostly in the private sector. Nevertheless, important advances in research on hydrogen and fuel cells have been developed in institutes and universities around the word, and significant open literature is available.

In response to the needs of developing the fuel cell science and technology, Brazil made the strategic decision to develop a hydrogen

economy that would introduce hydrogen in the energy matrix by 2020. Basic research in fuel cells in Brazil started early (TICIANELLI et al., 1989; WENDT, GOTZ, and LINARDI, 2000). But only in 2002 government initiatives were formalized through the "Ministério de Ciência e Tecnologia" and "Ministério de Minas e Energia" to introduce the *Brazilian Program of Hydrogen and Fuel Cell System- ProCaC*. In 2005 this program was reformulated and called *Program of Science, Technology and Innovation to the Hydrogen Economy – ProH2*. This program focused on hydrogen production and fuel cell development. Networks of public, private institutions and companies have been since working towards common objectives.

The present work follows previous efforts at UFSC on hydrogen and polymer electrolyte membrane (PEM) fuel cells (MATELLI, 2001; STEIDEL 2005; ACEVEDO, 2006; PIÑA, 2006; SILVA, 2010; NUNES, 2011, MARIÑO, 2011) and looks at detailed analysis of the PEM fuel cell and its operation. Here, a comprehensive analysis of the thermodynamic, electrochemistry and mass transport to develop a theoretical model for a PEM fuel cell is proposed. The modeling addresses the different reaction and mass transfer phenomena that take place within a fuel cell. A major requirement for the PEM fuel cell operation is to keep the polymer humid during operation. Water is locally generated on the cathode side and this water migrates to the cathode gas and also across the polymer. Alternatively, the anode gas can also be humidified, providing extra water vapor on the anode side. The understanding of the phenomena that occurs within the fuel cell provides a way to understand the water and heat management of the system allowing for system optimization and enhancement of the fuel cell life.

OBJECTIVES

The main objective of the present thesis is to develop a theory for mass transport in a PEM fuel cell from a phenomenological analysis based on the fundamentals of the multicomponent, multiphase mass transport in porous media. The model aims at predicting the electric and mass transport behaviors with a formulation suitable for solution with current computational resources. To this end, specific objectives are:

1. To investigate the characteristic length scales of the different components and phenomena within the fuel cell as a base for criteria to define the needs of simulation.

2. To review and organize the vast amount of information about PEM fuel cell theory, modeling and simulation.

3. To review the relations between thermodynamic, electric and electrochemical processes in a PEM fuel cell.

4. To measure the polarization curve for a fuel cell system with the purpose of identifying the controlling transport and chemical phenomena, assess the applicability of the available lumped models and to determine the orders of magnitude of global parameters characteristic of the fuel cell operation.

5. To review the fundamental continuum and thermodynamic theories of mass and charge transport in two-phase, multicomponent flow in porous media.

6. To develop a phenomenological model for mass and charge transfer applicable to PEM fuel cells from the fundamental continuum and thermodynamic theories for flow and mass transfer in porous media.

CONTRIBUTION

The available state-of-the-art models usually either develop overall lumped-component models using simpler semi-empirical equations for the components or blend different point-wise detailed models into a single simulation tool. More rarely the models focus on specific behavior of fuel cell components on an attempt to better understand the role of micro and nano phenomena on the macroscopic output. The major difficulty in using the detailed models and interpreting their results is that the large superposition and interrelation of different modeling principles, sometimes with conflicting requirements, like a patchwork, produces a very rich macroscopic picture with sometimes faulty local features.

As an example, consider the current models that blend CFD type models (Navier-Stokes, energy and conservation of mass) for the channel, extended forms of Darcy's and Fick´s laws for flow and mass diffusion across the GDL, the Focker-Planck equation for ionic transport across the MEA and empirical equilibrium relations and transport coefficients. Since the MEA forms a single diffusion media, why is there a change in framework, from Fick's law to Focker-Planck when one proceeds from the GDL to the membrane, requiring different solution methodologies and understanding for the local properties?

This patchwork is understandable since the fuel cell modeling grew linking traditional models from the CFD, porous media, membrane and electrochemistry communities into single usable algorithms. These models provided the basic footwork for fuel cell and stack developments, being now available commercially, for example, with FLUENT® and COMSOL®, but have reached some limitations. These

limitations rest on the detailed models themselves that need now to be improved to allow for the future developments.

In this work, we propose to return to the basics and look again the fundamentals continuum models applicable for modeling mass transport in fuel cell's MEA. From the basic description an integrated liquid, gas and species mass transport model is proposed and applied. The model will be used in future work to critically assess the importance of the different chemical and transport phenomena, pointing to the need for detailed molecular modeling and to the possibilities of design and operation of fuel cells.

STRUCTURE OF THE DOCUMENT

This document is divided into 3 parts. The first part includes chapters 2 to 4 and describes the thermal and electrochemical characteristics of PEM fuel cells, the measurement of the polarization curve and the modeling using lumped models. The second part includes chapters 5 and 6 and presents the basic continuum mechanics and thermodynamic theories for the transport in multicomponent mixtures. Finally, the third part comprises the remaining chapters and develops the fundamental theories for heat and mass transfer in fuel cells, with emphasis in the modeling of the membrane and porous layers.

The chapters cover the following contents.

Chapter 2 presents the fundamentals of PEM fuel cells. It presents a detailed description of the fuel cell components and the origin of the fuel cell operation voltages. Description of the components involves features as material, geometry and length scales, which are relevant to model development and numerical simulations. The presentation of the factors affecting the fuel cell voltage requires a description of the potential of working cells as well as a description of the polarization curves. A review of the models for PEM fuel cells is presented. First, there is a discussion about the complexities involved in the models, that is then followed by an attempt of a general classification of the available modeling efforts. Later, a chronological description of theoretical fundamental models since the pioneering works of Bernardi and Verbrugge (1991 and 1992) and Springer et al. (1991 and 1993); to present 3D CFD models is presented.

Chapter 3 presents the measurement of the polarization curve of a 200 W fuel cell stack. The values of current and overvoltage are determined for the activation and ohmic regimes for different operation temperatures using saturated hydrogen and oxygen.

Chapter 4 presents the application of a lumped-component model and the estimation of the basic macroscopic characteristic of the fuel cell

used in Chapter 3. Special emphasis is devoted to the treatment of the mass transfer limitations, using two different mass transfer models, validated against other measurements available in the literature. This chapter identifies operation features and magnitudes of fluxes and global transport parameters. It also points to the need of detailed modeling.

Chapter 5 reviews the modeling of flow with multicomponent diffusion. The basic conservation equations for mass, linear momentum, energy and entropy are presented and discussed within the frameworks of continuum mechanics and thermodynamics of irreversible processes. The constitutive relation for the mass transfer is then developed, within the classic framework of the Maxwell-Stefan treatment.

Chapter 6 presents a critique of these models and isolates a model for the driving force for mass diffusion with a minimum of limiting assumptions.

Chapter 7 reviews the modeling of mass transport in porous media, with emphasis to multicomponent mass transfer in two-phase flow. In this chapter different approaches based on volume-averaging and general Maxwell-Stefan formulation are critically revised.

Chapter 8 presents a general homogeneous one component model for multicomponent two-phase flow in porous media under the limits of low Reynolds and low Peclet number flows. The model is compared to alternatives from the literature and applied to simpler mass diffusion problems in order to elucidate the role of the bulk convective flow and pressure gradient.

Chapter 9 presents conclusions and recommendations for future work.

Part I

Proton exchange fuel cell (PEMFC): Description and semi-empirical modeling

The main objectives of this first part are to describe the thermal and electrochemical characteristics of PEM fuel cells, the measurement of the polarization curve and the modeling using lumped models. Both the measurement and modeling are applied to a specific 200 W PEM fuel cell stack operating under steady-state conditions with pure hydrogen and oxygen.

Initially, in chapter 2, the different components forming a typical PEM fuel cell are described, with special attention to the Nafion® structure, water and ion transport. The thermodynamic and electrochemical phenomena that are in the origin of the electrical potential are then presented following the classical approaches.

In chapter 3, a specific 200 W PEM fuel cell stack and the apparatus used to measure the polarization curve are presented. The measurements are done following traditional methodologies. In chapter 4, a set of lumped semi-empirical equations is applied to describe the measured polarization curve. The important macroscopic parameters are obtained from a curve fitting procedure and are compared to values from the literature. Special emphasis is devoted to the mass transfer limitation, modeled using two different mass transfer models, as a motivation for part II of this work.

2 FUNDAMENTALS OF PEM FUEL CELLS

A fuel cell is an electrochemical device that continuously converts chemical energy into electrical energy (and heat) as long as fuel and oxidant are supplied (HOOGERS, 2003). Fuel cells are today one of the most efficient electrical energy generation devices and are adapted to the current environmental and sustainable requirements for the electrical energy generation. They are one of the core components in a hydrogen-based energy economy (YANG and PITCHUMANI, 2006). Besides the environmental advantages, fuel cells have a high energy conversion efficiency, low pollution, and no dependency on depleting fossil resources (YANG and PITCHUMANI, 2006) when compared to other means of generation of electricity from fuel such as internal combustion engines and thermoelectric devices. Thermodynamically, when comparing fuel cells with heat engines, the most striking difference is that the latter are limited by the Carnot efficiency while fuel cells are not (HOOGERS, 2003). In addition, depending on their operation temperature, their exhaust gas can be used for cogeneration. They are also compact, noiseless, and provide a continuous and high quality reliable current. A general structure of a single cell is composed of two electrodes separated by an electrolyte. All fuel cells work with the same basic principle: at the anode a fuel, such as hydrogen, is oxidized into electrons and cations, while at the cathode, an oxidizer, such as oxygen, is reduced to oxide species. Depending on the electrolyte, either protons or oxide ions are transported through the ion-conducting, but electronically insulating, electrolyte, to combine with oxide or protons to generate products, electric power and heat. The most common way to classify the fuel cell is according to the nature of the electrolyte, as shown in Table 1. There are also differences in the operation temperatures, type of fuel and ions that cross the electrolyte.

Table 1 - A few fuel cells classified by the electrolyte material

Initial	Fuel cell type	Operating temperature
PEMFC	Proton Exchange Membrane FC or Polymer Electrolyte Membrane FC	30 – 100°C
AFC	Alkaline Fuel Cell	50 – 200 °C
SOFC	Solid Oxide Fuel Cell	750 – 1000 °C
MCFC	Molten Carbonate Fuel Cell	~ 650 °C
PAFC	Phosphoric Acid Fuel Cell	~ 220 °C
DMFC	Direct Methanol Fuel Cell	20 – 90 °C

Sources: U.S.A, 2006; Larminie and Dicks, 2003.

Proton Exchange or Polymer Electrolyte Membrane Fuel Cells (PEM fuel cell) stands out because of their simplicity and high power density, which makes them the choice for compact stationary electrical generation systems and mobile applications. PEM fuel cells can achieve efficiencies as high as 50% even for small size units (1 to 5 kW). They take their name from the polymeric membrane used as the electrolyte. Historically, they were also called the Solid Polymer Electrolyte Fuel Cell (SPEFC) and the first operational products were developed by General Electric in The United States in the 1960's for use by NASA. The polymer electrolyte works at low temperatures, which has the advantage of quickly starting. Because of the thinness of the membrane electrode assemblies (MEA) compact fuel cells can be made. Further advantages are that there are no corrosive fluid hazards and that the cell can work in any orientation. However, at the time of the Apollo program, the problem of water management in the cell was judged too difficult to overcome reliably and NASA ended up selecting the alkaline fuel cell in its Apollo vehicles. The developments over recent years have brought the current densities up to around 1 A/cm^2 or more in the best conditions, while at the same time reducing the use of platinum by a factor of over 100 compared with the first General Electrical fuel cell models. It could be argued that PEM fuel cells exceed all other electrical energy generating technologies with respect to the scope of their possible applications. They are a possible power source of a few watts for powering mobile phones and other electronic equipment such as computers, right through to a few kilowatts for boats and domestic systems, to tens of kilowatts for cars, to hundreds of kilowatts for buses and industrial CHP systems (LARMINIE and DICKS, 2003).

Among the most interesting challenges on low-temperature fuel cell research are the poisoning of the membrane by the effects of CO, the improvement of the biological route for hydrogen production, the direct electricity generation by microbes and the alcohol fuel cells.

By overcoming the CO poisoning of the MEA, a wide range of fuels originating from thermochemical, such as gasification, or biological, such as anaerobic digestion, processes will become available for use in PEM fuel cells. **(**RESHETENKO, BETHUNE, and ROCHELEAU 2012)

The improvement of biological routes for obtaining hydrogen and directly as biological fuel cells has significant advantages as an energy conversion process since they operate at ambient condition (low temperature and pressure), avoid the post treatment of the effluent, do

not transport or consume significant amounts of energy and use residual sources as wastewater and glycerol, the byproduct of the catalytic transesterification of bio-oil to biodiesel (BICAKOVA e STRAKA, 2012). Among the biological processes for energy generation, the microbial fuel cells (MFCs) show a promising future. MFCs are not a new technology, since they are known from the early 70s, but only recently this technology has been developed to the point of producing net power, providing possible opportunities for practical applications (RABEY and VERSTRAETE, 2005).

The direct alcohol systems, for example, the DMFC and DEFC converting methanol and ethanol, respectively, are more compact when compared to PEMFC because they do not require the presence of heavy and bulky external fuel reformers and can be applied especially for the generation of electric power in mobile and stationary applications. All these issues have encouraged scientists and researchers to directly use liquid fuels to power fuel cells, leaving aside the difficulties and the dangers associated with handling, storage, transport and distribution of reactant gases such as hydrogen (SONG et al., 2006).

2.1 DESCRIPTION AND FUNCTION OF COMPONENTS

A unit fuel cell is composed of three main sections: end plates, flow field plates and the membrane electrode assembly (MEA). End plates are two external plates that act as structural support for the fuel cell and can also act as total current collectors (in the case of having a current conductor side). Even when many individual fuel cells are stacked in a single fuel cell system, the amount of end plates remains the same, two. The number of flow field plates however increases with the amount of individual fuel cells, one for each new one. Flow field plates are generally made of graphite composites and among other functions they distribute the reactants to the surface of the MEA. When stacked, each individual cell is separated by at least one flow field plate. Generally, channels are etched in both sides of the internal flow field plates giving them dual function, as an anode plate on one side and cathode on the other (bipolar plates).

Figure 1 -A schematic description of the components of a PEM fuel cell.

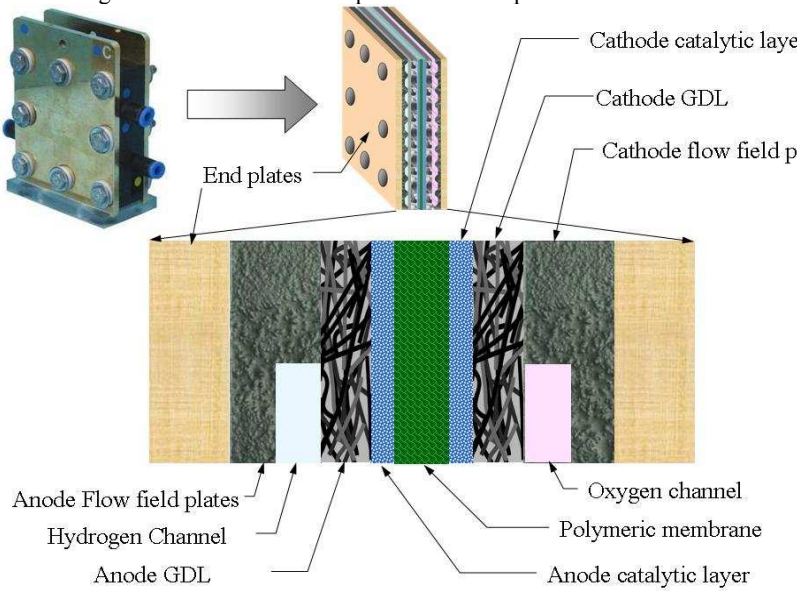

MEA consists of two porous electrodes separated by the electrolyte, an ion conducting membrane (PEM design). Each electrode is composed of two layers, a thin catalyst layer adhered to an electrically conductive porous substrate or gas diffuser layer GDL. The electrolyte, commonly called membrane, is a proton exchange, electrical insulator, gas impermeable polymeric membrane. Figure 1 is a rendering of a hydrogen-oxygen PEM fuel cell showing the different components and their location inside a unit hydrogen-oxygen PEM fuel cell in cross section.

The operation of the cell, can be explained as follows. When arriving to the fuel cell stack, hydrogen enters by the channel etched on the flow field plate of the anode side, diffuses across the GDL and reaches the anode catalyst layer. The correct spreading of the hydrogen especially onto the catalytic area underneath the support ribs of the flow field plate is one of the most important functions of the GDL. On the catalyst layer, hydrogen splits into protons and electrons. Protons continue the path in the same direction crossing the polymeric membrane, either as hydronium molecules or as free cations, reaching the cathode catalyst layer. Several transport mechanisms can be present in the proton´s transport. In most theoretical models they are all summarized on the drag coefficients. On the other hand and due to the

non-electrical conductor properties of the electrolyte, electrons are obliged to make an external path through the GDL and ultimately to the electric terminals of the fuel cell stack. Figure 2 shows a rendering of the different fluxes present when a fuel cell is working: The flux of electrons (orange), hydrogen gas and hydrogen cations (light green), oxygen (pink), water (light blue) and heat (orange arrow).

Figure 2 – Rendering of the different fluxes in an operating fuel cell.

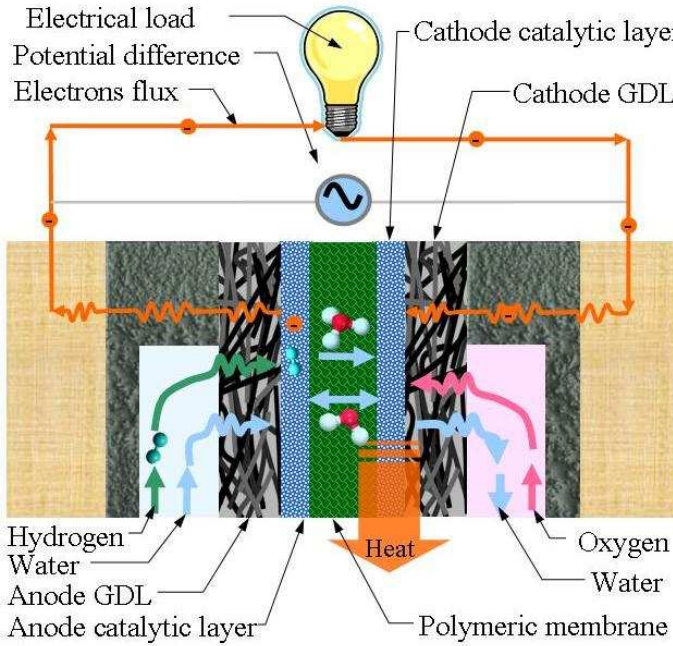

After passing through the load and delivering the energy, electrons enter by the end plates, the flow field plates and the GDL of the cathode to reach the cathode catalyst layer. The oxidant, O_2, coming from the cathode flow field plate channel diffuses through the gas diffusing layer and also reaches the cathode catalyst layer to react with protons and electrons in an exothermal reaction. In this case, water and heat are the only products. The generated heat is conducted back through the GDLs and flow field plates which form a link with the adjacent cells, cooling plates or end collector plates, finally reaching the external ambient.

Water has a more complicated path inside the fuel cell due to its function in the ionic transport process. In general, hydrogen must be humidified before entering the fuel cell. The polymeric membrane needs a minimum level of hydration in order to be able to conduct protons. That's because the proton conduction process relies on using the water channels as routes. This transport of protons produces an additional water flux from the anode to the cathode, which, depending on the electrical current delivered, could be greater than the water flux due to the concentration gradient that acts in the opposite direction. Efficient water management inside the fuel cell is necessary in order to guarantee a uniform water uptake in the membrane.

The dimensions of the components of typical fuel cells span many orders of magnitude, from the macro-scale, corresponding to the global cell and channel dimensions (height, width, thickness), passing through the micro-scale, corresponding to the thickness and pore diameters of the GDL, finally reaching the nano-scale that corresponds to the pore in the membrane and the catalyst crystallites. Table 2 presents a comparison of the order of magnitudes of the dimensions of the different components of the fuel cell.

Figure 3 presents a detailed rendering of the different layers showing the structure, materials and chemical species within them and the ideal transport processes that occur when the cell is operated. Some dimensions within the fuel cell can also be observed.

Table 2 - Characteristic length scales of fuel cell components

Dimension	1×10^{-3}m	1×10^{-6}m	1×10^{-9}m	1×10^{-10}m	Ref
	mm	μm	nm	Å	
Global dimension (Macro scale)					
Length	100				
Width	100				
Thickness	10				
Bipolar plates (Macro scale)					
Thickness	1,2				2,10
Channels height		700			
Channels width		700			
Gas diffusing layer (GDL) (Micro scale)					
Thickness		200-500			1,10
Carbon paper		190-270			6
Carbon cloth		380			6
Carbon cloth fiber diameter		7-10			2,4,
GDL pore diameter		10-30			6
					6
Catalyst layer (Micro-nano scale)					
Thickness		5-30			1,3,
					10
Carbon particle agglomerate			200-		5
Carbon agglomerate pores			300		5,6
Carbon support particles			40-500		1,5,
Carbon particle pore			20-40		7
Catalyst Particle			20-40		5
			<4		7,9
Membrane (Micro-nano scale)					
Thickness		25-250			1,3,
					10
Diameter of the pore throat				10	8,10
Diameter of the pore bulk				40	8,10
Distance between bulks				50	8
Molecules sizes (Nano scale)					
Water molecule				1.20	
Hydrogen molecule				0.74	
Oxygen molecule				2.90	

Sources: 1. LARMINIE and DICKS 2003.[fig1.6/pg73/75]; 2. HOOGERS 2003. [fig4-14/pg4-12/]; 3. ZIEGLER 2005. [fig 1.2]; 4. GURAU et al 2006. [fig3]; 5. GURAU et al 2007. [Pg 795]; 6. MATHIAS, M. et al 2003. [pg 3,4,5,6]; 7. NITTA, I. 2008. [pg17]; 8. HAMANN, C. 1998.[pg 297] ;9. USA DOE. 2004b. [pg3-6]; 10. BASCHUK, J.J. LI X. 2004

Figure 3 - Zoom representation of the different layers forming the fuel cell. A detailed rendering of the transport of participating species and the boundaries between adjacent layers is also presented

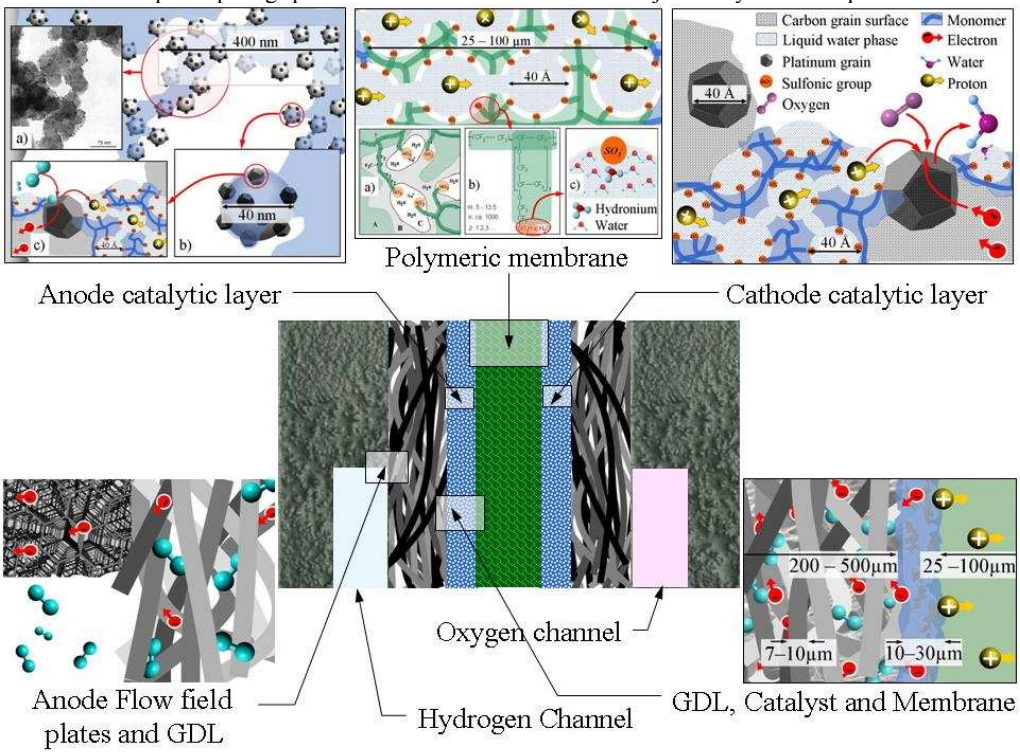

In the following, each component is analyzed separately.

2.1.1 End plates

The end plates of fuel cell assemblies are used to fasten the inner stack, as shown in Figure 4. The most important requisite for end plates is that they must be rigid throughout their length and height, so that they can provide even pressure over the MEA´s surface, (HURLEY, 2002). They also, reduce the contact resistance and provide a seal on the MEA. End plates therefore require sufficient mechanical strength to withstand the tightening pressure, small weight, and stable chemical/electrochemical properties, as well as providing electrical insulation. Since end plates should not deform under operating temperature, pressure and moisture conditions, they must have a certain degree of mechanical strength and stiffness (KIM et al, 2008). End plates were typically made from metals such as aluminum, titanium, and stainless steel alloys, but due to corrosion, heat losses, and their excessive weight, alternative material such as plastics have been considered. Composite materials consisting of combinations of metals and polymers have also been proposed for end plates to enhance their mechanical strength. Also, end plates can be used as total current collectors. In this case, a gold or copper thin coating can provide a conductive surface that connects with a graphite foil plate and conveys the electricity to the binding posts. Kim et al (2008) presents a review on end plates with a complete classification where three design criteria for end plates are considered: materials, connecting methods and shape.

Figure 4 - End plate localization inside the fuel cell (KIM, 2008).

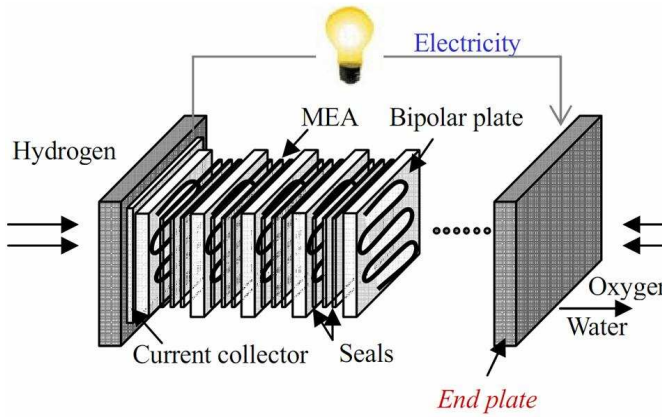

2.1.2 Bipolar plates

Bipolar collector/separator plates are plates that make a physical limit and electrical connection between each unit cell (Figure 4) when they are organized in a stack structure. They have a strong effect on the architecture, mass, volume and mechanical strength of the total stack (GRANIER et al., 2004). Bipolar plates must provide electric connection between two adjacent MEAs, adequate even gas distribution on the catalyst layer and also help with water (removal) and heat management in the overall cell. All these functions determine their required properties namely (BARBIR, 2006): high electrical conductivity for connect cells electrically in series; impermeability to reactant gases since they must separate the gases in adjacent cells; to have adequate mechanical strength and be lightweight due to the necessity to provide structural support for the stack; good thermal conductivity owing to their need to conduct heat from active cells to the cooling cells; to hold conformable properties since typically they house the flow-field channels; stability and corrosion resistance inasmuch as the corrosive environment inside the fuel cell. In addition, the material must be affordable and easy to machine, and the manufacturing process must be suitable for mass production.

Commonly two kinds of material have been used for PEM fuel cell bipolar plates, namely graphite-composite and metallic. Metals (steel, titanium nickel) have desirable characteristic like high electronic and thermal conductivity and exhibit excellent mechanical properties, nevertheless they are less desirables causes due to the difficulty and cost of machining and their limited corrosion resistances. Due to the very corrosive environment (pH 2-3 and temperature 60°- 80° C) they are exposed to inside fuel cell, they would corrode and dissolved metal ions toward the membrane reducing its ion conductivity. Corrosion layer also would increase electrical resistance. As a solution for the later trouble, metallic bipolar plates must be adequately coated with a non-corrosive yet electrically conductive layer (graphite, diamond-like carbon, conductive polymer, organic self-assembled polymer, noble metals, metal nitride, metal carbides, indium doped tin oxide etc.) (BARBIR, 2006). Graphite based materials are a good option because among other features they are low cost and chemically resistant. Some techniques include development of plates based on graphite foil, which can be cut, molded, or carved in relief in order to generate a flow field pattern. Another cost-effective volume production technique is injection or compression molding (HOOGERS, 2003). Common carbon composite

materials used are thermoplastics (polypro-pylene, polyethylene, or polyvinylidenefluoride) or thermoset resins (phenolic, epoxies and vinyl esters) with fillers (such as carbon/graphite powder, carbon black or coke-graphite) and with or without fiber reinforcements. They are typically chemically stable in fuel cell environments, and could be suitable for compression, transfer or injection molding.

One of the most important functions of bipolar plates is the electrical conduction. Values in the range of 50,000 to 200,000 S/m are typically found for bulk electrical conductivity of graphite-composite bipolar plates. Despite the lower values when compared with pure graphite and metallic plates, they are sufficient for the function in the cell. The most significant difficulties today are the fuel cell stack contact (interfacial) resistance and one of interesting research topic nowadays in the fuel cell area.

Bipolar plates also have the function of flow field plates for supplying the reactant gas from the inlet to the GDL, and as a structural support for the MEA. They must be several millimeters thick, mainly to give them mechanical strength and allow the engraving of flow channels. As a flow field, channels are etched into the side of the plate next to the GDL. Channels can exist on either side of the flow field plate such that it forms the cathode plate on one side and the anode plate on the other side, where the term bipolar plate is taken. The form and dimensions of the channel have strong influence on distribution of the reactant on the catalyst. Flow field design also affects water supply to the membrane and water removal from the cathode (HOOGERS, 2003). The Channel is typically rectangular in cross-section; however other configurations have been studied (LI and SABIR, 2005) such as trapezoidal, triangular, and semi-circular. The Channel width and depth are between 1 and 2 mm, less than 1 mm is not recommended. Product water removal at the cathode is even more complex as this represents a two-phase flow problem. Parallel channels can lower the pressure differential between the gas inlet and outlet but cannot avoid the droplet formation in the channel. Droplets tend to coalesce and form larger droplets partially obstructing the channel. The reactant flux will be redistributed and some part of the membrane will not receive a reactant becoming inactive (HONTAÑÓN et al., 2000).

Optimum equilibrium between dimensions of open area (channel) and contact area (landing ribs) is necessary. Open area is used to supply the reactant while contact area is used for current conduction. The size of the open structure depends on the resistivity of the material used, the size of the MEA, the operating pressure and the current range envisaged.

A solid blank sheet is the best electrical conductor, which does not allow any gas access, while an entirely open structure, convenient for good reactant distribution, does not allow any current to flow. The task of achieving the right structure can be done by fluid-dynamic modeling in combination with experimental evaluation of a large number of different designs. Some studies have determined that porous material plates instead of grooved flow field plates, show better performance (HONTAÑÓN et al., 2000).

Since bipolar plates constitute more than 60% of the weight and 30% of the total cost in a fuel cell stack, several configuration have been proposed (see Figure 5). Amongst all of the characteristics, the classification based on channel shape is one of the preferred ones.

Figure 5 - Flow field designs. a) Pin-type, b) straight and parallel channel, c) single serpentine, d) interdigitated (LI and SABIR, 2005)

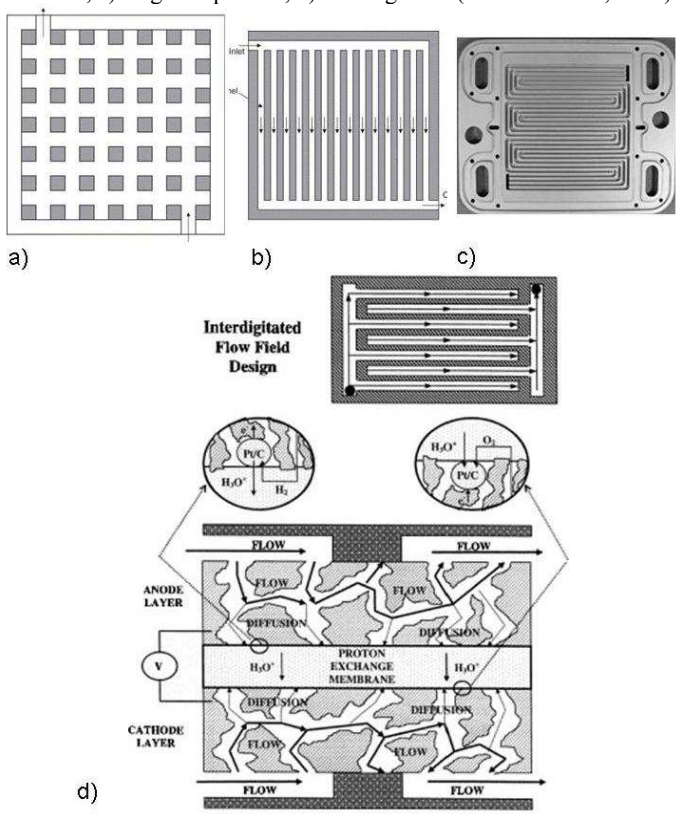

The typical designs are; pin-type, series-parallel, serpentine, integrated and interdigitated flow field. Interdigitated channels force the flow through the GDL from one channel to the other. Li and Sabir (2005) presents a description of all these types of bipolar plates, while Arato et al. (2006b) evaluated their advantages when compared to the serpentine flow field.

2.1.3 Membrane Electrode Assembly (MEA)

MEA is the unit responsible for the most important function in the fuel cell, the electrochemical reaction and the protons and electrons transport, whit the consequent electrical current generation. MEA consists of two gas diffusion electrodes, formed by a baking layer or substrate (commonly known as GDL) with a thin layer catalytic, and separated by the polymeric membrane (ion conducting membrane). The GDL are porous materials generally made of carbon cloth or paper, catalytic layer is platinum supported on carbon suspense in a polymeric matrix intimately glued to the electrolyte membrane, and the membrane is a solid polymer electrolyte. Table 3 summarizes the roles of the components of the MEA.

Table 3 - Characteristic MEA components and their roles (Source: HOOGERS, 2003).

MEA component	Role / Effect
Anode GDL	Fuel supply and distribution (hydrogen/gas fuel) Electron conduction Heat removal from reaction zone Water supply (vapor) into electro-catalyst
Anode Catalyst layer	Catalyst of anode reaction Proton conduction into membrane Water transport Heat transport
Proton exchange Membrane	Proton conduction Water transport Electronic and reactant insulation
Cathode catalyst layer	Catalysis of cathode reaction Oxygen transport to reaction sites Proton conduction from membrane to reaction sites Electron conduction from GDL to reaction sites Water removal from reactive zone into substrate Heat generation/removal
Cathode GDL	Oxidant supply and distribution (air/ oxygen) Electron conduction toward reaction zone Heat removal Water transport (liquid/water)

The electrodes are a complex structure of open gas pores, proton conducting ionomer and catalyst on highly porous carbon supports that serve as the electron conducting phase. The catalyst layer on either side of the membrane contains the necessary amount of electro-catalyst to allow the electrochemical reaction in the cell operating temperature. Membrane serves as an ion conductor and a species barrier, impermeable, as much as possible for the reactants and electrons.

2.1.3.1 Membranes

The main function of the membrane is the proton transport in wet condition, but also serves as electron insulator and gas barrier between the two electrodes (HOOGERS, 2003). PEM fuel cells were initially developed by General Electric around the middle of the 1960´s, but the membranes short durability was only solved in the late 1960´s when the E. I. DuPont Company developed Nafion®, a perfluorinated sulfonic acid membrane, developed from polymerized tetrafluoroethylene (DuPont trade name Teflon®).

Nafion® works as a cation selective membrane. These membranes are, in general, made of a cross-linked polymeric network in which functional active groups are fixed. The active groups may be carboxylic $-(CO_2)^-$ sulfonic $-(SO_3)^-$ and other organic radicals. Beyond Nafion, other examples of proton conducting membranes are polysulfone (PS), polybenzimidazole (PBI) and polyetheretherketone (PEK, PEEKK and PEEK) (ALBERTI and CASCIOLA, 2001; JESUS, 2005; KÄFER, 2010; FIMRITE, J. A. 2002.). Besides the application in PEM fuel cells, Nafion is also used for Cl_2 production via chlor-alkali cells (VAN der STEGGEN et al., 1999a).

Nafion is produced by copolymerization of a perfluorinated vinyl ether (4-methyl-3,6 –dioxa-7-octene-1-sulfoyl fluoride) co-monomer with tetrafluoroethylene (TFE) (MAURITZ and MOORE, 2004), resulting in long chains formed by repetition (100 to 1000 times) of a unit of monomer. Figure 6 shows a representation of a unit of monomer. One molecular chain can contain between 100 to 1000 units.

Figure 6 - Representation of the molecular unit of the Nafion® chain. (MAURITZ AND MOORE, 2004).

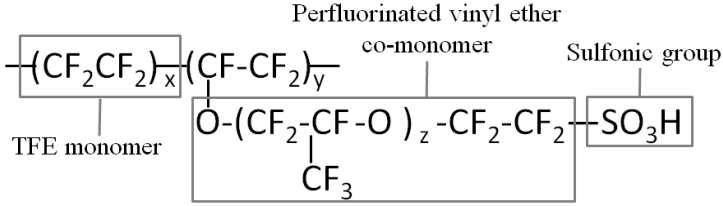

Structurally, Nafion® is formed by hydrophobic polytetrafluoroethhylene (PTFE) long backbone chain with regular spaced perfluorinated vinyl ether pendant chains each terminated by a strongly hydrophilic sulfonated ionic group $-(SO_3)^-$ (HAUBOLD, et al., 2001). The total amount of these pendant chains add up to at most 10% in moles of the whole polymer (HEITNER-WIRGUIN, 1996). The ratio $x/y = m$, shown in Figure 6, gives the average frequency of TFE-monomers into the unit and has a value between 5 and 13 (WENDT, GOTZ, and LINARDI, 2000) with average value around 6,5 (JANG et al., 2004). The number of O-CF_2-CF units within the co-monomer, z, usually has value of the unit (z=1) for Nafion® (SOUZY and AMEDURI, 2005). The equivalent weight EW is the mass in grams of dry Nafion per mole of sulfonic acid groups when the material is in the acid form. This is an averaged value related to m by $EW = 100m + 446$. The Nafion® membrane is identified by the value of EW divided by 100 followed by a digit that refers to the thickness of the membrane in mil (1mil = 0.001 inch = 0.0254 mm) (FIMRITE, J. A., 2002). For example, Nafion 117 is a 1100 EW (EW = 1100 g/mol) Nafion membrane with thickness 7 mil (0.007 in, ~ 0.1715 mm). On average, this membrane has 14 CF_2 groups (m = 7) separating adjacent side chains. The ion exchange capacity IEC = 1000/EW is commonly used to identify ion-exchange membranes (MAURITZ and MOORE, 2004).

When hydrated, the water molecules within Nafion® cluster around the sulfonic groups. The PTFE regions are hydrophobic, while the $-(SO_3)^-$ regions are hydrophilic, i.e., Nafion® presents a nanosegregated structure (JANG et al., 2004). Intermediate phases may exist between the hydrophilic and hydrophobic phases (YEAGER and STECK, 1981). Essentially, water is confined to form proton conducting channels and the sulfonic groups form the hydrophilic surfaces. The polymer chains, supporting the sulfonic groups, form the hydrophobic regions and provide flexibility to the membrane. Results from small

angle X-ray scattering (SAXS) combined to MD simulation indicate the presence of about 10 vol% Nafion® crystallites in the form of long rods parallel to the water channels embedded in the amorphous PTFE matrix (SCHMIDT-ROHR and CHEN, 2007, SCHMIDT-ROHR and CHEN, 2008a). These crystallites provide much of the membrane mechanical strength acting as physical crosslink preventing a complete dissolution at moderate temperatures (INZELT et al., 2000). The topology of the hydrophilic and hydrophobic surfaces creates size-dependent, wettability and long-range electrostatic effects and also a percolation threshold for ionic charge motion.

In order to develop an appropriate understanding of the behavior of hydrated Nafion® as a proton conducting membrane, the molecular and matrix structures and their interaction with water molecules must be described. This conceptual and quantitative description has been obtained by the combined use of observation, measurement and modeling techniques. Figure 7 presents the characterization of a Nafion® membrane at progressively smaller scales using various techniques. In the figure, (a) Optical photograph of the Nafion® membrane revealing details at the centimeter scale; (b) Membrane surface observed with atomic force microscope, revealing surface features as molecular roughness. Small- and wide-angle scattering techniques (SAS and WAS) provide additional characterizations in this scale; (c) Rendering of the polymer chain forming Nafion® in contact with water molecules, revealed at the nanometer scale. The sulfur atoms are depicted as yellow spheres

Figure 7 (a) presents a photograph of the Nafion® membrane revealing details at the centimeter scale. Details at the sub-millimeter scale are observed with optical microscopy techniques. Figure 7 (b) presents the membrane surface observed with atomic force microscope (AFM). At this micrometer scale, surface features such as molecular roughness are observed. Observation and measurement techniques include electron (SEM/TEM) and atomic force microscopes (AFM) and small- and wide-angle scattering techniques (SAS and WAS respectively). Figure 7 (c) presents a representation of the atoms forming the Nafion® molecule, which are features revealed at the nanometer scale.

Figure 7 - Characterization of a Nafion® membrane at progressively smaller scales using various techniques. (From: DIAT and GEBEL, 2008)

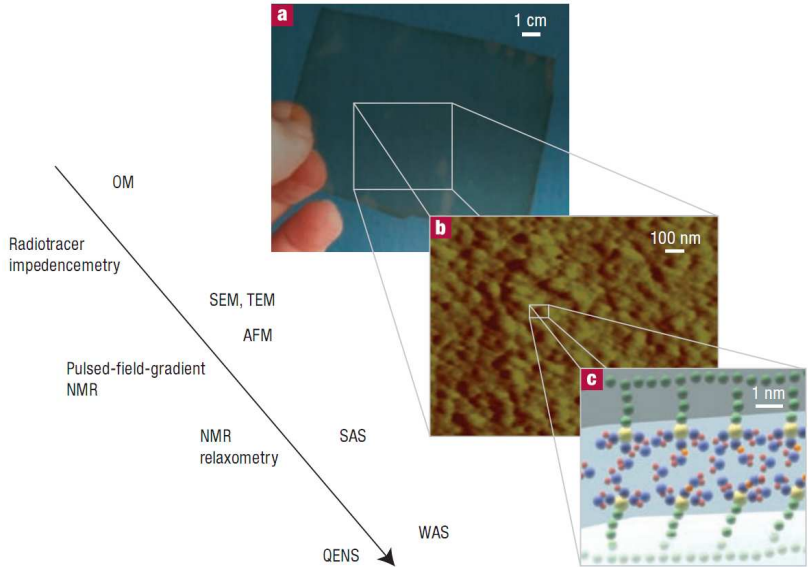

Dynamic observation techniques include quasi-elastic neutron scattering (QENS), NMR spectroscopy and diffusion techniques (DIAT and GEBEL, 2008). The modeling techniques are based mainly on Molecular Dynamic Simulation (MDS) models to calculate the scattering intensity in small-angle X-ray or neutron scattering (SAXS/SANS) for a tentative Nafion® structure, seeking to match the calculated and measured scattering results.

2.1.3.1.1 Structure

Gierke and co-workers (GIERKE et al., 1981; HSU and GIERKE, 1982; HSU and GIERKE, 1983) were the first to propose a cluster-network model for the Nafion morphology. In this pioneering work, from information obtained from small and wide-angle x-ray diffraction (SAXD and WAXD) and assuming the minimization of interfacial area, i.e., the minimization of the total energy of the membrane (WEBER and NEWMAN, 2003), Nafion® was thought as organized in a series of inverted spherical clusters (reverse micelles) with about 4 nm diameter connected by short cylindrical pores 1 nm diameter forming a three-dimensional network. According to the author, this configuration minimizes both, the hydrophobic interaction of water

with the backbone and the electrostatic repulsion of proximate sulfonated groups (HSU and GIERKE, 1983). The growth of clusters by increasing the water content occurred by a combination of expansion of cluster size and redistribution of sulfonated sites, yielding fewer cluster for higher water content. In this model, by assuming a simple-cubic lattice, the cluster diameter, the number of exchange sites per cluster and the number of water molecules per exchange site increased linearly with water content. From this initial model, other interpretations of SAXD, WAXD and transport data have led to slightly different models, however all of them rely on the same basic network structure (see the review by Mauritz and Moore, 2004).

This view endured more than 20 years and was replaced recently by a picture that depicts Nafion® as an amorphous/crystalline structure in which the water is not confined in spherical cavities but separating fibrillar objects, running in parallel through the material and, as hydration increases, it forms a continuous medium around an intrinsic anisotropic structure (ROLLET et al., 2002, RUBATAT et al., 2002. RUBATAT et al., 2004; RUBATAT, GEBEL, and DIAT, 2004; SCHMIDT-ROHR and CHEN, 2008a, SCHMIDT-ROHR and CHEN, 2008b). The new view of Nafion® is based on evidence of the crystallinity at low scattering vector q_{SA} ($q_{SA} = 4\pi \sin\theta/\lambda$,where θ is the scattering angle and λ is the X-ray or neutron wavelength) of SANS (ROLLET et al., 2002,). Schmidt-Rohr and Chen (2008a) comparing MDS simulation to SAXD measurements, the author suggested that Nafion is formed by straight water channel surrounded by sulfonic groups, supported by the PTFE backbone and Nafion crystallites. Figure 8 shows a representation of the water-channel model of Nafion, at a hydration level of 20 vol% (11wt%) water according to Schmidt-Rohr and Chen (2008a). In the figure (a) a) Longitudinal and cross-section view of the inverted-micelle cylinder, showing the polymer backbone and the ionic side groups lining the water channel. (b) Rendering of a bundle of channels forming an approximate hexagonal arrangement. (c) Representation of a cross section of a polymer layer showing the water channels in white, the amorphous polymer in light red and the crystalline regions as red rectangles, as used in the simulation of the small-angle scattering curves in d. (d) Small-angle scattering data (circles) at 20 vol% water content when compared to the results calculated from the structural model in (c). The simulations of the structure proposed by Gierke and co-workers, as well as other tentative structures, resulted in poor agreement with the

measurements at 20 vol% hydration. In the description that resulted in the best agreement, the channels, which are locally parallel to their neighbors and can be considered as cylindrical inverted micelles, are stabilized on the outside by the relatively straight helical backbone segments. Considering a length of between 3 to 5 nm for the Nafion® backbone, the densely packed cylinders with their shell of relatively stiff backbone can be expected to have a length of tens of nanometers (SCHMIDT-ROHR and CHEN, 2008a). The cluster diameter estimated from SANX peak position is around 4nm, however the water channels have diameters distributed between 1.8 and 3.5 nm, with an average of 2.4 nm. The crystallites (~ 14 vol%) are elongated and parallel to the water channels, with cross sections of about 5 nm^2 (SCHMIDT-ROHR and CHEN, 2008a)

Figure 8 -Parallel water channel model of Nafion® . (SCHMIDT-ROHR AND CHEN, 2008a)

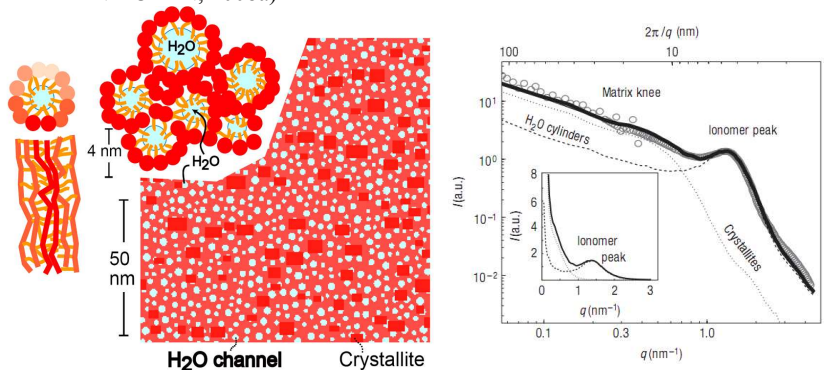

The crystallites have a relevant function in the membrane structure, they provide mechanical strength, acting as physical crosslinks (INZELT et al., 2000). They are elongated and approximately cylindrical. In particular, it is expected that the crystallites help align the water cylinders, and in a non-crystalline sample the water cylinders would meander more strongly (VAN der HEIJDEN; RUBATAT; DIAT, 2004) (KIM, et al., 2006). The crystallinity at 1100 equivalent weight has been estimated to range between 5 and 20%, based on wide-angle X-ray diffraction. The intercrystalline repeat length is 10 to 20 nm, according to the position of the 'matrix knee' in SAXS (SCHMIDT-ROHR and CHEN, 2008a). WASX and SANX results show that the degree of crystallinity does not strongly differ between Nafion® 117 and Nafion® 125, and the observations suggest that mainly the size and not the amount of the crystalline region changes by varying the equivalent weight (VAN der HEIJDEN, BOUZENAD and DIAT,

2004). Nafion also presents anisotropy induced by strain, probably generated during extrusion, aligning the aggregates in the machine direction and these aggregates present large-scale correlation (MAURITZ and MOORE, 2004).

2.1.3.1.2 Hydration

The hydration of Nafion apparently follows a two-stage process (RUBATAT, GEBEL and DIAT, 2004). First, there is the hydration of the charged surface around the polymeric aggregates followed by growth of the water layer beyond monolayers. Secondly, and only when the volume fraction was higher than 60%, there is the swelling of collapsed regions, opening the proton conducting channels up to the maximum diameter at saturation. These two regimes are represented in Figure 9 (RUBATAT et al., 2002) (a) Hydration of the charged surfaces followed by growth of water layers, (b) Opening of collapsed regions.

Figure 9 - Two-stage Nafion swelling: (RUBATAT et al., 2004)

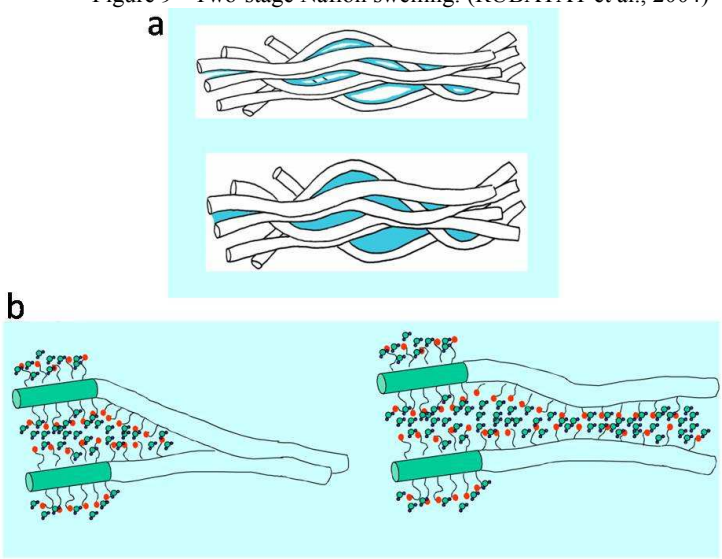

The collapsed dry regions keep the relative permeability to the gas phase very small, while hydrating increases the relative permeability to the liquid phase. Sulfonic acid has a very high water-of-hydration, absorbing 13 molecules of water for every sulfonic acid group in the polymer. Assuming the diameter of the water molecule as 1.2 A and the diameter of the water channel as 24 A at 20 wt% water content, from

about 400 water molecules filling the cross section of the water channel, 126 molecules on average fit adsorbed as double-layer lining the channel walls. The remaining 68% of the total amount of water molecules are relatively free to flow along the channel. This reinforces a view of a molecular water flow along the channels lined by a strongly adsorbed hydration layer covering the hydrophilic sites.

2.1.3.1.3 Transport Properties

The diameter of the channels increases with the hydration. As a result, the protonic conductance is strongly dependent on the humidification. The average distance between sulfonic groups at the channel surfaces is about 0.8 to 0.9 nm. Since the channels are relatively large, the water in the channels have bulk properties (dielectric constant $\varepsilon \simeq 80$), at least for water content above 20 wt% (JANG et al., 2004). Due to size, percolation and long range electrostatic effects both proton and water self-diffusivities are strongly humidity dependent, ranging from 10^{-7} to 10^{-4} cm^2/s at 300 K (SCHUSTER et al., 2010). Jang et al. (2004) report values of 0.7×10^{-5} cm^2/s and 1.5×10^{-5} cm^2/s at 27°C e 80°C (SCHMIDT-ROHR, 2008a).From the electrical point of view Nafion® membranes exhibit a protonic conductivity as high as 0,10S/cm under fully hydrated conditions. Specifically for Nafion® 117 (with 175 μm of thickness) this conductivity corresponds to a real resistance of 0,2 Ohm cm^2,i.e. , a voltage loss of about 150 mV at a current density of 750mA/cm^2 (DHATHATHREYAN and RAJALAKSHMI, 2007) The relatively higher diameter of the water channels, when compared to previous models (such as Gierke and co-workers), also explains why the water diffusivity at 20 wt% hydration is only 10 times smaller than the self-diffusivity in bulk water (SCHMIDT-ROHR, 2008a). The straight channels in Nafion® favor a large hydrodynamic component of the water diffusion, when compared to more tortuous structure present in other polymers (SCHMIDT-ROHR, 2008a). The hydration model presented above also suggests why percolation occurs for 4 vol% water, much lower than the 16 vol% water content for percolation in random packed structures. Observations suggest that, while the water in Nafion® seems to freeze at −20 ◦C (TASAKA, et al., 1988; THOMPSON, et al., 2006), diffusion in Nafion persist down to −50 ◦C (SAITO et al, 2005, CAPPADONIA et al., 1994, THOMPSON, et al., 2006). Allowing for a size distribution of water channels, while the water would freeze at the larger channels it would

still remain mobile in the smaller channels down to −70 ◦C, providing the observed relatively high diffusivity at sub-freezing temperatures. The model developed by Schmidt-Rohr (2008), however, does not specify on which length scales beyond 20 nm the channels bend and merge. Therefore, there is still a lack of fundamental information on pore branching and long range correlation in the flow direction.

The proton transport includes both the diffusion of hydronium ions H_3O^+ as well as the hopping of free hydrogen ions H^+ between water molecules. Measurements include the effects of both. Predictions of the diffusion of H_3O^+ by MDS only have reported values of 0.3×10^{-5} cm^2/s at 353 K (Jang et al., 2004). When a vehicle mechanism through H_3O^+ is responsible for proton transport, the migration of each proton would be linked with the transport of at least one water molecule. In practical fuel cells, a mixed transport process is believed to occur, leading to a certain electro-osmotic drag factor of water molecules per proton (in the order of 0.6 to 2.0). This flux is largely compensated by back diffusion (from cathode to anode) of neutral water molecules according to Fick´s law. The electro-osmotic drag depends primarily on the nature of the polymer and the temperature but not on thickness (HOOGERS, 2003). This will be discussed later.

2.1.3.2 Gas Diffusion Layers

The polymeric membrane is sandwiched between two sheets of porous backing layer (a more suitable name when considering all their functions).These sheets are commonly referenced as Gas Diffusion Layer GDL, or gas diffusion media substrate. GDLs are important for gas spreading and transporting, the electron/heat capture and transport and in water management. They are porous media commonly made of woven carbon cloth (Figure 10a) or carbon paper (Figure 10b and Figure 10c) with carbon fiber of about 7 µm diameter. Thicknesses between 100 µm to 500µm are available according to the material used and necessity. Thinner GDLs are desirable as they offer less electrical and mass transport resistance but they can have difficulty in providing good electrical contact with bipolar plates (MATHUR and CRAWFORD, 2007). Figure 10 shows photographs obtained by environmental scanning electron microscopy (SEM) of typical GDLs. a) SEM of carbon clothes material (MATHIAS 2003) b) SEM image of cross section of the GDL (GOSTICK, 2006) c) SEM of Toray® carbon fiber paper (GURAU, 2006). d) Water droplets formation on Toray carbon fiber paper (GURAU, 2006).

Figure 10 - Micrographs of gas diffusing media substrates for fuel cell.

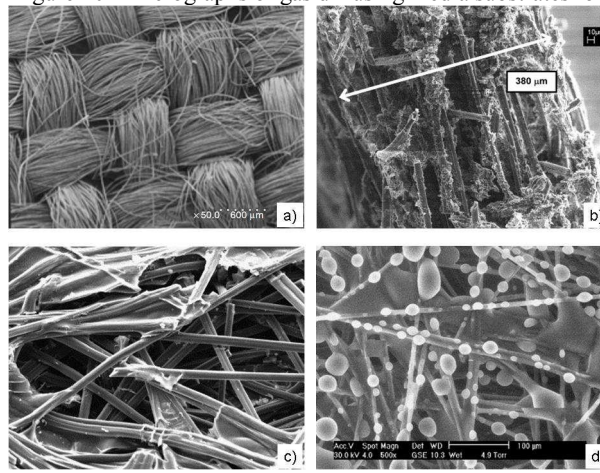

The properties of the GDL are ruled by their function. According to this concept, GDL must be porous enough to allow flow in both directions, through plane and in plane, of reactant gases and product water (which are in opposite directions in the cathode). At the same time it must have adequate size to match with the small discreet particles on facing the catalyst layer (average porous diameter between 40µm and 50µm for the carbon fiber paper is commonly found (MATHIAS, et al., 2003)); it must be electrically and thermal conducting again in both directions because of the electronic flux and for thermal management. GDL needs to be sufficiently rigid to support the flimsy MEA, but also it must have flexibility to maintain good electrical contact where the electrical resistance becomes relevant.

As a gas diffuser, GDL has the role of allowing the diffusion of hydrogen and oxygen from the respective channels down to the catalyst sites. Besides oxygen diffusion, the cathode GDL is an important component in water management. In the cathode GDL, the excess water should condensate in the form of small droplets on the fiber surface (Figure 10d). Part of the liquid water produced in the cathode flows out through the cathode GDL by capillary liquid flow and gas–phase concentration induced mass diffusion (GURAU et al., 2006). This liquid water increases the risk of liquid blocking the pores within the substrate affecting the effective porosity of the GDL and modifying its gas transport, a situation that affects the gas access to the reactive zone. Water management depends on the wettability (at the anode) and the hydrophobicity (at the cathode). Only water vapor and hydrogen should

be transported in the anode GDL. Surface features that increase the contact angle of the water as polarity and roughness can help to prevent flooding. The hydrophobicity of GDLs is obtained by using a hydrophobic material like PTFE or other special material to ensure the water is driven out. Wet proofing rejects excess liquid water so that the catalyst layer will not be flooded by water thus improving the catalyst performance. It also helps maintain the water balance in the membrane by allowing the appropriate amount of water to reach the membrane and draining the excess water. Moreover, PTFE is not electrically conductive then the amount used in the GDL composition must be carefully observed (nowadays 33% of the weight is a common value) (MATHUR and CRAWFORD, 2007). Gurau et al. (2006) present a discussion on the contact angle of water droplets in GDLs. Improvements in the catalyst performance have not been followed by corresponding advances in GDL technology and water management problems increase. The main macroscopic properties affecting the performance of the GDL are the capillary pressure, the water relative permeability and the fraction of hydrophilic and hydrophobic pores. These topics are analyzed by Gostick et al. (2006) and Nam and Kaviany (2003). The use of additional thin surface layers (less than 50 μm) on the GDL is common to improve the electrical contact with the catalytic layer and to help with water management. These additional layers are commonly called microporous layers and provide effective wicking of liquid water from the cathode toward the GDL. They have pore size on the order of carbon agglomerates, between 100 and 500 nm, almost two orders of magnitude lower than the GDL fibers. A common example is a micro-porous layer made of carbon or graphite particles mixed with a polymeric blinder (MATHIAS et al., 2003).

2.1.3.3 Catalyst Layer

Catalyst layers of PEM fuel cell are platinum-based catalysts for both anode and cathode and consist of nano-size platinum crystallites nested on carbon particles that in turn form agglomerates on a microporous matrix (the binder), as in Figure 11. This matrix gives origin to a highly porous reactive layer that is directly responsible for the reaction. A catalyst binder is an ionomer that supports the carbon particle, and is intended to have an optimum morphology and microstructure able to sustain and disperse the distribution of the catalyst. A catalyst layer can be applied either on the membrane or on the GDL by spreading, spraying, sputtering, painting screen printing

decaling, evaporative deposition and impregnation reduction and others, followed by a hot-pressing process (NITTA, 2008).

Neglecting the presence of CO, the overall anode reaction is hydrogen oxidation. Effective electrochemical and heterogeneous reaction is assumed to occur only at the interface between the electrolyte ionomer and the solid phase in the catalyst layer. Homogeneous reactions in the gas phase usually do not happen. In the anode catalyst, hydrogen molecules are absorbed (they can be absorbed as molecules or dissociated, according to the mechanism assumed (BREITER, 1969). Then these new radicals react with water to form the hydronium ion delivering two electrons. Electrons then travel through the carbon support, and protons (as hydronium ions) diffuse through the water inside the ionomer and ultimately inside the polymer membrane. Besides reactants, electrons and protons, the different layers also transport heat, which is produced mainly from the cathode reaction. Local thermal equilibrium can be assumed between the gas and liquid phases (BASCHUK, 2004). Figure 11 is a representation of the catalyst layer. The details attempt a better description of the structure of the carbon support and metallic particles. The agglomerates of particles can be seen, in detail a) the TEM image of fuel cell catalyst (LARMINIE and DICKS, 2003), the black specks are the catalyst particles finely divided over a carbon support. In b) the detail representing the ionomer reaching the catalyst particles. In c) it is represented the platinum particle and the hydrogen reaction on it. Figure 12 is the enlargement of detail c in Figure 11. This figure is a simplified sketch of the mechanism of the hydrogen reaction on the metallic particle. The ionomer (binder in blue) holds the carbon particles and let the water reach the platinum particle. The ionomer (binder in blue) holds the carbon particles and let the water reach the platinum particle. On the reaction site the three phase are present, to allow every species to move.

Figure 11 – Rendering representing (b) the platinum crystallites covering the carbon particles.

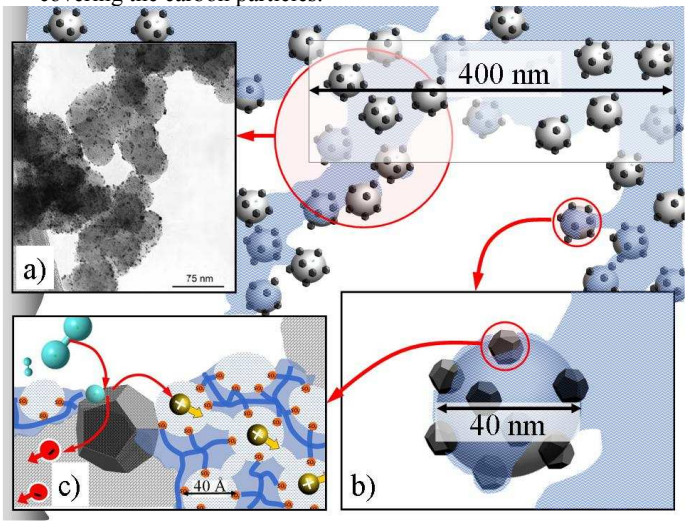

[(a) is a TEM micrograph], the pore structure, the polymer/water layers and (c) the hydrogen molecules undergoing adsorptive dissociation.

Figure 12 - Rendering of the platinum crystallites attached to a carbon particle.

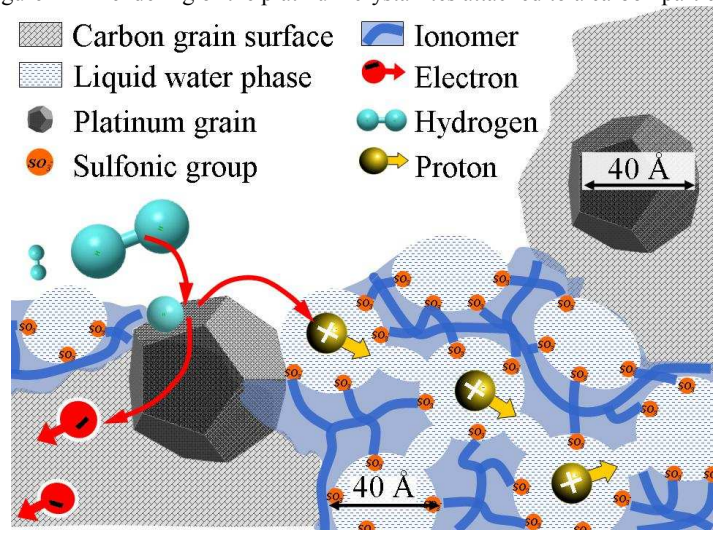

The polymer/water layers and the hydrogen molecules undergoing adsorptive dissociation to electrons (-) and hydrogen cations (+).

Since the species involved diffuse within different phases - electrons move on solid phase, reactants move in gaseous phase, and protons move in liquid phase - the catalytic site needs to be bound by a three phase boundary to make the reaction possible. The site by itself is the solid phase that allows the flow of electrons, which in turn is bound by a gas phase that allows access of the gas reactants and a liquid water phase, embedded in the polymer matrix, needed to take/deliver the protons that participate in the reaction. Setting the necessary amount of water is one of the most difficult tasks. Too much water can either flood the porous media or cover the catalytic sites preventing the access of the gas reactants. Some characteristics such as high hydraulic permeability and ionic conductivity are desirable in the catalytic layer (MATHIAS et al., 2003). Since the oxygen reduction reaction is slower than the hydrogen oxidation, more platinum catalyst is required in the cathode.

2.1.4 Other peripheral devices

Due to the chemical nature of the process, the fuel cell operation is highly dependent on the temperature, thus systems for thermal control are imperative. For very high power densities such as those attained in automotive stacks, liquid cooling is mandatory and fuel cell stacks need other components in order to humidify and remove heat. For less demanding applications air cooling is commonly applied. In the simplest case, the cathode flow fields are open to ambient, and reactant air is supplied by a fan, at the same time providing cooling. A typical fan cooled system in the PEM fuel cell bench at LabCET is described by Mariño (2011) and Nunes (2011). Recent studies (SILVA, 2010) have investigated the application of thermal management by a system based on capillary pumped loop CPL and heat pipes, which can save more useful energy increasing the global efficiency of the system. A second function sometimes integrated into the stack is reactant humidification. The literature describes several types of humidifiers, bubblers, membrane or fiber bundle humidifiers and water evaporators. The simplest humidifier is the well-known bubbler, i.e., the wash bottle design with gas directly passing through the liquid. This approach allows poor control of humidification is less suited within a complex fuel cell system and may cause potential safety hazards due to the direct contact of the fluid. Membrane humidifiers are an array where a semi-permeable membrane separates a compartment filled with water from a compartment with the reactant gas. Ideally the gas is conducted along the membrane and continually increases its humidity up to or close to

saturation as it passes from the gas inlet to the gas outlet. Instead of liquid water, the use of the water-saturated cathode off-gas has been suggested for cathode or cathode and anode humidification (HOOGERS, 2003).

2.2 BASIC THEORY OF PROCESSES OCCURRING IN FUEL CELLS

The operation of fuel cells can be explained qualitatively and quantitatively from the basic principles of Thermochemistry, Electrochemistry, Membrane Science, Interface Phenomena, Chemical Kinetics and Mass Transport. Based on these principles a general overview, considered necessary for the developing of the membrane model of the fuel cell operation, is presented in this section.

Initially a global description of the several macro fluxes within the operating cell will give the reader a main context. Then a thermodynamic overview attempts a comprehensive description of the electrochemical phenomena in fuel cells by describing thermodynamic potential commonly used but with focus on the electrochemical performance. Equilibrium criteria based on these thermodynamic potentials are defined and compared according to the kind of work that a system would perform. In the presence of the extra non-expansion work the equilibrium criteria are modified. Also the total useful work of a system and the maximum work from a process are defined. Aware of the electrical nature of the work performed by the fuel cell, the electrical work is defined as a function of charge movement and potential. Following the chemical potential is defined for ideal and real gas, and then the chemical equilibrium is discussed. In this discussion the reaction Gibbs energy is obtained. The reaction Gibbs energy identifies the spontaneous direction of a reaction and some conditions for chemical equilibrium are explored. Later, a comprehensive description of an electrochemical cell provides the relation between reaction Gibbs energy and electrical potential which is the central point of connection between thermodynamic and electric behavior of the fuel cell. The well-known Nernst equation is obtained and a simple analysis of the water global reaction will give the value of the standard electrical potential for the PEM fuel cell. Finally, first and second laws efficiencies provide a point of comparison between fuel cells and heat engines. One conclusion from this comparison is that an energy conversion process that occurs at a constant temperature is more efficient than a process that relies on large temperature differences.

2.2.1 Thermodynamics

Thermodynamics properties define the thermodynamic state of a substance or a system in equilibrium. A system is said to be in equilibrium if no changes in pressure, temperature, phase, and chemical composition occur within the system when it is isolated from its surroundings. In electrochemical process, the Gibbs energy G ($G = H - TS$) that measures the "useful" or process-initiating work obtainable from an isothermal, isobaric process, is useful for expressing the equilibrium conditions. The Gibbs free energy is the maximum amount of non-expansion work which can be extracted from a closed system. The maximum work can be attained only in a completely reversible process.

2.2.1.1 Equilibrium in Electrochemical Processes

For a closed system, neglecting kinetic and potential energy, the first law of the thermodynamics can be expressed as

$$dU = \delta Q + \delta W \tag{2.1}$$

where U is the internal energy, Q the net exchanged heat from the surroundings to the system and W is the total work performed by the system to the surroundings.

For an isolated system in equilibrium, the entropy is a maximum. The total work W can be divided in expansion work (-pV for reversible processes*)* and non-expansion work or extra work (W_e). Non-expansion work involves all the other forms of work that can cross the boundary of the system, including electrical work as in the case of fuel cells. The main fuel cell process is an electrochemical reaction that occurs at constant pressure and temperature. For this reason, in fuel cell, equilibrium criteria expressed in terms of the Gibbs free energy are convenient.

For a reversible process where only expansion work ($\delta W = -pdV$) exists, it is possible to express the second law as $(\delta Q)_{rev} = Td_eS$. Using the first law, equation (2.1), we have:

$$dU = Td_eS - pdV \tag{2.2}$$

were

$$dS = d_eS + d_iS \tag{2. 3}$$

In this form dU can be expressed as

$$dU = TdS - pdV - Td_iS \tag{2.4}$$

and for a closed system at constant S and V we have

$$dS = dV = 0 \tag{2.5}$$

then

$$dU = Td_iS \leq 0 \tag{2.6}$$

From the definition of Gibbs energy $G = H - TS$, and enthalpy $H = U + pV$ definition, we have $dG = dH - TdS - SdT$

$$dG = dU + d(pV) - TdS - SdT \tag{2.7}$$

For a process at constant temperature and pressure

$$(dG)_{p,T} = dU + pdV - TdS \tag{2.8}$$

Finally, using equation (2.6) we have

$$(dG)_{p,T} \leq 0 \tag{2.9}$$

Therefore, the change in Gibbs free energy indicates the direction of the spontaneous reaction for an isothermal and isobaric process. Conversely, the inequality $(dG)_{p,T} \leq 0$ indicates that, at constant temperature and pressure, chemical reactions are spontaneous in the direction of decreasing Gibbs energy. For a spontaneous endothermic reaction, despite $dG < 0$, H increases. It follows that the entropy of the system increases enough to guarantee that TdS is strongly positive and higher in magnitude than dH in $dG = dH - TdS$.

When other kinds of work different from expansion work occur, the equilibrium criteria change based on the contribution of this extra work. Taking again the Gibbs free energy, it can be seen that now the work in equation (2.1) is defined as

$$\delta W = -pdV - dW_e \tag{2.10}$$

Then, the inequality in equation (2.2) becomes

$$dU \leq TdS - pdV - dW_e \tag{2.11}$$

and at the end, comparing equation (2.11) with equation (2.8), we say that the equilibrium criteria based on Gibbs energy for a process at constant temperature and pressure where other work exists besides that of expansion is expressed as

$$(dG)_{p,T} + dW_e \leq 0 \tag{2.12}$$

This process at constant T and p applies to fuel cells.

2.2.1.2 Maximum Work and Electrical Work.

Substituting the first law of thermodynamics for a closed system, equation (2.1), in the Gibbs energy change equation (2.7) we have

$$dG = \left(\delta Q + \delta W\right) + d(pV) - TdS - SdT \tag{2.13}$$

For a process at constant pressure ($dp = 0$) and temperature ($dT = 0$), and considering a reversible process, we have that $\delta Q = dQ_{rev} = Tds$, and $\delta W = dW_{rev}$. Then, the expression for dG becomes

$$dG = dW_{rev} + d(pV) \tag{2.14}$$

Since $dW_{rev} = -pdV + dW_{e,rev}$ and $d(pV) = pdV$, equation (2.14) becomes

$$dG = \left(-pdV + dW_{e,rev}\right) + pdV$$

$$dG = dW_{e,rev} \tag{2.15}$$

Because the process is reversible, the work done has its maximum value, $dG = dW_{e,max}$, and the corresponding expression for a measurable change is

$$\Delta G = W_{e,max} \tag{2.16}$$

The maximum work that an electrochemical cell can perform from a change of state of the reactant to product is equal to the change in the Gibbs free energy as the reactants change to products. If this change is carried out down to the standard state, the Gibbs energy is also equal to the exergy of the system or the maximum useful work. A system delivers the maximum useful work as it undergoes a reversible process from the specified initial state to the state of its environment (ÇENGEL and BOLES, 2005).

The electrical work performed by the fuel cell can be understood as the work to move the electrical charge (electrons) from the anode to the cathode against a potential difference. Figure 13 shows the charge q moving from position $\vec{r} = 0$ to position $\vec{r} = L_i$, due to the electrostatic force exerted by an electrical field $\vec{\Theta} = \Theta\hat{i}$. The electrical field appears as a result of an electrical potential difference $\Delta\phi = \phi_L - \phi_o$. Since $\vec{\Theta}$ is the negative of the gradient of the electrical potential $\vec{\Theta} = -\vec{\nabla}\phi$, its magnitude is

$$\Theta = -\frac{\phi_L - \phi_o}{L} = -\frac{\Delta\phi}{L} \tag{2.17}$$

The force $\vec{F}$ that the electrical field applies on the charge (Lorentz Law, in electrostatic units) is

$$\vec{F} = q\vec{\Theta} \tag{2.18}$$

Figure 13 - Work made on an electrical charge in presence of an electrical field.

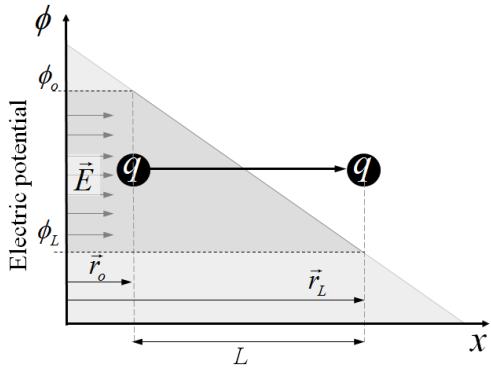

Then, the work made by the field on the charge can be defined as

$$W_{el} = \vec{F} \cdot \vec{r} = q\Theta L \tag{2.19}$$

or

$$W_{el} = -q\Delta\phi \tag{2.20}$$

Later this concept will be applied to evaluate the work made by moving electrons along the electrodes of the fuel cell.

2.2.1.3 Chemical Potential

For an open system, the Gibbs energy is a function of temperature, pressure and the number of moles of the chemical species, i.e.,

$$G = G(T, p, n_i) \tag{2.21}$$

For an infinitesimal change we have

$$dG = \left(\frac{\partial G}{\partial T}\right)_{p,n_i} dT + \left(\frac{\partial G}{\partial p}\right)_{T,n_i} dp + \sum_{i=1}^{N} \left(\frac{\partial G}{\partial n_i}\right)_{T,p,n_{j\neq i}} dn_i \tag{2.22}$$

where n_i is the number of moles of the chemical species *i*. The partial molar Gibbs energy, or chemical potential, is defined as

$$\mu_i = \left(\frac{\partial G}{\partial n_i} \right)_{T,p,n_{j \neq i}} \tag{2.23}$$

The chemical potential of a substance in a mixture is the contribution of the substance to the total Gibbs energy of the mixture. The chemical potential for an ideal gas is

$$\mu_i = \mu_i^o + RT \ln \left(\frac{p_i}{p^o} \right) \tag{2.24}$$

For real systems, it is desirable to preserve the form of the expressions that have been derived for the idealized system. For a non-ideal solution, the chemical potential of species *i* is related to its activity by

$$\mu_i = \mu_i^o + RT \ln a_i \tag{2.25}$$

where a_i is the activity of species *i* in the mixture. For an ideal gas, we have $a_i = p_i / p^o$ and expression (2.24) is recovered.

2.2.1.4 Electrochemical cells

In this section the electrochemical reactions involving an ideal electrical potential are considered. The purpose of this section is not to provide a basic discussion on electrochemical phenomena but only to provide the elements needed to determine its direct influence on the fuel cell operation.

An electrochemical cell consists of two electrodes, electrically connected, made of metallic conductors, in contact with an electrolyte, where a chemical reaction is linked to an electrical current (see Figure 14). The electrolyte is a chemical component that is dissociated into ions in solid or liquid forms. It plays the role of ionic conductor and electrical insulator. A galvanic cell is an electrochemical cell that produces electricity as the result of the spontaneous reaction (exergonic reaction) occurring inside it. An electrolytic cell is an electrochemical cell in which a non-spontaneous reaction (endergonic reaction) is driven by an external source of current.

The electrochemical reaction in a galvanic cell is a chemical reaction (at constant temperature and pressure) that is divided in two steps which occur in each electrode. There is a flow of electrons from one electrode where the first half-reaction occurs to the other where the second half-reaction occurs, generating an electric current and potential.

Figure 14 - Sketch of an electrochemical cell. Positive charges are cations and negative charges are electrons

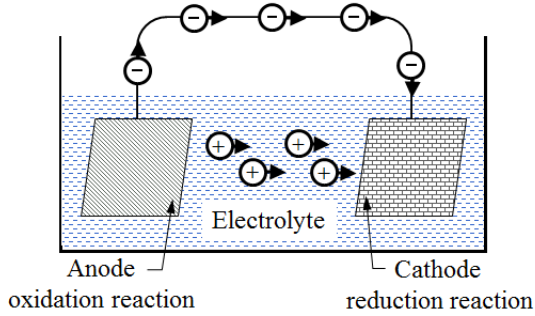

The first part of the reaction is the oxidation and consists of a loss of electrons of one of the reactants that becomes a positive ion (cation). These ions flow through the electrolyte. The electrode in which oxidation occurs is the anode (negative) and this half-reaction can be represented as

$$Red_1 \rightarrow Ox_1 + ze^- \tag{2.26}$$

The second part of the reaction is the reduction of the other reactant, consisting of the reception of electrons, forming the product of the global reaction. The electrode where the second half-reaction occurs is the cathode (positive) and this half-reaction can be represented as

$$Ox_2 + ze^- \rightarrow Red_2 \tag{2.27}$$

As the reaction proceeds, the electrons released in the oxidation reaction on the anode flow through the external circuit and return to the cell through the cathode, being absorbed in the reduction reaction. In a galvanic cell, the cathode has a higher electric potential than the anode because the species undergoing reduction, Ox_2, withdraws electrons from its electrode (the cathode), so leaving a relative positive charge on it (corresponding to a high electric potential). At the anode, the oxidation results in the transfer of electrons to the electrode, so giving it a relative negative charge (corresponding to a low electric potential).

A cell in which the overall cell reaction has not reached chemical equilibrium can do electric work as the reaction drives electrons through an external circuit. The work that a given transfer of electrons can accomplish depends on the potential difference between the two electrodes. This potential difference is called the cell potential and is measured in volts (V). When the cell potential is large, a given number

of electrons traveling between the electrodes can do a large amount of electrical work. The nature of this potential will be discussed later. A cell in which the overall reaction is at equilibrium can do no work, and then the cell potential is zero.

From equation (2.16) we know that the maximum electrical work that a system can do under reversible conditions is given by the value of ΔG. On the other hand, the variation of the Gibbs energy in a chemical reaction $\Delta_r G$ is evaluated at a *specific composition* of the reaction mixture. In order to obtain the relation between ΔG, maximum extra work, and $\Delta_r G$ both reversible operation and constant composition are necessary. These two conditions can be obtained by measuring the cell potential when it is balanced by an exactly opposing source of electric potential. The resulting potential difference is called the zero-current cell potential (theoretical), *E* (formerly, and still commonly, called the 'electromotive force', or emf, of the cell) (ATKINS, 1998). The relation between this potential and the change in Gibbs free energy when the reactants change composition by an amount $d\xi$ moles is,

$$dG = \Delta_r G d\xi \tag{2.28}$$

Substituting this value of the Gibbs energy change in equation (2.15) we obtain the value of maximum electrical work that the reaction can do as it advances by $d\xi$ at constant temperature and pressure,

$$dW_{e,max} = dW_e = \Delta_r G d\xi \tag{2.29}$$

This work is infinitesimal, and the composition of the system is virtually constant when it occurs. From the extent of reaction, we can obtain a relation for the electrical work of the electrons traveling from the anode to the cathode. Suppose that the reaction advances by $d\xi$ [moles], then $z\, d\xi$ moles of electrons must travel from the anode to the cathode. The total charge transported between the electrodes when this change occurs is $\left(-eN_A\right)\left(zd\xi\right)$, onde N_A is the Avogadro number and $-eN_A$ is the charge per mole of electrons. This can be expressed as $\left(-zFd\xi\right)$, where $F = eN_A$ is the Faraday constant. Since, from equation (2.20), the electrical work produced by a charge moving through a potential is $W_{el} = -q\Delta\phi$, we conclude that the work done when an infinitesimal charge $\left(-zFd\xi\right)$ travels from the anode to the

cathode is equal to the product of the charge and the potential difference E,

$$dW_e = \left(-zFd\xi\right) E \tag{2.30}$$

Comparing the electrical work from equation (2.29) and equation (2.30) we can obtain the relation between the reaction Gibbs energy and the theoretical cell potential E,

$$\Delta_r G = -zFE \tag{2.31}$$

In the literature, several names are used to refer to the cell potential E, such as: zero-current cell potential or equilibrium reduction potential (ATKINS, 1998); electromotive force (EMF) or theoretical open circuit voltage (TOCV) (KORDESCH and SIMADER, 1996); electromotive force, reversible open circuit voltage, Nernst voltage or reversible cell voltage (LARMINIE and DICKS, 2003).

Equation (2.31) is the key connection between electrical measurements on the one hand and thermodynamic properties on the other. Thus, by knowing the reaction Gibbs energy at a specified composition, we can state the theoretical cell potential E at that composition. Note that a negative reaction Gibbs energy, a spontaneous exergonic cell reaction, corresponds to a positive zero-current cell potential E. The above equation also shows that the driving power of a cell (that is, the theoretical cell potential E), is proportional to the slope of the Gibbs energy with respect to the extent of the reaction. Figure 15 presents a rendering of the relation of the reaction Gibbs energy and the potential with the extent of reaction, as described by equation (2.31). A spontaneous reaction occurs in the direction of decreasing Gibbs energy. The spontaneous direction of change can be expressed in terms of the cell potential E. The reaction is spontaneous when $E>0$. The reverse reaction is spontaneous when $E<0$ (it needs energy to happen). When the cell reaction is at equilibrium, the cell potential is zero.

Figure 15 – Rendering showing the relation between reaction Gibbs energy and electrical potential.

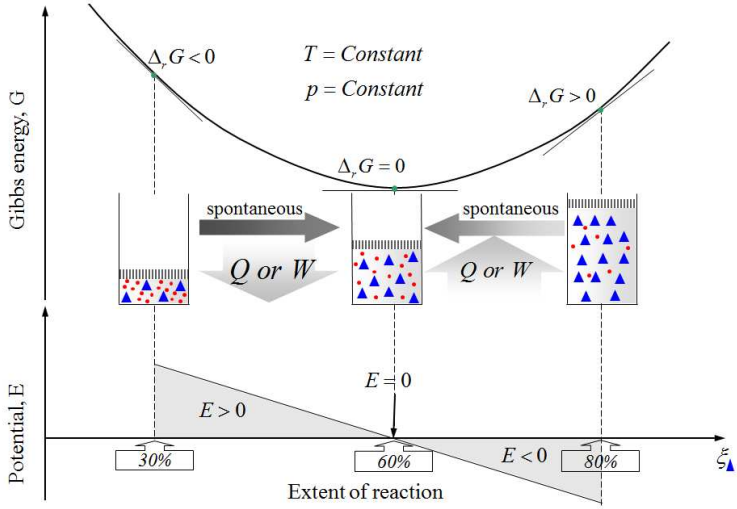

It is plausible that a reaction with $E>0$ that is far from equilibrium (when the slope is steep) has a strong tendency to drive electrons through an external circuit. When the slope is close to zero (when the cell reaction is close to equilibrium), the theoretical cell potential is small. Due to the fact that this potential corresponds to that of a fuel cell at open circuit (a condition of chemical equilibrium at the electrodes), it would give a maximum voltage but would not produce power because no net flow of electrons between the electrodes would occur. For a real situation of an idling cell, the measured potential difference between terminals (the open circuit voltages, OCV), is actually lower than E, because this is affected by the parasitic electrochemical process (irreversibilities) that occurs next to the two electrodes. To produce electricity, the electrodes must be polarized, i.e. there needs to be an electrical potential to move the reactions away from equilibrium.

The standard reaction Gibbs energy can also be expressed in terms of other standard potential, for example, the standard entropies and enthalpies of reaction,

$$\Delta_r G^o = \Delta_r H^o - T\Delta_r S^o \qquad (2.32)$$

We can also define the standard Gibbs energy of formation $\Delta_f G^o$ as the standard reaction Gibbs energy for the formation of a compound from its elements in their reference states. Then we can obtain the standard reaction Gibbs energy $\Delta_r G^o$ from

$$\Delta_r G^o = \sum_{\text{Product}} \upsilon \Delta_f G^o - \sum_{\text{Reactant}} \upsilon \Delta_f G^o \tag{2.33}$$

Both expressions are equivalent.

2.2.1.5 The Nernst Equation

The theoretical cell potential E can be related to the activities of reactants and products by the definition of the reaction quotient K_r as

$$\Delta_r G = \Delta_r G^o + RT \ln K_r \tag{2.34}$$

where $\Delta_r G^o$ is the standard reaction Gibbs free energy and the reaction quotient K_r is related to the activities of reactants and products by

$$K_r = \prod_i a_i^{\upsilon_i}$$

Dividing both sides by $-zF$ and using equation (2.31) gives

$$E = -\frac{\Delta_r G^o}{zF} - \frac{RT}{zF} \ln K_r \tag{2.35}$$

Defining the standard cell potential E^o (also called standard electromotive force (KORDESCH and SIMADER, 1996) and standard reduction potential (ATKINS, 1998)), as $E^o = -\Delta_r G^o \big/ zF$, which is the standard reaction Gibbs energy expressed as an electrical potential (in volts) at standard pressure, we have the Nernst equation

$$E = E^o - \frac{RT}{zF} \ln K_r \tag{2.36}$$

The Nernst equation is used to calculate the theoretical cell potential E at T and p of an electrochemical cell (or half-cell) from its standard cell potential E^o at T^o and p^o, and the activities of reactants and products. From the definition of K_r, the theoretical cell potential E and the standard potential E^o are unchanged if the chemical equation for the cell reaction is multiplied by a numerical factor. When the reaction Gibbs energy increases, the number of electrons transferred increases in the same proportion**.** Figure 16 shows the relation expressed by Nernst equation where the vertical axis is the difference between the standard

conditions potential and the theoretical potential at other conditions, times the factor *RT/F* which is 25.69 mV at 298K. The horizontal axis is the value of the reaction quotient. Every line in the figure corresponds to a different number of electrons transferred per mol. For fuel cells, high positive potential differences (E-E^o) are necessary, thus negative values of the reaction quotient are desired. This effect is improved in reactions that exchange only one electron.

Figure 16 - The variation of the cell potential with the value of the reaction

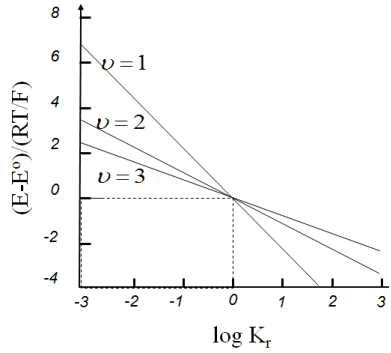

When $ln\ K_r = 0$, the standard cell potential can be interpreted as the theoretical cell potential E. In the case of equilibrium, the process does not generate work, generating zero potential difference between the electrodes. For this situation K_r=K, where K is the equilibrium constant of the cell reaction and the Nernst equation gives

$$\ln K = \frac{zFE^o}{RT} \tag{2.37}$$

This equation allows us to predict equilibrium constants from measured standard cell potentials. Electrochemical tables of standard potentials provide defined values for half reaction potentials from which it is possible to determine the sign of the cell potential. If the standard potential is a positive value, that would imply that $\Delta_r G^o < 0$ and hence that $K>1$ (ATKINS, 1998).

For a hydrogen-oxygen fuel cell, the electrochemical half-reactions that take place at the anode and the cathode catalyst layers, respectively, are (values of the potential will be analyzed below)

$$H_2 \rightarrow 2H^+ + 2e^- \quad E^o = 0V \tag{2.38}$$

$$1/2\,O_2 + 2H^+ + 2e^- \rightarrow H_2O \quad E^o = +1.23V \tag{2.39}$$

Electrons flow from the half-cell with lower electrical potential to the half-cell with higher electrical potential thus, performing work. In this direction hydrogen is consumed at the anode and oxygen is consumed at the cathode producing water. The overall stoichiometric reaction is

$$H_2 + 1/2\,O_2 \rightarrow H_2O \tag{2.40}$$

and summing the half-cell electrical potentials we obtain $E^o=1.23$ V. Since in this case $E^o>0$ it means that for equilibrium $\Delta_r G^o < 0$, and $K>1$ which means that equation (2.40) is the spontaneous direction that the reaction follows. In this reaction, two electrons are transferred, therefore, z = 2. Assuming ideal gas species we can write

$$E = E^o - \frac{RT}{zF}\ln\left(\frac{p_{H_2O}}{p_{H_2}\,p_{O_2}^{1/2}}\right) - \frac{RT}{zF}\ln\left(\frac{p^o\,p^{o1/2}}{p^o}\right) \tag{2.41}$$

Taking pressures in atmospheres, all the standard state pressures in the last term of equation (2.41) are 1, and this term is identically equal to zero. Substituting the values on the remaining equation we have

$$\begin{aligned} E &= E^o - \frac{RT}{zF}\ln\left(\frac{p_{H_2O}}{p_{H_2}\,p_{O_2}^{1/2}}\right) \\ E &= 1.23 - \frac{RT}{2F}\ln\left(\frac{p_{H_2O}}{p_{H_2}\,p_{O_2}^{1/2}}\right) \end{aligned} \tag{2.42}$$

When the denominator of the reaction quotient is smaller than the numerator, the *natural log* term subtracts from the standard electrode potential, lowering the performance of the fuel cell. Therefore, diluting the reactant gases will lower the maximum voltage that the cell can produce. For instance, when a fuel cell operates on products of a fuel reforming reaction, the hydrogen may be diluted with carbon dioxide and nitrogen. Likewise, if air is used as the reactant, then the mole fraction of oxygen is lowered.

2.2.1.6 Thermal and Second Law Efficiencies.

For a power producing device there are two definitions of conversion efficiency. The first is the thermal efficiency based on the first law of thermodynamics, comparing the net work output with the heat input (usually the heating value of the fuel). The second definition is based on the second law of thermodynamics, which compares the

actual performance of a device to the maximum possible work that it could produce. By using the concept of exergy, the second law is a measure of efficiency relative to the maximum work potential of the system.

The thermal efficiency η_{th} of the heat engine is determined by the amount of work the engine can perform with the thermal energy supplied to the system

$$\eta_{th} = \frac{W_{net}}{Q_{in}} \tag{2.43}$$

Contrary to combustion systems, electrochemical cells, such as storage batteries and fuel cells, operate at constant temperature. Because of this isothermal reaction, more of the chemical energy of the reactants is converted to electrical energy instead of being consumed to raise the temperature of the products. Therefore, the electrochemical conversion process is less irreversible than the combustion reaction. As shown before, the maximum work for an electrochemical cell, $W_{e,max}$, can be expressed as a function of the electrical potential of the cell. Thus the first law efficiency for an electrochemical cell is

$$\eta_{th,cell} = \frac{W_{cell}}{Q_{in}} \tag{2.44}$$

The thermal energy supplied to the electrochemical cell can be related to the higher heating value of the fuel. Then, (HOOGER, 2003)

$$\eta_{th,cell} = \frac{zFE_c}{HHV} \tag{2.45}$$

where *HHV* is the higher heating value (per mol of fuel), *z* is the number of moles of electrons per mol of fuel and E_c is the output cell potential. The maximum thermal efficiency of an electrochemical cell is given at the standard cell potential E^o, the equilibrium condition in which no current is being drawn from the cell. Then,

$$\eta_{th,cell,\max} = \frac{W_{cell,max}}{HHV} = \frac{zFE^o}{HHV} \tag{2.46}$$

For a hydrogen-oxygen fuel cell, considering the standard potential at 25°C (where the water produced is in liquid form), the maximum cell thermal efficiency is

$$\eta_{th,cell,max} = \frac{2\left[\frac{mol_e}{mol_f}\right] \times 96,485\left[\frac{C}{mol_e}\right] \times 1.23\left[\frac{J}{C}\right]}{141,880\left[\frac{J}{g}\right] 2,02\left[\frac{g}{mol}\right]} \tag{2.47}$$

$$\eta_{th,cell,max} = 0.83$$

The inefficiency is attributed to the entropy generated from the chemical reaction. For a Carnot cycle heat engine to match this thermal efficiency, the higher temperature of the cycle would have to be 1480°C (with the low temperature being 25°C).

The second law efficiency $\eta_{2nd,}$ of an energy conversion device indicates its degree of reversibility comparing the actual work against the maximum work potential,

$$\eta_{2nd} = \frac{W_{act}}{W_{rev}} \tag{2.48}$$

Another way to express this efficiency is in terms of the thermal efficiency, η_{th} , comparing the actual work to the maximum work,

$$\eta_{2nd,cell} = \frac{\eta_{th,cell}}{\eta_{th,cell,max}} \tag{2.49}$$

For fuel cells, using the thermal efficiencies in equation (2.45) and equation (2.46), the second law efficiency can be calculated in terms of the electrical potentials,

$$\eta_{2nd,cell} = \frac{E_c}{E^o} \tag{2.50}$$

This efficiency compares the actual voltage to the maximum voltage. Exergy is lost, dissipated as heat, because of the inefficiencies within the fuel cell.

2.2.2 Electrode potential and interfacial phenomena

In this section, we discuss how the electrode potential across the fuel cell is formed. Most of electrochemistry depends on the processes that occur at the interface between an electrode and an ionic solution. Fuel cells follow the same general behavior as galvanic cells. The main difference between the two devices is that in fuel cells both the electrodes are separated by an electrolyte while in the case of galvanic

cells, the electrodes are located within the electrolytes in separated ionic solutions.

At the interface between any pair of conduction phases a potential difference exists. Its magnitude is a function of both the composition and nature of the phase. The observed potentials are produced by the electrical double layer. Its structure is responsible for many of the properties of a given system. The double layer itself arises from an excess of charges at the interface which may be ions, electrons or oriented dipoles (CROW, 1994).

In the following, the double layer phenomenon is first described followed by the description of the electrode potential produced. Later the concept of electrochemical potential is discussed and finally the Nernst equation is again obtained but, now, from the electrochemical potential of the involved ions.

2.2.2.1 Double Layer

At the interface between any pair of conduction phases a potential difference exists. Its magnitude is a function of both the composition and nature of the phases. These observed potentials are produced by two parallel electrical layers known as double layer. This concept comes from the original simple view of an organized arrangement of positive ions (solvate), originated from the solution, that organize themselves to compensate the excess electrical charges at the interface, which may be ions, electrons or oriented dipoles (CROW, 1994).

As an example, we can take a metal immersed in a solution of ions of the same metal, as shown in left side of Figure 17. A metal consists of an ordered arrangement of positive nuclei surrounded by mobile electrons which occupy closely spaced levels. The level with the highest energy is known as the Fermi level. When the metal is dipped into the solution, surface equilibrium requires that the excess charge residing on the electrode surface (free electrons) must be exactly balanced by an equal charge of the opposite sign on the solution side. In a clean metal surface, when seeking the electrical equilibrium, positive charges from the solution (solvate) will align facing the metal. The line drawn through the center of such cations at the situation of closest approach marks a boundary known as the Outer Helmholtz Plane (OHP) or surface, and the region inside this boundary is the double layer (CROW, 1994).

In general, the surface of the metal is rarely clean. Ions, solvent dipoles and neutral molecules with or without dipole, as a result of

Coulombic or van der Waals interaction, may be adsorbed on the metal electrode surface (HAMANN, 1998). When only electrostatic interaction forces operate (and depending on the characteristic of the solution), cations from the solution phase are separated from the surface by a layer of solvent (anion or oriented water dipole molecules in the right side of Figure 17). Adsorption of anions by Van der Waals and Coulombic interaction gives rise to the existence of an inner Helmholtz plane.

Beyond the OHP a region is formed where the weaker electrostatic forces and also the thermal motion avoid the order of the ion groups. That region is the diffuse part of the double layer (HAMANN, 1998). The diffuse double layer may extend from less than 1 nm to more than 10 nm. For solutions with higher ionic strength the diffusion double layer can be neglected.

Electrically, the Helmholtz layer will behave as a capacitor with plate separation equal to the half of the diameter of the cation. Thus, the thickness of the double layer depends primarily on the ionic strength of the solution.

Figure 17 – Rendering of the molecular structure of the double layer.

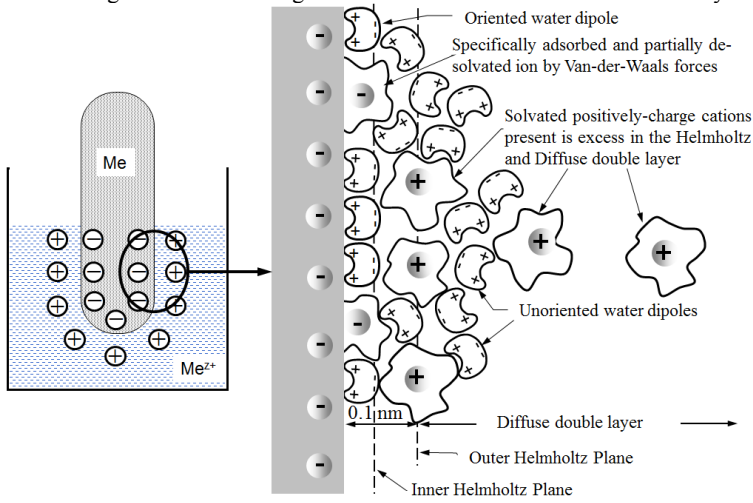

There are two general views of the arrangement of ions and electric dipoles in the solution. In the Helmholtz model of the double layer the solvated ions arrange themselves over the surface of the electrode but are held away from it by their hydration spheres (ATKINS, 1998). This model is incomplete because it does not take into account the thermal motion of the ions. In the Goüy-Chapman model of

the diffuse double layer, the disordering effect of thermal motion is taken into account. It does not consider an inner Helmholtz layer at all, but develops the idea of a diffuse layer consisting of ions of both charges. Neither the Helmholtz nor the Goüy-Chapman models are a very good representation of the structure of the double layer. The two are combined in the Stern model, in which the ions closest to the electrode are constrained within a rigid Helmholtz plane while outside that plane the ions are dispersed as in the Goüy -Chapman model (ATKINS, 1998)(BARD and FAULKNER, 1980). The description of these more advanced models lies beyond the objectives of the present work.

2.2.2.2 Electrode Potential

In this section, the transfer of electrons across the electrode/solution interface is considered. The electrode reactions are oxidation-reduction processes which obey the scheme

$$oxidant + ze^- \rightleftharpoons reductant \tag{2.51}$$

where ze^- represents a transfer of z unit charges (electrons).

As shown above, the global oxidation-reduction reaction

$$Ox_1 + Red_2 \rightleftharpoons Red_1 + Ox_2 \tag{2.52}$$

is formed of two individual half-reactions,

$$Ox_1 + ze^- \rightleftharpoons Red_1 \tag{2.53}$$

$$Red_2 \rightleftharpoons Ox_2 + ze^- \tag{2.54}$$

When a metal is dipped into a solution of ions, as shown in Figure 17a, the interface between the two phases will reach equilibrium. The driving force for equilibrium is the difference in electrochemical potential. Equilibrium will follow the electrochemical reaction

$$M^{z+} + ze^- \rightleftharpoons M \tag{2.55}$$

where M^{z+} represents the ions of the metal and M represents the metal.

During the process, electrical current flows between the two phases and once the surface reaches equilibrium no net electrical current remains. For many systems, equilibrium is established rapidly, which allows the potential difference to be measured easily by a potentiometer device. In other cases, the approach to equilibrium is slow, a continuously variable potential will be observed and no steady value may be determined experimentally (CROW, 1994). The electrochemical reaction can either produce deposition of metal ions onto the metal or

dissolution of metal ions into the solution according to the direction of the electrochemical reaction.

The literature usually describes the variation of potential in the interface by a mental exercise in which the electrodes and corresponding electrolyte are separated from one another but with the charge distributions considered to be the same as when combined. It is then possible to imagine the influence on a positive test charge approaching the metal from the solution side and passing through its surface. Similarly, it is possible to imagine the charge coming from the electrode to the electrolyte solution. Figure 18 shows the potential variation that a test charge would experiment as a function of the distance from a metallic electrode that has been separated from the electrolyte solution: Figure 18(a) represents the energetic path of a charge approaching the metal from the solution and Figure 18(b) represents the energetic path of a charge leaving the metal to the solution.

Figure 18 - Variation of potential with distance from a metallic electrode:.

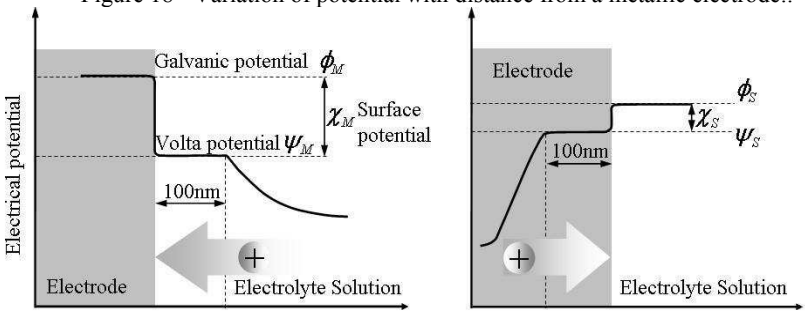

(a) represents the energetic path of a charge approaching the metal from the solution and (b) represents the energetic path of a charge leaving the metal to the solution

Far from the electrode, the test charge experiences a Coulomb potential that varies inversely with distance. In Figure 18a, as the test charge approaches the electrode it enters a region where the potential has a smaller variation. At about 100 nm from the surface the potential varies only slightly with distance, and its value in this region is called the Volta potential, or the outer potential, ψ. As the test charge is taken through the skin of electrons on the surface of the metallic electrode, it experiences a sharp variation of potential until the probe reaches the inner, bulk metal environment, where the potential is called Galvanic potential, ϕ. The difference between the Galvanic and Volta potential is called the surface potential, χ. Figure 18b represents the

complementary mental experiment for the electrode-to-solution journey. It is clear that in general the Galvanic potential may be expressed by

$$\phi = \chi + \psi \tag{2.56}$$

In a real system (that is the metallic electrode and the solution brought together), Volta potentials can be measured but not surface potentials. This means that galvanic potentials also cannot be measured. What can be measured is a value of $\Delta\phi$ relative to a reference $\Delta\phi_{ref}$, that is the value of the electrode potential E_e. In summary,

i) Electrode potential, $E_{el} = \Delta\phi_g = \phi_M - \phi_S$, is expressed in terms of non-measurable quantities, where the subscript M corresponds to the metal electrode and the subscript S corresponds to the solution.

ii) A reference electrode potential $E_{ref} = \Delta\phi_{ref}$ may be defined, quite arbitrarily, for convenience;

iii) The difference, E_{el}- E_{ref} = $\Delta\phi_g$ - $\Delta\phi_{ref}$, can be measured by potentiometric means.

If E_{ref} is designated zero and is the common reference for all measurements of E_{el}-E_{ref}, then it is possible to draw an internationally agreed series of values of E_{el} (CROW, 1994).

The relation between Volta and Galvanic potential is better understood when both Figure 18(a) and Figure 18(b) are brought together as shown in Figure 19: Figure 19 (a) represents the two thought experiments and Figure 19 (b) represents the total electric potential curve.

Figure 19 – Rendering of the electrical potentials in the electrode-electrolyte interface:

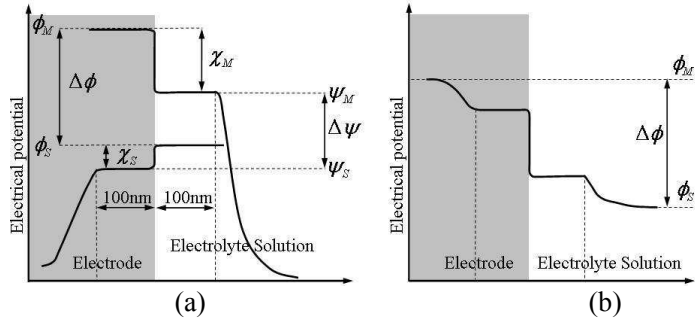

(a) The electrical potentials for charges approaching from the metal and from the solution sides and (b) the total electric potential curve.

The curve in Figure 19(b) basically shows a continuum variation of ϕ from the solution to the metal and the existence of a surface phase exhibiting a step change in ϕ.

2.2.2.3 The Electrochemical Potential for Ions

The presence of potential difference in the interface affects the chemical potential of the ions in equilibrium at the surface. A cation in a region of positive potential has a higher chemical potential (is chemically more active in a thermodynamic sense) than when it is in a region of zero potential. It is possible to incorporate this effect into the thermodynamic chemical potential by considering the work made by the electrical field on the electrical charge. The contribution of an electric potential to the chemical potential is calculated by noting that the electrical work of adding a charge ze^- to a region where the potential is ϕ (the galvanic potential, that is the potential between two phases in equilibrium when no net current flows) is $ze\phi$, and therefore the work per mol is $zF\phi$, where F is the Faraday constant. Because at constant temperature and pressure the maximum electrical work can be identified with the change in Gibbs energy, the difference in chemical potential of an ion with and without the electric potential present is $zF\phi$. The chemical potential of an ion in the presence of an electrical potential is called its electrochemical potential, $\overline{\mu}_i$. From the definition of chemical potential,

$$\mu_i = \left(\frac{\partial G}{\partial n_i} \right)_{p,T,n_{j \neq i}} \tag{2.57}$$

Since z electrons are produced per n moles of reactant consumed at the electrode,

$$\overline{G}_i - G_i = n_i z F \phi \tag{2.58}$$

Therefore, the electric contribution to the chemical potential is

$$\overline{\mu}_i - \mu_i = zF\phi \tag{2.59}$$

In this expression, μ_i is the chemical potential of the species when the electrical potential is zero. When $z=0$ (a neutral species), the electrochemical potential is equal to the chemical potential. The electrochemical potential can be finally expressed as

$$\overline{\mu}_i = \mu_i^o + RT \ln a_i + zF\phi \tag{2.60}$$

2.2.2.4 Nernst Equation for Redox Electrodes and Global Reaction in a Cell

For the first individual system or half reaction in a global oxidation-reduction system,

$$Ox_1 + ze^- \rightleftharpoons Red_1 \tag{2.61}$$

The substance contained in the solution can be converted into an oxidized or reduced form through the loss or gain of electrons from the electrode. This will generate the galvanic potential difference. At equilibrium, once the double layer has formed and a Galvanic potential difference has set up we can say that the electrochemical potential are equal on both sides of the reaction

$$\bar{\mu}_{ox} + z\bar{\mu}_{e^-} = \bar{\mu}_{red} \tag{2.62}$$

Applying the concept of electrochemical potential we have

$$\bar{\mu}^o_{ox} + RT\ln a_{ox} + zF\phi_S + z\bar{\mu}^o_{e^-} - zF\phi_M = \bar{\mu}^o_{red} + RT\ln a_{red} \tag{2.63}$$

Hence

$$\Delta\phi = \phi_M - \phi_S = \frac{\bar{\mu}^o_{ox} + z\bar{\mu}^o_{e^-} - \bar{\mu}^o_{red}}{zF} + \frac{RT}{zF}\ln\frac{a_{ox}}{a_{red}} \tag{2.64}$$

Since the standard Galvanic potential difference is defined as that for which the activities of *ox* and *red* are equal, equation (2.64) can be rewritten as,.

$$E = E^o + \left(\frac{RT}{zF}\right)\ln\left(\frac{a_{ox}}{a_{red}}\right) \tag{2.65}$$

Considering that n_{ox} species suffer oxidation and n_{red} species suffer reduction (HAMANN, 1998),

$$E = E^o + \left(\frac{RT}{zF}\right)\ln\left(\frac{\Pi a_{ox}}{\Pi a_{red}}\right) \tag{2.66}$$

For a hydrogen-oxygen cell we have that at standard condition (atmospheric pressure and temperature of 298K) the anode reaction is

$$H_2 \rightarrow 2e^- + 2H \tag{2.67}$$

From this, we write,

$$\begin{aligned}\Delta_r G_A^o &= G_{A,p} - G_{A,r} \\ &= 2\bar{\mu}(e^-) + 2\bar{\mu}(H^+) - \bar{\mu}(H_2) \\ &= 2\mu^o(e^-) + 2\mu^o(H^+) - \mu^o(H_2) + 2F\phi_S - 2F\phi_A \\ &= 2\mu^o(e^-) + 2\mu^o(H^+) - \mu^o(H_2) - 2F\Delta\phi_A\end{aligned}$$

and finally

$$\Delta_r G_A^o = \Delta_r G^o{}_1 - 2F\Delta\phi_A \tag{2.68}$$

For the cathode reaction in the same conditions

$$2e^- + 2H + \frac{1}{2}O_2 \rightarrow H_2O \tag{2.69}$$

We then have that

$$\begin{aligned}\Delta_r G_{Ct}^o &= G_{Ct,p} - G_{Ct,r} \\ &= \bar{\mu}(H_2O) - 2\bar{\mu}(e^-) - 2\bar{\mu}(H^+) - \frac{1}{2}\bar{\mu}(O_2) \\ &= \mu(H_2O) - 2\mu(e^-) - 2\mu(H^+) - \frac{1}{2}\mu(O_2) - 2F\phi_S + 2F\phi_{Ct} \\ &= \mu(H_2O) - 2\mu(e^-) - 2\mu(H^+) - \frac{1}{2}\mu(O_2) + 2F\Delta\phi_{Ct}\end{aligned}$$

and finally

$$\Delta_r G_{Ct}^o = \Delta_r G^o{}_2 + 2F\Delta\phi_{Ct} \tag{2.70}$$

For the global reaction

$$H_2 + \frac{1}{2}O_2 \rightarrow H_2O \tag{2.71}$$

$$\begin{aligned}\Delta_r G &= \Delta_r G_A + \Delta_r G_{Ct} \\ &= \Delta_r G_A^o - 2F\Delta\phi_A + \Delta_r G_{Ct}^o + 2F\Delta\phi_{Ct} \\ &= \Delta_r G_A^o + \Delta_r G_{Ct}^o + 2F\left(\Delta\phi_{Ct} - \Delta\phi_A\right)\end{aligned}$$

or,

$$\Delta_r G = \Delta_r G^o + 2FE \tag{2.72}$$

In equilibrium $\Delta_r G = 0$, then,

$$\Delta_r G^o = -2FE^o \tag{2.73}$$

or,

$$\Delta_r G = -2FE^o + 2FE \tag{2.74}$$

This equation can be inverted resulting in

$$E = E^o + \frac{\Delta_r G}{2F} \tag{2.75}$$

It is also possible to express $\Delta_r G$ as

$$\begin{aligned}\Delta_r G &= 2\mu(e^-) + 2\mu(H^+) - \mu(H_2) + \mu(H_2O) - \\ &\quad 2\mu(e^-) - 2\mu(H^+) - \frac{1}{2}\mu(O_2) \\ &= -\mu(H_2) - \frac{1}{2}\mu(O_2) + \mu(H_2O) \\ \Delta_r G &= -\left[\mu^o(H_2) + RT\ln(a_{H_2})\right] - \\ &\quad \frac{1}{2}\left[\mu^o(O_2) + RT\ln(a_{O_2})\right] + \\ &\quad \left[\mu^o(H_2O) + RT\ln(a_{H_2O})\right] \\ &= -\mu^o(H_2) - \frac{1}{2}\mu^o(O_2) + \mu^o(H_2O) + RT\ln\left(\frac{a_{H_2O}}{a_{H_2}a_{O_2}}\right)\end{aligned}$$

$$\Delta_r G = \Delta_r G^o\left(p^o, T^o\right) + RT\ln\left(\frac{a_{H_2O}}{a_{H_2}a_{O_2}}\right) \tag{2.76}$$

Then, equation (2.75) gives

$$E = E^o + \frac{\Delta_r G^o\left(p^o, T^o\right)}{2F} + \frac{RT}{2F}\ln\left(\frac{a_{H_2O}}{a_{H_2}a_{O_2}}\right) \tag{2.77}$$

2.2.3 Kinetics of electrochemical reactions

This section describes the dynamics of the electrochemical reactions. The current density, under steady-state, is proportional to the hydrogen reaction rate at the anode. Starting with a simple redox reaction, the cell current density is obtained as a function of the electrical potential in the electrode. Then, the theory of the activated complex is used to discuss the transfer coefficient. The Butler-Volmer equation, that expresses the current density as a function of the activation losses, is derived. Finally the well-known Tafel equation is obtained.

2.2.3.1 The Redox Reaction and Current Density

In the previous sections, only equilibrium conditions were addressed. On an electrode at equilibrium conditions, chemical reactions in both directions occur at equal rates, giving no net current from the electrode. At this condition the theoretical maximum potential of the cell is obtained. In non-equilibrium conditions, a net current flow occurs which is a consequence of the development of the reaction in a preferred direction.

In a galvanic cell process, each of the half-reactions can be understood as two competing forward and backward reactions, one producing the oxidation and the other producing the reduction of the electrode,

$$Red \rightarrow Ox + ze^{-} \tag{2.78}$$

$$Ox + ze^{-} \rightarrow Red \tag{2.79}$$

Figure 20 shows a rendering of the pathway of the half reaction. Here, only the surface reaction mechanism is considered, which includes diffusion controlled and chemical kinetic controlled steps. In this mechanism, reactant from the bulk solution diffuses through the Nernst diffusion layer driven by mass concentration gradient. Upon reaching the outer Helmholtz plane, the chemical reaction begins and an activated complex is produced. The activated complex adsorbs on the electrode surface and the reaction proceeds to completion. The backward reaction proceeds in the same way. Since the electrode reaction is heterogeneous, it is natural to express its rate per unit time and area of the electrode surface.

Figure 20 - Pathway of a general electrode reaction

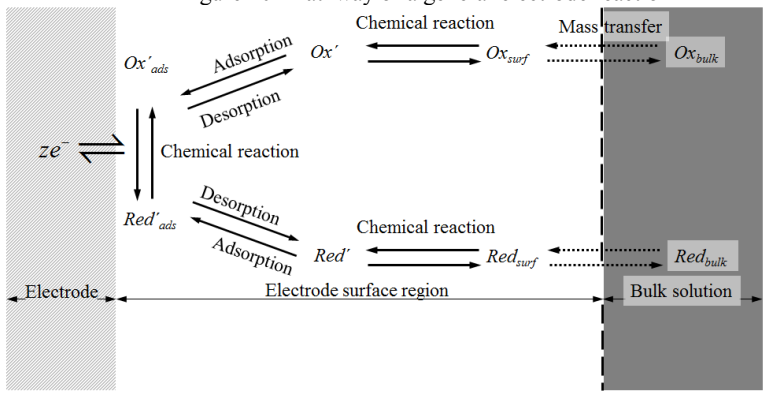

(Adapted from Bard and Faulkner, 1980).

In the following, the simpler case of a one-step, global, first-order reaction is analyzed, leading to the *Butler-Volmer* equation.

Denoting the molar concentrations of the oxidized and reduced species outside the double layer as *[Ox]* and *[Red]* respectively, the rate of oxidation of *Red* in equation (2.78), v_{red} , is

$$v_{red} = k_{ox}\left[Red\right] \tag{2.80}$$

where k_{ox} is the rate constant (pseudo) for the oxidation reaction, and the rate of reduction of *Ox* in equation (2.79), v_{ox} , is

$$v_{ox} = k_{red}\left[Ox\right] \tag{2.81}$$

where k_{red} is the rate constant for the reduction reaction.

Both, oxidation and reduction reactions occur on the same electrode even if one direction is dominant. The net current density (current per unit of catalytic area $i=I/A$) at the electrode is the difference between the current densities arising from the reduction of *Ox* and the oxidation of *Red*. Because the redox processes at the electrode involve the transfer of one electron per reaction event, the current densities, *i*, arising from the redox processes are equal to the rates multiplied by the charge transferred per mole of reaction, which is given by the Faraday constant. Therefore, there is a cathodic current density of magnitude

$$i_c = Fk_{red}\left[Ox\right] \tag{2.82}$$

arising from the reduction and there is an opposing anodic current density of magnitude

$$i_a = Fk_{ox}\left[Red\right] \tag{2.83}$$

arising from the oxidation. The net current density at the electrode is the difference

$$i = i_a - i_c \tag{2.84}$$

or expressed as a function of the concentration

$$i = Fk_{ox}\left[Red\right] - Fk_{red}\left[Ox\right] \tag{2.85}$$

The rate constant k_i can be obtained from the activated complex theory as discussed below.

2.2.3.2 Rate Constant - Activated Complex Theory

The activated complex theory (ATC) is an attempt to identify the main features governing the magnitude of the rate constant in terms of a model of the events that take place during the reaction.

For two reactants *A* and *B* changing along a reaction coordinate, as the reaction event proceeds, *A* and *B* come into contact, distort, and begin an exchange of discard atoms. The potential energy rises to a maximum, and the cluster of atoms that corresponds to the region close to the maximum is called the activated complex as shown in Figure 21. In the reaction profile, the horizontal axis is the reaction coordinate, and the vertical axis is the potential energy. The activated complex is the region near the potential maximum, and the transition state corresponds to the maximum itself. After the maximum, the potential energy falls as the atoms rearrange in the cluster, until it reaches a value characteristic of the products.

Figure 21 - A reaction profile and activated complex

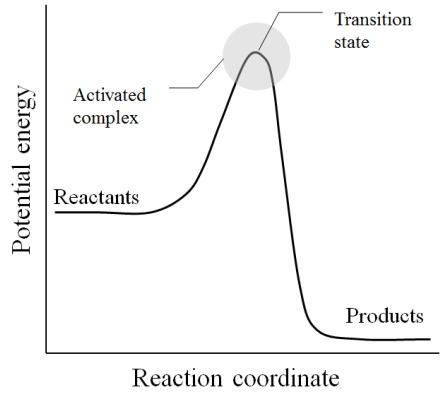

The climax of the reaction occurs at the peak of the potential energy. There two reactant molecules have come to such a degree of closeness and distortion that a small further distortion will send them in the direction of products. This crucial configuration is called the transition state of the reaction.

The speed of the reaction involving *A* and *B* can be written as

$$\mathrm{v} = k_r[A][B] \tag{2.86}$$

Here,

$$k_r = k^{\mp}K^{\mp} \tag{2.87}$$

where $k^{\mp}$ is the unimolecular rate constant for transition reaction and $K^{\mp}$ is a proportionality constant, defined as follows. Activated complex theory depicts a reaction between *A* and *B* as proceeding through the formation of an activated complex, $C^{\mp}$, that falls apart by unimolecular decay into products, *P*, with a rate constant $k^{\mp}$

$$C^{\mp} \rightarrow P \qquad \mathrm{v} = k^{\mp}\left[C^{\mp}\right] \tag{2.88}$$

An activated complex can form a product if it passes through the transition state. It is supposed that the rate of passage of the complex through the transitions state is proportional to the vibration frequency (ν) along the reaction coordinate, then

$$k^{\mp} = \kappa\nu \tag{2.89}$$

where κ is the transmission coefficient (assumed to be about 1) and ν is the frequency in which the cluster of atoms forming the complex approaches the transition state.

The concentration of the activated complex is likely to be proportional to the concentration of the reactants, thus

$$\left[C^{\mp}\right] = K^{\mp}\left[A\right]\left[B\right] \tag{2.90}$$

It is assumed that a pre-equilibrium between the reactants and the complex exist, with equilibrium constant given by

$$A + B \rightleftharpoons C^{\mp}$$

$$K = \frac{(p_{C^{\mp}} / p^{o})}{(p_A / p^{o})(p_B / p^{o})} = \frac{p_{C^{\mp}} p^{o}}{p_A p_B} \tag{2.91}$$

The partial pressure can be expressed as a function of the molar concentration to obtain

$$\left[C^{\mp}\right] = K\frac{RT}{p^{o}}\left[A\right]\left[B\right] \tag{2.92}$$

Comparing equation (2.92) with equation (2.90) we conclude that

$$K^{\mp} = K\frac{RT}{p^{o}} \tag{2.93}$$

The equilibrium constant K (proportionality constant) can be defined from structural data as

$$K = \frac{N_A q^{o}_{C^{\mp}}}{q^{o}_A q^{o}_B}\exp\left(-\Delta E^{o}/RT\right) \tag{2.94}$$

then

$$K^{\mp} = \left[\frac{N_A q^{o}_{C^{\mp}}}{q^{o}_A q^{o}_B}\exp\left(-\Delta E^{o}/RT\right)\right]\frac{RT}{p^{o}} \tag{2.95}$$

This definition of the equilibrium constant contains the standard molar partition function, $q^{o}_{C^{\mp}}$, that, due to lower frequency, is simplified and expressed in terms of a partition function for all the other modes of the complex, $\overline{q}^{o}_{C^{\mp}}$

$$q^{o}_{C^{\mp}} \approx \frac{\mathbb{k}T}{h\nu}\overline{q}^{o}_{C^{\mp}} \tag{2.96}$$

Then, we have

$$K^{\mp} = \frac{\mathbb{k}T}{h\nu}\left[\underbrace{\frac{RT}{p^o}\left(\frac{N_A \overline{q}^o_{C^{\mp}}}{q^o_A q^o_B}\exp\left(-\Delta E^o/RT\right)\right)}\right] \tag{2.97}$$

where $\mathbb{k}$ is the Boltzmann constant, T is the temperature, h is the Plank constant, N_A is the mole number of reactant, and q's are the molar partition functions.

Denoting $(p^o/RT)\overline{K}$ as an equilibrium constant in the form

$$\overline{K} = \frac{RT}{p^o}\left(\frac{N_A \overline{q}^o_{C^{\mp}}}{q^o_A q^o_B}\right)\exp\left(-\Delta E^o/RT\right) \tag{2.98}$$

we have

$$K^{\mp} = \frac{\mathbb{k}T}{h\nu}\overline{K} \tag{2.99}$$

Substituting equation (2.89) and (2.99) in equation (2.87) we obtain the so-called Eyring equation

$$k_r = \kappa\frac{\mathbb{k}T}{h}\overline{K} \tag{2.100}$$

The difficulty in using the Eyring equation, however, lies in the calculation of the partition function of the activated complex $C^{\mp}$. Because both processes are activated, we can expect to write their rate constant as a function of a Gibbs free energy of activation, $\Delta G^{\neq}$ thus we accept that $(p^o/RT)\overline{K}$ is an equilibrium constant and use the definition

$$\Delta G^{\mp} = -RT\log\left[\left(\frac{p^o}{RT}\right)\overline{K}\right] \tag{2.101}$$

$\Delta G^{\neq}$ can be understood as the free energy difference for the forward reaction between the initial reactant and the activated complex.

From (2.101) we have that

$$\overline{K} = \frac{RT}{p^o}\exp\left(-\frac{\Delta G^{\mp}}{RT}\right) \tag{2.102}$$

Then, the rate constant becomes (Atkins, 1998)

$$k_r = \kappa \frac{\mathbb{k}T}{h} \frac{RT}{p^o} \exp\left(\frac{-\Delta G^{\neq}}{RT}\right) \tag{2.103}$$

It is possible to notice that any alteration in $\Delta G^{\neq}$ will affect the reaction rate: When $\Delta G^{\neq}$ is lowered, the reaction rate will increase, and when $\Delta G^{\neq}$ is increased, the reaction rate will decrease (HAMANN, 1998).

Up to this point, we have developed expressions that relate thermodynamic entities with potential energy and we have a definition for the electrical current in a Redox reaction as a function of the reactants, products and a constant, defined by the activated complex theory. From here on, we will establish the relation between the electrical current and the electrode potential, considering that both a cathodic and an anodic reaction occur on the same electrode. This can be done by the Butler-Volmer equation which is valid when the electrode reaction is controlled by electrical charge transfer at the electrode (and not by the mass transfer to or from the electrode surface from or to the bulk electrolyte). First, it is necessary to describe the activation Gibbs energy in terms of the electrical potential.

2.2.3.3 Activation Gibbs Energy in a Redox Reaction

A species that participates in reduction or oxidation at an electrode has to either migrate through the electrical double layer and adjust its hydration sphere as it receives or discards electrons, or detach and migrate into the bulk if it is already activated (see Figure 20). Because both processes are activated, it is possible to express their rate constants according to the activated complex theory (ATKINS, 1998). For this, equation (2.103) is rewritten here as

$$k_r = \left(\kappa \frac{\mathbb{k}T}{h} \frac{RT}{p^o}\right) \exp\left(\frac{-\Delta G^{\neq}}{RT}\right) \tag{2.104}$$

where κ is the transition coefficient, $\mathbb{k}$ is the Boltzmann constant, T is the temperature, h_p is the Plank constant, R is the gas universal constant, $\Delta G^{\neq}$ is the Gibbs energy of activation and p^o standard pressure. The oxidation reduction reaction involves the existence of an activated complex $C^{\mp}$ that has to pass through a transition state on the top of an energy barrier as shown in Figure 22. For both directions of the reaction there would be one Gibbs energy of activation, one for oxidation

(anodic) $\Delta G_{ox}^{\neq}$, and one for the reduction (cathodic) $\Delta G_{red}^{\neq}$. Figure 22 represents the change in Gibbs energy that a species undergoes during the oxidation-reduction reaction given by equation $Red \underset{R}{\overset{O}{\rightleftharpoons}} Ox + ze^-$. In the figure, the vertical axis accounts for the Gibbs energy and the horizontal axis is the distance beginning in the electrode crossing the double layer and reaching the outer Helmholtz plane. The figure on top represents the activation energy barrier and relative positions of reactant, product and activated complex with respect to distance from the electrode surface and OHP. The bottom part presents the complementary Gibbs energy parabolas for reactant ad product with crossing point at the transition state. It is assumed that the reaction occurs in this space near to the electrode, where the species has to overcome the energy barrier $\Delta G_{ox}^{\neq}$ to become *Ox* while losing one electron. The minimum of the parabolic curve on the right side of the bottom figure corresponds to the stable configuration of the species *Red*, while the minimum on the left curve on the same figure corresponds to the stable configuration of the specie *Ox*. The intersection of the two curves represents the transition state. ϕ_M represents the electrode potential (Metal),which is the highest of the two, and ϕ_S represents the electrolyte potential (Solution). The horizontal axis can also be understood as the nuclear configuration (BREITER, 1969).

The overall Gibbs energy change is given by

$$\Delta G = \Delta G_{red}^{\mp} - \Delta G_{ox}^{\mp} = n\Delta\phi F \qquad (2.105)$$

where $\Delta\phi = \phi_M - \phi_S$.

Figure 22 - Electrode reaction Gibbs energy profile for a reversible process.

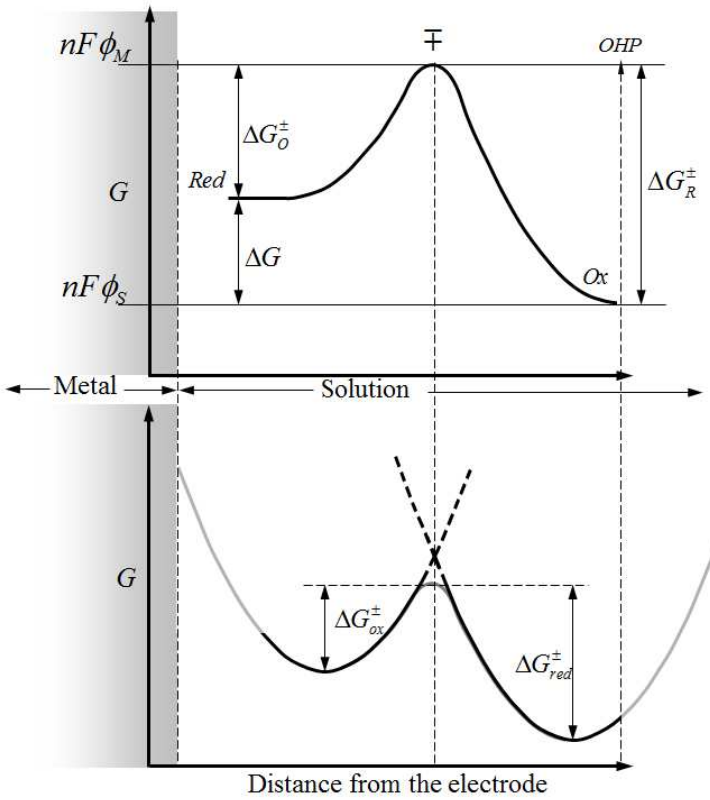

Using the definition of rate constant for the oxidation-reduction process at the electrode it is possible to express the current density of equation (2.85) as

$$i = \underbrace{F\left(\kappa\frac{kT}{h}\frac{RT}{p^o}\right)_A \exp\left(-\frac{\Delta G_{ox}^{\mp}}{RT}\right)}_{ox}[Red] - \underbrace{F\left(\kappa\frac{kT}{h}\frac{RT}{p^o}\right)_{Ct} \exp\left(-\frac{\Delta G_{red}^{\mp}}{RT}\right)}_{red}[Ox] \tag{2.106}$$

Because electrochemical reactions occur in the presence of an electric field, the Gibbs energy of activation must include both chemical

and electrical terms. Likewise, it is important to find an expression that describes how the electric current on an electrode depends on the electrode potential, considering that both cathodic and anodic reactions occur on the same electrode. Figure 23 shows three Gibbs energy profiles for the oxidation reaction. The reaction is assumed as having *red* as reactant and *ox* as product, that is, oxidized on the electrode and reduced in the electrolyte ($Red \underset{red}{\overset{ox}{\rightleftharpoons}} Ox + ze^-$). The black dashed line is the reaction profile without the influence of the electrical field potential and the green line is the same profile with the electrical field effect. In Figure 23(a), a situation in which the transition state of the activated complex is reactant-like (the peak of the Gibbs energy profile is close to the electrode) is shown. For the reduction reaction (going from the electrolyte to the electrode ←), a cathodic current is generated and the cathodic activation Gibbs energy is changed from $\Delta G_{Ct}^{\mp}(0)$ to $\Delta G_{Ct}^{\mp} = \Delta G_{Ct}^{\mp}(0) + F\Delta\phi$. Here the cathodic activation Gibbs energy is increased. Thus if the electrode is more positive than the solution, $\Delta\phi > 0$, then more work has to be done to form an activated complex from *Ox*. In Figure 23b a situation in which the transition state is product-like (the peak of the Gibbs energy profile is close to the *OHP*) is shown.

Figure 23 - Reaction profiles for the oxidation reduction reaction.

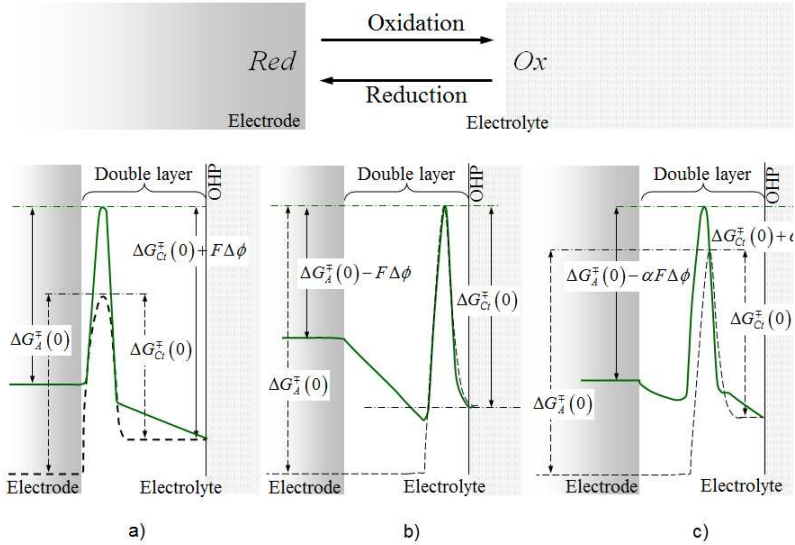

For the reduction reaction (←), the cathodic activation Gibbs energy $\Delta G_{Ct}^{\mp}(0)$ is independent of $\Delta\phi$.

In a real system, the transition state has an intermediate resemblance to these extremes, Figure 23 c, and the cathodic activation Gibbs energy for reduction may be written as

$$\Delta G_{Ct}^{\mp} = \Delta G_{Ct}^{\mp}(0) + \alpha F\Delta\phi \qquad (2.107)$$

The parameter α is called the (cathodic) transfer coefficient. In theory, it varies between zero and one, depending on the symmetry of the transition in the electrochemical reaction. Value α=0 favors reduction and value α=1 favors oxidation. Experimentally is has been determined to be about 0.5 (HOOGERS, 2003).

The same analysis on Figure 23(c), can be made for the oxidation reaction (the process goes from the electrode to the electrolyte while discarding an electron to the electrode →). In this case an anodic current is generated. If the transition state is reactant-like, Figure 23(c),(a), the extra work is zero. In cases where the transition state is product-like, Figure 23 (c), (b), the extra work is the full $-F\Delta\phi$. In general the activation Gibbs energy for this anodic process is

$$\Delta G_{A}^{\mp} = \Delta G_{A}^{\mp}(0) - (1-\alpha)F\Delta\phi \qquad (2.108)$$

To summarize, when the transition state resembles species that has undergone reduction (Figure 23 c, a), the activation Gibbs energy for the anodic current is almost unchanged, but the full effect applies to the cathodic current. When the transition state resembles a species that has undergone oxidation (Figure 23 c, b), the cathodic current activation Gibbs energy is almost unchanged but the anodic current activation Gibbs energy is strongly affected. When the transition state is intermediate in its resemblance to reduced and oxidized species, both activation Gibbs energies are affected.

The two activation Gibbs energies can now be inserted in the electrical current equation (2.106),

$$i = F\left(\kappa\frac{kT}{h}\frac{RT}{p^o}\right)_A [Red]\exp\left(-\frac{\Delta G_A^{\mp}(0)-(1-\alpha)F\Delta\phi}{RT}\right)- F\left(\kappa\frac{kT}{h}\frac{RT}{p^o}\right)_{Ct} [Ox]\exp\left(-\frac{\Delta G_{Ct}^{\mp}(0)+\alpha F\Delta\phi}{RT}\right) \quad (2.109)$$

These expressions, in order to evidence the chemical and electrical characteristics, can also be expressed as

$$i = F\left(\kappa\frac{kT}{h}\frac{RT}{p^o}\right)_A [Red]\exp\left(-\frac{\Delta G_A^{\mp}(0)}{RT}\right)\exp\left(\frac{(1-\alpha)F\Delta\phi}{RT}\right)- F\left(\kappa\frac{kT}{h}\frac{RT}{p^o}\right)_{Ct} [Ox]\exp\left(-\frac{\Delta G_{Ct}^{\mp}(0)}{RT}\right)\exp\left(-\frac{\alpha F\Delta\phi}{RT}\right) \quad (2.110)$$

2.2.3.4 The Butler-Volmer Equation

If the cell is balanced against an external potential that is equal and opposite to the cell potential then it is possible to obtain a dynamic equilibrium where no net current is obtained from the cell. The value of this potential has been shown to be the theoretical cell potential *E*, and under the sole effect of this potential the current equation gives

$$i = F\left(\kappa\frac{kT}{h}\frac{RT}{p^o}\right)_A [Red]\exp\left(-\frac{\Delta G_A^{\mp}(0)}{RT}\right)\exp\left(\frac{(1-\alpha)FE}{RT}\right)- F\left(\kappa\frac{kT}{h}\frac{RT}{p^o}\right)_{Ct} [Ox]\exp\left(-\frac{\Delta G_{Ct}^{\mp}(0)}{RT}\right)\exp\left(-\frac{\alpha FE}{RT}\right) \quad (2.111)$$

Disregarding other effects different to these of activation of the reaction we can say that when the cell is producing current (that is,

when a load is connected between the electrode being studied and a second counter-electrode) the electrode potential changes from its zero-current value, E, to its working value, E_c. The difference in potential is called the overpotential, η (under the current condition it corresponds to the activation overpotential)

$$\eta = E - E_c \tag{2.112}$$

When assuming only activation resistances to the electrochemical process, only activation overpotential will be present. For the hydrogen oxygen fuel cell, the reversible potential of the anode, where hydrogen oxidation occurs, is 0 V. For the oxygen reduction reaction at the cathode, the reversible potential is +1.23 V at 25°C. In an operating fuel cell, the activation overpotential of the anode is positive, which means the electrode potential is higher than 0 V. For the cathode, the electrode potential is below 1.23 V, which means the overpotential is negative (HOOGERS, 2003).

Substituting the overpotential definition given by equation (2.112) in the current cell definition, equation (2.111) for a working cell, we have

$$i = F\left(\kappa\frac{kT}{h}\frac{RT}{p^o}\right)_A [Red]\exp\left(-\frac{\Delta G_A^{\mp}(0)}{RT}\right)\exp\left(\frac{(1-\alpha)FE_c}{RT}\right)\exp\left(\frac{(1-\alpha)F\eta}{RT}\right) - F\left(\kappa\frac{kT}{h}\frac{RT}{p^o}\right)_{Ct}[Ox]\exp\left(-\frac{\Delta G_{Ct}^{\mp}(0)}{RT}\right)\exp\left(-\frac{\alpha FE_c}{RT}\right)\exp\left(-\frac{\alpha F\eta}{RT}\right) \tag{2.113}$$

All the terms except for the rightmost exponent can be consolidated into a constant for both of the directions.

$$i = F[Red]\underbrace{\left(\kappa\frac{kT}{h}\frac{RT}{p^o}\right)_A \exp\left(-\frac{\Delta G_A^{\mp}(0)}{RT}\right)\exp\left(\frac{(1-\alpha)FE_c}{RT}\right)}_{k_{o,A}}\exp\left(\frac{(1-\alpha)F\eta}{RT}\right) - F[Ox]\underbrace{\left(\kappa\frac{kT}{h}\frac{RT}{p^o}\right)_{Ct} \exp\left(-\frac{\Delta G_{Ct}^{\mp}(0)}{RT}\right)\exp\left(-\frac{\alpha FE_c}{RT}\right)}_{k_{o,Ct}}\exp\left(-\frac{\alpha F\eta}{RT}\right) \tag{2.114}$$

then defining these pre-exponential constants of the current density definition,

$$k_{o,A} = \left(\kappa\frac{kT}{h}\frac{RT}{p^o}\right)_A \exp\left(-\frac{\Delta G_a^{\mp}(0)}{RT}\right)\exp\left(\frac{(1-\alpha)FE_c}{RT}\right) \tag{2.115}$$

$$k_{o,Ct} = \left(\kappa\frac{kT}{h}\frac{RT}{p^o}\right)_{Ct} \exp\left(-\frac{\Delta G_c^{\mp}(0)}{RT}\right)\exp\left(-\frac{\alpha FE_c}{RT}\right) \tag{2.116}$$

we have

$$i = F\left[Red\right]k_{o,A}\exp\left(\frac{(1-\alpha)F\eta}{RT}\right) - F\left[Ox\right]k_{o,Ct}\exp\left(-\frac{\alpha F\eta}{RT}\right) \quad (2.117)$$

When the electrode is in equilibrium and at its reversible potential, the overpotential and external current are both zero. Since equilibrium applies, the bulk concentrations of *Red* and *Ox* are also found on the surface. Although no net current flow out of the fuel cell, the dynamic characteristic of the equilibrium state allows the presence of an internal current that flows equally in both directions. That current is defined as the exchange current density, i_o.

$$F\left[Red\right]k_{o,A} = F\left[Ox\right]k_{o,Ct} \equiv i_o \quad (2.118)$$

The exchange current density incorporates the kinetic term that includes the chemical portion of the electrochemical Gibbs energy of activation. Because of this, it can be used as a comparison between different catalysts: the smaller the activation energy, the larger the exchange current density and the better the catalyst (HOOGERS, 2003). Exchange currents are generally large when the redox process involves no bond breaking or if only weak bonds are broken. They are generally small when more than one electron needs to be transferred, or when multiple or strong bonds are broken. A few values of the exchange current are shown in Table 5 exchange current and transfer coefficients at 298K (ATKINS, 1998).

After substituting the exchange current density in the current density equation, its final form result is the so called Butler-Volmer equation.

$$i = i_o\left[\exp\left(\frac{(1-\alpha)F\eta}{RT}\right) - \exp\left(-\frac{\alpha F\eta}{RT}\right)\right] \quad (2.119)$$

This equation is the general description of an electrochemical reaction, containing both reduction (left term) and oxidation (right term) components (Hoogers, 2003). This equation only strictly holds in the above form for process involving a single electron. When electrochemical reactions involving more than one electron are considered, more rigorous analysis is require to use different coefficients instead of α and (1-α), because their sum may not be one (1) anymore. Thus (CROW, 1994)

$$i = i_o\left[\exp\left(\frac{\alpha_A nF\eta}{RT}\right) - \exp\left(-\frac{\alpha_{Ct} nF\eta}{RT}\right)\right] \quad (2.120)$$

According to the Butler-Volmer equation the low exchange current density (which is an expression of the inhibited low speed reaction) must be compensated by a high overvoltage (KORDESCH and SIMADER, 1996). The exchange current density i_o is a direct measure of the electrode reaction rate; a high value means that the reaction proceeds reversibly (BLOMEN and MUGERWA 1993).

2.2.3.5 Tafel Equation

In contrast with the anode reaction, the oxygen reduction reaction at the cathode is an activated process and therefore exhibits a much higher overpotential (HOOGERS, 2003). The plot of the logarithm of the current density against the overpotential in equation (2.121) is called a Tafel plot. The slope gives the value of α , and the interception at $\eta=0$ gives the exchange current density i_o (ATKINS, 1998)

$$\ln\left(i\right)=\ln\left(i_o\right)+\frac{\alpha F\eta}{RT} \tag{2.121}$$

Rearranging this equation it is possible to obtain an expression for the overpotential (of activation).

$$\eta=\frac{RT}{\alpha F}\ln\left(\frac{i}{i_o}\right) \tag{2.122}$$

And using its definition from equation (2.112) we have

$$E_c=E-\frac{RT}{\alpha F}\ln\left(\frac{i}{i_o}\right) \tag{2.123}$$

The above equation is known as the ***Tafel equation***. The Butler-Volmer equation gives a mathematical description of such activated processes; even so, it is the Tafel equation that is more useful for practical work on MEAs. The Tafel equation is more commonly expressed in logarithms in base 10. Correcting of the logarithms Tafel equation reads

$$E_c=E-\frac{2.3RT}{\alpha F}\log\left(\frac{i}{i_o}\right) \tag{2.124}$$

The Tafel equation has been known, more as a result of experiments than of theoretical consideration since 1905. For a general case where more than one electron can be considered in the redox reaction, the amount of electrons *z*, must be included in the denominator of pre-exponential coefficient.

2.2.4 Overpotential and polarization curve

As explained in the sections above, the origin of the reversible electrical work delivered in an electrochemical reaction is the Gibbs energy delivered from the fuel cell by an exergonic reaction. Thus negative reaction Gibbs free energy produces positive potential difference between the electrodes spontaneously, whereas reaction with positive reaction Gibbs free energy would need an external potential to occur. The **EpErCd** curve in Figure 24 is used here to explain this concept.

EpErCd is a three orthogonal axes curve that shows the variation of the electrical potential difference developed at the electrical contacts E (V), as a function of the extent of reaction ξ and the current density i (A/cm^2). On plane E-ξ, the Gibbs energy as a function of the extent of reaction is also shown, proving the region of spontaneous reaction ($\Delta_r G < 0$) and the condition for electrochemical equilibrium ($\Delta_r G = 0$) whose corresponding electrical potential difference is nil. On the same plane, but on an arbitrary different scale, the standard cell potential E^o is related to the derivate of the reaction Gibbs energy and draws a straight line with negative slope. Along the current density i (A/cm^2) axis, the potential diminishes as current increases while conserving the same extent of reaction position. Parallel to plane E-I, and in the adequate extent of reaction, the polarization curve will appear. Figure 24 shows the **EpErCd** general curve for any general electrochemical reaction.

Figure 24 Rendering of a typical potential surface in a fuel cell as a function of the extent of reaction and the current density, the **EpErCd** curve.

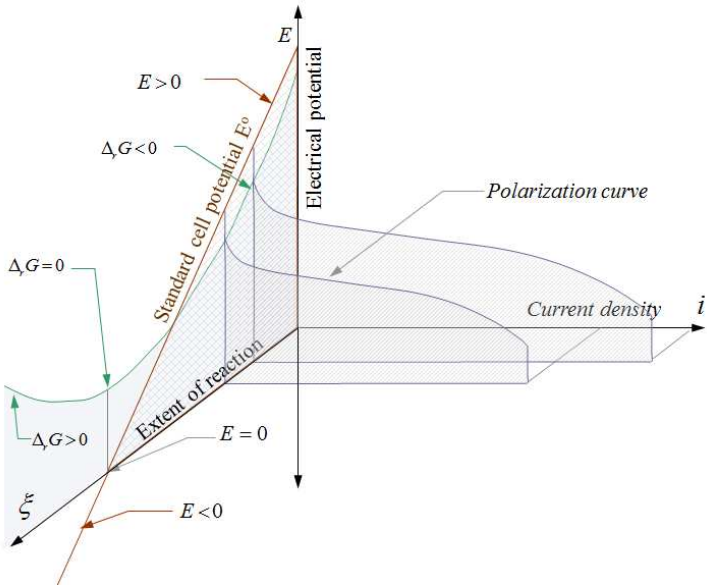

The electric potential follows the standard cell potential as long as the current is zero, i.e., no net current exists - therefore no power would be delivered. For a given specific composition (represented by the extent of reaction) a net current can be generated, being represented as the two curved lines parallel to the axis that represents the current, *i*. Once a current flows, there is a progressive decrease in the cell's electrical potential difference because of the working potential losses as the current increases.

Figure 25 shows a rendering of the relation between the extent of reaction, electrical potential and current density as three orthogonal axes. The hydrogen-oxygen curve in Figure 25 is located in the stoichiometric point on the extent of reaction axis, for which the standard cell potential with liquid water production is 1.229 V at 298°C. Under power demand, a unitary cell can deliver from 0.6 to 0.7 V, for current density that varies according to fuel cell and fuel between 0.15 to 1.0 A/cm^2 (LINARDI, 2010). The highest potential in a fuel cell for a defined extent of reaction and temperature is the standard cell potential E^o. It is defined at standard pressure and, according to the

temperature; the state of the water produced can be different. The theoretical cell potential E is the standard potential E^o reduced by the effect of the change in partial pressure of reactants or products, the double layer activation and the crossover phenomenon. The open circuit voltage OCV is the measured potential difference between terminals in the open circuit of an idling cell. Irreversibilities of the OCV were analyzed by Arato and Costa (2006a).

Figure 25 - Relation among fuel cell potential E (V), extent of reaction and current density i(A/cm2).

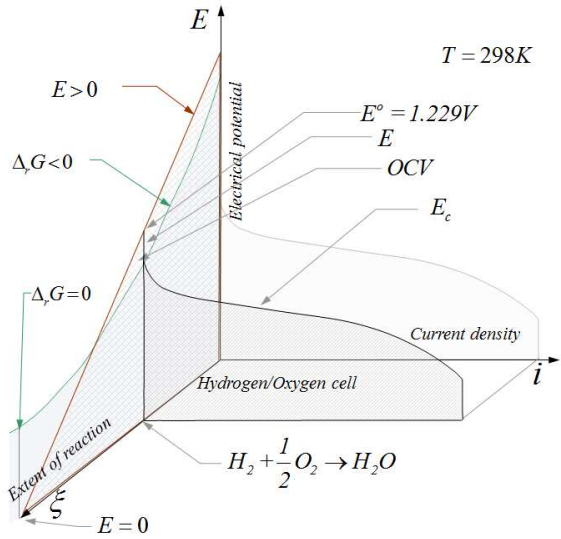

The OCV usually does not reach the value of the theoretical cell potential E at the given temperature and partial pressures, because of the parasitic electrochemical process that occurs next to the main two reactions. Some voltage loss at open circuit voltage is due to the crossover of some hydrogen through the membrane electrolyte to the cathode; also, corrosion processes might take place, depending on the composition of the electrodes. Finally, the cell potential E_c that is the measured potential during a fuel cell operation depends on the current density i (A/cm^2). The polarization curve describes the relation between the potential and the current density as will be shown later.

Table 4 shows the values for the standard reaction Gibbs energy and standard cell potential for the case of a hydrogen-oxygen cell. Efficiency limits based on HHV are also shown.

Table 4 - Standard reaction Gibbs energy and standard cell potential for different temperatures.

Temperature °C	$\Delta_r G^o$ (kJ/mol)	E^o at p^o V	$\eta_{th,cell,max}$	State of the water produced
25	-237.2	1.23	83	Liquid
80	-228.2	1.18	80	Liquid
100	-225.2	1.17	79	Gas
200	-220.4	1.14	77	Gas
400	-210.3	1.09	74	Gas
600	-199.6	1.04	70	Gas
800	-188.6	0.98	66	Gas
1000	-177.4	0.92	62	Gas

Larminie and Dicks, 2003

When a current is established in the system the potential decays and as current increases more losses diminish the delivered tension of the cell. Now the phenomena which cause this tension loss or overpotentials are described.

Useful amounts of work are obtained from a fuel cell only when a reasonably large current is drawn. The overpotentials are potential losses in the fuel cell under the condition of delivering current. Different names are used for the same variable according to the point of view of the scientific field. According to the electrochemists, they are also called, polarization, irreversibilities (thermodynamic point of view), losses (so vague) and voltage drop (not a very scientifically precise term) (LARMINIE and DICKS, 2003). Indifferently of the general name overpotentials receive, they are classified according to their nature. The most significant overpotentials are the activation, concentration, and the ohmic, but the literature also describes other overpotentials, such as crossover, reaction and transfer.

In the following, the overpotentials are described and the simpler semi-empirical models, usually linear, are reviewed. This modeling allows bringing together the entire phenomenology of equilibrium, reaction, charge and species transport. These simpler models will also be used in the next chapter in a basic lumped-model to assess the main operation characteristics and macroscopic properties of a PEM fuel cell.

2.2.4.1 Activation overpotential

This overpotential is caused due to the fact that the reactions (transferring of electrons) taking place on the surface of the electrodes have a limited speed. The limitations commonly considered are those which typically can be influenced by applying an “activation catalyst”.

Temperature usually has a large influence on this type of overpotential (KORDESCH and SIMADER, 1996). One expression for overpotential can be obtained by taking the Tafel equation and considering activation as unique effect. By defining a coefficient *A*

$$A = -\frac{2.3RT}{z\alpha F} \tag{2.125}$$

it is possible to obtain a simple expression for the activation overpotential

$$\eta = A\log\left(\frac{i}{i_o}\right) \tag{2.126}$$

Figure 26 shows a typical pattern of a Tafel plots. It is observed that for most of the values of overvoltage, the graph approximates to a straight line (LARMINIE and DICKS, 2003). The coefficient *A* is the slope of the Tafel plot. It is higher for an electrochemical reaction that is slow. For the oxygen reduction reaction (*z=2*) in a practical fuel cell, *A* is usually between 40 and 80 mV.

Figure 26 - Tafel plots for slow and fast electrochemical reaction

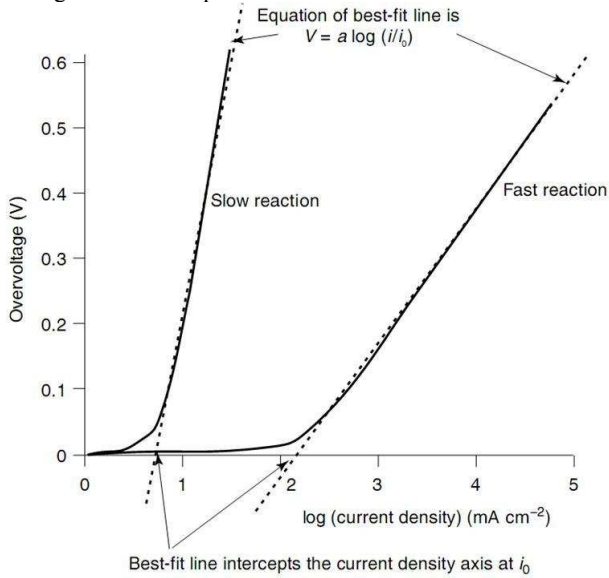

(from Larminie and Dicks, (2003))

For a real cell working, this overpotential is identified as the activation overpotential, which expressed in natural logarithm is

$$\eta^a = \frac{RT}{z\alpha F}\ln\left(\frac{i}{i_o}\right) \tag{2.127}$$

The main factor controlling the activation overpotential and hence the cell potential, E_c, is the exchange current density i_o. From equation (2.123) it can be seen that a tenfold increase in i_o leads to an increase in the cell potential of typically 60 mV. While the Tafel slope A is dictated by the chemical reaction (and temperature), the value for i_o depends on reaction kinetics. Thus, it is supposed that the magnitude of i_o can be increased by adding more electrocatalyst to the cathode (HOOGERS, 2003). Figure 27 shows the effect of the i_o on the cell potential when only activation overvoltage are considered as a loss. Curves for values of i_o equal to 0.01, 1.0, 100 (mA/cm^2) using a typical value for A of 0.06V were plotted. From there, it can be seen that the smaller the i_o, the greater the voltage drop.

Figure 27 – Typical curves of cell voltage against current density.

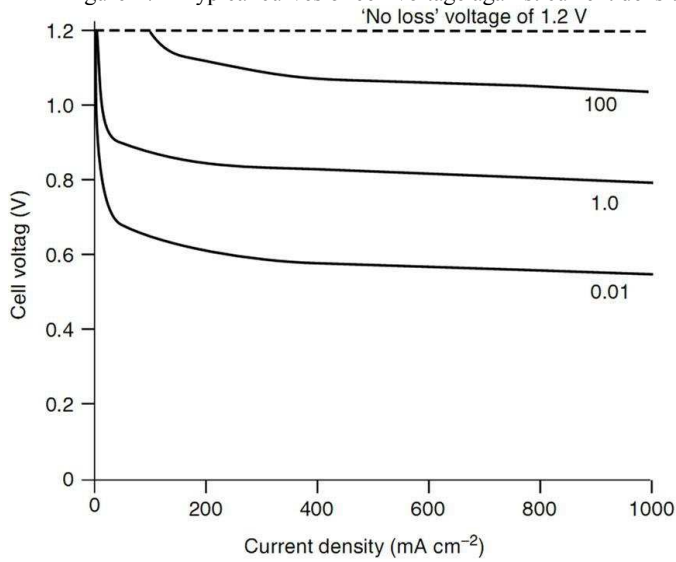

(from Larminie and Dicks, (2003))

It is worth recalling that i_o at the oxygen electrode (cathode) is much smaller than that at the hydrogen anode, sometimes 10^5 times smaller. For a low temperature, hydrogen-fed fuel cell running on air at ambient pressure, a typical value of i_o would be about 0.1mA/cm^2 at the cathode and about 200mA/cm^2 at the anode (LARMINIE and DICKS,

2003). Experimental values of the Butler-Volmer parameters for the hydrogen formation on some electrodes are shown in Table 5.

Table 5 - Exchange current and transfer coefficients at 298K (ATKINS, 1998).

Reaction	Electrode	i_o [A/cm^2]	α
$2H^+ + 2e^- \rightarrow H_2$	Pt	7.9×10^{-4}	
	Cu	1×10^{-4}	
	Ni	6.3×10^{-4}	0.58
	Hg	7.9×10^{-4}	0.50
	Pb	5.0×10^{-4}	

Due to the relevant effect the exchange current density has on reducing the activation overvoltage, it is desirable to increase its value, especially at the cathode. Some ways to increase the i_o are as follows (LARMINIE and DICKS, 2003):

- Raising the cell temperature. For a low-temperature cell, i_o at the cathode will be about 0.1m/Acm-2, whereas for a typical 800°C cell, it will be about 10m/Acm-2, a 100-fold improvement,
- Using more effective catalyst,
- Increasing the interfacial surface area of the electrodes,
- Increasing reactant concentration (using O_2 instead of air),
- Increasing the pressure.

2.2.4.2 Ohmic overpotential (Ohmic resistance).

This overpotential has no correlation with any chemical process at the electrodes and is the straightforward resistance to the flow of electrical charge through the different material in the fuel cell. This resistance involves the electron Ohmic resistance of the conductors (metals, carbon including cell stack components, and interface contact resistances) and the resistance of the ionic conductors (electrolyte and catalyst layers) which, under certain assumptions, can be modeled by the same linear dependence with the current density (Ohm's law) but are based on ion-mobility characteristics. The total resistance controls the slope of the pseudo-linear middle portion of the polarization curve, region II in Figure 29, the larger the resistance, the faster the drop of the polarization curve with increasing current density (HOOGERS, 2003).

The speed of charge transfer by electron flow compared with ionic flow is about 100:1. This difference is important for electrolyte reactions, which always occur on the interfaces between conductors and electrolytes. If the electrodes are porous, the supply of ions and the charge transfer is usually the limiting process (KORDESCH and SIMADER, 1996). Electronically, a fuel cell can be regarded as a series circuit of an ideal voltage source and a total internal resistance that is the combination of the electronic resistances of various fuel cell components (ohmic losses occur during transport of electrons and ions). The higher the current flow, the larger the ohmic voltages drop across the sum of all internal resistance inside the fuel cell. Ohmic correction by numerical fitting is made on the data to analyze the fuel cell current/voltage curve in order to separate the different effects on the performance (HOOGERS, 2003). Ohmic overpotential can be expressed by the simple expression

$$\eta^{o} = iR_{cell} \tag{2.128}$$

Where R_{cell} is the total resistance of the fuel cell and is the most difficult variable to obtain because of the wide range of dependent variable.

2.2.4.3 Mass transport or concentration overpotential (Nernstian).

These overpotentials result from the change in concentration of the reactants at the surface of the electrodes as the fuel is used. The lack of reactant is caused by diffusion processes (pressure gradient, changes in the usage rates of gases or liquid). The delay in reaching steady state conditions, or the absence of equilibrium conditions as a result of the current flow using up or producing materials, are sources of concentration difference. Other parameters are, for examples, the porosity of materials which influence the gas or liquid flow, or the permeability of membranes changing the ionic flow (KORDESCH and SIMADER, 1996). One of the assumptions in the derivation of the *Butler-Volmer* equation is the negligible conversion of the electroactive species at low current densities, resulting in uniformity of concentration near to the electrode. This assumption fails at high current density because the consumption of electroactive species close to the electrode results in a concentration gradient. Diffusion of the species toward the electrode from the bulk is slow and may become rate-determining. Part of the electric potential will be used to overcome that situation

generating a potential drop which is known as concentration overpotential, η^c.

In cases where the rate determining step is the mass transport in a redox reaction, the Nernst equation on surface under zero-current conditions, can be written as

$$E = E^o - \frac{RT}{zF}\ln a \tag{2.129}$$

where K_r (activities relation for a general reaction) has been substituted for a (activity of the ions in the solution). Now, assuming there is a large excess of support electrolyte so as to keep the mean activity coefficient γ, approximately constant and expressing this activity as a function of the local concentration we can write

$$E = \underbrace{E^o + \frac{RT}{zF}\ln\gamma}_{E^0} + \frac{RT}{zF}\ln c \tag{2.130}$$

Therefore, the constant activity coefficient is included into E, and we write the formal potential, E^0 of the electrode as

$$E^0 = E^o + \frac{RT}{zF}\ln\gamma \tag{2.131}$$

The theoretical cell potential is then expressed as a function of the formal potential as:

$$E = E^0 + \frac{RT}{zF}\ln c \tag{2.132}$$

When the cell is producing current, the active ion concentration at the OHP changes to c', see Figure 28, then the electrode potential changes to

$$E' = E^0 + \frac{RT}{zF}\ln c' \tag{2.133}$$

In a simple model of the Nernst diffusion layer there is a linear variation in concentration between the bulk and the outer Helmholtz plane; the thickness of the layer depends strongly on the state of flow of the fluid. The difference of potential between both situations is

$$\eta^c = E' - E = \frac{RT}{zF}\ln\left(\frac{c'}{c}\right) \tag{2.134}$$

We now suppose that the solution has its bulk concentration, c, up to a distance δ from the outer Helmholtz plane, and then falls linearly to c' at the plane itself. This Nernst diffusion layer (about 100 μm, and strongly dependent on the conditions of the hydrodynamics due

to any stirring or convective effects) has a thickness quite different from that of the electrical double layer (which is typically less than 1 nm, and unaffected by stirring).

Figure 28 - Linear variation in concentration on the model of the Nernst diffusion layer.

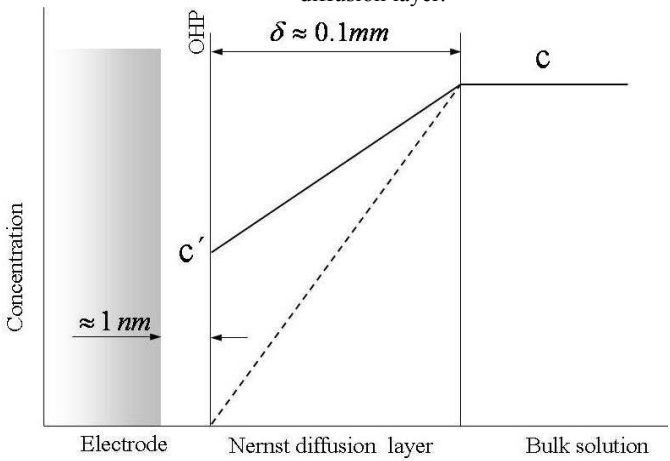

The molar flux J is proportional to the concentration gradient, and, using a simple integrated form of Fick's law, that flux is approximated as

$$J = D_{im}\frac{c - c'}{\delta} \tag{2.135}$$

where D_{im} is the diffusivity of species i in the mixture. The cathodic current density towards the electrode is the product of the particle flux and the charge per mole, zF of ions

$$i = zFJ = zFD_{im}\frac{c - c'}{\delta} \tag{2.136}$$

The limiting current density is reached when $c'=0$,

$$i_{lim} = zFJ_{lim} = \frac{zFD_{im}c}{\delta} \tag{2.137}$$

then, the concentration c' is related to the current density at the double layer by

$$c' = c - \frac{i\delta}{zFD_{im}} \tag{2.138}$$

Hence, as the current density is increased, the concentration falls below the bulk value. However, this decline in concentration is small

when the diffusion constant is large, for then the ions must be very mobile and quickly replenish any removed ions. Finally the expression for the overpotential in terms of the current density is obtained.

$$\eta^c = \frac{RT}{zF}\ln\left(1-\frac{i\delta}{zcFD_{im}}\right) \tag{2.139}$$

Empirical expression for this overpotential is commonly used especially in the case of fuel cells supplied with air rather than pure oxygen, a situation in which last equation is not a good approximation. There are also problems with lower-temperature cells, and those supplied with hydrogen mixed with other gases such as carbon dioxide for the fuel. An empirical approach has shown to be more favored, and yields an equation that fits the result very well (KIM et al., 1995 and LAURENCELLE et al., 2001).

$$\eta^c = A_E \exp(B_i i) \tag{2.140}$$

Where A_E and B_i are constant. A_E will typically be about 3×10^{-5}V , and B_i about 5×10-3cm 2/mA.

This overpotential is particularly important in cases where the hydrogen is supplied from some kind of reformer, as there might be a difficulty in increasing the rate of supply of hydrogen quickly to respond to demand. Another important case is at the air cathode, if the air supply is not well circulated.

2.2.4.4 Other Overpotentials

Other overpotentials are identified but are not as relevant or their effect can be included in one of those discussed above . They are:

2.2.4.4.1 Fuel crossover and internal current overpotential

Electrolytes should only transport ions; however, a certain amount of fuel diffusion and electron flow will always be possible. The crossover is the overpotential resulting from that phenomena where not only the waste of fuel passing through the electrolyte but also the opposite potential caused when it reacts on the cathode, contribute to the potential drop (LARMINIE and DICKS, 2003).

2.2.4.4.2 Reaction overpotential.

This is a term for the voltage difference appearing when an earlier or simultaneous (related) chemical reaction produces another compound which changes the operating conditions.

2.2.4.4.3 Transfer overpotential.

This is unfortunately used vaguely in many connections and should be limited to the description of the change in potential under load conditions as fundamental interrelation of current and potential.

Other effects such as the poison of the catalyst or membrane can affect the fuel cells performance generating an “overpotential”. This is the situation when using reformer as a fuel for the fuel cell. If the reformate of any hydrocarbons is not efficient it can contain compost like CO which can poison the catalytic layer and the membrane

2.2.4.5 Polarization Curve

The polarization curve of a fuel cell is the curve defined by the cell potential E_c as a function of the current density. Before the production of any net current density, the potential presents a sharp drop from the theoretical cell potential E to the open circuit voltage OCV. The causes of these drops remain when the current is drawn from the cell. As the current increases, the potential drops progressively as a consequence of the overpotentials. Figure 29 shows a sketch of a typical polarization curve where the vertical axis represents the cell potential in volts and the horizontal axis represents the current density delivered from the cell. The cumulative contribution of the main overpotential can be observed along the current density. The Lilac strip represents the activation overpotential of the cathode, the orange strip represents the ohmic overpotential, the pink strip represents the activation overpotential of the anode, the blue strip represents the mass transport overpotential and the green area is the net cell potential and its boundary, represented by the black line is the result of the standard cell potential (horizontal limit at approximately 1.23 V) diminished by the total of the overpotential in any current density .

Figure 29 - Typical polarization curve for a PEM fuel cell

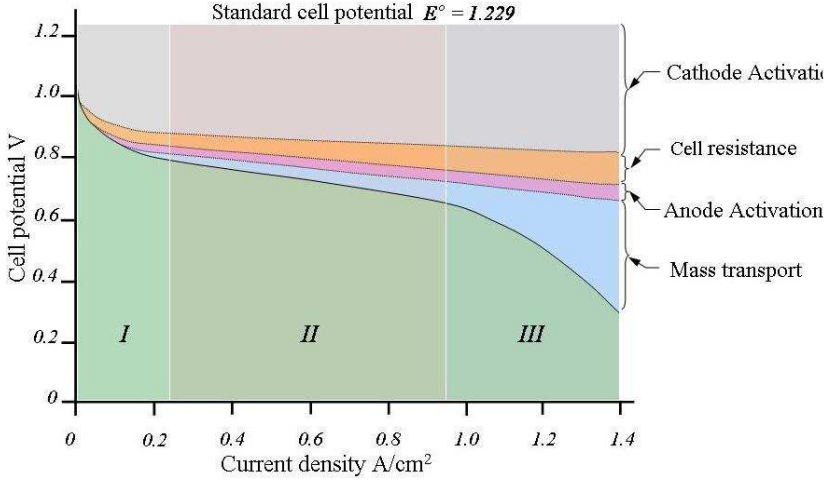

The polarization curve can be divided in three regimes according to the preponderant overpotential in each one (see Figure 29). The three regimes shown are: (I) the activation limited regime, (II) the resistance limited regime and (III) the mass transport limited regime. In regime I, (the activation limited regime) at low current density, the shape of the polarization curve is governed by the charge transfer at the electrode interface and reproduced by the activation overpotential. This overpotential represents the magnitude of activation energies when reactions propagate at the rate required by the current and depends on the type of reactions and catalyst materials, electrode microstructure, reactant activities, electrolyte material (acidic/alkaline), temperature and current density.

After the rapid drop of the activation overpotential, a second regime, the resistance limited regime, begins where the cell potential exhibits a pseudo-linear behavior as the current density increases. In this region, the shape of the curve is governed by the ohmic overpotential, which arises from the electrical resistance of fuel cell conductor. Bulk materials and interfaces between components display an intrinsic resistance to electron flow, and electrolyte materials offer resistance to transportation of ions, which carry the current in the electrolyte phase. The magnitude of ohmic overpotential is proportional to current and cell resistance. Resistance of rigid bulk material depends mainly on material properties, but bulk conductivity of pliable materials and contact resistance are also affected by surface properties and contact pressure between the components. Electrolyte conductivity depends primarily on

temperature and for most PEM electrolyte types, water content. The largest single contributor to cell resistance is usually the electrolyte resistance to ionic current. At the end of the pseudo-linear region, regime III, the mass transport limited regime, begins. In this region, the shape of the curve is determined by the mass transfer overpotential. When current density reaches a certain level, sluggishness of mass transfer processes starts to limit the supply of reactants to the electrodes, and cell voltage begins to decrease rapidly with increasing current demand, reaching the limit current density. Mass transfer overpotential can be viewed as an activation energy required to drive mass transfer at the rate needed to support the current.

Prediction of the polarization curve is not easy due to the fact that both concentrations and different overpotentials are not constant everywhere on the electrode surface. Local variations in temperature; reactant flow velocity and concentration in the flow channel; layer transport properties (material porosity, pore size distribution, permeability, thickness, presence of inert species etc.); humidity conditions; and so on have an effect on the reactant concentration on the electrode surface and magnitude of overpotentials. Therefore, an accurate description of fuel cell polarization must take into account both local variations in operating conditions and species transport by convection and multicomponent diffusion. If liquid water is present, mass transport in both phases should be considered (MIKKOLA, 2007).

2.2.5 A Simple Mathematical Expression for the Polarization Curve

Authors have proposed semi-empirical models that can be analytical and global, or numerical and local, which have a considerably complex level. However, it is useful to construct a simple semi-empirical mathematical equation that allows one to estimate the potential curve. the fuel cells potential can be expressed as the theoretical potential at a pressure and a temperature established, diminished of the main overpotentials

$$E_c = E - \eta^a - \eta^o - \eta^c \tag{2.141}$$

Using simple models for all the overpotentials, we obtain,

$$E_c = E - \frac{RT}{z\alpha F}\ln\left(\frac{i}{i_o}\right) - iR_{cell} - \frac{RT}{zF}\ln\left(1 - \frac{i\delta}{zcFD_{im}}\right) \tag{2.142}$$

Kim et al. (1995) and Laurencelle et al. (2001) have proposed one expression similar to equation (2.142) but with the concentration overpotential changed to a simpler empirical equation as

$$E_c = E - \frac{RT}{z\alpha F}\ln\left(\frac{i}{i_o}\right) - iR_{cell} - A_E \exp(B_i i) \tag{2.143}$$

Then, they collapse the theoretical potential *e* and the constant part of the activation overpotential into one term to obtain

$$E_c = \underbrace{E + \frac{RT}{z\alpha F}\ln\left(i_o\right)}_{OVC} - \frac{RT}{z\alpha F}\ln\left(i\right) - iR_{cell} - A_E \exp(B_i i) \tag{2.144}$$

The new term is the real, practical, open circuit voltage *OCV*, given by

$$OCV = E + \frac{RT}{z\alpha F}\ln\left(i_o\right) \tag{2.145}$$

Due to the tiny value of i_o, the *OCV* will always be less than *E*. Finally we have the expression

$$E_c = OCV - \frac{RT}{z\alpha F}\ln\left(i\right) - iR_{cell} - A_E \exp(B_i i) \tag{2.146}$$

This equation has been found to provide a reasonable curve fit to the result of a real fuel cell. However, the logarithmic part of the model does not work well at very low currents (LARMINIE and DICKS, 2003).

With the definition of potential as a function of the overpotential it is also possible to establish an expression for the electrical power density of the fuel cell.

Fuel cells electrical power density is given by

$$P = iE_c \tag{2.147}$$

Table 6 presents some values of the constants for equation (2.146).

Table 6 - Values for the semi- empirical cell potential equation.

Constant	Ballard Mark V PEMFC at 70°C
OCV (V)	1.031
R_{cell} (kΩcm^2)	2.45×10^{-3}
$\frac{RT}{n\alpha F}$ (V)	0.003
A_E (V)	2.11×10^{-5}
B_i (cm^2/mA)	8×10^{-3}

Laurencelle et al. (2001). Apud Larminie and Dicks, 2003)

When introducing the cell definition in equation (2.146) we have

$$P = iE_c = i\left(OCV\right) - \frac{iRT}{z\alpha F}\ln\left(i\right) - i^2 R_{cell} - iA_E \exp(B_i i) \quad (2.148)$$

The first term on the right hand side is the ideal power that the fuel cell would produce just before beginning the net current production. The second term accounts for the power necessary to overcome the remaining activation losses as the net current increases. The third term is the power used to overcome the resistance during the transport of the electrical charges and is dissipated as heat. The last term is the power employed to allow the transport of the chemical species to the catalytic surface in order to react.

Figure 30 represents the electrical power density as the black line that surrounds the orange light area. As current increases, the cell potential decreases while the power increases in the first two regimes, reaching the highest position in regime III where the cell current collapses due to the concentration overpotential and a rapid drop in power is observed.

Figure 30 - Sketch of the polarization curve with the electrical power density curve.

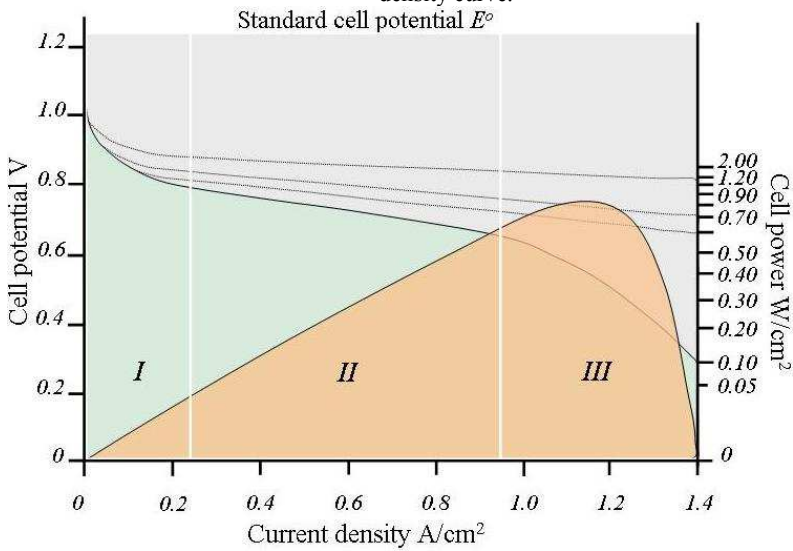

Generally, high power is required by end users. According to the figure, high power means lower voltage and, taking in to account that efficiency and voltages are directly proportional it can be affirmed that high power performance of fuel cell involves low efficiency due to the poor electrochemical conversion on this working range. So, when high efficiency is necessary as in stationary applications, fuel cell has to operate above 0.8 to 0.9 V, and even for applications where power is more important than efficiency, high value of voltage is required (HOOGERS, 2003).

The discussion and models presented so far provide the basic framework to the theoretical description of the operation of hydrogen PEM fuel cells. The models that will be developed in the later chapters will complete this view by providing a more thorough treatment of the different mass transports. In order to assess the state of the art in the fuel cell modeling, in the following sections the many models available in the literature are reviewed and critically discussed.

2.3 REVIEW OF THE MODELS FOR PEM FUEL CELLS

In a general way, the first purpose of the modeling is to predict the performance of a PEM fuel cell (predicting the polarization curve). The second purpose is to provide insight into the processes within the fuel cell.

Complex electrochemical processes, mass, heat and energy transport make the experimental activities with fuel cells a challenging activity. This difficulty in experimental measurements summing to the economical restriction as well as the time consumption in the constructive process of the fuel cell turns computational simulation, as in most of the engineering areas, into an indispensable tool for improving the technology on fuel cells.

Besides addressing the technological advances with their well-known results, modeling and simulation have become the predominant tools for better understanding and optimization (BASCHUK, 2006). Computational modeling makes it possible to investigate complex geometries and different situations by spending less time and effort than experimental investigation. Many difficulties have been faced in the construction of a complete computational model for fuel cell stacks combining all the phenomena. In the same way, availability of experimental data (and modeling) is very restricted and idealized situations are frequently assumed (BIYIKOGLU, 2005).

Some of the most important uses of mathematical fuel cell models are: To help to understand the internal physics and chemistry of fuel cells; to focus experimental development efforts; to support system design and optimization; to support or form the basis of control algorithms; to evaluate the technical and economic suitability of fuel cell applications. Models also help with the understanding of the effect of parameters on the fuel cells performance (U.S. DOE, 2004b).

2.3.1 General Classifications of the Fuel Cell Models

Classification of simulation is not straightforward and in most cases the boundaries are not well defined. Some criteria commonly used to classify the model are the origin of the equations (empirical or phenomenological), its physical scope (part of the fuel cell, the whole cell or the system including peripheral devices) or complexity level. Some variables like number of dimensions, operation regime (dynamic or steady-state), king of electrode kinetic expression used (simple Tafel type expression, Butler-volmer- type expression, complex multistep

reaction kinetics), phases (gas phase, gas- liquid phase), mas transport mechanism in different layers (Fick law, Nernst-Planck expression with Darcy's law or Schlogl's formulation for convective flow) and energy balance (isothermal or non-isothermal approaches) can also be useful for classification.

2.3.1.1 Empirical and Phenomenological Models

The classification by the origin of the equations looks to be the most general. Empirical models concerned with predicting PEM fuel cell performance with a single, algebraic equation. They are effective at predicting performance, but provide little insight into the processes occurring within PEM fuel cell (BASCHUK, 2006). Models that employ artificial neural network (ANN) are examples of empirical models but despite the matches with experimental results, these models are only valid for the specific cell or stack for which the experimental data were obtained and for the range of operating conditions at which the experiment was performed. This makes these models limited in scope (WISHART, 2008).

Phenomenological models, on the other hand, can consider both, internal local behavior condition and overall cell performance. These internal details include mass, momentum, and energy transport in the gaseous reactant and liquid water of the gas flow channel, GDL´s, catalysts layer, and polymer electrolyte membrane. These processes can be described, by fundamental conservation laws, subject to assumptions such as idealizations of the physical structures or the relative importance of some of them. Additionally, a distinction should be made between micro-scale and macro-scale models. In micro-scale models, transport phenomena are modeled at the molecular level. Nevertheless this scale of modeling is impractical for entire PEM fuel cells, since the number of molecules that can be modeled using the molecular dynamics (MD) method are limited. Thus molecular iterations are represented by quantities such as diffusion coefficients in macro –scale models to make the entire fuel cell simulation possible (BASCHUK, 2006).

2.3.1.2 MEA-Center and Channel-Center Approaches

Classification according to the physical scope is applied to macro-scale phenomenological models by Baschuk (2006). According to the author, there is a first group where the processes occurring within the MEA are modeled in detail, while the flow in the gas flow channels is either ignored or characterized by a boundary condition. A second

group of models directs their efforts to modeling the flow in the gas flow channels using techniques of Computational Fluid Dynamics (CFD). The MEA-centered approach (first group) predated the channel-center approach (second group) and as a result the channel-centered approach used many of the equations of the MEA-center approach.

2.3.2 Level of Complexity of the Model

Classification of the mathematical models according to the complexity of the model was presented in the Fuel Cell Handbook (U. S. DOE, 2004b). The author affirms that according to the application of the model, it should have a specific requirement with respect to the level of detail and rigor. For higher level applications the predictive requirements are modest, on the other side of the spectrum, models intended to improve understanding of complex physical and chemical phenomena or to optimize cell geometries and flow patterns that are necessarily very sophisticated, and usually have intensive computational requirements (U. S. DOE, 2004b). Those characteristics give origin to a different fuel cell model. If it is true that the constitutive equations remain in all models, it is also true that their level of detail, level of aggregation, and numerical implementation methods vary widely. The output of the more detailed fundamental models can be used in lower-order models. This flow of information is, in fact, a critical application for high fidelity models. Much work has been done in the development of algorithms to integrate or embed high-fidelity models into system analysis simulation tools. Much of the data on fuel cell performance reported in the literature is, while phenomenologically often interesting, insufficiently accurate and accompanied by far too little detail on the test conditions to be usable for model validation (U. S. DOE, 2004b). According to Wishart (2008) there is a lack of comprehensive fuel cell stack models. This absence of a fully-developed stack model should be addressed in order to obtain accurate modeling results that can be empirically validated.

Figure 31 shows a sketch representing the flow of information from the more complex model (at the bottom of the figure) to the higher level application (at the top of the figure), where relatively simple models are satisfactory and appropriate. These different levels of information are then briefly described.

Figure 31 - Sketch of the classification according to the complexity level.

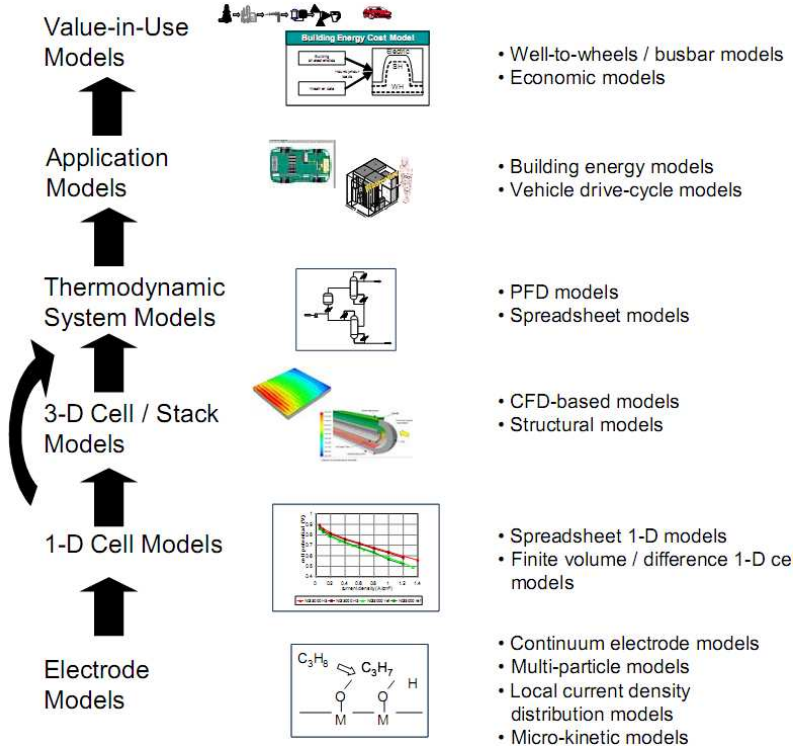

Font: (U. S. DOE, 2004b).

2.3.2.1 Value-in-Use Models

Value-in-use models are mathematical models that allow the user to predict how the unique features of fuel cells will create value or benefits in a given application. One well-known type of value-in-use model is the well-to-wheels analysis, in which the energy consumption, environmental impact, and sometimes cost of different transportation options are compared to consider all steps from the primary resource to the vehicle. One example of this model is the Argon National Laboratories' GREET model (WANG, 2001). A critical subset of value-in-use models is that used to help establish the manufacturing cost of fuel cells. These models typically consider the individual processing steps required to produce particular cell and stack geometries at a given production volume (U. S. DOE, 2004b).

2.3.2.2 Application Models

Fuel cell application models are used to assess the interactions between the fuel cell power system and the application environment. The most common use is in vehicle applications where the dynamic interactions between the power system and the vehicle are too complex to analyze without the help of a mathematical model. Some commercial fuel cell models and software modules are available, such as Emmeskay (LMS, 2008), ADVISOR 2002 from the National Renewable Energy Laboratory, General Computational Toolkit (CGTool) from Argonne National Laboratory –ANL (ANL, 2008), the fuel cell modules in Easy 5_from Ricardo, and FEMLAB from COMSOL. More commercial models are being developed, especially multi-dimensional models. For example, Ansoft Corporation and Synopsys (formerly Avant!) will make PEM fuel cell system models available in the near future, and Fluent and CD ADAPCO Group have recently released CFD PEM fuel cell packages (CD-ADAPCO, 2008). Other available programs include Gamma Technologies' GT Power, and MSC Software's MSC.EASY5. The first ADVISOR is written in MathWorks MATLAB and Simulink. The second ADVISOR 2002 fuel cell system model has a similar approach except that its fuel cell performance is based on a polarization curve, the associated fuel use per cell, and the number of individual cells within the stack. One drawback of the two ADVISOR 2002 models is that thermal and water management is not included. A more detailed fuel cell model is provided in the Chemical Engineering Module of FEMLAB. FEMLAB uses the MathWorks simulation code MATLAB (U. S. DOE, 2004b).

2.3.2.3 Thermodynamic System Models

Most fuel cell models are based on thermodynamic process flow simulators such as Aspen Plus (DOE´s National Energy Technology Laboratory), HYSIS (U. S. DOE, 2004a), GCTool (Argonne National Laboratory) and ChemCAD. This kind of model has an intrinsic objective of helping in the understanding of the interactions between various unit operations within a fuel cell system. They are used routinely by fuel cell developers, and have become an indispensable tool for system engineers. The accuracy of the basic thermodynamic models is quite good, but because the fuel cell sub-models are typically lumped parameter models or simply look-up tables, their accuracy depends heavily on model parameters that have been developed and validated for relevant situations. Stand-alone fuel cell power systems have been

investigated, as well as hybrid systems using a wide variety of fuels and process configurations (U. S. DOE, 2004b).

2.3.2.4 3-D Cell / Stack Models

These models are mainly used to evaluate different cell and stack geometries and to help to understand the impact of stack operating conditions on fuel cell stack performance. It is almost impossible to infer kinetic data without spatially resolved data on current density, temperature and species concentrations. Given the wide range of possible stack geometries and the wide range of operating parameters that influence stack operation, optimization of stack design under specific application requirements is difficult without the help of a model that represents the key physico-chemical characteristics of stacks. At a minimum, the models must represent electrochemical reactions, ionic and electronic conduction, and heat and mass transfer within the cell.

Most of these models rely on existing modeling platforms such as Computational Fluid Dynamics (CFD) – based Fuel Cell Codes. These are based on commercial CFD codes (e.g. StarCD, Fluent (FLUENT, 2008), AEA Technologies' CFX, COMSOL (COMSOL, 2008)) that have been adapted in order to regard the electrochemical reactions and electronic and ionic conduction. In many cases, refinements in the treatment of catalytic chemical reactions and flow through porous media are also incorporated to represent various electrode processes.

Computational Structural Analysis – based codes are based on publicly or commercially available 3-dimensional structural analysis codes (e.g. ANSYS, Nastran, Abacus). Having similar adaptation as those CFD-based codes (ionic conduction, fluid flow, and electrochemical and chemical reactions) they do not provide as much insight into the impact of complex flows as the CFD-based codes. Computational Structural Analysis are usually more efficient (run faster) than CFD-based codes and can be used to assess mechanical stresses in the stack; a key issue in some of the high-temperature fuel cell technologies.

Three-dimensional CFD models can address critical issues such as temperature profiles and fuel utilization; important considerations in fuel cell development. CFD analysis computes local fluid velocity, pressure, and temperature throughout the region of interest for problems with complex geometries and boundary conditions. By coupling the CFD-predicted fluid flow behavior with the electrochemistry and accompanying thermodynamics, detailed predictions are possible.

Improved knowledge of temperature and flow conditions at all points in the fuel cell lead to improved design and performance of the unit. Some examples of these models are the National Energy Technology Laboratory model (NETL's model) and Fluent. Other CFD used as a basis for fuel cell model are the ABACUS, StarCD, MARC and COMSOL.

Computational fuel cell dynamics (CFCD) simulation model are used to efficiently attack difficulties related to the flow of the reactants and products, chemical reaction, and hydrodynamic behavior of the fluid inside the different layer that compounds the fuel cell (WISHART, 2008). These models are based on the iterative solution of the conservation equation of mass, momentum, energy and chemical species. Their performance facing the complicated behavior of the fuel cell can overcome the other models, however, as in all mechanistic fuel cell models, the scope of the CFCD simulation models is often very limited, and it is difficult to arrive at an assessment of the performance of the fuel cell as a whole, let alone an entire fuel cell stack. Some drawbacks with these models are the requirement of powerful computers and the mesh dimension. The computational fluid dynamics (CFD) software Fluent has been used to develop some interesting models. Li and Becker (2004), have developed a three-dimensional PEM fuel cell model that includes multiple phenomena. Sivertsen and Djilali (2005), have developed a single-phase, three-dimensional, non-isothermal CFCD model that takes the distributed overpotential in the catalyst layer of the cathode into account and keeps the heat sources and sinks separate for each electrode.

2.3.2.5 One-dimension Cell Models

These models regard the more critical phenomena of the fuel cell and are indispensable for constructing the 3-D cell models. They are also highly useful in interpreting and planning button cell experiments. Variables considered on this model involve transport phenomena such as: Convective mass transport of reactants and products to/from the surface of the electrodes; Mass transport of reactants and products through the porous electrodes; Conduction of electronic current through the electrodes and current collectors; Conduction of ions through the electrolyte and electrodes (where applicable); Conduction, convection, and radiation of heat throughout the cell, and chemical reactions (Electrochemical reactions at or near the triple phase boundary); Internal reforming and shift reactions taking place inside the anode.

2.3.2.6 Electrode Models

These models look to reproduce the local phenomenology occurring on the electrode surface. They are the fundamental models from which the others are constructed. One can distinguish four levels of electrode models:

a) Continuum electrode approach. These models consider the electrode as a homogeneous zone for diffusion, electrochemical reaction and ion and electron conduction. Using this model it is impossible to distinguish between rate-determining steps in the electrochemically active zone but it is possible to evaluate the importance of the mass transfer versus kinetic processes.
b) Multi-particle approach. These models are similar to the continuum electrode approach but with some modifications which allow them to recognize that electrodes are typically made up of many particles that have different phases.
c) Local current density distribution approach is a refinement on the multi-particle approach. It considers that current-densities are not necessarily homogeneous within the particles, which can strongly impact electrode resistance.
d) Micro-kinetics approach. In this approach the individual reaction steps at or near the triple phase boundary are considered. Although analytical solution (in Butler-Volmer form) can be found, generally a numerical solution is necessary for multi-step reaction. This approach can be embedded in the multi-particle of local-current density approaches, or directly used in a 1-D model. This is the only approach that can give insight into the rate-determining electrochemical processes that takes place in the fuel cell.

2.3.3 Other Classifications

According to Biyikoglu (2005) until 2005 most of the efforts in modeling had been pointed to the water profile inside the PEM fuel cell, particularly in the membrane; modeling of air cathode losses, and integrated modeling of the combined losses in the cell. On the other hand the CFD modeling of PEM fuel cell includes the flow in the gas channel and the influence of convection in the gas diffuser. The models consider phenomena that include mass, momentum, and energy transport through gas channel, electric current transport to porous media and electrochemical reaction at the catalyst layer. The author presents a classification and comparison of experimental and numerical studies which consider modeling of process in the membrane, modeling of

electrode losses, membrane models, CFD modeling and interdigitated flow field.

Haraldsson (2004) proposes interesting key features for model evaluation. These features are summarized in Figure 32. In this option the first four characteristics stand out, these are applied on some of the most well-known references by the author according to Figure 33. Using this classification, the author proposes distinctions according to the origin of the model, whether it is semi-empirical based on experimental data specific to each application, or theoretical (mechanistic), which is based on electrochemical, thermodynamic and sometimes fluid dynamic relationships.

Figure 32 - Key features of fuel cell models according to Haraldsson (2004).

Key features of fuel cell models
Model approach (theoretical, semi-empirical)
State (steady-state, transient)
System boundary (fuel cell, stack, system)
Spatial dimension (zero to three dimensions)
Complexity/details (electrochemical, thermodynamic, fluid dynamic relationships)
Time step (fixed, variable, real-time)
Speed
Accuracy
Flexibility
Source code (open, proprietary)
Graphical representation of model
Library of models, components and thermodynamic properties
Documentation
Validation

For learning objectives, theoretical models are more recommended. They use phenomenological equations such as the Nernst-Planck equation for species transport, the Stefan-Maxwell equation for gas-phase transport and the Buter-Volmer equation for cell potential. The main problems these models face is the time for development and the difficulty in validation. The state of the model refers to steady-state or transient. Although fuel cell response is immediate, other parts of the system cannot respond so rapidly, which is why transient analysis are relevant to fuel cell systems. The system boundary refers to the identification of the domain of the simulation. It can be the MEA, the total fuel cell or fuel cell system which includes other devices like more cells (stacks), compressors, and reformers.

Spatial dimension and complexity are also important criteria and are strongly related. Complexity of the model is associated with the amount of phenomena that it takes into account. A zero-dimension model has a smaller degree of complexity and can be used in the case of initial system optimization. Transport phenomena description obliges the use of at least one dimension. More complex models address the proper treatment of the thermal and water management through the use of electrochemical and thermodynamic relations with the transport equations for flow, energy, mass and charge transfer (HARALDSSON, 2004). The author also presents a comparison between two specific zero-dimensional models based on MATLAB/Simulink with open source, the Virginia Tech model and the Royal Institute of Technology (KTH) model

2.3.4 Review of Theoretical Fundamental Works

The objective of this section is to review the formulation mainly of the pioneer mathematical models available in the literature. The literature is vast and later a shorter and more objective description of the features of the different models will be attempted.

As a methodology for comparison and evaluation we propose in Table 7 some groups of research that have working in the beginning of fuel cell modeling approaches.

After a brief description in chronological order of the more relevant models is done, indicating the main features of every one.

Finally it is find a table that resumes most of the pioneer works and group doing a comparative organization.

Figure 33 - Overview of the fuel cell models available in literature and commercially according to Haraldsson (2004).

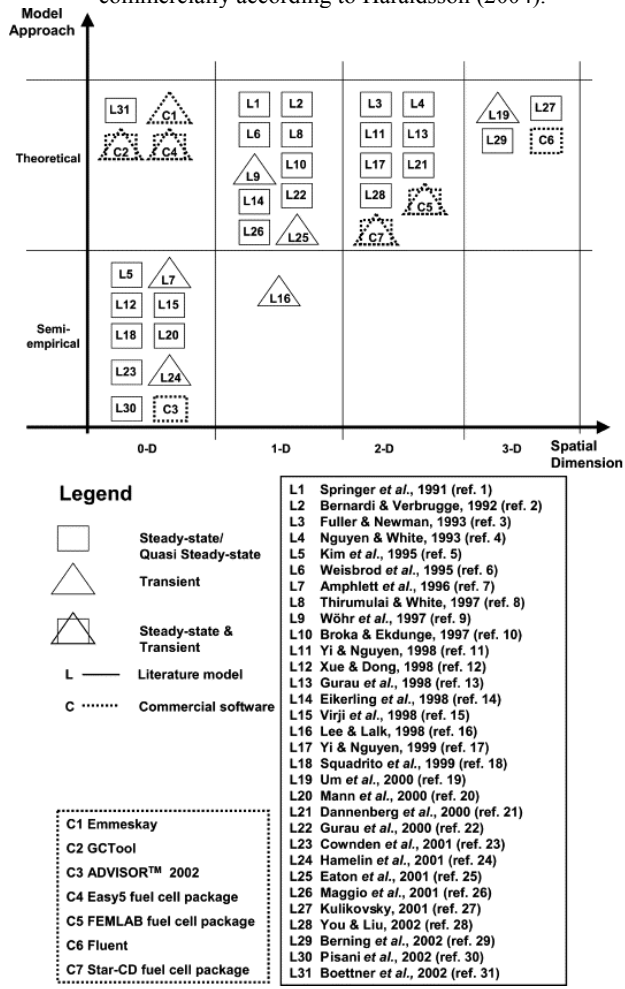

Table 7 shows 21 research group consider relevant by the author and list publications of some of them which are described or cited in this document. Most of the groups are from the U.S.A and belongs to either chemical or mechanical engineering.

Table 7 – Some researches groups on fuel cell

Group and Researchers	Reference
1 General Motors Research and Environmental Staff - *Physical Chemistry Department - Michigan.*Mark W. Verbrugge; Dawn M. Bernardi.	Bernardi and V, 1991/1993
2 Los Alamos National Laboratory - *Electronic Materials and Device Research* Grou*p – NM USA* S. Gottesfeld; M. S. Wilson; T. E. Springer; Cruz Lopez; Roger Jestel; John Davey; Thomas A. Zawodzinski; Partha P. Mukherjee.	Springer et al, 1991/1993
3 University of California Lawrence Berkeley - *Department of Chemical Engineering and Materials Sciences Division Laboratory.* Thomas F. Fuller / John Newman / Adam Z. Weber	Fuller - Newman, 1993
4 University of South Carolina. *Dep. of Chemical Engineering*: Trung Van Nguyen; Ralph E. White; Michael J. Martinez; *Dep. of Mechanical Engineering*: Sandip Dutta; Sirivatch Shimpalee; W.-k. Lee; J.W., Van Zee.	Nguyen and White 1993/ Shimpalee et al 1999/ Dutta et al 2000/ Dutta et al 2001
5 The University of Kansas- *Department of Chemical and Petroleum Engineering* -Lawrence, Kansas Trung Van Nguyen; Xuhai Wang; Dilip Natarajan; Jung Seok Yi; Guangyu Lin; Wensheng He; David L.Wood.	Yi and Nguyen 1998 and 1999/ Wood et al 1998/ Natarajan Nguyen 2001/Natarajan Nguyen 2003
6 Royal MilitaTy College of Canada, Kingston, Ontario, Canada K7K 5LO J. C. Amphlett, R. M. Baumert, R. F. Mann, B. A. Peppley, and P. R. Roberge C.P. Thurgood	Amphlett, el al, 1995a, 1995b
7 Western Reserve University – *Chemical Engineering Department - Cleveland - USA* Vladimir Gurau; Michael J. Bluemle; Thomas A. Zawodzinski Jr; J. Adin Mann Jr.	Gurau et al 1998 / 2000 / 2006 / 2007
8 University of Victoria, Victoria, Canada D. Singh; D.M. Lu; Ned Djilali; Phong Thanh Nguyen; Torsten Berning; J. Fimrite; B. Carnes; H. Struchtrup; David H. Schwarzz; Kyle J. Lange; P.-C.Sui; S. Litster; D. Sinton,; Andrew Rowe.	Singh et al 1999/ Nguyen et al. 2004/ Rowe and Li 2001, Berning, et al. 2002, Berning and Djilali 2003a, 2003b
9 Pennsylvania State University - Electrochemical Engine Laboratory Department of Mechanical and Nuclear Engineering. Chao -Yang Wang; Yun Wang; Sukkee Um; Hyunchul Ju; Hua Meng; Ugur Pasaogullari; Qinjun Kang; I.S. Hussaini	Um et al. 2000/ Um and Wang 2000/ 2004; Wang et al 2001/ Wang et al 1993 /1999
10 University of Waterloo, *Department of Mechanical Engineering Waterloo, Ontario, Canada*,	Baschuk and Li 2000 / Rowe

Xianguo Li; J.J. Baschuk; G. Karimi.	and Li 2001
11 Fossil Fuel Department, CIEMAT- Madrid Spain E. Hontanon; M.J. Escudero; C. Bautista; P.L. Garcıa-Ybarra; L. Daza .	Hontañon 2000
12 Institute for Materials and Processes in Energy Systems Jülich- Germany. A. A. Kulikovsky.	Kulikovsky 2003a, 2003b
13 Virginia Polytechnic and State University, *Department of Mechanical Engineering* Blacksburg, VA, USA N.P. Siegel; M.W. Ellis; D.J. Nelson; M.R. von Spakovsky; M. Coppo	Siegel et al 2003
14 University of Pittsburgh *Department of Mechanical Engineering, Pittsburgh, USA* Pei-Wen Li; Laura Schaefer; Qing-Ming Wang; Tao Zhang; Minking K. Chyu.	Li et al 2003
15 Texas A&M University System - Center for Electrochemical Systems and Hydrogen Research, Texas, USA. Junbom Kim; Seong-Min Lee; Supramaniam Srinivasan.	Kim, et al 1995
16 Département de Recherche Fondamentale sur la Matière Condensée, Groupe Polymères Conducteurs Ioniques, CEA - France P. C. van der Heijden; L. Rubatat; Olivier Diat; Gérard Gebel.	
17 Institute for Fuel Cell Innovation, National Research Council, Vancouver, Canada Datong Song; Qianpu Wang; Zhongsheng Liu; Titichai Navessin; Michael Eikerling -Steven Holdcroft	
18 Simon Fraser University - *Department of Chemistry, Burnaby, BC, Canada* Titichai Navessin; Michael Eikerling; Steven Holdcroft.	
19 AKZO-Nobel Central Research- *RTB department Netherlands***.** J.H.G. Van der Stegen; A.J. van der Veen; H. Weerdenburg; J.A. Hogendoorn; G.F. Versteeg	Van der Stegen (1999a, 199b)
20 Fraunhofer Institute of Solar Energy System, - Freiburg, Germany C. Hebling M. Zobel; M. Oszcipok; C. Ziegler; H.M. Yu	
21 University of Connecticut - Advanced Materials and Technologies Laboratory, Storrs, USA R. Pitchumani; F. Yang,; V. Mishra.	Yang and Pitchumani, 2006

Most of the transport model for MEA in the literature are based on two pioneering models, the Bernardi and Verbrugge (1991 and 1992), and the Springer et al. (1991 and 1993) models. These two models were proposed as one-dimensional, steady-state and isothermal models. While species transport was assumed to be one-dimensional through the MEA, the flow channels were considered to be one-dimensional along the channel with a uniform flow velocity distribution (a plug flow). The most important feature of these models is the treatment of mass and charge transfer across the membrane, along with a treatment of the membrane water content.

The model of Bernardi and Verbrugge (1991 and 1992) focuses on cell polarization characteristics, water transport, and catalyst utilization. They used only the conservation of mass of species equation to describe the concentration distribution along the direction of the main flow in the channels, and no pressure drop was assumed. This flow was analyzed in order to obtain the average concentration of the reaction along the flow channel and then these values were used as a boundary condition at the interface channel-GDL. The GDL was assumed isotropic and both gaseous reactant and liquid water were assumed to exist in the pore regions, each one was assumed as traveling in separate pore networks. No pressure drop was considered in the gaseous phase and the only transport mechanism assumed was the diffusive flux simulated by the Stefan- Maxwell equation. In the liquid phase, conservation of mass and momentum using Darcy's law were considered. The electron migration in the GDL was modeled using Ohm's law. The membrane was assumed as a porous network of channels filled with liquid water and H+ ions. The liquid water transport was described by the mass and momentum conservation equations. The momentum equation was modeled as Darcy's law including a body force term proportional to the gradient of electric potential. The conservation of mass of charge species was modeled with a diffusive flux proportional to concentration and electric potential gradient (called a Nernst – Planck equation). They assumed a fully hydrated membrane which resulted in a constant H+ concentration through the membrane, allowing ion transport only by electric potential gradient. The catalyst layer was assumed to be a porous media containing polymer electrolyte in the void regions. They used measured hydraulic permeabilities for both membrane and electrodes. Unlike the polymer of the membrane, this polymer embedded in the catalyst layer allows the diffusion of reactant gas, that's diffusional flux was described by Fick's law. The redox reaction at anode and cathode was modeled by using the Butler-

Volmer equation. The conservation equations are written for each layer of the MEA, coupled with boundary conditions and solved using the Newton-Raphson method. The restriction in the reactant access due to the presence of the liquid water was not modeled and this effect on the polarization curve could not therefore be simulated.

Springer et al. (1991 and 1993) used detailed, experimentally derived diffusion and electroosmotic drag coefficient of water in Nafion® in a model for steady-state water migration along the membrane. They modeled the conservation of water mass in the membrane using a diffusion flux with two laws. The first is a Fick's law based on the gradient of concentration and the other is a flux of H^+ ions multiplied by an osmotic-drag coefficient. The diffusional velocity of the H^+ ions was assumed to depend on the electric potential gradient. The electrical conductivity of the membrane is related, to the potential through Ohm's law and it was allowed to be variable as well as a function of membrane hydration. In turn, the membrane hydration was modeled as a function of the relative humidity of the gas mixture by an equilibrium condition established experimentally (a liquid/vapor equilibrium condition). The electroosmotic coefficient is linearly dependent of the water content. Although the channels and GDL were modeled as in Bernardi and Verbrugge (1991 and 1992), the catalyst layer was simplified by assuming an infinitely fast electrochemical reaction occurring on the surface (sharp) of the GDL-Membrane interface. Thus, the coupling of mass transfer, electron and proton migration, and electro-chemical reactions within the catalyst layer was included as a boundary condition. Another difference between both models is that Springer et al (1991 and 1993) developed a way of simulating the concentration overpotential by conditioning the GDL porosity with the current density. The first work disregards the flow of liquid water through the electrodes, and the effects of such flow through the electrodes and membrane.

In the above one-dimensional models, the flow in the channel and GDL was always solved separately. Because of that condition, it was not considered an important interaction in the interface channel-GDL like that of dragging of the water coming from GDL by convection phenomenon of air in the channel, and the depletion of reactant along the channel.

This delicate interaction was modeled by Fuller and Newman (1993) in a one dimensional MEA model that coupled the flow channels and MEA along the channel. They applied the concentrated-solution theory and employed limited earlier literature data on transport

properties to produce a general description of water transport in fuel cell membranes. The results emphasize water distribution within the membrane. Similar to Bernardi and Verbrugge (1991 and 1992), the model assumed that there was no pressure drop in the PEM fuel cell, and the transport of species was assumed to occur only by diffusion (using a Stefan-Maxwell formulation) in the GDL and catalyst layer.

Nguyen and White (1993) developed a quasi-two-dimensional, PEM fuel cell model that accounted for the gas channel by assuming a plug flow and linear concentration distribution in the channel. The influence of the liquid water content on the ionic conductivity and the enthalpy change due to phase change is taken into account, but the temperature is considered constant in the solid materials and heat transfer by conduction in the gas phase is neglected. Water concentration, temperature, partial pressures and current density profiles along the flow channels, voltage losses due to oxygen reaction and cell performances are presented (BIYIKOGLU, 2005). The water and heat management model used to investigate the effectiveness of various humidification designs, was similar to that of Fuller and Newman (1993), except that the membrane was modeled using the variable hydration model of Springer et al. (1991 and 1993) and the catalyst layer was considered to be at the interface. The results showed the necessity of anode humidification to avoid the ohmic loss in high current densities. This work was modified by Yi and Nguyen (1998) who developed an along-the-channel model with an improved description of the heat transfer processes. They further refined the energy transport analysis by allowing the bipolar plate, MEA, and the gas within the channel to have different temperatures. They included the convective water transport across the membrane by a pressure gradient, temperature distribution in the solid phase along the flow channel, and heat removal by a natural convection and co-flow and counter-flow heat exchangers. Results show that the performance of a PEM fuel cell could be improved by anode humidification and positive differential pressure between the cathode and the anode to increase the back transport rate of water across the membrane. Results also show that effective heat removal is necessary for preventing membrane dehydration.

Amplhett et. al. (95a and 95b) developed parametric model for predicting the performance of a PEM fuel cell by using a combination of mechanistic and empirical modeling techniques. The model was applied to a Ballard Mark IV FC system. In the mechanistic model, mass transport was modeled by a Maxwell-Stefan, the thermodynamics equilibrium by the Nernst equation , activation loss by Tafel equation,

internal resistances by a Nernst Planck equation, and the uses the ohms law for the ohmic overpotentials. The empirical model allows to obtain the parametric coefficients to predict with accuracy the performance of the fuel cell in the parameters range evaluated.

More recent models included the solution of the flow and mass transfer in the gas distribution channels using CFD techniques. These include the works developed at the University of Miami, Pennsylvania State University, and University of South Carolina.

Gurau et al. (1998), from University of Miami, developed a single-phase, two-dimensional model that included the channels, GDL, catalyst layer, and membrane. The mathematical model was based on the conservation equations of mass, momentum, species and energy in each layer. They were written such as to have the same form, differing only on the source terms. The water transport in the membrane was modeled by a generalized Darcy equation. Current flow was modeled with Ohm's law, and the electrical conductivity was allowed to vary with membrane hydration using the conductivity model of Springer et al. (1991, 1993). The diffusional flux of each species was modeled with Fick's law, and the temperature of the solid and gas phases were assumed to be the same (local thermal equilibrium). The results showed a non-linear oxygen mole fraction distribution along the flow channel direction, which is different from previous linear assumption in pseudo-2D models such as Nguyen and White (1993). They also obtained the oxygen and water concentrations in the gas channel and gas diffuser and studied the influences of some parameters including porosity, temperature, and fluid velocity on the fuel cell performances. This model was later complemented by a

The advantages of the use of interdigitated flow field were discussed by Wood et al. (1998). They investigated the effectiveness of the direct liquid water injection scheme and the interdigitated flow field design towards providing adequate gas humidification to maintain membrane optimal hydration and mitigating the mass transport limitations of the reactants and electrode flooding. They found that liquid water injection when used with the interdigitated flow field design is an extremely effective water management scheme. Kazim et al. (1999) proposed a simple single-component model and found that the interdigitated flow field can increase both the limiting current density and maximum power density. The multi-component model by Yi and Nguyen (1999) found that the higher gas flow rate improves the electrode performance only when the diffusion layer is thinner.

Another way of coupling the MEA and flow in channels is by modeling the MEA in a multi-dimensional manner and simulating any variation along the channel as a boundary condition at the channel-MEA interface. Singh et al. (1999) developed a two-dimensional model consisting of the GDL, catalyst layer and membrane, using the same approach as Bernardi and Verbrugge (1991, 1992). The model takes into account diffusion of the humidified fuel (H_2, CO_2 and $H_2O(v)$) and oxidant gases (O_2, N_2 and $H_2O(v)$) through the porous electrodes, and convective and electro-osmotic transport of liquid water in the electrodes and the membrane. The thermodynamic equilibrium potential is calculated using the Nernst equation. Reaction kinetics are determined using the Butler–Volmer equation. A finite volume procedure is developed to solve the system of differential equations. The model is validated against available experimental data, and numerical simulations are presented for various 1D and 2D isothermal cases. The results indicate that the cathode potential loss, associated with the slow O_2 reaction rate, is dominant at all practical current densities. The simulations also show that two-dimensionality has a significant effect on water management and on some aspects of fuel cell performance. In particular, the anode and cathode water fluxes are found to vary considerably along the oxidant and fuel flow channels, and two new transitional water transport regimes are revealed by the 2D simulations. The influences of flow configuration and electrode porosity on predicted cell performance are also discussed. this study was similar to that presented by Kazim et al. (1999) who applied the conservation of mass, momentum and species to the GDL. The conservation of momentum was assumed to take the form of Darcy's law, and the catalyst layer was assumed to be a surface.

The research group in the University of South Carolina began their approach with the three-dimensional, single phase model of Shimpalee et al. (1999). They considered the situation of steady state in a straight channel and focused their attention on the heat transfer. The isothermal three dimensional model was implemented in a commercial CFD software (FLUENT), and included channels and MEA. The generalized Darcy's law was used for the conservation of momentum equation in the GDL and Fick's law accounted for the diffusive flux. The membrane model of Springer et al. (1991, 1993) was used for the current flow and water transport in the membrane. The conservation of energy was added in Shimpalee and Dutta et al. (2000).

The group from Pennsylvania State University developed a two-phase, two-dimensional model of the cathode gas flow channel and

GDL using the Multiphase Mixture Model (MMM) presenting the results in Wang C.Y. and Cheng, (1997). There the catalyst layer was treated as a sharp surface, and modeled with a jump condition. The conservation equation of mass was solved as well as momentum and species for the liquid and gas phases. The conservation of momentum in the cathode GDL was in the form of Darcy´s law, and through algebraic manipulations, the flux of liquid water was found as a function of the capillary pressure and gravitation body force. The capillary pressure, in turn, was modeled as a function of the saturation, or volume fraction of liquid water in the electrode backing void space. Thus, although the conservation equations were solved for different values of velocity, pressure, and concentration, the values for each phase could be determined with algebraic relationships

In 2000s multi-dimensional models based on the continuum approach and solving a complete set of conservation equation (continuity, Navier-Stokes, Energy) coupled with electrochemical reaction were broadly developed.

A complete mathematical model is presented by Baschuk and Li (2000) from the University of Waterloo, for the performance and operation of a single PEM fuel cell. The model incorporates all the essential fundamental physical and electrochemical processes occurring in the membrane electrolyte, cathode catalyst layer, electrode backing and flow channel. The author attempted to improve the model of Bernardi and Verbrugge (1991, 1992) by allowing the void space of the catalyst layer to be occupied by gas reactants, liquid water and polymer electrolyte. This allowed the model to simulate the concentration overpotential region of the polarization curve through the variation of a parameter called the degree of water flooding in the cathode catalyst layer and/or cathode electrode backing region. It also included the effect of variable degree of water flooding on the cell performance.

A single phase, isothermal, two-dimensional, transient model, using a similar formulation as in Gurau et al. (1998), was presented in Um et al. (2000) from the Pennsylvania State University. Unlike the FLUENT model of the University of South Carolina group the recent models do not assume that the catalyst and polymer electrolyte layers are one-dimensional. This model paid special attention to the jump oxygen condition at the gas diffuser/catalyst layer interface, which used Henry´s law to account for the difference of oxygen concentration between the liquid and the gas phase. They studied the influence of hydrogen dilution on the polarization curve and found that the cell voltage decreases when reformate gas is used. A transient response of

current density with the change in output voltage is also presented. The model intended to extend the efficient single-domain CFD formulation previously developed for batteries to PEM fuel cells. The author shows a transient and multidimensional model that accounts simultaneously for electrochemical kinetics, current distribution, hydrodynamics, and multicomponent transport. One objective of this work was to develop a transient, multidimensional model for electrochemical kinetics, current distribution, fuel and oxidant flow, and multicomponent trans-port in a realistic fuel cell by finite volume based computational fluid dynamics (CFD). The second goal, and one of practical importance, was to explore hydrogen dilution effects in the anode feed on PEM fuel cells running on gas from fuel reforming. In Um and Wang C.Y. (2000), the authors applied this multidimensional model to study electrochemical kinetics, current distribution, fuel and oxidant flow, and multicomponent transport in a PEM fuel cell with the interdigitated air cathode. There, fully three dimensional computations were performed, and results of the flow field, species profiles and current density distribution were presented with emphasis on the air cathode. Polarization curves for conventional and interdigitated flow fields were simulated and compared.

The enhancement of the performance of the PEM fuel cells by optimizing the gas flow distribution system was studied by Hontañón et al. (2000). In this study, 3D numerical simulations of the gas flow in the assembly, consisting of the fuel side of the bipolar plate and the anode, are performed using FLUENT. Two types of flow distributors are investigated: a grooved plate with parallel channels of the type commonly used in commercial fuel cells, and a porous material. The simulation showed that the permeability of the gas flow distributor is a key parameter affecting the consumption of reactant gas in the electrodes. Fuel utilization increased with decreasing permeability of the flow distributor. In particular, fuel consumption increased significantly when the permeability of the cathode porous material decreased to values below that of the anode. Even though the permeability of the grooved plate can be diminished by reducing the width of the channels, values lower than 1mm are difficult to attain in practice. They showed that porous materials are more advantageous than grooved plates in terms of reactant gas utilization.

Dutta et al. (2000), also from the University of South Carolina, presented a three dimensional numerical simulation of straight channel PEM fuel cells, at steady state, for an isothermal and single phase flow. The model considered water transport in the flow channels as vapor, the

electrical resistance was neglected and the chemical reaction was assumed infinitely fast. The FLUENT software was used as a flow solver. The domain included the anode flow channel and diffusion layer on both sides and considered five chemical species, H_2, O_2, CO_2, N_2 and H_2O. The model related the channel fluid-dynamic with the electrode and membrane processes and provided the axial distribution of the current density and rate of water transport as a function of stoichiometric ratios of reactants and products, thickness of the MEA, flow conditions and cell voltage. Local current density was found to decrease with an increase in the membrane thickness and when the cell voltage is increased. The current density was found higher near the hydrogen inlet and the inlet orientation of the cathode side did not significantly influence the results for this operating condition because the axial velocity on the anode side was relatively high. They concluded that the effect of the GDL added to both sides of the MEA is to create a large reaction area. In the GDL the reactant are transported by both convective and diffusive transport mechanisms and convection is not negligible even for low porosity. The model was validated against published experimental data. A transient simulation of the cell current density response to a step change in cell voltage was also analyzed. They concluded that at high current densities (>1 A/cm^2) a large amount of liquid water produced within the air cathode generates a two phase flow in this region, that becomes a limiting mechanism for cell performance.

This model was later completed by Dutta et al. (2001) modeling a complete fuel cell with a serpentine flow field. They presented the numerical prediction of the velocity distribution, the gas-mixture distribution, and the detailed reactant consumption on the MEA. The model was intended to predict the mass flow between channels with a serpentine flow path. Electro-chemical reactions were modeled as source/sink terms in the solution of the complete three-dimensional Navier-Stokes equation with multicomponent mixture. It was demonstrated that flow distribution in both anode and cathode channels are significantly affected by the mass consumption patterns on the MEA. The water transport was found governed by both electro-osmosis and diffusion processes.

The research group from the Pennsylvania State University presented an improvement on their later work in Wang et al. (2001). They studied analytically and numerically two-phase flow and transport of reactants and products in the air cathode of PEM fuel cells. Single- and two-phase regimes of water distribution and transport are classified

by a threshold current density corresponding to the first appearance of liquid water at the membrane/cathode interface. When the cell operates above the threshold current density, liquid water appears and a two-phase zone forms within the porous cathode. A two-phase, multicomponent mixture model in conjunction with a finite-volume-based computational fluid dynamics (CFD) technique was applied to simulate the cathode operation in this regime. The model was able to handle the situation where a single-phase region co-exists with a two-phase zone in the air cathode. Capillary action was found to be the dominant mechanism for water transport inside the two-phase zone of the hydrophilic structure. The liquid water saturation within the cathode was predicted to reach 6.3% at 1.4 A/cm^2 for dry inlet air.

In the study of Costamagna (2001), the transport equations are the basis of a simulation model which allowed the evaluation of the distribution of the physico-chemical parameters within the structure of a PEM fuel cell reactor. Model validation was presented and the validated model was then used to investigate the behavior of the fuel cell, with particular attention to critical operating conditions. Critical conditions appeared in a number of cases: flooding, membrane drying and degradation due to temperature peaks were discussed in this paper.

Rowe and Li (2001) developed a non-isothermal model of a PEM fuel cell that accounted for variable membrane hydration. The author incorporated the transport of mass, momentum, species, and energy in the GDL, catalyst layer and membrane. It also included mass and species transport in the gas flow channels in a manner similar to Bernardi and Verbrugge (1991, 1992). In the catalyst layers, the reaction kinetics was modeled with the Butler-Volmer equation. The diffusion was assumed to be described by Stefan-Maxwell equations, as the only transport media of species in the GDL and catalyst layer. Transport of liquid water was not analyzed, but the amount of flooding was included as an input parameter in order to simulate the entire polarization curve. Thus the influence of mass transport limitations, temperature variation, and evaporation and condensation of water are regarded. Reactants in GDL and catalyst layer were allowed to have a variable amount of humidification, which left the variable humidification membrane model of Springer et al. (1991, 1993) in the membrane. The model was used to investigate different fuel cell designs and operating conditions. The effect of the membrane hydration on the temperature of the cell was studied.

Natarajan and Nguyen (2001) developed a transient, two-phase, two-dimensional model for the cathode electrode backing layer. For the

gas transport, the author used multicomponent diffusion equations and they used an adapted form of Darcy's law to account for the capillary flow of liquid water in the porous GDL. Measurements were used to validate the model. The performance of the cathode was found to be dominated by the dynamics of liquid water, especially in the high current density range. Conditions that promoted faster liquid water removal such as temperature, dryness of the inlet gas stream, reduced diffusion layer thickness, and higher porosity improved the performance of the cathode. The model results showed that for a fixed electrode width, a greater number of channels and shorter shoulder widths are preferred. The transient profiles clearly showed that liquid water transport is the slowest mass-transfer phenomenon in the cathode and, is primarily responsible for mass-transfer restrictions especially over the shoulder. This two-dimensional model was extended into a quasi-three-dimensional model by Natarajan and Nguyen (2003). As in the quasi-two-dimensional models, the flow in the gas flow channels was analyzed by assuming that it was one-dimensional along the flow direction. This analysis supplied boundary conditions to the two-dimensional analysis, coupling the flow in the gas flow channels and electrode backing layers. The channel was discretized into control volumes. An iterative solution procedure was incorporated into each control volume to determine the average current density and the corresponding oxygen consumption and water generation rates. Downstream channel concentrations were calculated based on stoichiometric flow rates and the solution obtained from the preceding control volumes. Comparison of the model results with experimental data and the existing 2D model showed that accounting for the oxygen concentration variations along the channel and its effect on the current density is critical for accurately predicting the cathode performance. Variations in the current density along the channel were strongly influenced by the changes in oxygen concentration caused by consumption due to reaction and dilution caused by water evaporation. Operating parameters that facilitated better water removal by evaporation like higher temperature and stoichiometric flow rates and lower inlet stream humidity resulted in a higher net current. Operating conditions that resulted in minimal loss in oxygen concentrations led to a more uniform current density distribution along the channel.

The group from the University of Victoria developed a computational, three dimensional, non-isothermal model for PEM fuel cell in Berning et al. (2002). The model incorporates both MEA and channel and can account for major of the transport phenomena inside the

fuel cell. The model was implemented into a computational fluid dynamics code and has focus in physical insight and fundamental understanding. This objective was leaded by the author afforded by the detail three dimensional distribution of reactant concentration, current densities, temperature and water fluxes. The results evidenced the strong temperature gradients presents inside the fuel cell even in the MEA. It was also possible to significant impact fo t eh three dimensional nature of the transport on the current distribution and current density.

Li et al. (2003) developed a 3D numerical model associating the heat and mass transfer and the electrochemical reaction in a PEM fuel cell and simulated a miniaturized PEM fuel cell with complex flow channels. The numerical computation is based on the finite-volume method. Governing equations for flow and heat and mass transfer are coupled with the electrochemical reactions and are solved simultaneously. The perimeters of the bipolar plates are also included in the computational domain to account for their heat conduction effect. The miniaturized PEM fuel cell has an MEA sandwiched by two brass bipolar plates etched with a number of winding gas channels with a flow area of 250 × 250 microns. The influence of anode gas humidity on the performance of the fuel cell is investigated through model prediction. Finally, field details of velocity, mass fraction and electromotive force are illustrated and discussed.

A few works considered the porous media to have small pore size such that Knudsen diffusion dominates the transport of the chemical species. Kulikovsky (2003b) coupled a three-dimensional flow channel and electrode backing model with a one-dimensional model of the transport in the catalyst layers and polymer electrolyte. The transport of water in the electrolyte was modeled on the same approach as Springer et al. (1991, 1993), while gas transport in the catalyst layer was assumed to be due to Knudsen diffusion only. In the catalyst layer, the conservation of water included the water flux due to a gradient in gas phase water concentration and a gradient in the hydration of the membrane; thus, there were two unknowns but only one equation. However, the membrane hydration and the concentration of water in the gas phase were not independent, but rather related through the hydration versus relative humidity curves of Springer et al. (1991, 1993). Thus, the gradient of membrane hydration could be transformed to a gradient of gas phase water concentration and the conservation of total water was solved.

A different approach for steady state simulation in a two-dimensional geometry was presented by Siegel et al. (2003). The model

accounted for species transport, electrochemical kinetics, energy transport, current distribution, and water uptake and release in the catalyst layer. The authors solved the gas phase and liquid water transport separately and coupled them with an interfacial mass transfer term. The model for the catalyst region was based on an agglomerate geometry, which required water species to exist in both dissolved and gaseous forms simultaneously. The author assumed that the void space of the catalyst layer was filled with both gas and polymer electrolyte. The conservation of mass, momentum and species was applied to the gas phase, while the conservation of water was considered in the membrane. The membrane model of Springer et al. (1991, 1993) was used to describe the water and current transport in the polymer electrolyte. The commercial CFD solver CFDesign ^{TM} was used. Results showed the relation between the fuel cell performance and the catalyst structure. A similar model but including the transport of liquid water within the porous electrodes as well as the transport of gaseous species, protons, energy and water dissolved in the ion condition polymer, was presented by Siegel et al. (2004). The author used measurements to validate the computational model. It is illustrated the importance of the transport of water within the porous sections of the cell and in the polymer region of the MEA.

The detailed thermal and water management in the membrane of PEM fuel cells is investigated numerically by Yan et al. (2004). The coupling effects of mass diffusion and temperature gradient on the water distribution in the membrane were taken into account with consideration of the temperature dependent diffusivity. Thermal and water transport equations with various boundary conditions were solved by the control volume method. Predictions showed that under the conditions of fixed water concentration at the cathode side, the effect of cathode temperature, T_c, on the water concentration is significant. Increasing T_c may lead to an increase in membrane dehydration. At the water-flux condition on the cathode side, the influence of the operating temperature on the water distribution in the membrane showed a similar trend. The effects of the anode temperature, T_a, on water management in the membrane were also examined. It was found that T_a has a considerable impact on the water content in the membrane. In addition, high current density may cause non-uniformity in the temperature distribution in the membrane.

Um and Wang (2004) presented a computational fuel cell dynamics (CFCD) model to elucidate 3D interactions between mass transport and electrochemical kinetics in polymer electrolyte fuel cells

with straight and interdigitated flow fields, respectively. The model features a detailed MEA sub model in which water transport through the membrane with spatially variable transport properties and spatial variations of the reaction rate and ionic resistance through the catalyst layer are accounted for. Emphasis was placed on obtaining a basic understanding of how 3D flow and transport phenomena in the air cathode impact the electrochemical process in both types of flow field. Fully 3D results of the flow structure, species profiles and current distribution were presented for PEM fuel cells with an interdigitated cathode flow field. The model results indicated that forced convection induced by the interdigitated flow field substantially improves mass transport of oxygen to, and water removal from, the catalyst layer, thus leading to a higher mass-transport-limiting current density as compared to that of the straight flow field.

Nguyen et al. (2004) presented a three dimensional CFD model of a PEM fuel cell with serpentine flow field channels. The model accounted for the major transport phenomena in a PEM fuel cell: convective and diffusive heat and mass transfer, electrode kinetics, and potential fields. A unique feature of the model is the implementation of a voltage to-current (VTC) algorithm that solves for the potential fields and allows for the computation of the local activation overpotential. The coupling of the local activation overpotential distribution and reactant concentration makes it possible to predict the local current density distribution more accurately. The simulation results reveal current distribution patterns that are significantly different from those obtained in studies assuming a constant surface overpotential. Whereas the predicted distributions at high load show current density maxima under the gas channel area, low load simulations exhibit local current maxima under the collector plate land areas. A parallelized 3D CFD model is presented by Shimpalee et al. (2004) to a 480 cm^2 PEM fuel cell flow field selected from US patent literature to demonstrate that analysis of large-scale cells is possible. The distributions of pressure, temperature and electrochemical variables for stationary and automotive operating conditions were examined. Using parallel computing techniques, the computational time was shown to be significantly reduced by increasing the number of processors while maintaining less than 1% error in mass balance.

To master and organize the vast information in PEM fuel cell model in tabular form is one of the intension here. Table 8 presents some of the last described articles in that way that allow the comparison

between them. It is important to highlight that none article is related to the fundamentals of the approach focus specifically on fuel cell.

Table 8 - Fuel cell pioneer model in literature

Topic		Reference	Bernardi and V 91/93	Springer et al 91/93	Fuller-Newman 93	Nguyen and White 93	Amplett 95a/95b/96	Yi and Nguyen 98/99	Gurau et al 98/00	Singh et al 99	Shimpalee et al 99/00	Wang C. Y. et al 97	Baschuk and Li 00	Um et al. 00	Um and Wang C.Y. 00	Hontañón et al. 00	Dutta et al 00/01	Wang Wang C.Y.et al 01	Rowe and Li 01	Berming et al 02/03	Natarajan - Nguyen01/ 03	Li et al. 03	Kulikovsky 03a/03b	Siegel et al 03/04	Um and Wang C.Y 04	Nguyen et al. 04
Characteristic	Theoretical		N				N		N	N			N		N	N	N	N	N	N	N		N			
	Semi-empirical			X			A				X							A					A				
	Regime		S	S	S	S	ST	S	S	S			T				S/T			S	T		S	S		
	Dimension		1	1	2	2	0	2	2	2		2	1	2	3	3	3	3		3	2/3	3	3	2	3	3
	Species			M	M					M		M			M		M	M		M						
	Phases		M			M		M		M		M			M			M	M		M			M	M	M
	Non-isothermal								X										X	X						
Domain	Membrane		X	X	X	X	X	X	X	X			X		X	X	X		X	X			X	X	X	X
	Electrode		X		X	X	X	X	X	X			X	X	X	X	X	X	X	X			X		X	X
	Channel				X	X		X	X				X	X		X	X		X	X			X		X	X
	Single cell							X					X									X				
	Stack																									X
Channel	Straight		X	X					X		X						X				X				X	
	Serpentine																X									X
	Interdigitated							X							X										X	
	Other															X										
Code	Commercial								X					X		X	X	X		X	X			X	X	X
	In house		X	X	X	X	X	X	X						X									X		
Focus	Losses: Activation			X	X	X	X	X	X				X	X			X	X	X		X	X	X	X	X	X
	Losses: Ohmic			X	X	X	X	X	X				X	X			X	X	X		X	X	X	X	X	X
	Losses: Mass Transport			X	X	X	X	X	X	X			X	X			X	X	X		X	X	X	X	X	X
	Channel Design															X	X				X	X	X		X	X
	Water management		X	X	X	X	X	X	X	X			X				X		X	X	X			X	X	X

	Heat management			X	X	X	X	X	X			X						X	X				X	X	
	Catalyst	X						X					X										X		
	Fuel utilization																								
	Fundamentals																								
Modeling approach	Navier Stokes							X	X							X									
	Drag Relation		X						X							X					X	X			
	Darcy	X						X	X	X	X	X				X				X		X			
	Diff Diluted	X		X				X	X	X		X	X			X									
	Diff Concentrate			X												X			X	X					
	Diff Knudsen																				X				
	Dusty Gas																								
	Maxwell-Stefan	X	X	X		X												X	X						
	Convection						X	X	X					X		X			X					X	X
	Conduction						X												X						
	Nernst -Planck	X				X			X										X						
	Variable Hydration		X		X	X	X	X				X				X	X	X			X	X			
	Buttler-Volmer	X				X			X									X	X						
	Chem. Mechanist											X											X		
	Electrochem Kinet											X		X					X		X		X	X	X
	Ohm Law	X	X			X		X				X							X						
	Henry Law	X											X												
	Electric Potential	X											X			X								X	X
Profile	Water				X	X			X							X	X							X	X
	Temperature				X		X						X												X
	Partial pressure				X	X	X													X					
	Current density				X	X	X							X		X				X		X	X	X	
	Potential											X				X									X
	Species Concentr				X	X	X	X					X	X		X	X			X				X	
Group		1	2	3	4	6	5	7	8	4	9	10	9	9	11	4	9	8/10	8	5	14	12	13	10	8
A	Analytical	N	Numerical					S	Steady stead					T	Transient					M	Multi-				

More recently, several analyses with a single phase model that uses the membrane water transport equations of Springer et al. (1991, 1993) have been presented, with sample works being Wang and Wang (2006), Shimpalee (2006a, 2006b), Lister (2006), Arato and Costa (2006a 2006b), and Arato et al. 2006. More complete and comprehensive works have been presented in the latest year by Baschuk (2006), Ren (2007) and Wishart (2008).

The literature review revealed the vast amount of information that exists in PEM fuel cell modeling and simulation (WEBER and NEWMAN, 2004; WANG C.Y., 2004; SOUSA and GONZALEZ, 2005; SIEGEL, 2008; DJILALI 2007; WANG ET AL. 2011, JIAO and LI 2011).

Most of the recent works are improvements of the earlier models and implementations known as Computational Fuel Cell Dynamics – CFCD. They explore multidimensional and multiphysics effects. The higher computational capacity available today allows to use more refined grids, explore more detailed geometries and to develop optimization routines aimed at optimizing certain design or operation features. The basic phenomenology has remained unchanged, based on the classical mass and charge transport models. Here, a review of these models is proposed in order to assess their limitations and propose more general formulations which will allow exploring more detailed phenomena.

Before advancing to the transport models, the measurement of a polarization curve and the application of the simpler lumped models is presented with the aim of providing a hands-on implementation of a fuel cell stack produced in Brazil and determining the magnitude of the many macroscopic properties of a typical PEM fuel cell.

3 MEASUREMENT OF THE POLARIZATION CURVE

This section presents the measurement and the zeroth dimensional modeling of the polarization curve of a 200 W PEM fuel cell operating in the Laboratory for Combustion and Thermal System Engineering (LabCET) at UFSC-Florianopolis. This test bench was first conceived by Silva (2010) and later improved by Nunes (2011) and Mariño (2011), simultaneously to this work.

3.1 MATERIALS AND APPARATUS

The test bench is composed of a 200 W PEM fuel cell manufactured by Electrocell, Brazil, a supply and control gas station, a dynamic load, pressure and temperature measurement sensors.

The gas station was designed for be used with three cylinders, two for reactants gases and one for the inert gas used for purge and humidification. The reactant gases used were high purity oxygen and hydrogen and the inert gas was high purity nitrogen. All these gases are stored in a standard type T cylinder according to Table 9.

Table 9 - Characteristics of the standard T type cylinder for gas storage

Gas	Charging Pressure at 21°C	Volume STP (m3)	Purity type (Analitico)	Function
H2	16.475,18 (kPa) (168kgf/cm2)	7,2	99,999 %	Reactant
O2	19.613,3 (kPa) (200kgf/cm2)	10	99,99 %	Reactant
N2	19.613,3 (kPa) (200kgf/cm2)	9	99,999 %	Purge and humidification

Figure 34 presents a schematic representation of the gas station formed by three cylinders, hydrogen, nitrogen and oxygen, and pipe lines made of ¼ inch steel pipe with metallic junction

Figure 34 - Gas distribution and control network

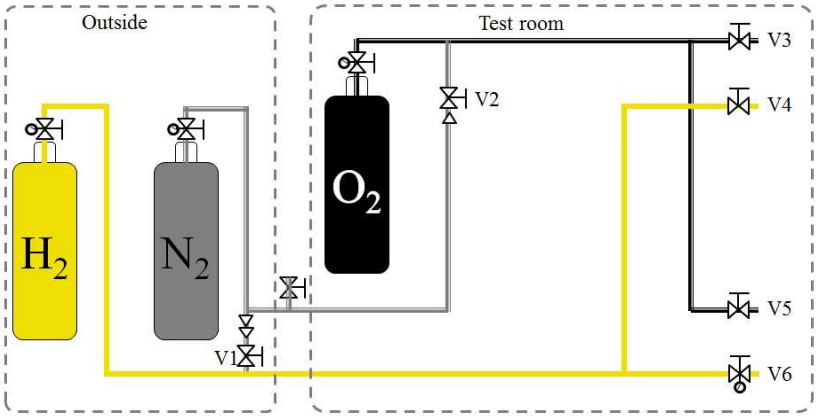

The 200W fuel cell bench is composed by two sub-systems, *a*) the gas control measurement and humidification system; and *b*) the fuel cell stack electrical performance system.

Figure 35 presents the humidification system. This system is a bubbling system that guarantees water saturation of the gas at the chosen temperature. Temperature at humidifier is established with an electrical resistance controlled by a relay. Mass controllers in the range of 5 l/min are used for both reactants. The controllers have a measurement uncertainty of ± 0.005 l/min.

Figure 36 is a representation of the Fuel cell stack load and temperature control. The power delivered by the PEMFC stack is controlled by a dynamic load. The dynamic load has an estimated uncertainly of ± 0.01% of the reading. Thermal control is performed by forced convection of an air flow in rectangular channels placed among the bipolar plates, using a variable power DC fan

Figure 35 - Gas control measure and humidification system

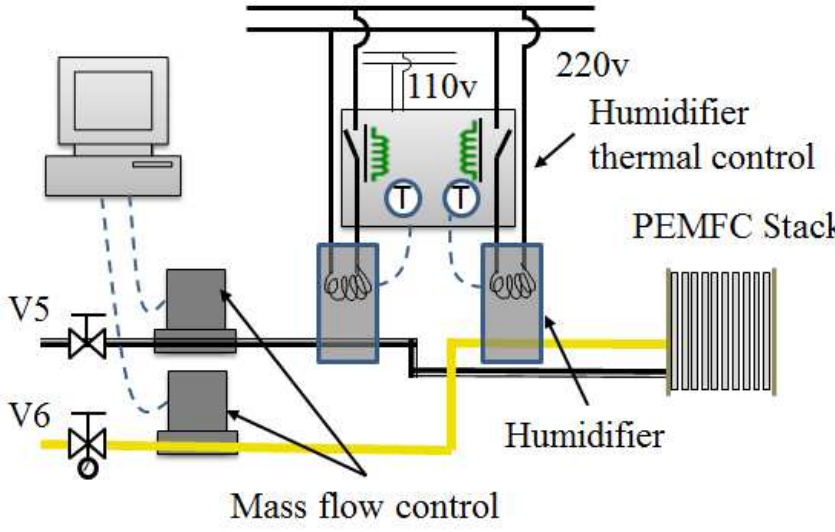

Figure 36 - Fuel cell stack electrical performance system

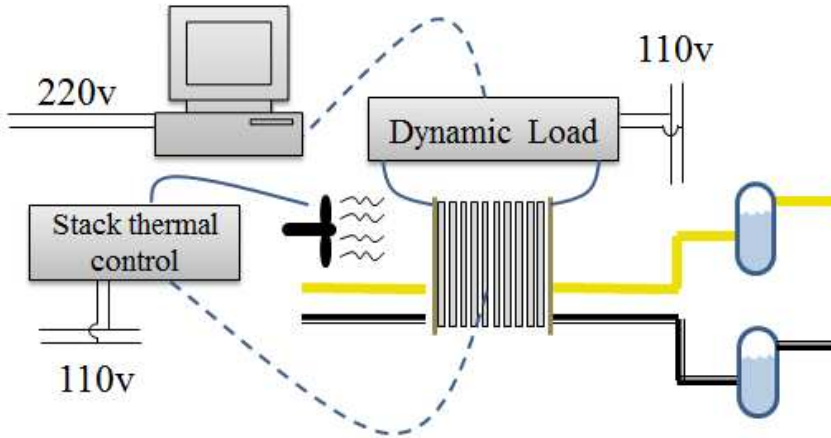

The gas control, measurement and humidification sub-system, is composed by: i) two mass flow controllers controlled by a PC with LabView® routine, one for oxygen and the other for hydrogen, and ii) the humidification system. Figure 37 shows a picture of the bench inside the test room.

Figure 37 - 200W PEM Fuel cell stack bench at LabCET

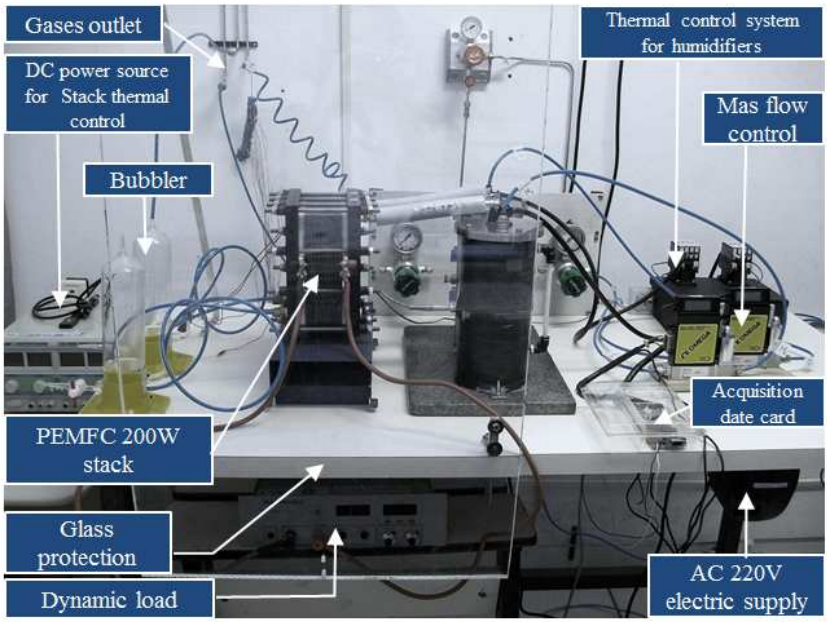

The humidification system are two steel cylinders of 490 cm^3 of internal volume (25 cm height and 10.16 cm internal diameter), thermally insulated from the environment and with a deionized water column, Figure 38. The humidifiers are designed to obtain full saturation at the set-point temperature for both gases. Besides humidification, this system is also responsible for the gas heating at the cell temperature in order to avoid condensation inside it.

The thermal control in the humidifier water is done by electrical resistance, thermocouples (K-type) and a relay device to regulate the power input to the resistance to follow the set-point temperature. A porous stone at the bottom of the inlet line is responsible for spreading the gas in mini-bubbles to increase the total contact area with the heated water and guarantee the total humidification during the rising of the bubbles along the deionized water column with height of 10 cm. The gas pipes from the humidifier to the fuel cell inlet are thermally insulated.

Figure 38 - Gas humidifier and thermal control

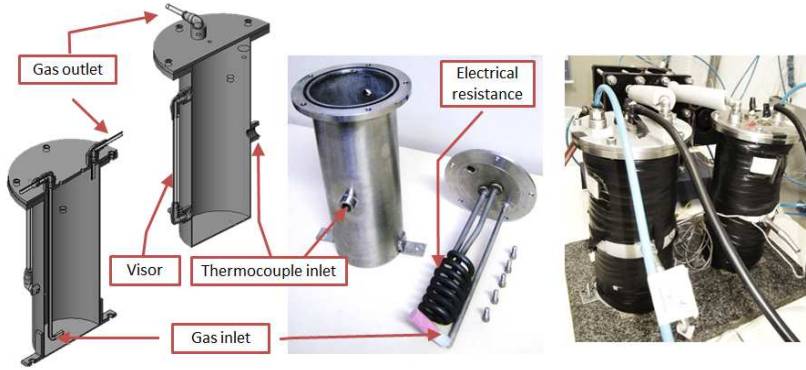

The fuel cell stack's electrical performance system allows the control of the power taken from the fuel cell (or delivered to it). This control is done by a dynamic load, device capable of setting a defined variable (current) in order to demand another variable (tension). The dynamic load used in the 200 W bench has a current limit equal to 25 A and it is operated by computer. When the fuel cell is operating, heat is produced from the cathode reaction. This would increase the temperature if it was not removed from the stack. For this reason a cooling system is necessary. The cooling system of the stack is based on convective cooling by air blown by a 7 W DC air fan, fed by a 48 V variable power load source. Currently, the control of the power load is manual but a new automatic system is being implemented as proposed by Mariño (2011). As a visual verification of the gas flux, two bubblers are located at the gas outlet of the fuel cell stack. After the bubblers, the remaining reactant gas is exhausted into the atmosphere. A more detail description of the 200 W bench can be found in Nunes (2011).

3.2 METHODOLOGY

The methodology used to characterize the 200W fuel cell stack is the measurement of voltage as a response to a set current. The polarization curve is a direct measure of the fuel cell performance and efficiency.

The uncertainties related to the measurements are expressed as

$$RM = I \pm E_{\max} \tag{3.1}$$

where RM is the result of the measurement, I is the average of the indications of "n" repeated measurements, and E_{max} is the maximum

error of the measurement process for the measured conditions (ALBERTAZZI and SOUSA, 2008).

The values for Eq. (3.1) corresponding to the two lines of measurement, the dynamic load and the flow controller are shown in Table 10.

Table 10 - Measurement uncertainties of the measurement systems.

Dynamic load from Electrocell CDE25A-20V			
Accuracy	±1% full scale	Maximum error	±0.25A

User's guide OMEGA mass flow controllers FMA 5400/ FMA 5500			
Accuracy	±1.5% if full scale, including linearity for gas temperatures from 15°C to 25°C and pressure of 0.35 to 4.1 bar	Maximum error	±0.15 l/min
Repeatability	±0.5% of full scale	Random error	±0.05 l/min

The standard test procedure consisted in operations for purging, heating, activation and testing:

- Purging: A nitrogen flow of 1 l/min was established for 40 minutes at 50°C to purge and humidify.
- Activation: An oxygen flow of 1.5 l/min and a nitrogen flow of 3 l/min were established in the open circuit cell (idling) for 10 minutes at 50°C in order to active the cell.
- Heating: A current of 15 A was imposed in the circuit in order to heat the fuel cell up to 5°C above that of the test temperature.
- Testing: The initial oxygen and hydrogen flux were held constant during the tests. Pressure was equal to 50 kPa manometric on both sides of the membranes. The polarization curve was obtained by setting a current and waiting for 2 minutes, which was determined sufficient for the stabilization of the cell before reading the voltage (NUNES, 2011).
- Different conditions were tested and a set of three tests were performed in order to check the repeatability of the results.

3.3 RESULTS

An early test evidenced that the maximum current of the dynamic load (25 A) was under dimensioned for the fuel cell stack used. Using the effective area provided by the manufacturer (144 cm^3), it was found

that at this maximum current the fuel cell stack remained in the ohmic-loss regime and the mass transfer-limited regime could not be reached. This limited the amount of information that could be obtained directly from the tests. The modeling will allow for obtaining additional information but at the cost of further validation against other polarization curves available from the literature.

Batteries of tests were run to determine the response of the stack when operating in different humidification and cell temperatures, set both at the same values. Three temperatures were selected: 50°C, 60°C, 70°C, and 80°C. Smaller current steps were used at low currents in order to better describe the performance during the rapid voltage drop in the activation regime. Figure 39 shows the averaged (a) polarization curve and (b) electrical power observed for each temperature. The electric power curve was calculated after smoothing out the measurements using the model that will be described shortly.

Although the averaged polarization curves are superposed, the fuel cell stack presented a slightly better performance at 70°C, with maximum power of about 183 W, more uniformity between runs and less oscillation. At low currents, there was no noticeable difference among the different runs. The run at 50°C presented higher oscillation at higher currents. The tests performed later presented better stability, probably due to better activation as the extent of utilization of the fuel cell increased. Given the higher stability, the test at 70°C was taken as the base polarization curve, characteristic of the performance of this unit.

Figure 39 -Average curves of (a) polarization and (b) electrical power for the four temperatures in the first group of tests

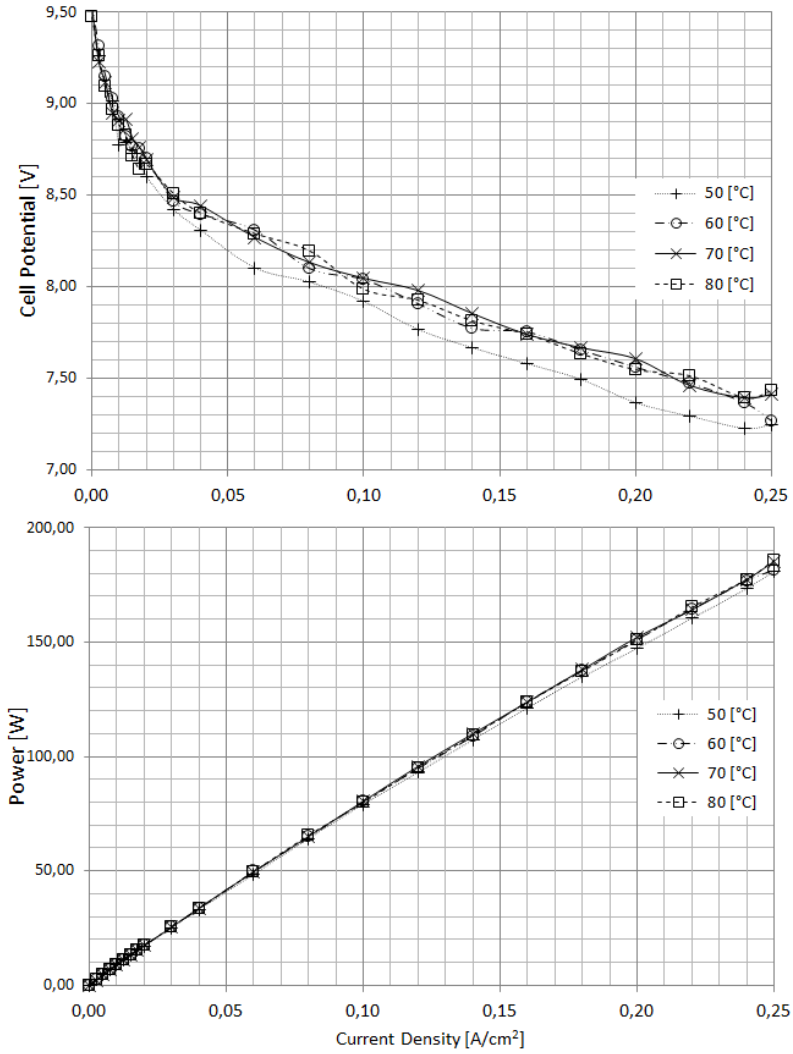

Figure 40 presents the averaged polarization curve for this temperature.

Figure 40 – Polarization curve for the 200W PEM fuel cell operating in the base conditions (at 70°C).

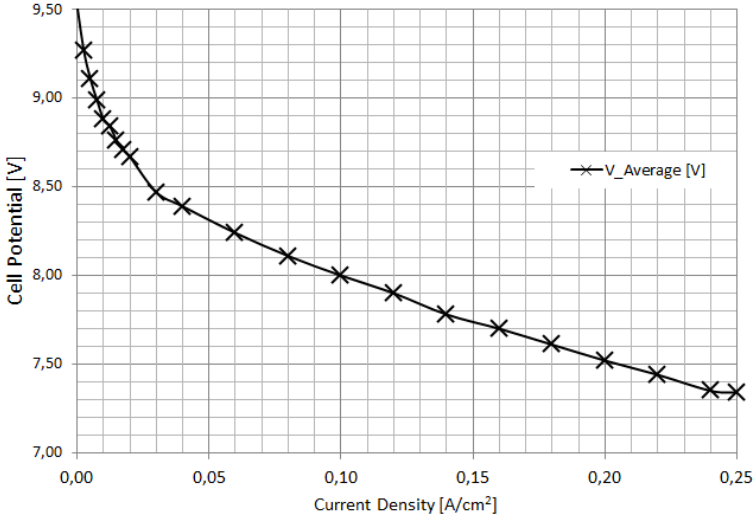

4 ZERO DIMENSIONAL MODELING AND EMPIRICAL PARAMETERS

A zeroth dimensional steady state, isobaric model was implemented in MATLAB by Mariño (2011) for the global simulation of the fuel cell stack (MARIÑO et al., 2012). The model is largely based on Spiegel (2008) and Larminie and Dicks (2003), with improvements in the calculation of the (mass-transfer limited) limiting current. The main hypotheses assumed are:

- Hydrogen, oxygen and water vapor are ideal gases.
- Water can only enter in gas phase mixed with the reactants.
- The relative humidity of reactant gases changes as the temperature change from the gas inlet to the cell temperature. Both evaporation and condensation are allowed.
- Reactant is assumed to be 100% humidified at the gas inlet temperature.
- The same pressure is assumed for the cell and humidifiers.

The modeling was developed based on the principles and equations described in Chapter 2. The solution of the model follows the same steps as the experiments. The current is increased at given steps and the corresponding fuel cell stack voltage is calculated.

The fuel cell electrical potential is given by:

$$E_c = E - \eta^a - \eta^o - \eta^c \tag{4.1}$$

The equilibrium (Nernst) potential is calculated from

$$E = -\frac{\Delta_r G^o}{zF} + \frac{RT}{zF}\ln\left(\frac{p_{H_2O}\, p_{ref}^{0,5}}{p_{H_2}\, p_{O_2}^{0,5}}\right) \tag{4.2}$$

where the partial pressures of the inlet gases is kept constant at the gas channels.

The total activation overpotential is obtained from

$$\eta^a = \frac{RT}{z\alpha F}\ln\left(\frac{i + i_{loss}}{i_o}\right) \tag{4.3}$$

where α accounts for the behavior of the catalyst layer, i_o represents the exchange equilibrium current and i_{loss} is the parasitic current.

The exchange current i_o is highly dependent on the temperature according with

$$i_o = k_1 \left(\frac{p}{p_{ref}} \right)^{\Upsilon} \exp\left(-\frac{k_2}{T} \left(1 - \frac{T}{T_{ref}} \right) \right) \tag{4.4}$$

where k_1 and k_2 are adjustable parameters.

The ohmic overpotential is obtained from

$$\eta^{o} = i\left(R_{elect} + R_{ion} \right) \tag{4.5}$$

where the ion transfer resistance in the membrane is a function of the water content λ and temperature as

$$R_{ion} = \int_0^{\delta} \frac{dz}{\sigma_{(\lambda(z))}} \text{ and } \qquad \sigma_{(\lambda(z))}$$
$$R_{ion} = \left(0,005139\lambda - 0,00326 \right) \exp\left(1286 \left(\frac{1}{303} - \frac{1}{T} \right) \right) \tag{4.6}$$

The water content λ is the ratio of the number of water molecules to the number of charge sites $SO_3^- H^+$. This expression is only valid for $1 < \lambda <= 14$. The water content is obtained from an equilibrium water sorption curve, such as the classical expression of Springer et al., (1991):

$$\lambda = 0,043 + 17,18 a_{v,H_2O} - 39,85 a_{v,H_2O}^2 + 36 a_{v,H_2O}^3$$
$$0 < a_{v,H_2O}^2 <= 1 \tag{4.7}$$

where $a_{v,H_2O} = p_{H_2O} / p$ is the water vapor activity.

The concentration overpotential is calculated from

$$\eta^{c} = C_1 \frac{RT}{zF} \ln\left(\frac{i_L}{i_L - i} \right) \tag{4.8}$$

$$C_1 = \left(1 + \frac{1}{\alpha} \right) \tag{4.9}$$

The limiting current i_L was not directly measured from the experiments. Therefore, the modeling had to be improved in order to obtain a reasonable theoretical estimate. For this, two models were evaluated. Figure 41 shows the control volume used for developing the models. The arrows indicate the convective flow in the channel and the GDL surface mass transfer. The models for the mass transfer across the GDL are basically *film models*. The first assumes constant surface oxygen concentration and the second allow the oxygen concentration to vary along the gas channel, as oxygen is depleted in the electrochemical reaction.

Figure 41 – Control volume used for analysis including channel, GDL and Catalyst layer.

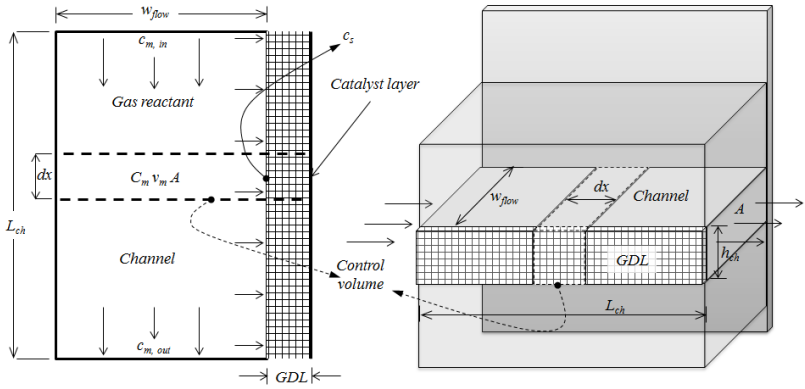

Constant surface concentration mass-transport model:

The first model assumes that the oxygen concentration at the surface of the cathode is constant. This assumption is considered acceptable for high current densities, since, at high currents, the largest resistance to mass transfer occurs within the GDL, which favors to approximate the surface oxygen concentration to the bulk channel concentration. Assuming that the channel cross-sectional area, the pressure and the convective mass transfer coefficient are constant along the channel, and that diffusion along the channel is negligible when compared to convection, the conservation of mass of oxygen in the channel, under steady-state, becomes

$$\frac{d}{dx}\left(c_m - c_s\right) = \frac{-h_m}{v_m w_{flow}}\left(c_m - c_s\right) \tag{4.10}$$

Here c_m refers to the mean concentration of oxygen in the channel, c_s refers to the concentration in the surface of the GDL, h_m refers to the convection mass transfer constant, v_{m} is the channel flow averaged velocity and w_{flow} refers to the channel depth.

The integration of this equation along the channel results in

$$\frac{\left(c_{m,out}-c_s\right)}{\left(c_{m,in}-c_s\right)}=\exp\left(\frac{-h_m L_{Ch}}{v_m W_f}\right)$$
$$c_s=\frac{c_{m,out}-c_{m,in}\exp\left(\frac{-h_m L_{Ch}}{v_m W_f}\right)}{1-\exp\left(\frac{-h_m L_{Ch}}{v_m W_f}\right)} \tag{4.11}$$

For a constant GDL surface concentration, the limiting current is reached when the catalyst oxygen concentration becomes zero. Assuming that the oxygen mass transport along the GDL occurs by diffusion only, the effective diffusion coefficient across the GDL is constant and assuming a linear binary diffusion behavior, the limiting current can be expressed as

$$i_L=\frac{zFD_{eff}}{\delta}c_S \quad or$$
$$i_L=\frac{zFD_{eff}}{\delta}\left(\frac{c_{m,out}-c_{m,in}\exp\left(\frac{-h_m L_{Ch}}{v_m W_f}\right)}{1-\exp\left(\frac{-h_m L_{Ch}}{v_m W_f}\right)}\right) \tag{4.12}$$

where D_{eff} is the effective mass diffusion and δ the thickness of the GDL. These assumptions are the most limiting and will be discussed thoroughly in the sections that will follow.

The oxygen concentration at the channel inlet, $c_{m,in}$, is obtained from the inlet oxygen pressure and relative humidity (assumed 100%). The flow velocity v_m is prescribed by the inlet conditions, regulated in the experiments. The oxygen outlet concentration, $c_{m,out}$, is obtained from Eq. (4.11) and substituted in Eq. (4.12). After a little algebra, denoting $\exp\left(\frac{-h_m L_{Ch}}{v_m w_{ch}}\right)=\exp\left(\frac{-h_m L_{Ch} h_{ch}}{v_m A}\right)=\exp\left(\frac{-h_m \beta A_{cell}}{v_m A}\right)=k$, where β is the ratio of the area covered by the channels $L_{ch}.h_{ch}$ over the total MEA surface area A_{cell}, the result is

$$\frac{i_L\delta}{zFD_{eff}}=\frac{c_{m,in}-\frac{\frac{i_L A_{cell}}{zF}-c_{m,in}k}{v_m A}}{1-k}=\frac{c_{m,in}}{1-k}-\frac{i_L A_{cell}}{zFv_m A\left(1-k\right)}-\frac{c_{m,in}k}{1-k} \tag{4.13}$$

or,

$$\frac{i_L}{zF}\left(\frac{\delta}{D_{eff}}+\frac{A_{cell}}{v_m A(1-k)}\right)=c_{m,in} \tag{4.14}$$

Finally, solving for i_L in terms of known quantities, we have

$$i_L = zF\frac{c_{m,in}}{\left(\frac{\delta}{D_{eff}}+\frac{A_{cell}}{v_m A(1-k)}\right)} = zF\frac{c_{m,in}}{R_{diff}+R_{conv}} \tag{4.15}$$

where the mass transfer resistances are defined as

$$R_{diff}=\frac{\delta}{D_{eff}} and \quad R_{conv}=\frac{A_{cell}}{v_m A\left(1-\exp\left(\frac{-h_m \beta A_{cell}}{v_m A}\right)\right)} \tag{4.16}$$

The variation of the diffusivity with temperature can be taken into account by

$$D_{eff}=D_{ref}\left(\frac{T}{T_{ref}}\right)^{\frac{3}{2}} \tag{4.17}$$

Constant values of tortuosity and porosity are used to evaluate the effective diffusivities from the molecular diffusivities.

It can be seen from the expressions above that the prediction of the limiting current density takes into account inlet flow rates, diffusive and convective mass transfer coefficients, temperatures and pressures as desired. Looking at the expression for the convective mass transfer resistance R_{conv} in eqs. (4.16) it is possible to note that fuel cells with large areas difficult the mass transfer, and thus smaller fuel cells are more efficient than larger ones. The denominator of eq. (4.16) increases as the volumetric flow rate increases. When the flow rate tends to infinite, R_{conv} tends to $1/(h_m \beta A_{cell})$. This is not surprising since it reflects a constant concentration in the flow channel. It can also be seen that increasing the area covered by the flow field channels, i.e., increasing β, can improve the performance. This is probably more cost effective than to obtain a small increase in the convective mass transfer coefficient by increasing the flow velocity.

Although the derivation was based on the cathode, it's important to recall that there are two different limiting currents, one for the anode, related to the hydrogen mass transport, and the other for the cathode, related to the oxygen mass transport. In the model, both limiting currents are calculated and the lowest current is adopted as the fuel cell limiting current.

Variable surface concentration mass-transport model:

The second mass transfer model is based in a similar approach, but the supposition of uniform concentration in the GDL surface is removed. Under the same assumptions as above, the conservation of mass of oxygen in the channel, under steady-state, becomes

$$\frac{d}{dx}\left(c_m v_m A\right) = -h_m W_{ele}\left(c_m - c_s\right) \tag{4.18}$$

A mass balance at the surface of the GDL equates the surface convective oxygen flux with the diffusion flux of oxygen across the GDL

$$h_m \beta A\left(c_m - c_s\right) = A\frac{D_{eff}}{\delta}\left(c_s - 0\right) \tag{4.19}$$

where β accounts for the ratio of the area covered by the channel flow and the total area of the GDL. Solving for the surface concentration results in

$$c_s = \frac{c_m}{1+\frac{D_{eff}}{h_m \delta \beta}} = \frac{c_m Bi_m \beta}{1+Bi_m \beta} \tag{4.20}$$

where $Bi_m = h_m.\delta/D_{eff}$ is the mass transport Biot number. A new variable $\phi = c_s / c_m$ is defined as

$$\phi = \frac{Bi_m \beta}{1+Bi_m \beta} \tag{4.21}$$

This variable can only take values between zero and one: Values close to zero are obtained with low *Biot* numbers, while values close to 1 are obtained with high *Biot* numbers.

The resultant differential equation taking into account the expression found for the surface concentration and its solution are:

$$\frac{dc_m}{dx} = \frac{-h_m W_{ele} c_m \left(1-\phi\right)}{v_m A} = \frac{-h_m W_{ele} c_m \left(1-\phi\right)}{\dot{V}_m} \tag{4.22}$$

$$c_m\left(x\right) = c_{m,in} \exp\left[\frac{-h_m W_{ele} c_m \left(1-\phi\right)}{\dot{V}_m}\right] \tag{4.23}$$

The concentration at the outlet of the channel is:

$$c_{m,out} = c_{m,in} \exp\left[\frac{-h_m \beta W_{ele} c_m (1-\phi)}{\dot{V}_m}\right] \tag{4.24}$$

The total molar flow that enters the catalyst layer, taking into account that v_m and A_m are constants, is given by

$$\dot{n}_{cell} = \dot{V}_m \left(c_{m,in} - c_{m,out}\right) \tag{4.25}$$

Finally an expression for the limiting current density is obtained as

$$\begin{aligned} i_L &= \frac{zF\dot{V}_m}{A_{cell}}\left(c_{o,in} - c_{o,out}\right) \\ &= \frac{zFc_{o,in}\dot{V}_m}{A_{cell}}\left(1 - \exp\left[-\frac{h_m \beta A_{cell}(1-\phi)}{\dot{V}_m}\right]\right) \end{aligned} \tag{4.26}$$

when the flow rate tends to infinite the expression simplifies to

$$\begin{aligned} i_{L,\max} &= zFh_m \beta A_{cell}(1-\phi)c_{o,in} \\ &= zF\frac{c_{o,in}}{\frac{1}{h_m \beta} + \frac{D_{eff}}{\delta_{cell}}} \end{aligned} \tag{4.27}$$

The application of the model, to be shown next, reveals that both approaches in fact predict the same limiting currents for high flow rates. The model used here has the advantage that it calculates the electric and ionic resistances as a function of temperature, pressure and relative humidity. Therefore, the basic set of parameters obtained can be used for any temperature of operation.

4.1 MODEL VALIDATION

The validation of the model relied in literature measurements, to validate the activation and ohmic loss regimes and the limiting current mass transfer model. In the activation and ohmic loss regime, the parameters that characterize the fuel cell behavior and that are identified from the measurements are k_1, α, R_{elect} and i_{loss}.

In the mass transfer limited region, the parameters that characterize the fuel cell behavior, for a given set of pressure, temperature and flow rates, are D_{eff}/δ and h_m/β. From these, the limiting current i_L can be obtained.

An empirical model available in the literature (KIM et al., 1995) was used for the validation of the model developed here, including the mass transfer limited regime. The authors obtained measurements for a 50 cm^2 fuel cell at temperatures of 50°C and 70°C and pressures of 100 kPa, 300 kPa and 500 kPa. Then, an overall model, written as,

$$E = E_o - b\log(i) - Ri - m\exp(ni) \tag{4.28}$$

was curve fitted to their measurements. The constants appearing in Eq. (4.12) are reported in Kim et. al. (1995).

The model presented in Kim et. al. (1995) is basically equivalent to the one used here in regards to activation and ohmic losses. The methodology used for the estimation of parameters separates the activation and ohmic regimes from the mass transfer limited regime. The activation and ohmic losses are first determined, by direct comparison to the author's empirical equation, and then the remaining concentration losses parameters are determined by linear regression of the model developed to the author's measurements.

In the activation and ohmic losses regimes, the parameter α is obtained from,

$$b = \frac{RT}{\alpha nF\ln(10)} \tag{4.29}$$

where *b* and *R* are the values reported by Kim et al. (1995).

The equilibrium exchange current density is obtained from

$$i_o = 10^{\frac{E_o - E_{Nernst} + C_2}{b}} \tag{4.30}$$

where E_o is taken from the article and E_{Nernst} is obtained from eq. (4.2) taking into account the pressure and temperature of the inlet gases, assuming a relative humidity of 100 %. A loss current i_{loss} of 0.001 A/cm^2 is used in order to couple the model in the zero current density potential.

For the mass transport controlled regime, the concentration losses in the anode are neglected as being small in comparison to those in the cathode. As the paper lacks information about the dimensions of the GDL and flow field channels, the curve fit of the model to the measurements allow for the determination of the combined parameters D_{eff}/δ and h_m/β. In the results shown, these combined parameters are denotes as:

$$D = \frac{D_{eff}}{\delta}; \qquad H = h_m\beta; \qquad Bi_m = \frac{H}{D} \tag{4.31}$$

With these definitions, the equations for the mass transfer limiting model can be recast as

$$i_L = zF\frac{c_{m,in}}{R_{diff}+R_{conv}}$$
$$R_{diff} = \frac{1}{D} \tag{4.32}$$
$$R_{conv} = \frac{A_{cell}}{\dot{V}_m\left(1-\exp\left(-\frac{HA_{cell}}{\dot{V}_m}\right)\right)}$$

$$i_L = \frac{zFc_{m,in}\dot{V}_m}{A_{cell}}\left(1-\exp\left[-\frac{HA_{cell}(1-\phi)}{\dot{V}_m}\right]\right) \quad \phi = \frac{Bi_m}{1+Bi_m} \tag{4.33}$$

For the presentation of the data, the concentration loss potential is written as

$$n_{conc} = C_1\frac{RT}{zF}\ln\left(\frac{i_L}{i_L-i}\right)+C_2 \tag{4.34}$$

where the constants C_1 and C_2, obtained from the curve fitted parameters, are presented below.

A multi-variable, multi-parameter algorithm based on Levenberg-Marquardt method was used for the parameters estimation from known polarization curves. For this, the function ***lqscurvefit*** already available in **MATLAB** was used. The model was assumed acceptable when the deviations from the measurements were minimized and then, the curve fitted set of parameters is taken as the characteristic parameters of the fuel cell.

4.1.1 Results of the validation

The presentation of the validation results will begin by analyzing the concentration loss overpotential and then the complete polarization curve.

Figure 42 shows the result of the fitting procedure of the concentration overpotential at 50 ^{o}C and 70 ^{o}C and at different feed pressures (P 1 =100 kPa, P 2 = 300 kPa and P 3=500 kPa). In Figure 42a both temperatures (50 ^{o}C and 70 ^{o}C) for the model using constant concentration shows that the largest deviations are present at the pressure of 100 kPa mainly at low temperatures. The model predicts a faster fall down due to mass transfer limitation, above 1.2 A/cm^2, while

the measurements suggest a less steep variation. A better prediction of this region for both temperatures is obtained using the second mass transfer model (variable concentration), as presented in Figure 42 (b). In general, the curve fitting may be considered acceptable.

The full set of parameters obtained from the curve fits are now used to calculate the full polarization curves and compared to the empirical function obtained from the measurements by Kim et al. (1995). Figure 43 present the comparison between the reference and the models at 50^{o}C using a) constant c_s, and (b) variable c_s. The same situation at 70^{o}C is presented in Figure 44(a) and (b). The model curve fits very closely the results of the empirical equation. The curve fitting is better at the higher temperature, probably because the hypothesis used better approximate the operation of the fuel cell during the experiments.

Table 11 and Table 12 present a summary of the fitted parameters for the experiments at 50 °C and 70 °C at the three pressures tested. The mass transport parameters in Table 11were obtained from the curve fitting using the first mass transfer model, while for the parameters in Table 4, the second mass transfer model was used. Both the correlation coefficient and the sum of the squares of the deviations do not present a noticeable improvement for the second mass transfer model, since in most of the polarization curve, both mass transport models result in a good agreement.

Figure 42 – Comparison of concentration overpotential losses between reference model (Kim et al.1995) and both a) model 1 and b) model 2.

a)

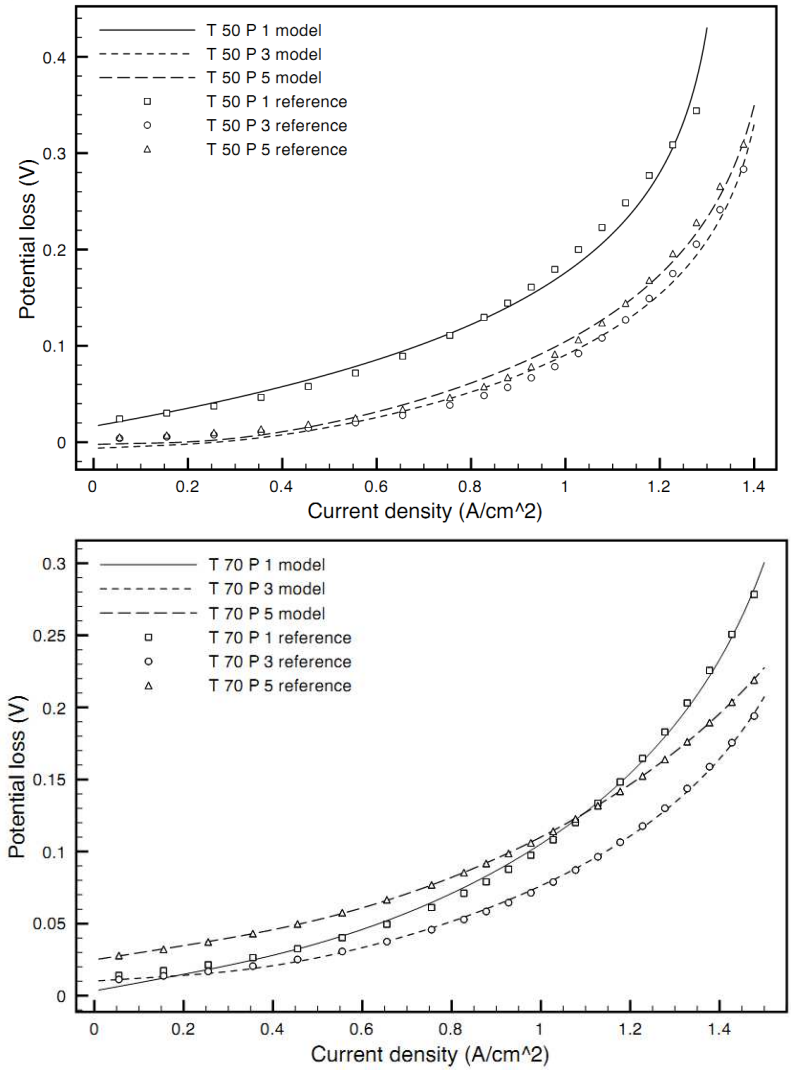

b)

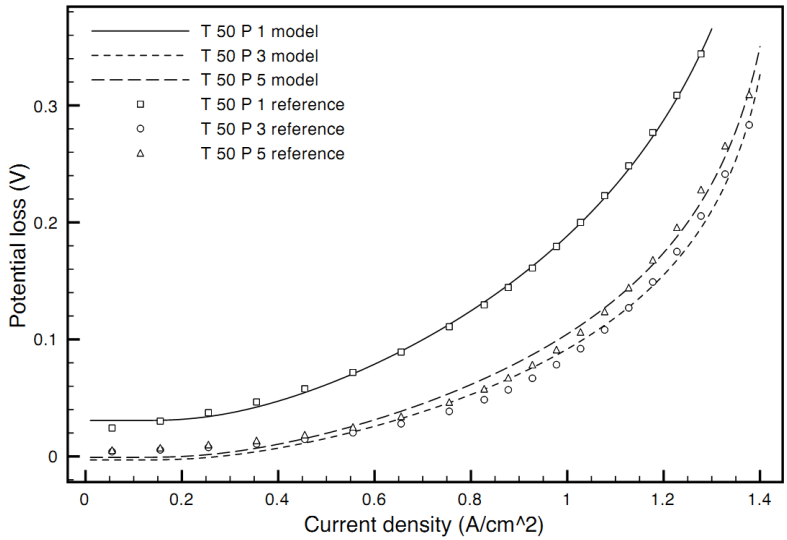
T 50 P 1 model
T 50 P 3 model
T 50 P 5 model
T 50 P 1 reference
T 50 P 3 reference
T 50 P 5 reference
Potential loss (V)
Current density (A/cm^2)
0
0.1
0.2
0.3
0.2
0.4
0.6
0.8
1
1.2
1.4

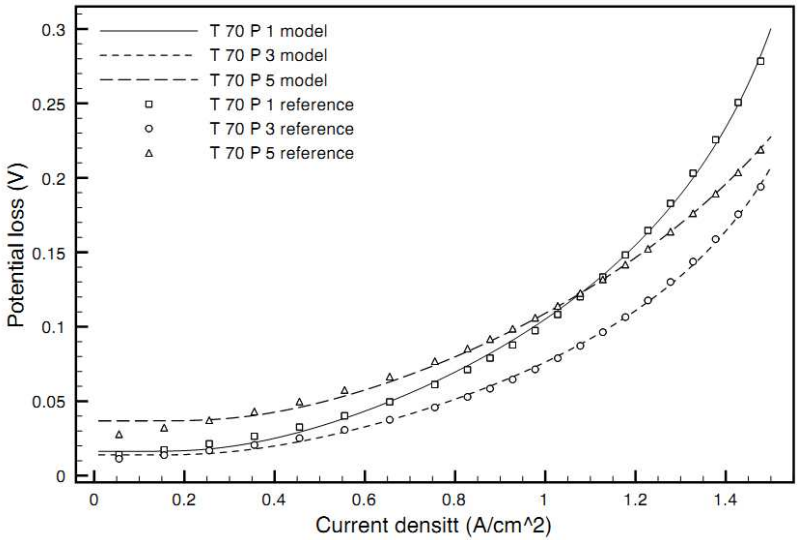
T 70 P 1 model
T 70 P 3 model
T 70 P 5 model
T 70 P 1 reference
T 70 P 3 reference
T 70 P 5 reference
Potential loss (V)
Current densitt (A/cm^2)
0
0.05
0.1
0.15
0.2
0.25
0.3
0.2
0.4
0.6
0.8
1
1.2
1.4

Figure 43 - – Comparison of polarization curve between reference model (Kim et al.1995) and both a) model 1 and b) model 2 at 50°C

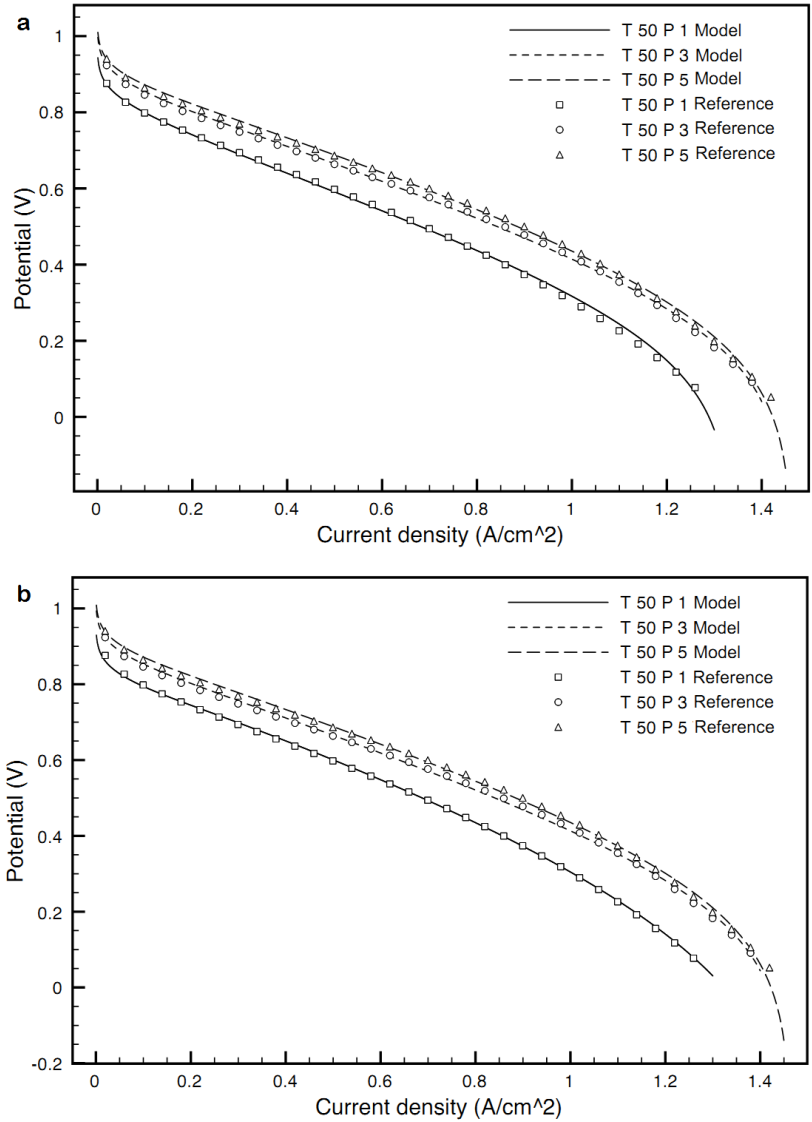

Figure 44 - Comparison of polarization curve between reference model (Kim et al.1995) and both a) model 1 and b) model 2 at 70°C

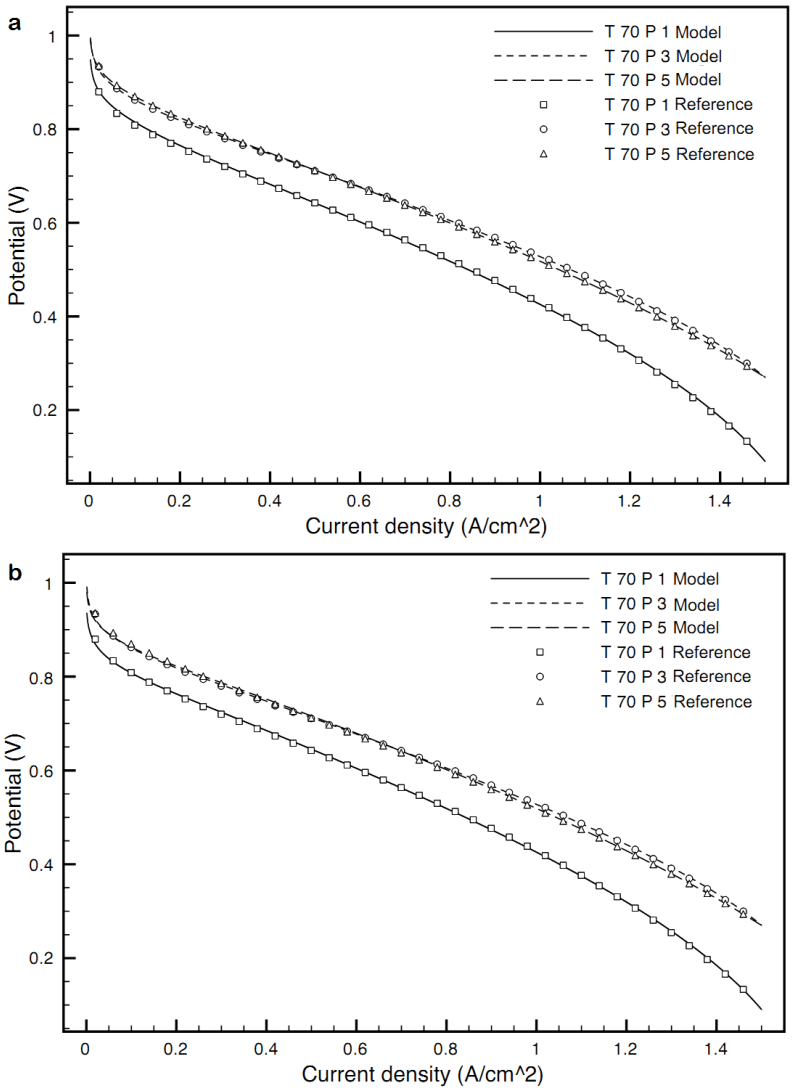

Table 11- Parameters obtained using the first mass transfer model (constant c_s).

T (^{o}C)	P (atm)	C_1 (V)	C_2 (V)	D (m/s)	H (m/s)	i_o (A/cm^2)	R (ohm.cm^2)	α	R^2	Sum of squared deviations (V)
50	1	8,32	$-6{,}37 \times 10^{-2}$	$2{,}09 \times 10^{-3}$	$2{,}09 \times 10^{-3}$	$2{,}22 \times 10^{-7}$	0,300	0,5169	0,99773	$2{,}97 \times 10^{-4}$
50	3	7,86	$-8{,}21 \times 10^{-2}$	$2{,}57 \times 10^{-3}$	$2{,}57 \times 10^{-3}$	$1{,}21 \times 10^{-6}$	0,313	0,5007	0,99895	$1{,}91 \times 10^{-4}$
50	5	9,04	$-8{,}95 \times 10^{-2}$	$3{,}14 \times 10^{-3}$	$3{,}34 \times 10^{-3}$	$2{,}31 \times 10^{-6}$	0,298	0,5087	0,99611	$3{,}88 \times 10^{-4}$
70	1	9,76	$-9{,}66 \times 10^{-2}$	$4{,}64 \times 10^{-3}$	$5{,}01 \times 10^{-3}$	$5{,}52 \times 10^{-7}$	0,259	0,5672	0,99968	$9{,}44 \times 10^{-5}$
70	3	7,24	$-6{,}40 \times 10^{-2}$	$8{,}22 \times 10^{-4}$	$2{,}74 \times 10^{-3}$	$1{,}04 \times 10^{-6}$	0,231	0,5401	0,99993	$3{,}66 \times 10^{-5}$
70	5	11,93	$-9{,}73 \times 10^{-2}$	$7{,}12 \times 10^{-4}$	$1{,}05 \times 10^{-3}$	$1{,}57 \times 10^{-6}$	0,242	0,6302	0,99963	$1{,}10 \times 10^{-5}$

Table 12 - Parameters obtained using the second mass transfer model (variable c_s).

T (^{o}C)	P (atm)	C_1 (V)	C_2 (V)	D (m/s)	H (m/s)	i_o (A/cm^2)	R (ohm.cm^2)	α	R^2	Sum of squared deviations (V)
50	1	14,58	$-1{,}10 \times 10^{-1}$	$1{,}77 \times 10^{-3}$	$2{,}16 \times 10^{-2}$	$1{,}25 \times 10^{-6}$	0,300	0,5169	0,99980	$8{,}84 \times 10^{-5}$
50	3	7,97	$-7{,}99 \times 10^{-2}$	$2{,}54 \times 10^{-3}$	$5{,}93 \times 10^{-4}$	$1{,}12 \times 10^{-6}$	0,313	0,5007	0,99897	$1{,}88 \times 10^{-4}$
50	5	9,02	$-8{,}78 \times 10^{-2}$	$3{,}40 \times 10^{-3}$	$3{,}12 \times 10^{-4}$	$2{,}16 \times 10^{-6}$	0,298	0,5087	0,99591	$3{,}98 \times 10^{-4}$
70	1	9,81	$-8{,}42 \times 10^{-2}$	$7{,}03 \times 10^{-3}$	$3{,}56 \times 10^{-3}$	$3{,}42 \times 10^{-7}$	0,259	0,5672	0,99983	$6{,}94 \times 10^{-5}$
70	3	7,17	$-5{,}96 \times 10^{-2}$	$2{,}71 \times 10^{-3}$	$8{,}12 \times 10^{-4}$	$8{,}86 \times 10^{-7}$	0,231	0,5401	0,99989	$4{,}59 \times 10^{-5}$
70	5	12,04	$-8{,}76 \times 10^{-2}$	$1{,}14 \times 10^{-3}$	$6{,}61 \times 10^{-4}$	$1{,}04 \times 10^{-6}$	0,242	0,6302	0,99963	$8{,}85 \times 10^{-5}$

4.1.2 Discussion of the validation

The prediction of the values for the mass transport parameters listed in Table 11 and Table 12 with known theories is hampered by the absence of data on the dimensions and shape of the flow channels and GDL thickness and properties. Nonetheless, from the data in Table 12, a few observations can be made.

Regarding the values of H, at the expected low Reynolds number typical of the flow in these channels, the flow regime is laminar, leading to a constant Sherwood number ($Sh = h_m\, d_h /D$), say 3.67. The value for the binary diffusion coefficient for oxygen and water vapor at 70°C, 1 atm, from the Chapmann-Enskog model, is approximately 3.3×10^{-5} m^2/s. Assuming that the channel height and width is 1 mm, that only 1 side is in contact to the GDL, and that β=0.5, we obtain $H = 6 \times 10^{-2}$ m/s, one order of magnitude higher than the values listed in Table 12.

Regarding the effect of pressure in the parameter H, at a constant temperature and electrical current, the molar consumption of gases remains the same. At higher pressures, the mixture molar concentration increases. Therefore, the flow velocity decreases proportionally to the increase in pressure. However, since the molar rate is constant and the dynamic viscosity at low pressure (p < 10 atm) is independent of pressure ($\mu \approx$ constant), the Reynolds number is independent of pressure. Likely, the flow will remain laminar. The mass diffusivity at low pressure is inversely proportional to pressure ($pD \approx$ constant). Therefore, the convective mass transfer coefficient decreases proportionally to the increase in pressure, causing a decrease in the value of H. The decrease observed of H observed in Table 12 at 70°C follows this trend closely: At 3 atm, it drops to 30% of the value at 1 atm and at 5 atm, it drops to 20% of the value at 1 atm. At 50°C, however, the value of H decreases 36 times from 1 atm to 3 atm and then decreases as expected from 3 atm to 5 atm. This may be justified if we can argue that the effect of pressure at low temperature is higher in the activation of the catalytic reactions than it is in the mass transfer coefficient. The test of that hypothesis requires a more refined modeling.

The effect of temperature on H can be understood in the same way. From the Chapman-Enskog model for gases at low pressure, the temperature dependency of the binary mass diffusivity for the pair water-air follows $T^{2.01}$. Therefore, changing the temperature from 50°C to 70°C causes a 13% increase in H. The increase in H at 3 and 5 atm is

37% and 200% respectively. At 1 atm, H experiences a decrease. The behavior in H cannot be described entirely by the change experienced in the mass diffusivity, expressing that there are important changes in the flow field within the GDL and effectiveness of the catalyst layer which are not appropriately accounted for with the model at hand.

The parameter D is the ratio of the effective diffusivity and the GDL thickness. Porosity and tortuosity for the dry GDL are estimated in ε=0.50 and τ=1.25, from models for the effective diffusivity (KAVIANY, 1995). This provides a dry effective diffusivity of 1.2×10^{-5} m^2/s. The GDL thickness is taken as δ = 100 μm = 1×10^{-4} m. This would give D_{AB} = $1{,}2\times10^{-1}$ m/s. Considering, however, that near the limiting current the GDL would be flooded and could hold as much as 99% liquid water (per pore volume), this value would be reduce to D = $1{,}2\times10^{-3}$ m/s, compatible to the values reported in Table 12. Therefore, this order of magnitude analysis shows that the correct modeling of the transport in the GDL, considering the presence of liquid water, is important for the prediction of the mass transport limit of the fuel cell.

The electrochemical parameters can also be qualitatively checked. The values for α are in the range (0.3-0.7) commonly found in the literature (SPIEGEL, 2008). The values for i_o listed in Table 12 are within the expected range according to the literature (SPIEGEL, 2008; BARBIR, 2011; LARMINIE and DICKS, 2003). Also, Eq. (4.4), provides a model for the exchange current as a function of temperature and pressure (repeated here to facilitate the discussion)

$$i_o = k_1\left(\frac{p}{p_{ref}}\right)^{\gamma}\exp\left(-\frac{k_2}{T}\left(1-\frac{T}{T_{ref}}\right)\right) \qquad (4.35)$$

Using the values calculated and reported in Table 11 and Table 12, the parameters k_1, k_2 and γ in Eq. (4.4) can be curve-fitted. Table 13 compares the values of the exchange current obtained from this curve-fit of Eq. (4.4) to those listed in Table 11 and Table 12, for both mass transfer models. The adherence of the model given by Eq. (4.4) is adequate. The values obtained for k_1, k_2 and γ are listed in Table 14. The value of k_1 is found to be in the expected range from the literature (SPIEGEL, 2008) and the mass transfer model has a strong effect on the curve-fitted value for k_1. k_2 is found to be negative in both cases. This is much unexpected, as we show in the next section, and we provide no explanation for this result. Regarding γ it can be seen that the reaction kinetics depends on pressure with an exponent smaller than one, which

is an expected behavior due to progressive saturation of the catalyst layers (CANDUSSO et al, 2006).

Table 13 - Exchange current densities (in A/cm2) from Table 4 and from the curve-fitted model for io (parameters k1, k2 and γ), using both mass transfer models

T (°C)	P (atm)	Model 1 (c_s constant)		Model 2 (c_s variable)	
		From Table 11	Curve-fitting	From Table 12	Curve-fitting
50	1	$2{,}22\times10^{-7}$	$6{,}00\times10^{-7}$	$1{,}25\times10^{-6}$	$6{,}07\times10^{-7}$
50	3	$1{,}21\times10^{-6}$	$1{,}48\times10^{-6}$	$1{,}12\times10^{-6}$	$1{,}50\times10^{-6}$
50	5	$2{,}31\times10^{-6}$	$2{,}25\times10^{-6}$	$2{,}16\times10^{-6}$	$2{,}19\times10^{-6}$
70	1	$5{,}52\times10^{-7}$	$4{,}36\times10^{-7}$	$3{,}42\times10^{-7}$	$3{,}70\times10^{-7}$
70	3	$1{,}04\times10^{-6}$	$1{,}07\times10^{-6}$	$8{,}86\times10^{-7}$	$8{,}90\times10^{-7}$
70	5	$1{,}57\times10^{-6}$	$1{,}63\times10^{-6}$	$1{,}04\times10^{-6}$	$1{,}21\times10^{-6}$

Table 14 - Regression parameters for exchange current density

Mass transfer model	k_1 (A/cm^2)	k_2 (K)	γ
First	$5{,}99\times10^{-2}$	-1775,19	0,8198
Second	$6{,}67\times10^{-7}$	-3289,55	0,7344

Table 15 - Fitting Parameters of the model to the measured polarization assuming a constant membrane water saturation.

Regression	k1 (A/cm^2)	k2 (K)	$R\left(\Omega cm^2\right)$	α	$i_{loss}\left(\frac{A}{cm^2}\right)$	Error
With MM[1]	1.7419e10^{-7}	6140.68	0.1856	0.4469	1.3817e10-3	0.1126
Without MM	1.6944e10^{-7}	6542.10	0.3365	0.4464	1.4069e10-3	0.1278
Reference[2]	8.0631e10^{-9}	6844.7	0.28-0.41	0.3-0.7	5.00e10-7	

(1) MM = membrane model
(2) Spiegel (2008).

Considering all the complex electrochemical and transport effects that take place within the fuel cell, the present model allows for a global analysis of the fuel cell, providing global parameters that can compare the performance of different systems, or, at different operation conditions. The analysis of the results also revealed the inherent limitations of the simpler global parameter models.

This model is now applied to the results measured to the Electrocell 200 W fuel cell.

4.2 RESULTS AND ANALYSIS

Table 15 presents the parameters obtained from the curve fitting of the model to the measured polarization curves using the first mass transfer model (constant c_s). With MM stands for membrane model and without MM stands for assuming constant membrane water saturation.

We note that the same values of k_1, k_2 and γ are used for predicting the polarization curves in all temperatures. Table 15 presents the results considering the full model for the membrane (following Springer et al., (1991)) and also assuming constant membrane saturation. The value of the ohmic resistance responds strongly to the membrane model, while the other parameters are not as sensitive.

Figure 45 presents the curves obtained from the models compared to the measurements. It can be seen that the model fits the data accurately for all the temperatures. Only at 50^oC the model apparently over predicts the measured potential at lower currents. Also, the model including the membrane model presents the best behavior overall.

Figure 45 -Polarization curve of the model for temperatures of a) 50°C, b) 60°C, c) 70°C and d) 80°C

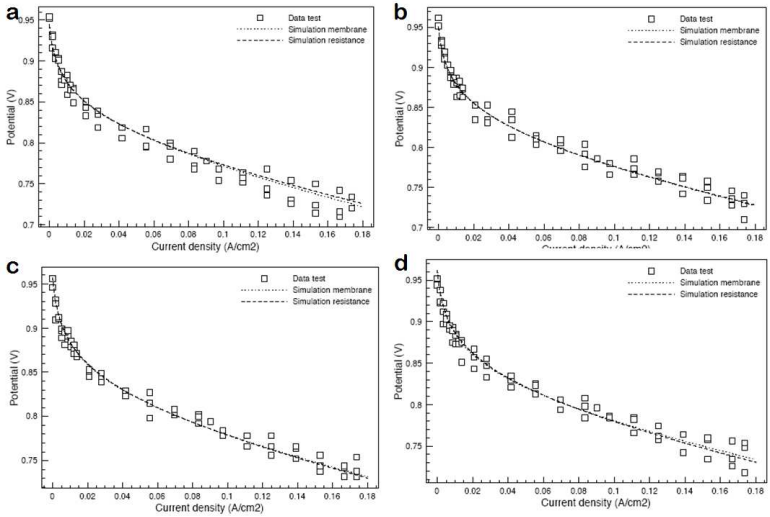

The curve-fitted parameters presented in Table 15 are within the expected order of magnitude Spiegel (2008). We also observe that the values of k_1 reported in Table 15 have the same order of magnitude of the ones reported on Table 14, although smaller. k_2, on the other hand, present positive values, leading to the usual behavior with temperature, as reported by Spiegel (2008). The value of γ was not obtained since all measurements were performed at atmospheric pressure.

4.3 CONCLUSION

The global model used allowed the characterization of the fuel cell stack at four different temperatures predicting the polarization curve with good accuracy. The model can be used to obtain global parameters that can compare the performance of different systems, or, of the same system at different operation conditions, using a single set of parameters, as the ones reported in Table 15. The use of the membrane model by Springer et al. (1991) and the variable GDL surface concentration model (model 2) gave better overall fitting, both for the literature as well as for the measured polarization curves. The analysis employed known mass transfer models showed that the mass transport phenomena

that occurs within the GDL requires a more detailed modeling in order to be fully understood.

This detailed modeling must rely on the basic conservation equations for the species mass transport within the two-phase flow (water-gas) in the porous medium that forms de GDL. The analysis of these detailed models is done in the next chapters and a more complete model for mass transport in MEA is proposed.

Part II

Multicomponent, multiphase modeling of heat and mass transfer in porous layers of PEM fuel cells

The objectives of this second part to review the available continuum mechanics and thermodynamic models for heat and mass transfer in continuum media,

The emphasis is devoted to the development of the constitutive relations for mass transfer in the context of the Maxwell-Stefan formulation for a general concentration, pressure, temperature and body force (e.g., electrical) driving potential. The traditional derivations based on the dissipation function and the species linear momentum equation are criticized and the general formulation devoid of excessive limiting assumptions is isolated

5 MODELING FLOW WITH MULTICOMPONENT DIFFUSION

The Stefan-Maxwell equations for multicomponent mixtures are a well-known result from both the Kinetic Theory of Gases (CHAPMAN and COWLING, 1970; VICENTI and KRUGER, 1965) and from the Thermodynamic of the Irreversible Processes (PRIGOGINE, 1968; LIGHTFOOT, 1974; BIRD et al., 2002; DE GROOT and MAZUR, 1984; HAASE, 1986; KUIKEN, 1994; KONDEPUDI and PRIGOGINE, 1998). An equivalent equation for the mass diffusion fluxes can also be obtained using the conservation of the species linear momentum (WILLIAMS, 1958; WHITAKER, 1994, 2009; CURTISS AND BIRD, 1996; LAM, 2006). However, the procedures lead to different forms of the Maxwell-Stefan equations, that have been rendered equivalent using order of magnitude arguments (WHITAKER, 2009), which hold exact only for static mechanical equilibrium. During flow in porous media, the microscopic viscous effects play a very important role and it is still not clear how these effects should be taken into account in the general transport equations for mass diffusion in porous media. This has generated different models such as the Dusty Gas Model (MASON et al, 1983), the Binary Friction Model (KERKHOF, 1996) and several variations. In order to elucidate the hypothesis behind and the significance of each of the terms in the different models, a thorough review of the derivation of the basic equations is provided.

The main purpose of this chapter is, based on the literature, to arrive at the proper form of the entropy conservation equation for a multicomponent mixture. The equation for the conservation of energy is obtained as a step needed to derive the equation for the conservation of entropy. The main interest rests on isothermal mass transport. The Maxwell-Stefan formulation of the diffusion fluxes is then obtained based both on the inversion of the species linear momentum equation and on Irreversible Thermodynamics reasoning from the entropy dissipation function. The main differences between the approaches of Lightfoot (1974), Curtiss and Bird (1996), Lam (2006) and Whitaker (2009) are presented with the aim at arriving at a general formulation for the Maxwell-Stefan equation for mass diffusion.

This chapter is basically a comprehensive review of the literature. Next chapter will present a critical analysis of the different formulations.

5.1 BASIC DEFINITIONS

In order to clearly define the meaning of the variables and to facilitate the presentation of the transport equations for multicomponent systems some definitions relevant for the next sections are given.

The mass concentration of component *i* is defined as the ratio of the mass of component *i* (m_i) and the total volume of the mixture *V*, i.e.,

$$\rho_i = \frac{\mathrm{m}_i}{V} \tag{5.1}$$

The *density* of the mixture is given as the ratio between the total mass *m* and the total volume *V*, i.e.,

$$\rho = \frac{\mathrm{m}}{V} \tag{5.2}$$

Since $m = \sum_{i=1}^{Ne} m_i$

$$\rho = \sum_{i=1}^{N_c} \rho_i \tag{5.3}$$

The mass fraction of component *i* is defined as

$$Y_i = \frac{m_i}{m} = \frac{\rho_i}{\rho} \tag{5.4}$$

and, as a consequence of Eq. (5.3),

$$\sum_{i=1}^{Nc} Y_i = 1 \tag{5.5}$$

Molar properties are related to the mass properties through the molar mass of component *i* (M_i). The *number of moles* of component *i* is

$$n_i = \frac{m_{\mathrm{i}}}{M_i} \tag{5.6}$$

The molar concentration of component i is

$$c_i = \frac{n_{\mathrm{i}}}{V} = \frac{\rho_{\mathrm{i}}}{M_i} \tag{5. 7}$$

and the mixture molar concentration of the mixture is

$$c = \sum_{i=1}^{Nc} c_i \tag{5.8}$$

The molar fraction X_i is

$$X_i = \frac{n_i}{n} = \frac{c_i}{c} \tag{5.9}$$

The transformation from mass to molar basis can be easily made using Eqs. (5.6) to (5.9). The total volume of the mixture, as a consequence of Euler's theorem, is given by

$$V = \sum_{i=1}^{Nc} \left(\frac{\partial V}{\partial n_i} \right)_{T,p,n_{j\neq i}} \qquad n = \sum_{i=1}^{Nc} \overline{v}_i n_i \tag{5.10}$$

where $\overline{v}_i$ is the molar partial volume i.

The specific volume is defined as

$$v_i = \left(\frac{\partial V}{\partial m_i} \right)_{T,p,m_{j\neq i}} = \frac{\overline{v}_i}{M_i} \tag{5.11}$$

The mixture specific volume v is

$$v = \frac{V}{m} = \frac{1}{\rho} \tag{5.12}$$

Analogously to Eq. (5.4) and (5.9) a volume fraction ϕ_i is defined as

$$\phi_i = \frac{m_i v_i}{V} = \rho_i v_i = c_i \overline{v}_i \tag{5.13}$$

and

$$\sum_{i=1}^{Nc} \phi_i = 1 \tag{5.14}$$

The total density ρ Eq. (5.1) can also be expressed as

$$\rho = \sum_{i=1}^{Nc} \frac{\phi_i}{v_i} \tag{5.15}$$

The density of the pure component i is

$$\rho_i^* = \frac{m_i}{V_i^*} \tag{5.16}$$

where V_i^* is the volume that *i* would occupy if it were a pure substance.

For an ideal mixture (for which $v_i m_i = V_i^*$), Eq. (5.15) can also be written as

$$\rho = \sum_{i=1}^{N_c} \rho_i^* \phi_i \tag{5.17}$$

Euler's theorem allows for the determination of derivatives of different concentration measures. For any homogeneous function A of the first degree on Y_i, Euler's theorem gives

$$\left(da\right)_{T,p} = \sum_{i=1}^{N_c} a_i dY_i \tag{5.18}$$

where $a = A/m$ a is the specific value of A and $a_i = \left(\partial A/\partial Y_i\right)_{T,p,Y_i,j\neq i}$ is the partial value of A. As the dY_i are not all independent from each other

$$\left(da\right)_{T,p} = \sum_{i=1}^{N_c-1} \left(a_i - a_{N_c}\right) dY_i \tag{5.19}$$

Now, extracting the derivative in respect to Y_k and retaining only the *k-th* term, we obtain

$$\left(\frac{\partial a}{\partial Y_k}\right)_{T,p} = \left(a_k - a_{N_c}\right) \tag{5.20}$$

The application of this equation can be illustrated using the volume. Then, $A = V$ and $a = v$ and

$$\left(\frac{\partial v}{\partial Y_k}\right)_{T,p} = \left(v_k - v_{N_c}\right) \tag{5.21}$$

As $v = 1/\rho$ we have accordingly

$$\left(\frac{\partial \rho}{\partial Y_k}\right)_{T,p} = \rho^2 \left(v_{N_c} - v_k\right) \tag{5.22}$$

As $\rho = \rho_i / Y_i$ we also obtain

$$\left(\frac{\partial \rho_i}{\partial Y_k}\right)_{T,p} = \rho\left[\delta_{ik} + \rho_i \left(v_{N_c} - v_k\right)\right] \tag{5.23}$$

where δ_{ik} is the Kronecker delta. Table 16 summarizes the different concentration measures that have been defined.

Table 16 - Summary of the different concentration measures. The summations refer to all species, from 1 to N_c

Mass-based measures		Molar-based measures	
Mass	m_i	Number of moles	n_i
Mixture mass	$m = \sum m_i$	Mixtures number of moles	$n = \sum n_i$
Mass concentration	$\rho_i = \frac{\mathrm{m}_i}{V} = c_i M_i$	Mole concentration	$c_i = \frac{\mathrm{n}_i}{V} = \frac{\rho_i}{M_i}$
Mixture density	$\rho = \sum \rho_i$	Mixture mole concentration	$c = \sum c_i$
Mass fraction	$Y_i = \frac{m_i}{m} = \frac{\rho_i}{\rho}$	Mole fraction	$X_i = \frac{n_i}{n} = \frac{c_i}{c}$
	$Y_i = X_i \frac{M_i}{M}$		$X_i = Y_i \frac{M}{M_i}$
	$\sum Y_i = 1$		$\sum X_i = 1$
Mixture molar mass	$M = \left(\sum \frac{Y_i}{Mi}\right)^{-1}$	Mixture molar mass	$M = \sum X_i M_i$
Volume-based measures			
Species volume	V_i		
Species specific volume	$v_i = \frac{V_i}{\mathrm{m}_i}$		
Partial molar volume		$\overline{v}_i = \frac{V_i}{\mathrm{n}_i}$	
Volume fraction	$\phi_i = v_i \rho_i = v_i \rho Y_i$	$\phi_i = \overline{v}_i c_i = \overline{v}_i c X_i$	

In the following, all the equations will be expressed in a mass basis, unless otherwise noted.

5.2 GIBBS-DUHEM RELATION

The Gibbs-Duhem equation establishes a relation among continuous variations of temperature, pressure and chemical potential that will be useful in the developments that follow. Writing the Gibbs free energy as a function of T, p, and n_i, and using the definitions for entropy, volume and chemical potential, a variation of the Gibbs free energy is written as

$$dG = -SdT + Vdp + \sum_i \overline{\mu}_i dn_i \tag{5.24}$$

where $\overline{\mu}_i = (\partial G / \partial n_i)_{T,p,n_{j,j\neq i}}$ is the partial molar Gibbs free energy.

The Gibbs free energy of the system can also be calculate from *Euler's relation*,

$$G = \sum_i \bar{\mu}_i n_i \tag{5.25}$$

A variation in *G*, from equation (5.25) is given by,

$$dG = \sum_i \bar{\mu}_i dn_i + \sum_i n_i d\bar{\mu}_i \tag{5.26}$$

Now, comparing eq. (5.24) and eq. (5.26), we obtain

$$-SdT + Vdp - \sum_i n_i d\bar{\mu}_i = 0 \tag{5.27}$$

multiplying by 1/T,

$$-\frac{1}{T}SdT + \frac{V}{T}dp - \frac{1}{T}\sum_i n_i d\bar{\mu}_i = 0$$

$$Ud\left(1/T\right) + Vd\left(p/T\right) - \sum_i n_i d\left(\bar{\mu}_i/T\right) = 0$$

with a little manipulation we can show that the equation above can be rewritten as

$$Ud\left(1/T\right) + Vd\left(p/T\right) - \sum_i n_i d\left(\bar{\mu}_i/T\right) = 0 \tag{5.28}$$

With further manipulation and recalling that

$$\begin{aligned} &\frac{H}{V} = \frac{U}{V} + p = \rho h = \sum \rho_i h_i; \\ &\rho_i = \frac{M_i n_i}{V}; \quad \mu_i = \frac{\bar{\mu}_i}{M_i} \end{aligned} \tag{5.29}$$

we obtain

$$-\frac{1}{T^2}\sum_i \rho_i h_i dT + \frac{1}{T}dp - \sum_i \rho_i d\left(\frac{\mu_i}{T}\right) = 0 \tag{5.30}$$

Writing the variations in terms of gradients, we have

$$-\frac{1}{T^2}\sum_i \rho_i h_i \nabla T + \frac{1}{T}\nabla p - \sum_i \rho_i \nabla\left(\frac{\mu_i}{T}\right) = 0 \tag{5.31}$$

This equation can also be rewritten in a more convenient form taking the summation outside as

$$\sum_i \left[\rho_i h_i \frac{1}{T^2}\nabla T - \frac{1}{T}\frac{\rho_i}{\rho}\nabla p + \rho_i \nabla\left(\frac{\mu_i}{T}\right)\right] = 0 \tag{5.32}$$

This is the *Gibbs-Duhem* equation written for continuous variations of properties, assuming that the local (molecular) thermodynamic equilibrium holds.

A different form may be written using

$$\nabla\left(\frac{\mu_i}{T}\right)=\frac{1}{T}\nabla_T\mu_i-\frac{\mu_i}{T^2}\nabla T \tag{5.33}$$

Then, Gibbs-Duhem can also be written as

$$\begin{aligned}\sum_i\left[\rho_i h_i\frac{1}{T^2}\nabla T-\frac{1}{T}\frac{\rho_i}{\rho}\nabla p+\rho_i\frac{1}{T}\nabla_T\mu_i-\rho_i\mu_i\frac{1}{T^2}\nabla T\right]=0\\ \sum_i\left[\rho_i\left(h_i-\mu_i\right)\frac{1}{T^2}\nabla T-\frac{1}{T}\frac{\rho_i}{\rho}\nabla p+\rho_i\frac{1}{T}\nabla_T\mu_i\right]=0\\ \sum_i\left[\rho_i s_i\nabla T-\frac{\rho_i}{\rho}\nabla p+\rho_i\nabla_T\mu_i\right]=0\end{aligned} \tag{5.34}$$

A useful form for the gradient of chemical potential is obtained considering the thermodynamic relations

$$\left[\frac{\partial\left(\mu_i/T\right)}{\partial T}\right]_{p,n_i}=\frac{h_i}{T^2} \tag{5.35}$$

$$\left[\frac{\partial\left(\mu_i/T\right)}{\partial p}\right]_{T,n_i}=\frac{V_i}{T} \tag{5.36}$$

where $h_i=\overline{h}_i/M_i$ is the specific enthalpy, $v_i=\overline{v}_i/M_i$ is the specific volume. Then, the ***Gibbs-Duhem*** equation becomes

$$T\nabla\left(\frac{\mu_i}{T}\right)=\nabla_{T,p}\mu_i-\frac{h_i}{T^2}\nabla T+v_i\nabla p \tag{5.37}$$

or,

$$\nabla\mu_i=\nabla_{T,p}\mu_i-s_i\nabla T+v_i\nabla p \tag{5.38}$$

Multiplying Eq. (5.38) by ρ_i and summing over *i*, recalling that $\rho_i v_i=\phi_i$,

$$\begin{aligned}\sum_{i=1}^{N_c}\rho_i\nabla\mu_i&=\sum_{i=1}^{N_c}\rho_i\nabla_{T,p}\mu_i-\sum_{i=1}^{N_c}\rho_i s_i\nabla T+\sum_{i=1}^{N_c}\rho_i v_i\nabla p\\ &=\sum_{i=1}^{N_c}\rho_i\nabla_{T,p}\mu_i-S\nabla T+\nabla p\end{aligned} \tag{5.39}$$

From *Gibbs-Duhem*, $-S\nabla T + \nabla p = \sum_i \rho_i \nabla_T \mu_i$,

$$\sum_{i=1}^{N_c} \rho_i \nabla \mu_i = \sum_{i=1}^{N_c} \rho_i \nabla_{T,p} \mu_i + \sum_{i=1}^{N_c} \rho_i \nabla_T \mu_i \tag{5.40}$$

At constant T,

$$\sum_{i=1}^{N_c} \rho_i \nabla_{T,p} \mu_i = 0 \tag{5.41}$$

5.3 BASIC CONSERVATION EQUATIONS FOR MULTICOMPONENT FLUIDS

The conservation equations of interest are the mass of chemical species, species linear momentum, energy and entropy. These equations are given by Bird at al. (2002), Haase (1969), De Groot and Mazur (1984), Slattery (1981), Rosner (1986), Kuiken (1994) and Kaviany (2001b), among others.

The development assumes that the continuum fluid phase is formed by N_c chemical species, each one of them forming its own continuum capable of motion and interaction with the remaining species. The fluid is then a superposition of N_c continua. At each point $\boldsymbol{r}$ in time t, a mixture particle may be found that contains molecules of all the chemical species. Therefore, in this point, all material particles of all species share the same total volume and may be followed independently as they flow with their own velocity vector $\mathbf{u}_i$.

In order to state the conservation of mass of species i in a multicomponent fluid, we define a material volume V_i of species i that contains species i and whose material surface S_i follows species i as it flows and reacts. At time $t = 0$, the material volume for the mixture V also contains a fraction of the other species j. After an elapsed time t, in general, we admit that V_i has suffered deformation, there has been separation and chemical reaction among i and j.

5.3.1 Conservation of mass

For any chemical species i the conservation of mass can be written as

$$\frac{d}{dt} \int_{V_i(t)} \rho_i dV = \int_{V_i(t)} \dot{w}_{r,i} dV \tag{5.42}$$

The term in the left-hand side is the time variation of the mass of species *i* within the material volume and the term in the right-hand side is the volumetric mass rate of formation/destruction of species *i* by chemical reaction. We admit that both the mass concentration and the reaction rate of species *i* are continuous functions of the thermodynamic, time and space variables. The mass rate of reaction for all the *i = 1, 2, ..., N_c* species must satisfy

$$\sum_{i=1}^{N_c} \dot{w}_{r,i} = 0 \tag{5.43}$$

The generalized Reynolds Transport Theorem,

$$\frac{d}{dt}\int_{V_i(t)} \rho_i dV = \int_{V_i(t)} \left(\frac{d_i \rho_i}{dt} + \rho_i \nabla \cdot \mathrm{u}_i \right) dV \tag{5.44}$$

can be used to give

$$\int_{V_i(t)} \left(\frac{d_i \rho_i}{dt} + \rho_i \nabla \cdot \mathrm{u}_i - \dot{w}_{r,i} \right) dV = 0 \tag{5.45}$$

where $\mathbf{u}_i$ is the velocity vector of species *i* and d_i/d_t is the specie material derivative taken by following the material element as it flows with the species velocity.

This equation must be valid for any simply connected material volume V_i. This requires that

$$\frac{d_i \rho_i}{dt} + \rho_i \nabla \cdot \mathrm{u}_i - \dot{w}_{r,i} = 0 \tag{5.46}$$

The material derivative of mass concentration of component *i* in respect to the species velocity is

$$\frac{d_i \rho_i}{dt} = \frac{\partial \rho_i}{\partial t} + \mathrm{u}_i \cdot \nabla \rho_i \tag{5.47}$$

Therefore, the equation for the conservation of the mass of the chemical species *i* can be written in the conservative form as

$$\frac{\partial \rho_i}{\partial t} + \nabla \cdot \left(\rho_i \mathrm{u}_i \right) = \dot{w}_{r,i} \tag{5.48}$$

When species i participates in many reactions the homogeneous reaction rate $\dot{w}_{r,i}$ is the net effect of the reaction rates of the individual reactions, i.e.,

$$\dot{w}_{r,i} \equiv \sum_{j=1}^{N_R} v_{ij} M_i r_j \tag{5.49}$$

where N_R is the number of independent chemical reactions, $v_{ij} = v''_{ij} - v'_{ij}$ is the stoichiometric coefficient difference of species i in reaction j (v'_{ij} as a reactant and v''_{ij} as a product), and r_j is the reaction rate (from the *Law of Mass Action*) of reaction j.

Summing up the reaction rates over all the species, we have

$$\sum_{i=1}^{N_c} \dot{w}_{r,i} \equiv \sum_{i=1}^{N_c} \sum_{j=1}^{N_R} v_{ij} M_i r_j = 0 \tag{5.50}$$

The ***mass flux vector*** of component i, $\dot{\mathrm{m}}_i$ is defined by

$$\dot{\mathrm{m}}_i \equiv \rho_i \mathrm{u}_i \tag{5.51}$$

Summing up the conservation equation of the mass for all the chemical species we obtain the *equation for the conservation of mass of the mixture*,

$$\frac{\partial \rho}{\partial t} + \nabla \cdot (\rho \mathrm{u}) = 0 \tag{5.52}$$

where ρ is the mixture density.

The mass-average velocity vector of the mixture **u** is then defined as

$$\rho \mathrm{u} \equiv \sum_{i=1}^{N_c} \rho_i \mathrm{u}_\mathrm{i} \tag{5.53}$$

The mass average velocity is the velocity of the center of mass of the mixture, also called the *barycentric velocity*. The difference between the species and the average velocity is the or *drift velocity*,

$$\mathrm{V}_\mathrm{i} \equiv \mathrm{u}_i - \mathrm{u} \tag{5.54}$$

And the *mass diffusion flux in respect to the* barycentric velocity vector is defined as

$$\mathrm{j}_i \equiv \rho_i V_i \equiv \rho_i (\mathrm{u}_i - \mathrm{u}) \tag{5.55}$$

From Eq. (5.51) and (5.53) it can be shown that the drift flux vector satisfies

$$\sum_{i=1}^{N_c} \mathrm{j}_i \equiv \sum_{i=1}^{N_c} \rho_i (\mathrm{u}_i - \mathrm{u}) = 0 \tag{5.56}$$

From the definition of the mass diffusion flux, the equation for the conservation of the mass of the chemical species i can be written as

$$\frac{\partial \rho_i}{\partial t} + \nabla \cdot \left(\rho_i \mathrm{u} \right) = -\nabla \cdot \mathrm{j}_i + \dot{w}_{r,i} \tag{5.57}$$

Different reference velocities may be defined leading to different forms of the equation for the conservation of mass of species *i* depending on the choice of reference velocity and measure of the species *i* concentration. This will be explored further below.

The material derivative in respect to the barycentric velocity is defined as

$$\frac{d\rho}{dt} = \frac{\partial \rho}{\partial t} + \mathrm{u} \cdot \nabla \rho \tag{5.58}$$

Then, the conservation of mass can also be written as

$$\frac{d\rho}{dt} + \rho \nabla \cdot \mathrm{u} = 0 \tag{5.59}$$

For an isochoric flow (also in the limit of an ideal incompressible fluid) Eq. (5.52) becomes

$$\nabla \cdot \mathrm{u} = 0 \tag{5.60}$$

5.3.2 Conservation of linear momentum

In writing the conservation of linear momentum, one assumes that the fluid particles for the various species *i* can accelerate as a response to body forces, surface forces and the exchange of momentum with the other species *j* particles. The conservation of the linear momentum for species *i* for the material volume V_i, neglecting the electromagnetic momentum, is postulated as (Newton's second law)

$$\frac{d_i}{dt} \int_{V_i(t)} \rho_i \mathrm{u}_i dV = \int_{V_i(t)} \rho_i \mathbf{f}_i dV + \int_{A_i(t)} \mathrm{t}_{i(n)} dA + \int_{V_i(t)} \sum_{j=1}^{N_c} \mathrm{P}_{ij} dV + \int_{V_i(t)} \dot{w}_{r,i} \mathrm{u}_{r,i} dV \tag{5.61}$$

where d_i / dt is the material derivative in respect to species *i*, $\mathbf{f}_\mathrm{i}$ is an external body force applied on species *i*, $\mathrm{t}_{\mathrm{i(n)}}$ is a vector expressing the flux of momentum entering the material surface A_i by other mechanisms (actually, it is not the partial stress vector for species *i*, as it will be shown below), P_{ij} is the drag force exerted by species *j* over species *i* (by elastic collisions) and $\dot{w}_{r,i} \mathrm{u}_{r,i}$ accounts for the production/destruction of linear momentum due to chemical reaction

(from inelastic collisions). Whitaker (2009) remarks that $\mathrm{u}_{r,i} \neq \mathrm{u}_i$. The exchange of momentum between species by elastic and inelastic collisions is the result of mutual interactions. Therefore, it is required that

$$\sum_{i=1}^{N_c}\sum_{j=1}^{N_c}\mathrm{P}_{ij} = 0 \tag{5.62}$$

which is satisfied by $\mathbf{P}_{ij} = \mathbf{P}_{ji}$, and

$$\sum_{i=1}^{N_c}\dot{w}_{r,i}\mathrm{u}_{r,i} = 0 \tag{5.63}$$

The momentum diffusion vector is the projection of the momentum diffusion tensor $\mathrm{T_i}$ over area A_i, i.e.,

$$\mathrm{t}_{\mathrm{i}(n)} = \mathrm{n}\cdot\mathrm{T}_{\mathrm{i}} \tag{5.64}$$

where **n** is the normal unit vector pointing out of area A_i.

Assuming symmetry of the momentum diffusion tensor and using the *divergence theorem*,

$$\begin{aligned}\int_{A_i(t)}\mathrm{t}_{\mathrm{i}(n)}\,dA &\equiv \int_{A_i(t)}\left(\mathrm{n}\cdot\mathrm{T}_i\right)dA \\ &= \int_{A_i(t)}\left(\mathrm{T}_i\cdot\mathrm{n}\right)dA = \int_{V_i(t)}\left(\nabla\cdot\mathrm{T}_i\right)dV\end{aligned} \tag{5.65}$$

As before, using the *Reynolds Transport Theorem* and invoking the invariance over the integration volume V_i, the conservation of momentum for species *i* becomes

$$\frac{\partial}{\partial t}\left(\rho_i u_i\right) + \nabla\cdot\left(\rho_i \mathrm{u}_i u_i\right) = \nabla\cdot\mathrm{T}_i + \rho_i \mathrm{f}_i + \sum_{j=1}^{Nc}\mathrm{P}_{ij} + \dot{w}_{r,i}\mathrm{u}_{r,i} \tag{5.66}$$

This is equivalent to Whitaker (2009) in his Eq.(23). In order to make the symbology compatible with Curtiss and Bird (1996) in their Appendix A, and with the Thermodynamics of Irreversible Processes to be developed below, a minus sign will be added to the divergence of the momentum flux tensor, obtaining

$$\frac{\partial}{\partial t}\left(\rho_i u_i\right) + \nabla\cdot\left(\rho_i \mathrm{u}_i u_i\right) = -\nabla\cdot\mathrm{T}_i + \rho_i \mathrm{f}_i + \sum_{j=1}^{Nc}\mathrm{P}_{ij} + \dot{w}_{r,i}\mathrm{u}_{r,i} \tag{5.67}$$

Therefore, $\mathbf{T}_\mathrm{i}$ from Curtiss and Bird (1996), and in the form that will be used here, is equivalent to $-\mathrm{T_A}$ as used by Whitaker (2009).

A different form of expressing the species momentum equation is by using the species material derivate

$$\frac{d_i u_i}{dt} = \frac{\partial u_i}{\partial t} + u_i \cdot \nabla u_i \tag{5.68}$$

The conservation of mass of chemical species *i*, Eq. (5.48) is multiplied by u_i and added to Eq. (5.67) obtaining,

$$\rho_i \frac{d_i u_i}{dt} = -\nabla \cdot \mathrm{T}_i + \rho_i \mathrm{f}_i + \sum_{j=1}^{Nc} \mathrm{P}_{ij} \tag{5.69}$$

Whitaker (2009) arrives at the same equation but he maintains a last term $\dot{w}_{r,i}\left(\mathrm{u}_{r,i} - \mathrm{u}_\mathrm{i}\right)$ by remarking that the species velocity for the reaction term $\mathrm{u}_{r,i}$ may not be equal to the velocity for the species u_i. From asymptotic analysis, Lam (2006) suggests that the contribution of inelastic collisions to the equation above is negligible (see also, De Groot and Mazur, 1984). We note that only the elastic momentum exchange is retained here. Lam (2006) denotes the elastic collisions term as

$$\sum_{j=1}^{Nc} \mathrm{P}_{ij} = G_i^{coll} \tag{5.70}$$

In analogy to the *stress tensor for a Newtonian fluid*, the momentum diffusion tensor is separated in a pressure and a viscous component

$$\mathrm{T}_\mathrm{i} = p_\mathrm{i}\mathrm{I} + \tau_\mathrm{i} \tag{5.71}$$

where p_i is the partial pressure of species *i*, I is the identity matrix and τ_i is a tensor related to viscous phenomena, whose identity is still unknown. Then,

$$\rho_i \frac{d_i u_i}{dt} = -\nabla p_i - \nabla \cdot \tau_i + \rho_i \mathrm{f}_i + \sum_{j=1}^{Nc} \mathrm{P}_{ij} \tag{5.72}$$

Curtiss and Bird (1996) do not make this separation into pressure and viscous effects, but this will prove itself useful below. Summing up over all the chemical species *i*, we should obtain the equation for the conservation of the momentum of the mixture. To accomplish that, the identity

$$\rho_i \mathrm{u}_i \mathrm{u}_i = \rho_i \left(\mathrm{u}_i \mathrm{u} + \mathrm{u}\mathrm{u}_i - \mathrm{u}\mathrm{u}\right) + \rho_i \left(\mathrm{u}_i - \mathrm{u}\right)\left(\mathrm{u}_i - \mathrm{u}\right) \tag{5.73}$$

is substituted in the left-hand side of Eq. (5.67) and the resulting equation is summed over *i* obtaining

$$\frac{\partial}{\partial t}\left(\rho \mathrm{u}\right)+\nabla \cdot\left(\rho \mathrm{uu}\right)=-\nabla p+\rho \mathrm{f}-\nabla \cdot \mathrm{S} \tag{5.74}$$

where

$$p=\sum_{i=1}^{Nc} p_i \tag{5.75}$$

$$\rho \mathrm{f}=\sum_{i=1}^{N_c} \rho_i \mathrm{f}_i \tag{5.76}$$

$$\mathrm{S}=\sum_{i=1}^{N_c}\left[\tau_i+\rho_i\left(\mathrm{u}_i-\mathrm{u}\right)\left(\mathrm{u}_i-\mathrm{u}\right)\right]=\sum_{i=1}^{N_c}\left[\tau_i+\rho_i V_i V_i\right] \tag{5.77}$$

Since the last term can be equated to the stress tensor for a mixture that behaves as a Newtonian fluid, Cauchy's equation of motion for a Newtonian fluid is recovered. This assumption also implies that the stress tensor for the mixture can be written as

$$T=p\mathrm{I}+\mathrm{S} \tag{5.78}$$

If a partial stress tensor $\mathrm{S_i}$ can be defined such that

$$\mathrm{S}=\sum_{i=1}^{Nc} \mathrm{S}_i \tag{5.79}$$

then, we can identify

$$\mathrm{S}_i=\tau_i+\rho_i V_i V_i \tag{5.80}$$

This still does not evidence what the terms τ_i are. In this form, τ_i can be only identified as the difference between $\mathrm{S_i}$ and $\rho_i V_i V_i$. Eq. (5.74) is equivalent as that presented by Whitaker (2009), except for the sign of $\mathrm{S_i}$ as remarked above. Eq. (5.74) can also be written using the total material derivative as

$$\rho \frac{du}{dt}=-\nabla p+\rho \mathrm{f}-\nabla \cdot \mathrm{S} \tag{5.81}$$

where

$$\frac{du}{dt}=\frac{\partial u}{\partial t}+u \cdot \nabla u \tag{5.82}$$

Table 19, Table 17, Table 18 and Table 19 summarize the forms of the momentum equations developed by the different authors.

Table 17 - Different forms of expressing the conservation of species *i* and mixture momentum, and the corresponding stress-relations.

Reference	Specie momentum equation	Mixture momentum equation	Stress relation
Curtiss and bird (1996)	$\frac{\partial}{\partial t}\left(\rho_i \mathrm{u}_i\right)+\nabla\cdot\left(\rho_i \mathrm{u}_i \mathrm{u}_i\right)=$ $\rho_i \mathrm{f}_i-\nabla\cdot\sigma_i+\sum_{j=1}^{N_c}\mathrm{P}_{ij}$	$\frac{\partial}{\partial t}\left(\rho \mathrm{u}\right)+\nabla\cdot\left(\rho \mathrm{u}\mathrm{u}\right)=$ $\rho \mathrm{f}-\nabla\cdot\Pi$	$\Pi=\sum_{i=1}^{N_c}\Pi_i$
			$\Pi_i=\sigma_i+\rho_i V_i V_i$
Whitaker (1999)	$\frac{\partial}{\partial t}\left(\rho_i \mathrm{u}_i\right)+\nabla\cdot\left(\rho_i \mathrm{u}_i \mathrm{u}_i\right)=$ $\rho_i \mathrm{f}_i-\nabla\cdot\mathrm{T}_i$ $+\sum_{j=1}^{N_c}\mathrm{P}_{ij}+\dot{w}_{r,i}\mathrm{u}_{r,i}$	$\frac{\partial}{\partial t}\left(\rho \mathrm{u}\right)+\nabla\cdot\left(\rho \mathrm{u}\mathrm{u}\right)=$ $\rho \mathrm{f}+\nabla\cdot\sum_{i=1}^{N_c}\left(\mathrm{T}_i+\rho_i V_i V_i\right)$	$\Pi=\sum_{i=1}^{N_c}\Pi_i$
			$\Pi_i=T_i-\rho_i V_i V_i$
			$\mathrm{T}_i=-p_i\mathrm{I}+\tau_i$
			$p=\sum_{i=1}^{N_c}p_i$
			$\tau=\sum_{i=1}^{N_c}\tau_i$
Lam (2006)	$\frac{\partial}{\partial t}\left(\rho_i \mathrm{u}_i\right)+\nabla\cdot\left(\rho_i \mathrm{u}_i \mathrm{u}_i\right)=$ $\rho_i \mathrm{f}_i+\nabla\cdot\tau_i+\sum_{j=1}^{N_c}\mathrm{P}_{ij}$	$\frac{\partial}{\partial t}\left(\rho \mathrm{u}\right)+\nabla\cdot\left(\rho \mathrm{u}\mathrm{u}\right)=$ $\rho \mathrm{f}+\nabla\cdot\tau-\nabla\cdot\sum_{i=1}^{N_c}\rho_i V_i V_i$	$\mathrm{T}=\tau-\sum_{i=1}^{N_c}\rho_i V_i V_i$
			$\tau=\sum_{i=1}^{N_c}\tau_i$
			$\tau_i=x_i\mu\nabla\mu$

Table 18 - Comparison of Curtiss and Bird (1996) definitions and the ones used here.

	Curtiss and Bird (1996)	Here
Species surface momentum flux	$\sigma_\alpha =$	$\mathrm{T}_i = p_i\mathrm{I}+\tau_i$
Species stress tensor	$\Pi_\alpha = \sigma_\alpha + \rho_\alpha V_\alpha V_\alpha$	(not defined)
Species viscous stress tensor	(not defined)	$\mathrm{S}_i = \tau_i + \rho_i V_i V_i$
Mixture stress tensor	$\Pi = \sum_{\alpha=1}^{N_c} \Pi_A =$	$\mathrm{T} = \sum_{i=1}^{N_c}\left(T_i + \rho_i V_i V_i\right)$ $= \sum_{i=1}^{N_c}\left(p_i\mathrm{I}+\mathrm{S}_i\right) \quad = p\mathrm{I}+\mathrm{S}$

Table 19 - Comparison of Whitaker (1999) definitions and the ones used here.

	Whitaker (2009),	Here
Species surface momentum flux	$\mathrm{T}_A = -p_A\mathrm{I}+\tau_A =$	$-\mathrm{T}_i = -\left(p_i\mathrm{I}+\tau_i\right)$
Species stress tensor	$\Pi_A = \mathrm{T}_A + \rho_A V_A V_A$	(not defined)
Species viscous stress tensor	(not defined)	$-\mathrm{S}_i = -\left(\tau_i + \rho_i V_i V_i\right)$
Mixture stress tensor	$\Pi = \sum_{A=1}^{N_c} \Pi_A =$	$-\mathrm{T} = -\sum_{i=1}^{N_c}\left(T_i + \rho_i V_i V_i\right)$ $= -\sum_{i=1}^{N_c}\left(p_i\mathrm{I}+\mathrm{S}_i\right) = -\left(p\mathrm{I}+\mathrm{S}\right)$
Mixture pressure	$p = \sum_{A=1}^{N_c} p_A =$	$p = \sum_{i=1}^{N_c} p_i$
Mixture viscous stress tensor	$\tau = \sum_{A=1}^{N_c} \tau_A$	$\mathrm{S} = \sum_{i=1}^{N_c} \mathrm{S}_i$

The major differences in the approaches of Curtiss and Bird (1996), Whitaker (1999) and Lam (2006) are of notation only. Neither Curtiss and Bird (1996) nor Whitaker (1999) define a species viscous stress tensor similar to S_i as defined here. In Whitaker (1999) the term $\rho_A V_A V_A$ is left out of τ_A and therefore of $\tau = \sum_{A=1}^{N_c} \tau_A$. Here, however, this term is included as part of S_i and therefore, is taken within $S = \sum_{i=1}^{N_c} S_i$. The advantage of this approach will appear below

5.3.3 Conservation of energy

From the First Law of Thermodynamics, neglecting the electromagnetic energy, the conservation of energy can be written as

$$\frac{\partial}{\partial t}(\rho e) + \nabla \cdot (\rho \mathrm{u} e) = -\nabla \cdot \left(\mathrm{q} + \mathrm{T} \cdot \mathrm{u} + \sum_{j=1}^{Nc} \psi_i \mathrm{j}_\mathrm{i} \right) \tag{5.83}$$

where **q** is the heat transfer flux by diffusion and the total specific energy *e*, includes specific kinetic, potential and internal energies,

$$e = \frac{1}{2}|\mathrm{u}|^2 + \psi + u \tag{5.84}$$

The form of Eq. (5.83) has been limited to conservative body forces $\mathbf{f}_\mathrm{i}$ which are related to the specific potential energy ψ_i (independent of time) by

$$\mathbf{f}_i = -\nabla \psi_i, \quad \frac{\partial \psi}{\partial t} = 0 \tag{5.85}$$

This form excludes time-varying magnetic fields. It does include, however, quasi-steady electric fields. In the right-hand side of Eq. (5.83) the first term is the net heat transfer flux by diffusion, the second term is the net mechanical power performed on the fluid element and the third term is the net power produced by the transport of potential energy to the control volume.

5.3.3.1 Conservation of Mechanical energy

The equation for the conservation of the specific kinetic energy (of the center of mass) can be obtained from the dot product of the linear momentum equation Eq. (5.74) by u, resulting in

$$\frac{\partial}{\partial t}\left[\rho\left(\frac{1}{2}|\mathrm{u}|^2\right)\right]+\nabla\cdot\left[\rho\mathrm{u}\left(\frac{1}{2}|\mathrm{u}|^2\right)\right]=-\nabla\left(\mathrm{T}\cdot\mathrm{u}\right)+ \mathrm{T}:\nabla\mathrm{u}+\sum_{j=1}^{N_c}\rho_i\mathrm{f}_i\cdot\mathrm{u} \tag{5.86}$$

where $\mathrm{T}:\nabla\mathrm{u}$ is the trace of $\mathrm{T}\cdot\nabla\mathrm{u}$.

The equation for the conservation of the specific potential energy (of the center of mass) is

$$\frac{\partial}{\partial t}\left(\rho\psi\right)+\nabla\cdot\left(\rho\mathrm{u}\psi\right)=-\nabla\cdot\left(\sum_{i=1}^{Nc}\psi_i\mathrm{j}_i\right)- \sum_{i=1}^{Nc}\rho_i\mathrm{f}_i\cdot\mathrm{u}-\sum_{i=1}^{Nc}\mathrm{j}_i\cdot\mathrm{f}_i+\sum_{i=1}^{Nc}\psi_i\dot{w}_{r,i} \tag{5.87}$$

where the potential energy is $\psi=\sum_{i=1}^{Nc}\psi_i$.

The last term vanishes if the potential energy is conserved during the reaction, i.e.,

$$\sum_{i=1}^{Nc}\psi_i\nu_{ij}M_i=0,\quad j=1,2,...,N_R \tag{5.88}$$

This occurs when the property of the fluid responsible for its interaction with the field of force (e.g., the mass in a gravitational fields and the charge in an electrical field) is conserved during the reaction. With this assumption, and adding Eq. (5.86 and Eq. (5.87), the equation for the conservation of the mechanical energy (kinetic plus potential) is obtained as

$$\frac{\partial}{\partial t}\left[\rho\left(\frac{1}{2}|\mathrm{u}|^2+\psi\right)\right]+\nabla\cdot\left[\rho\mathrm{u}\left(\frac{1}{2}|\mathrm{u}|^2+\psi\right)\right]=-\nabla\cdot\left(\mathrm{T}\cdot\mathrm{u}\right)+ \mathrm{T}:\nabla\mathrm{u}-\nabla\cdot\left(\sum_{i=1}^{Nc}\psi_i\mathrm{j}_i\right)-\sum_{j=1}^{Nc}\mathrm{j}_i\cdot\mathrm{f}_i \tag{5.89}$$

On the right-hand side of Eq. (5.89) the first term is the net mechanical power performed on the fluid element, the second term is the power produced by normal and tangential forces, the third term is the net potential energy flux due to mass diffusion of the various species in the field of force, and the last term is the mechanical power converted to diffuse the chemical species against the field of force..

5.3.3.2 Conservation of thermal energy

The equation for the conservation of the thermal energy e is obtained subtracting the mechanical energy equation from the total energy equation, resulting in

$$\frac{\partial}{\partial t}(\rho e) + \nabla \cdot (\rho \mathrm{u} e) = -\nabla \cdot \mathrm{q} - \mathrm{T}:\nabla \mathrm{u} + \sum_{j=1}^{Nc} \mathrm{j_i} \cdot \mathrm{f}_i + \dot{s} \tag{5.90}$$

Substituting Eq. (5.78) into Eq. (5.90) we obtain

$$\frac{\partial}{\partial t}(\rho e) + \nabla \cdot (\rho \mathrm{u} e) = -\nabla \cdot \mathrm{q} - p\nabla \cdot \mathrm{u} - \mathrm{S}:\nabla \mathrm{u} + \sum_{j=1}^{Nc} \mathrm{j_i} \cdot \mathrm{f}_i + \dot{s} \tag{5.91}$$

On the right-hand side of Eq. (5.91) the first term is the net heat transfer to the differential volume element, the second term includes the mechanical work performed on the differential element (flow work) and the mechanical to thermal energy conversion by volume change due to pressure forces, the third term is the mechanical to thermal energy conversion by shear stress (viscous dissipation), the fourth term is the power generated due to the mass diffusion of the various species against the field of force, and the last term represents any other form of thermal energy conversion.

In terms of the specific enthalpy $h = e + pv$, the conservation of the thermal energy becomes

$$\frac{\partial}{\partial t}(\rho h) + \nabla \cdot (\rho \mathrm{u} h) = -\nabla \cdot \mathrm{q} + \frac{dp}{dt} - \mathrm{S}:\nabla \mathrm{u} + \sum_{j=1}^{Nc} \mathrm{j_i} \cdot \mathrm{f}_i + \dot{s} \tag{5.92}$$

where the material derivative of the pressure, dp/dt, (accounts for compression / expansion of the fluid element) is

$$\frac{dp}{dt} = \frac{\partial p}{\partial t} + \mathrm{u} \cdot \nabla p \tag{5.93}$$

An alternative form of the thermal energy equation may be written in terms of the species velocity $\mathrm{u_i}$ as

$$\frac{\partial}{\partial t}(\rho h) + \nabla \cdot \left(\sum_{j=1}^{N_c} \rho_\mathrm{i} \mathrm{u_i} h_\mathrm{i} \right) = -\nabla \cdot \left(\mathrm{q} - \sum_{j=1}^{N_c} \mathrm{j_i} h_\mathrm{i} \right) + \frac{dp}{dt} - \mathrm{S}:\nabla \mathrm{u} + \sum_{j=1}^{N_c} \mathrm{j_i} \cdot \mathrm{f}_i + \dot{s} \tag{5.94}$$

In this form, there appears a so called “reduced heat flux” (PRIGOGINE, 1968) given as

$$q_h = q - \sum_{j=1}^{N_c} j_i h_i \tag{5.95}$$

The term $\sum_{j=1}^{N_c} j_i h_i$ represents the effect of "diffusing heat capacities" (KUIKEN, 1994, pg. 126). We note that $\mathbf{q_h}$ is independent of the choice of the reference for h_i, and, most importantly, independent of the choice of reference velocity. Therefore, $\mathbf{q_h}$ appears as the correct definition for the heat transfer by diffusion in a multicomponent fluid. For a single component fluid, q is classically modeled by Fourier's Law. This will be explored further below.

5.3.4 Entropy balance

For a multicomponent mixture, the time variation of the internal energy of a material volume undergoing a process in which the entropy, the volume and the number of moles of components change, can be expressed as

$$\frac{dU}{dt} = T\frac{dS}{dt} - p\frac{dV}{dt} + \sum_i \bar{\mu}_i \frac{dn_i}{dt} \tag{5.96}$$

Where $\bar{\mu}_i$ is the molar chemical potential, i.e., the partial molar Gibbs free energy. In this equation we have assumed that thermodynamic equilibrium is valid for the material volume while it changes. Solving for *dS* and writing the chemical potential on a mass basis, we have

$$T\frac{dS}{dt} = \frac{dU}{dt} + p\frac{dV}{dt} - \sum_i \frac{\bar{\mu}_i}{M_i}\frac{dm_i}{dt} \tag{5.97}$$

or, *using intensive properties* and $\mu_i = \bar{\mu}_i / M_i$ we have

$$T\frac{ds}{dt} = \frac{du}{dt} + p\frac{d(1/\rho)}{dt} - \sum_i \mu_i \frac{d(Y_i)}{dt} \tag{5.98}$$

In the equation above, all material derivatives are taken in respect to the barycentric velocity **u**, as in Eq. (5.93). Using the conservation of mass of chemical species *i* Eq. (5.48), total mass Eq. (5.52), and thermal energy Eq.(5.92), we obtain the equation for the entropy balance *s (second law of thermodynamics)* as

$$\frac{\partial}{\partial t}(\rho s)+\nabla\cdot(\rho \mathrm{u} s)=-\frac{1}{T}\nabla\cdot\mathrm{q}-\frac{1}{T}\mathrm{S}:\nabla\mathrm{u}+\frac{1}{T}\sum_{j=1}^{Nc}\mathrm{j}_i\cdot\mathrm{f}_i-\frac{1}{T}\sum_{i=1}^{Nc}\mu_i(-\nabla\cdot\mathrm{j}_i+\dot{w}_{r,i}) \tag{5.99}$$

From the definition of homogeneous reaction rate Eq. (5.49) we have

$$\mu_i\dot{w}_{r,i}=\sum_{j=1}^{N_R}v_{ij}M_i\mu_i r_j$$

and the last term in eq. (5.99) become

$$-\frac{1}{T}\sum_{i=1}^{Nc}\mu_i(-\nabla\cdot\mathrm{j}_i+\dot{w}_{r,i})=\frac{1}{T}\sum_{i=1}^{Nc}\mu_i\nabla\cdot\mathrm{j}_i-\frac{1}{T}\sum_{i=1}^{Nc}\sum_{j=1}^{N_R}v_{ij}M_i\mu_i r_j$$

The chemical affinity of reaction j (de Donder), A_j, is defined as

$$A_j=\sum_{i=1}^{Nc}v_{ij}M_i\mu_i,\ j=1,2,...N_R \tag{5.100}$$

for a fluid in chemical equilibrium, $A_j = 0$. As it will be shown below, the affinity acts as the driving force for chemical reaction. Then, using the elementary reaction rate for reaction j (in units of $1/(\mathrm{sm}^3)$) such that the reaction rate for component i is given by $\dot{w}_{r,i}=\sum_{j=1}^{N_R}v_{ij}M_i r_j$, we have

$$\frac{\partial}{\partial t}(\rho s)+\nabla\cdot(\rho \mathrm{u} s)=-\frac{1}{T}\nabla\cdot\mathrm{q}-\frac{1}{T}\mathrm{S}:\nabla\mathrm{u}+\frac{1}{T}\sum_{j=1}^{Nc}\mathrm{j}_i\cdot\mathrm{f}_i+\frac{1}{T}\sum_{j=1}^{Nc}\mu_i\nabla\cdot\mathrm{j}_i-\frac{1}{T}\sum_{j=1}^{N_R}A_j r_j \tag{5.101}$$

Now, using the identities

$$\frac{1}{T}\nabla\cdot\mathrm{q}=\nabla\cdot\left(\frac{1}{T}\mathrm{q}\right)+\frac{1}{T^2}\mathrm{q}\cdot\nabla T \tag{5.102}$$

$$\frac{\mu}{T}\nabla\cdot\mathrm{j}=\nabla\cdot\left(\frac{\mu}{T}\mathrm{j}\right)-\mathrm{j}\cdot\nabla\frac{\mu}{T} \tag{5.103}$$

The right-hand side of Eq. (5.99) can be rewritten in terms of entropy flux j_s and entropy generation σ_s as

$$\frac{\partial}{\partial t}(\rho s)+\nabla\cdot(\rho \mathrm{u} s)=-\nabla\cdot\mathrm{j}_s+\sigma_s \tag{5.104}$$

where

$$\mathrm{j}_s = \frac{1}{T}\left(q - \sum_{i=1}^{Nc} \mu_i \mathrm{j}_i \right) \tag{5.105}$$

and

$$\sigma_s = -\mathrm{q}\cdot\frac{1}{T^2}\nabla T + \sum_{j=1}^{Nc} \mathrm{j}_i \cdot \left[\nabla\left(\frac{\mu_i}{T}\right) - \frac{\mathrm{f}_i}{T} \right] - \frac{1}{T}\mathrm{S}:\nabla \mathrm{u} \; - \; \frac{1}{T}\sum_{j=1}^{N_R} r_j A_j \tag{5.106}$$

This is equivalent to De Groot and Mazur (1984, pg. 24) and Kuiken (1994, pg. 129). Eq. (5.105) is the *entropy flux due to heat transfer and mass diffusion*. In Eq. (5.106), the first term is the *entropy generation due to heat transfer by diffusion*, the second term is the *entropy generation due to mass diffusion,* the third term is the *entropy generation due to shear stress* (and related to the diffusion of linear momentum), and the last term is the *entropy generation due to the different affinities of the chemical reactions* (and related to the kinetics of the chemical reaction rates). This form of the entropy generation satisfies three basic requirements:

1. It vanishes when the system reaches equilibrium,
2. it is invariant under a ***Galileian transformation*** and,
3. Upon integration over a closed system, it retries ***Clausius statement*** for the second law (DE GROOT and MAZUR, 1996).

The generation of entropy has a central role in the *Thermodynamics of Irreversible Process* (TPI) in defining the forces that drive the system to equilibrium from a non-equilibrium condition.

5.3.5 Constitutive relation for mass diffusion

The constitutive relations for the mass diffusion flux vector **j**, the heat flux vector **q**, and the viscous stress tensor **S** depend on the nature of the fluid under consideration. The objective of this section is to develop the correct form of the driving force for the mass diffusion.

A general expression for the mass flux by diffusion (as well as heat and momentum diffusion) may be obtained from postulates of the ***Thermodynamics of Irreversible Processes*** **(TIP).** Initially, however, an almost entirely continuum mechanics approach, based on the *Species* ***Linear Momentum equation*** **(SLM),** will be provided. This approach

suggests that the equation for the diffusive fluxes obtained from TIP, when applied to *ideal gases*, is a simplified form of the SLM, and the later, with the equation for the conservation of mass of the species, could be used to solve mass transfer problems. However, when dealing with non-ideal multicomponent mixtures the approach from TIP provides a more complete view. This is explored next.

5.3.5.1 Derivation from the inversion of the species momentum equation

Only macroscopic arguments were invoked in the derivation of the conservation of species linear momentum. Let's use now a minimum of molecular information to attempt a solution for the diffusion velocities from the species linear momentum equation. The development will follow closely Furry (1948) and Williams (1958) as reviewed by Lam (2006). From the kinetic theory (CHAPMAN and COWLING, 1991), it is suggested that the elastic collision term in Eq. (5.72) can be modeled as

$$\sum_{j=1}^{Nc} \mathrm{P}_{ij} = G_i^{coll} = \sum_{j=1}^{Nc} M_{ij} Z_{ij} \left(\mathrm{V}_i - \mathrm{V}_j \right) \tag{5.107}$$

where

$$M_{ij} = \frac{M_i M_j}{M_i + M_j} \tag{5.108}$$

is the reduced mass and Z_{ij} is the frequency of collisions between *i* and *j*.

Following Lam (2006), this term may be rewritten as

$$G_i^{coll} = \sum_{j=1}^{Nc} \widehat{K}_{ij} \mathbf{V}_j \tag{5.109}$$

where

$$\widehat{K}_{ij} = \delta_{ij} \sum_{k=1}^{Nc} (M_{ik} Z_{ik}) - M_{ij} Z_{ij} + b_i \rho_i \tag{5.110}$$

where b_i are N_c arbitrary numbers satisfying

$$\sum_{i=1}^{Nc} b_i \neq 0 \tag{5.111}$$

The inclusion of the $b_i \rho_i$ term in Eq. (5.110) transforms the singular matrix $K_{ij} = \delta_{ij} \sum_{i=1}^{Nc} \left(M_{ij} Z_{ij} \right) - \left(M_{ij} Z_{ij} \right)$ to the nonsingular form $\widehat{K}_{ij}$ allowing for the inversion of the momentum equation. The inversion

will provide an equation for the diffusion velocities V_i as a function of the remaining flow variables. The matrix $\widehat{K}_{ij}$ is also nonunique, since it depends on the choice for number b_i. It becomes symmetric only when $b_i = b$. The condition

$$\sum_{i=1}^{Nc} G_i^{coll} = -\sum_{i=1}^{Nc}\sum_{j=1}^{Nc} \widehat{K}_{ij}\mathbf{V}_j = 0 \tag{5.112}$$

is still satisfied, since the diffusion fluxes $\mathbf{j}_i = \rho_i \mathbf{V}_i$ for all species add up to zero. Using this form, the species linear momentum equation, Eq. (5.72) can be rearranged as

$$\sum_{j=1}^{Nc} \widehat{K}_{ij}\mathbf{V}_j = -\left(\nabla\cdot\mathbf{T}_i - \rho_i \mathbf{f}_i + \rho_i \frac{d_i \mathbf{u}_i}{dt} \right) \tag{5.113}$$

Whitaker (1999) in his Eq. (45) takes this equation to derive a constitutive equation for the diffusive velocity $\mathbf{V}_i$. He then advances several order of magnitude arguments to arrive at the classic Maxwell-Stefan form. Lam (2006), on the other hand, finds a solution for $\mathbf{V}_i$ by matrix inversion. Since $\widehat{K}_{ij}$ is nonsingular, Eq.(5.113) can be inverted by multiplying both sides by the inverse matrix of $\widehat{K}_{ij}$ to obtain the vector for the diffusion velocities as

$$\mathbf{V}_j = -\sum_{i=1}^{Nc}\left[\widehat{K}_{ij}\right]^{-1}\left(\nabla\cdot\mathbf{T}_i - \rho_i \mathbf{f}_i + \rho_i \frac{d_i \mathbf{u}_i}{dt} \right) \tag{5.114}$$

This provides a constitutive relation for the diffusion velocities as a function of the interactions with the remaining species. From the decomposition $\mathbf{T}_i = p_i \mathbf{I} + \boldsymbol{\tau}_i$ we obtain

$$\mathbf{V}_j = -\sum_{i=1}^{Nc}\left[\widehat{K}_{ij}\right]^{-1}\left(\nabla p_i - \rho_i \mathbf{f}_i + \nabla\cdot\boldsymbol{\tau}_i + \rho_i \frac{d_i \mathbf{u}_i}{dt} \right) \tag{5.115}$$

This equation provides a useful working formula. The term within brackets may be identified as the driving force for diffusion **d**i. In the classic form, we would write

$$cRT\mathrm{d}_i = \nabla p_i - \rho_i \mathrm{f}_i + \nabla\cdot\boldsymbol{\tau}_i + \rho_i \frac{d_i \mathrm{u}_i}{dt} \tag{5.116}$$

In Eq. (5.115), $\mathbf{V}_i$ is the drift velocity in respect to the barycentric velocity.

5.3.5.2 Derivation from the dissipation function

The driving force for the diffusive flux can also be obtained from the dissipation function and the postulates of the Irreversible Thermodynamics.

We begin with the entropy generation, from Eq. (5.106), neglecting temporarily for convenience the viscous and reaction terms,

$$\sigma_s = -\mathbf{q}\cdot\frac{1}{T^2}\nabla T - \sum_{i=1}^{N_c}\mathbf{j}_i\cdot\left[\nabla\left(\frac{\mu_i}{T}\right)-\frac{\mathbf{f}_i}{T}\right]\geq 0 \tag{5.117}$$

where the equality holds for equilibrium.

The term within brackets will be identified with the driving force for diffusion. The magnitude of this term depends on the choice of reference velocity, since $\mathbf{j}_i$ is calculated based on that reference. If this term within brackets could be made to add up to zero, the value of the expression would be independent of the choice of reference velocity. This can be shown to be the case if we rewrite this term using the barycentric velocity

$$\sum_{i=1}^{N_c}\rho_i\left(\mathbf{V}_i-\mathbf{u}\right)\cdot\left[\nabla\left(\frac{\mu_i}{T}\right)-\frac{\mathbf{f}_i}{T}\right] \tag{5.118}$$

and a general reference velocity *w*

$$\sum_{i=1}^{N_c}\rho_i\left(\mathbf{V}_i-\mathbf{w}\right)\cdot\left[\nabla\left(\frac{\mu_i}{T}\right)-\frac{\mathbf{f}_i}{T}\right] \tag{5.119}$$

Both equations result in the same value if the term within brackets would add up to zero. This is not the case, since taking this term, multiplying by ρ_i, using *Gibbs-Duhem* and summing over all the chemical species *i* one obtains

$$\sum_{i=1}^{N_c}\left[\rho_i\left(\nabla\left(\frac{\mu_i}{T}\right)-\frac{\mathbf{f}_i}{T}\right)\right]=\frac{1}{T}\sum_{i=1}^{N_c}\left[\rho_i h_i\frac{1}{T}\nabla T+\frac{\rho_i}{\rho}\nabla p-\rho_i\mathbf{f}_i\right] \tag{5.120}$$

$$=\frac{1}{T}\left(-\frac{\rho h}{T}\nabla T+\nabla p-\rho\mathbf{f}\right)$$

$$\sum_{i=1}^{N_c}\left[\rho_i\left(\nabla\left(\frac{\mu_i}{T}\right)-\frac{\mathbf{f}_i}{T}\right)\right]=-\frac{\rho h}{T^2}\nabla T+\frac{1}{T}\left(\nabla p-\rho\mathbf{f}\right) \tag{5.121}$$

Following the conservation of linear momentum for the mixture,

$$\frac{\partial}{\partial t}\left(\rho\mathbf{u}\right)+\nabla\cdot\left(\rho\mathbf{u}\mathbf{u}\right)=-\nabla p-\nabla\cdot\mathbf{S}+\rho\mathbf{f} \tag{5.122}$$

the existence of mechanical equilibrium (here defined as the existence of both, $d\mathbf{u}/dt=0$ and $\nabla\mathbf{u}=0$) would provide

$$\nabla p - \rho \mathbf{f} = -\frac{\partial}{\partial t}\left(\rho \mathbf{u}\right) - \nabla \cdot \left(\rho \mathbf{u}\mathbf{u}\right) - \nabla \cdot \mathbf{S} = 0 \quad (5.123)$$

Therefore, Eq.(5.121) would be zero only for an isothermal mixture under static equilibrium. A Theorem by Prigogine (also, De Groot and Mazur (1984), pg. 44; Haase (1969), pg. 243) states that when mechanical equilibrium exists, $\nabla p - \rho \mathbf{f} = \mathbf{0}$, we have

$$\sum_{i=1}^{N_c}\left[\rho_i \left(\nabla_T \mu_i - \mathbf{f}_i\right)\right] = 0 \quad (5.124)$$

and the dissipation function, written with the term

$$-\sum_{i=1}^{N_c} \mathbf{j}_i \cdot \left(\nabla_T \mu_i - \mathbf{f}_i\right) \quad (5.125)$$

would not depend on the choice of the reference velocity for the diffusion flux. This can be shown by replacing $\mathbf{j}_i$ by $\rho_i\left(\mathbf{V}_i - \mathbf{w}\right)$ in the same way as above. Therefore, the *existence of mechanical equilibrium*, or more generally, the enforcement of

$$\sum_{i=1}^{N_c} \rho_i \mathbf{d}_i = 0 \quad (5.126)$$

allows for a more general definition of the diffusion flux, facilitating the change of reference system. This is the traditional approach taken by Lightfoot and others to arrive at a form of the dissipation function valid *when mechanical static equilibrium* $\left(\nabla p - \rho \mathbf{f} = \mathbf{0}\right)$ is established faster than thermal and chemical equilibrium. This approach is detailed next.

5.3.5.3 Lightfoot formulation

Lightfoot formulation has been the starting point for models of transport across membranes, such as in PEMFC. With this condition in mind, in the classical treatment, the dissipation function is manipulated in a way that the sum of the driving force for diffusion is forced to be zero. Following Lightfoot's original development (LIGHTFOOT, 1974), as well as further developments by Taylor and Krishna (1993) and Krishna and Wesselingh (1997) [in their Eq. (50)], the term, identically equal to zero,

$$\sum_{i=1}^{N_c} \mathbf{j}_i \cdot \left[\frac{h_i}{T^2}\nabla T - \frac{h_i}{T^2}\nabla T - \frac{1}{\rho}\left(\frac{1}{T}\nabla p - \frac{1}{T}\rho \mathbf{f}\right)\right] = 0 \quad (5.127)$$

is added to the right-hand side of Eq. (5.117). As before, the notation

$$\rho\mathbf{f} = \sum_{j=1}^{N_c} \rho_j \mathbf{f}_j$$

is used.

This is equivalent to Whitaker (2009) set of assumptions (in his equations 48a to 48e) that lead basically to $\mathbf{u} = 0$. Therefore, the term within parentheses in Eq. (5.127) would be identically equal to zero when we assume that mechanical equilibrium is reached much faster than chemical equilibrium. In order to obtain the classic Lightfoot's formulation, with this assumption in mind, we add Eq. (5.127) to Eq. (5.117) and rearrange, obtaining

$$\sigma_s = -\mathbf{q}\cdot\frac{1}{T^2}\nabla T - \sum_{i=1}^{N_c}\frac{\mathbf{j}_i}{\rho_i}\cdot\left[\begin{array}{l}\rho_i\nabla\left(\frac{\mu_i}{T}\right) - \frac{\rho_i}{\rho}\frac{1}{T}\nabla p + \rho_i\frac{h_i}{T^2}\nabla T - \\ \rho_i\frac{h_i}{T^2}\nabla T - \frac{\rho_i}{T}\left(\mathbf{f}_i - \mathbf{f}\right)\end{array}\right] \quad (5.128)$$

Now, the term containing $-\rho_i h_i / T^2 \nabla T$ is added to the heat transfer term obtaining

$$\sigma_s = -\left(\mathrm{q} - \sum_{i=1}^{N_c} h_i \mathbf{j}_i\right)\cdot\frac{1}{T^2}\nabla T - \sum_{i=1}^{N_c}\frac{\mathbf{j}_i}{\rho_i}\cdot\left[\begin{array}{l}\rho_i\nabla\left(\frac{\mu_i}{T}\right) - \frac{\rho_i}{\rho}\frac{1}{T}\nabla p + \rho_i\frac{h_i}{T^2}\nabla T \\ -\frac{\rho_i}{T}\left(\mathbf{f}_i - \mathbf{f}\right)\end{array}\right] \quad (5.129)$$

The *reduced heat flux* $\mathbf{q}_\mathrm{h}$ is defined as,

$$\mathbf{q}_h = \mathbf{q} - \sum_{i=1}^{N_c} h_i \mathbf{j}_i \quad (5.130)$$

and the *dissipation function*, i.e., the entropy generation times temperature, can be written as

$$T\sigma_s = -\mathbf{q}_h\cdot\frac{1}{T}\nabla T - \sum_{i=1}^{N_c} T\frac{\mathbf{j}_i}{\rho_i}\cdot\left[\begin{array}{l}\rho_i\nabla\left(\frac{\mu_i}{T}\right) - \frac{\rho_i}{\rho}\frac{1}{T}\nabla p + \\ \rho_i h_i\frac{1}{T^2}\nabla T - \frac{\rho_i}{T}\left(\mathbf{f}_i - \mathbf{f}\right)\end{array}\right] \quad (5.131)$$

A generalized mass diffusion potential is defined as

$$cR\mathbf{d}_i = \rho_i\nabla\left(\frac{\mu_i}{T}\right) - \frac{\rho_i}{\rho}\frac{1}{T}\nabla p + \rho_i h_i\frac{1}{T^2}\nabla T - \frac{\rho_i}{T}\left(\mathbf{f}_i - \mathbf{f}\right) \quad (5.132)$$

The summation over *i* of the first three terms forms the ***Gibbs-Duhem*** equation. Therefore, the driving force $\mathbf{d_i}$ has the property that $\sum_{i=1}^{N_c}\mathbf{d}_i = 0$ as it was desired.

More conveniently, we can write

$$\frac{cR\mathbf{T}}{\rho_i}\mathbf{d}_i = T\nabla\left(\frac{\mu_i}{T}\right) + h_i\frac{1}{T}\nabla T - \frac{1}{\rho}\nabla p - \left(\mathbf{f}_i - \mathbf{f}\right) \tag{5.133}$$

and the *dissipation function*, including back the terms that were temporarily removed (entropy generation by shear stress and chemical reaction), becomes

$$T\sigma_s = -\mathbf{q}_h \cdot \frac{1}{T}\nabla T - \left[\sum_{i=1}^{N_c}\mathbf{j}_i \cdot \frac{cRT}{\rho_i}\mathbf{d}_i\right] - \left(\mathbf{S} : \nabla\mathbf{u}\right) - \sum_{j=1}^{N_R} r_j A_j \tag{5.134}$$

Each of the entropy generation terms is formed by the product of a flux (heat flux $\mathbf{q}_h$, mass flux $\mathbf{j}_i$, momentum flux $\mathbf{S}$, or chemical reaction rate $\dot{w}_{r,j}$) and a *thermodynamic potential* (the gradient of an intensive state variable $\nabla T, \nabla\mu_i, \nabla p$, a body force $\mathbf{f}_i$, a gradient of flow velocity $\nabla\mathbf{u}$ or the difference of a thermodynamic state variable A_j). Further, the process fluxes can be classified as:

- Scalar (zeroth order tensor):r_j
- Vector (first tensor order): $\mathbf{q}_h$, $\boldsymbol{j}_i$
- Second order tensor: $\mathbf{S}$
- Analogously, the conjugate forces associated with the fluxes can be classified as:
- Scalar (zeroth order tensor): A_j
- Vector (first order tensor): $\frac{1}{T}\nabla T$, $\frac{cR\mathbf{T}}{\rho_i}\mathbf{d}_i$
- Second order tensor: $\nabla\mathbf{u}$

For isotropic fluids, forces and fluxes of different orders do not mix. This is the Currie principle (KUIKEN, 1994, pg. 76) and it is related to the invariance of the phenomenological coefficients in respect to transformations in materials that present a symmetry center.

Therefore, the development of constitutive relations can focus separately in the odd-order process (vector) and the even-order processes (scalar and second order tensors) separately.

Considering Eq. (5.37),

$$T\nabla\left(\frac{\mu_i}{T}\right) = \nabla_{T,p}\mu_i - \frac{h_i}{T}\nabla T + v_i\nabla p$$

the driving force can be written in a shorter form as

$$\frac{cRT}{\rho_i}\mathbf{d}_i = \left[\nabla_{T,p}\mu_i + v_i\nabla p - \mathbf{f}_i\right] - \left[\frac{1}{\rho}\left(\nabla p - \rho\mathbf{f}\right)\right] \tag{5.135}$$

The terms within the second pair of brackets are the macroscopic momentum equation under the assumption of mechanical equilibrium. This equation can be manipulated further as

$$\frac{cRT}{\rho_i}\mathbf{d}_i = \nabla_{T,p}\mu_i + \frac{1}{\rho_i}\left(\phi_i - Y_i\right)\nabla p - \mathbf{f}_i + \mathbf{f} \tag{5.136}$$

where $\phi_i = \rho_i v_i = c_i \overline{v}_i$ and $\overline{v}_i$ is the partial molar volume.

For an ideal gas, $\phi_i = X_i$, and

$$\nabla_{T,p}\mu_i = \frac{1}{M_i}\nabla_{T,p}\overline{\mu}_i = \frac{RT}{M_i}\nabla_{T,p}\ln\left(X_i\right) = \frac{RT}{M_i X_i}\nabla X_i = \frac{cRT}{\rho_i}\nabla X_i \tag{5.137}$$

then

$$\frac{cR_uT}{\rho_i}\mathbf{d}_i = \frac{cR_uT}{\rho_i}\nabla X_i + \frac{1}{\rho}\left(X_i - Y_i\right)\nabla p - \mathbf{f}_i + \mathbf{f} \tag{5.138}$$

or

$$\mathbf{d}_i = \nabla X_i + \frac{1}{\rho}\left(X_i - Y_i\right)\nabla p - \frac{\rho_i}{\rho}\left(\mathbf{f}_i + \mathbf{f}\right) \tag{5.139}$$

This is the form usually taken as Lightfoot's formulation [Hirschfelder, Curtiss and Bird (1954); Williams (1958); Lam (2006), Eq. (1a) to (1c); Whitaker (2009), Eq. (49), Eq. (52)]. Equation (5.139) can also be written in a more compact form as

$$\mathbf{d}_i = \frac{1}{p}\left[\left(\nabla p_i - \rho_i \mathbf{f}_i\right) - Y_i\left(\nabla p - \rho \mathbf{f}\right)\right] \tag{5.140}$$

from which one can easily check that it satisfies $\sum_{i=1}^{N_c}\mathbf{d}_i = 0$

The development of an expression for the driving force for diffusion allows the Maxwell-Stefan equations.

5.3.6 Maxwell-Stefan equations

To obtain Maxwell-Stefan equations for the mass diffusion, we start defining *constitutive relations for the diffusion (or drift)* velocities $\mathbf{V}_i$ of species *i* and *k* as

$$\mathbf{V}_i = -\sum_{j=1}^{N_c}\tilde{D}_{ij}\mathbf{d}_j - \frac{D_i^T}{\rho_i}\nabla\ln\left(T\right) \tag{5.141}$$

$$\mathbf{V}_k = -\sum_{j=1}^{N_c}\tilde{D}_{kj}\mathbf{d}_j - \frac{D_k^T}{\rho_k}\nabla\ln\left(T\right) \tag{5.142}$$

where $\tilde{D}_{ij}$ are the generalized Fick diffusion coefficients and D_k^T is the thermal diffusion coefficient. This relation is similar to that obtained from the inversion of the species linear momentum equation.

The diffusion velocities satisfy

$$\sum_{i=1}^{N_c} \rho_i \mathbf{V}_i = 0 \tag{5.143}$$

then,

$$\begin{aligned} \sum_{i=1}^{N_c} \rho_i \mathbf{V}_i &= -\sum_{j=1}^{N_c}\sum_{i=1}^{N_c} \rho_i \tilde{D}_{ij} \mathbf{d}_j - \sum_{i=1}^{N_c} \rho_i D_i^T \nabla \ln(T) \\ 0 &= -\sum_{j=1}^{N_c} \mathbf{d}_j \sum_{i=1}^{N_c} \rho_i \tilde{D}_{ij} - \nabla \ln(T) \sum_{i=1}^{N_c} \rho_i D_i^T \end{aligned} \tag{5.144}$$

therefore, it is required that

$$\sum_{j=1}^{N_c} Y_i \tilde{D}_{ij} = 0; \sum_{j=1}^{N_c} Y_i D_i^T = 0 \tag{5.145}$$

Subtracting $\mathbf{V}_i$ from $\mathbf{V}_k$ we have

$$\mathbf{V}_k - \mathbf{V}_i = -\sum_{j=1}^{N_c} \left(\tilde{D}_{kj} - \tilde{D}_{ij} \right) \mathbf{d}_j - \left(\frac{D_k^T}{\rho_k} - \frac{D_i^T}{\rho_i} \right) \nabla \ln(T) \tag{5.146}$$

Multiplying both sides by $\tilde{C}_{ik}$ and summing over k, $k \neq i$

$$\sum_{k=1;k\neq i}^{N_c} \tilde{C}_{ik} \left(\mathbf{V}_k - \mathbf{V}_i \right) = -\sum_{k=1;k\neq i}^{N_c} \sum_{j=1}^{N_c} \tilde{C}_{ik} \left(\tilde{D}_{kj} - \tilde{D}_{ij} \right) \mathbf{d}_j - \sum_{k=1;k\neq i}^{N_c} \tilde{C}_{ik} \left(\frac{D_k^T}{\rho_k} - \frac{D_i^T}{\rho_i} \right) \nabla \ln(T)$$

$$\begin{aligned} \sum_{k=1;k\neq i}^{N_c} \tilde{C}_{ik} \left(\mathbf{V}_k - \mathbf{V}_i \right) = &-\left(\sum_{j=1}^{N_c} \mathbf{d}_j \left[\sum_{k=1;k\neq i}^{N_c} \tilde{C}_{ik} \left(\tilde{D}_{kj} - \tilde{D}_{ij} \right) \right] \right) - \\ &\nabla \ln(T) \sum_{k=1;k\neq i}^{N_c} \tilde{C}_{ik} \left(\frac{D_k^T}{\rho_k} - \frac{D_i^T}{\rho_i} \right) \end{aligned} \tag{5.147}$$

Now, we define $\tilde{C}_{kj}$ such that there is symmetry in respect to i, j, i.e.,

$$\sum_{k=1,\, k\neq i}^{N_c} \tilde{C}_{ik} \left(\tilde{D}_{kj} - \tilde{D}_{ij} \right) = -\delta_{ij} + y_j \tag{5.148}$$

From this, for the first term on the right-hand side, when $\sum_{j=1}^{N_c} \mathbf{d}_j = 0$, we have

$$\sum_{j=1}^{N_c} \mathbf{d}_j \left[\sum_{k=1;k\neq i}^{N_c} \tilde{C}_{ik} \left(\tilde{D}_{kj} - \tilde{D}_{ij} \right) \right] = \sum_{j=1}^{N_c} \left(\delta_{ij} - y_j \right) \mathbf{d}_j = \mathbf{d}_i \tag{5.149}$$

Then, we write

$$\sum_{k=1;k\neq i}^{N_c} \tilde{C}_{ik} \left(\mathbf{V}_k - \mathbf{V}_i \right) = \mathbf{d}_i - \sum_{k=1;k\neq i}^{N_c} \tilde{C}_{ik} \left(\frac{D_k^T}{\rho_k} - \frac{D_i^T}{\rho_i} \right) \nabla \ln(T) \tag{5.150}$$

This is the *generalized Maxwell-Stefan equation*. The coefficients $\tilde{C}_{kj}$ may be interpreted as drag coefficients that the motion of species *i* experiences when diffusing against species *j*. The expression was written using a barycentric velocity reference system and this development is strictly valid when $\sum_{j=1}^{N_c} \mathbf{d}_j = 0$, which is enforced by Lightfoot's formulation for the driving force $\mathbf{d}_i$. From the kinetic theory of gases, it is convenient to define

$$\tilde{C}_{ik} = \frac{X_i X_k}{D_{ik}} \tag{5.151}$$

where D_{ik} are the *Maxwell-Stefan diffusivities*. Equations (5.148) and (5.151) provide a relation among the generalized Fick diffusivities $\tilde{D}_{ik}$ and the Maxwell-Stefan diffusivities D_{ik}. Given by

$$\sum_{k=1;k\neq i}^{N_c} \frac{X_i X_k}{D_{ik}} \left(\tilde{D}_{kj} - \tilde{D}_{ij} \right) = \delta_{ij} + Y_i \tag{5.152}$$

$$i, j = 1, 2, \ldots N_c$$

Using Eq. (5.151), we can write

$$\sum_{k=1;k\neq i}^{N_c} \frac{X_i X_k}{D_{ik}} \left(\mathbf{V}_k - \mathbf{V}_i \right) = \mathbf{d}_i - \sum_{k=1;k\neq i}^{N_c} \frac{X_i X_k}{D_{ik}} \left(\frac{D_k^T}{\rho_k} - \frac{D_i^T}{\rho_i} \right) \nabla \ln(T) \tag{5.153}$$

For diluted gases, we can approximate $D_{ik} = \bar{D}_{ik}$ where $\bar{D}_{ik}$ is the *binary diffusion coefficient*. In general, D_{ik} is a function of concentration of all the species in the mixture. The left-hand side can be expressed freely using different frames of reference:

Total species mass flux,

$$\dot{\mathrm{m}}_i = \rho_i \mathbf{u}_i = \rho_i \mathbf{u} + \mathbf{j}_i = \rho_i \mathbf{u} + \rho_i \mathbf{V}_i$$

$$\mathbf{V}_k - \mathbf{V}_i = \frac{\dot{\mathbf{m}}_k}{\rho_k} - \frac{\dot{\mathbf{m}}_i}{\rho_i} \tag{5.154}$$

Diffusion fluxes in respect to the barycentric velocity **u**,

$$\mathbf{j}_i = \rho_i \mathbf{V}_i = \rho_i \left(\mathbf{u}_i - \mathbf{u} \right)$$

$$\mathbf{V}_k - \mathbf{V}_i = \frac{\mathbf{j}_k}{\rho_k} - \frac{\mathbf{j}_i}{\rho_i} \tag{5.155}$$

Total species molar flux,

$$\dot{\mathbf{n}}_i = c_i \mathbf{u}_i = \frac{\rho_i}{M_i} \mathbf{u}_i + \frac{1}{M_i} \dot{\mathbf{m}}_i$$

$$\mathbf{V}_k - \mathbf{V}_i = \frac{\dot{\mathbf{n}}_k}{c_k} - \frac{\dot{\mathbf{n}}_i}{c_i} \tag{5.156}$$

Diffusion fluxes in respect to the molar frame of reference $\overline{\mathbf{u}}$,

$$\dot{\mathbf{n}}_i = c_i \mathbf{u}_i = c_i \overline{\mathbf{u}}_i + \mathbf{j}_i$$

$$\mathbf{V}_k - \mathbf{V}_i = \frac{\mathbf{J}_k}{c_k} - \frac{\mathbf{J}_i}{c_i} \tag{5.157}$$

therefore, all representations are equivalent. There is no imposition on $\mathbf{d}_i$ other than $\sum_{i=1}^{N_C} \mathbf{d}_i = 0$. The many different choices obtained from the dissipation function can be used. Using the classical result by Lightfoot, in any of the three forms below (from Eq. (5.135) and (5.136)),

$$\frac{cRT}{\rho_i} \mathbf{d}_i = T \nabla \left(\frac{\mu_i}{T} \right) + h_i \frac{1}{T} \nabla T - \frac{1}{\rho} \nabla p - \left(\mathbf{f}_i - \mathbf{f} \right)$$

$$= \nabla_{T,p} \mu_i + s_i \nabla T - \frac{1}{\rho} \nabla p - \left(\mathbf{f}_i - \mathbf{f} \right)$$

$$= \nabla_{T,p} \mu_i + v_i \nabla p - \mathrm{f}_i - \frac{1}{\rho} \left(\nabla p - \rho \mathbf{f} \right)$$

$$= \nabla_{T,p} \mu_i + \frac{1}{\rho_i} \left(\phi_i - Y_i \right) \nabla p - \mathbf{f}_i - \mathbf{f}$$

one has

$$\sum_{k=1;k\neq i}^{N_c}\frac{X_iX_k}{D_{ki}}\left(\mathbf{V}_k-\mathbf{V}_i\right)=\frac{\rho_i}{cRT}\left[\nabla_{T,p}\mu_i+\frac{1}{\rho_i}\left(\phi_i-Y_i\right)\nabla p-\mathbf{f}_i-\mathbf{f}\right] - \sum_{k=1;k\neq i}^{N_c}\frac{X_iX_k}{D_{ik}}\left(\frac{D_k^T}{\rho_k}-\frac{D_i^T}{\rho_i}\right)\nabla\ln\left(T\right) \quad (5.158)$$

Using $X_i=Y_iM/M_i$ the Maxwell-Stefan model expressed in mass variables becomes,

$$\sum_{k=1;k\neq i}^{N_c}\frac{M^2}{M_iM_k}\frac{Y_iY_k}{\rho D_{ik}}\left(Y_i\mathbf{j}_k-Y_k\mathbf{j}_i\right)=\frac{\rho_i}{cRT}\left[\nabla_{T,p}\mu_i+\frac{1}{\rho_i}\left(\phi_i-Y_i\right)\nabla p-\mathbf{f}_i-\mathbf{f}\right] - \sum_{k=1;k\neq i}^{N_c}\frac{M^2}{M_iM_k}\frac{1}{\rho D_{ik}}\left(Y_iD_k^T-Y_kD_i^T\right)\nabla\ln\left(T\right) \quad (5.159)$$

The Maxwell-Stefan model, when expressed in molar variables, becomes,

$$\sum_{k=1;k\neq i}^{N_c}\frac{1}{cD_{ik}}\left(X_i\mathbf{J}_k-X_k\mathbf{J}_i\right)=\frac{X_i}{cRT}\nabla_{T,p}\overline{\mu}_i+\frac{\left(\phi_i-Y_i\right)}{cRT}\nabla p-\frac{\rho_i}{cRT}\left(\mathbf{f}_i-\mathbf{f}\right) - \sum_{k=1;k\neq i}^{N_c}\frac{1}{cD_{ik}}\left(\frac{X_iD_k^T}{M_k}-\frac{X_kD_i^T}{M_i}\right)\nabla\ln\left(T\right) \quad (5.160)$$

This is equivalent to Eqs. (17) and (55) of Krishna and Wesselingh (1997).

A final remark regarding the change of reference is important. When mechanical static equilibrium in the form $\nabla p-p\mathbf{f}=0$ is not imposed, $\sum_{i=1}^{N_C}\mathbf{d}_i$ returns some sort of balance of linear momentum and the form that comes from the conservation of entropy, expressed in terms of total species velocity, should be the starting point (HAASE, 1969, pg. 231).

The developments presented above are considered classic. In the following, a critique of the mass transfer formulations is presented seeking at identifying a general model for the driving force for diffusion with the minimum hypothesis possible.

6 ANALYSIS OF THE CLASSIC FORMULATIONS FOR THE DRIVING FORCE FOR DIFFUSION

In this section, a critical analysis of the results presented in the previous chapter is presented, with the objective of isolating a general formulation for application in transport in porous media.

6.1 ANALYSIS OF THE FORMULATION FROM THE SPECIES MOMENTUM EQUATION

The formulation developed from the inversion of the species linear momentum equation can be compared to the corresponding developments by Lam (2006) and by Whitaker (2009).

6.1.1 Reduction to Lam.

In order to arrive at the result by Lam (2006), we add and subtract $Y_i\mathbf{F}/p$ to the right-hand side of Eq. (5.115), where $\mathbf{F}=\sum_{i=1}^{N_c} Y_i\mathbf{F}_i$, and reorganize obtaining

$$\mathbf{V}_j = -p\sum_{i=1}^{N_c}\left[\widehat{K}_{ij}\right]^{-1}\left[-\frac{1}{p}\left(\mathbf{F}_i - Y_i\mathbf{F}\right)-\frac{Y_i}{p}\left(\mathbf{F}-\frac{1}{Y_i}\nabla\cdot\boldsymbol{\tau}_i-\rho\frac{d_i\mathbf{u}_i}{dt}\right)\right] \tag{6.1}$$

where

$$\mathbf{F}_i = -\nabla p_i + p_i\mathrm{f}_i$$

When this equation is compared to Lam's, we find a difference in the term $1/Y_i(\nabla\cdot\boldsymbol{\tau}_i)$ which appears here but was not present in Lam's. In Lam's formulation, *considering an incompressible newtonian fluid*, a term $\nabla\cdot\hat{\eta}_i\nabla\mathbf{u}$ was added heuristically to the ("catch-all", as Lam calls it) body-force term,

$$\rho_i\mathrm{f}_i = \rho_i\mathrm{f}_i + \nabla\cdot\hat{\eta}_i\nabla\mathrm{u} \tag{6.2}$$

obtaining (in Lam's notation)

$$\widehat{\mathbf{V}}_j = -p\sum_{i=1}^{N_c}\left[\widehat{K}_{ij}\right]^{-1}\left[-\frac{1}{p}\left(F_i - Y_iF\right)-\frac{1}{p}\left(\nabla\cdot\hat{\eta}_i\nabla\mathrm{u}\right)-\frac{Y_i}{p}\left(\mathrm{F}-\rho\frac{d_i\mathrm{u}_i}{dt}\right)\right] \tag{6.3}$$

Comparing Lam´s $\widehat{\mathbf{V}}_j$ from Eq. (6.3) with $\mathbf{V}_j$ from Eq. (6.1) we note that Lam in fact postulates that

$$\tau_i = -\hat{\eta}_i \nabla \mathrm{u} \tag{6.4}$$

where $\hat{\eta}_i$ takes the role of *partial dynamic viscosity.*
More generally, this could be expressed as

$$\tau_i = \frac{\hat{\eta}_i}{\eta}\mathbf{S} \tag{6.5}$$

where η is the dynamic viscosity and $\mathbf{S}$ is the viscous stress tensor for the mixture. This is similar to the hypothesis advanced by Whitaker (1999) in his Equations (42) and (45), as long as $\eta = \sum_{i=1}^{N_C} \hat{\eta}_i$.

Furthermore, Lam suggests that a simple model for the partial viscosity that recovers the viscous stress for the mixture would be

$$\hat{\eta}_i = X_i \eta \tag{6.6}$$

and

$$\tau_i = -X_i \eta \nabla \mathrm{u} \tag{6.7}$$

Then,

$$\nabla \cdot (X_i \eta \nabla \mathrm{u}) = X_i \nabla \cdot (\eta \nabla \mathrm{u}) + \nabla X_i \cdot \eta \nabla \mathrm{u} \tag{6.8}$$

For an ideal gas,

$$\nabla p_i = p \nabla X_i + X_i \nabla p$$

then, Eq. (6.1) becomes

$$\mathbf{V}_j = -\sum_{i=1}^{N_c} \left[\widehat{K}_{ij}\right]^{-1} \begin{bmatrix} -\nabla X_i \cdot (-p\mathbf{I} + \mu \nabla \mathbf{u}) + \mu \nabla \mathbf{u} - \\ X_i(-\nabla p + \nabla \cdot \mu \nabla \mathbf{u}) - \rho_i \mathbf{f}_i + \rho_i \dfrac{d_i \mathbf{u}_i}{dt} \end{bmatrix} \tag{6.9}$$

Using the conservation of the mixture momentum

$$\rho \frac{d\mathbf{u}}{dt} - \rho \mathbf{f} = -\nabla p - \nabla \cdot \mathbf{S} \tag{6.10}$$

for the term containing $-\nabla p + \nabla \cdot \mu \nabla \mathbf{u}$ We have

$$\mathbf{V}_j = -\sum_{i=1}^{N_c} \left[\widehat{K}_{ij}\right]^{-1} \begin{bmatrix} -\nabla X_i \cdot (-p\mathbf{I} + \mu \nabla \mathbf{u}) - \\ X_i \left(\rho \dfrac{d\mathbf{u}}{dt} - \rho \mathbf{f} \right) - \rho_i \mathbf{f}_i + \rho_i \dfrac{d_i \mathbf{u}_i}{dt} \end{bmatrix} \tag{6.11}$$

rearranging, we obtain the SLM equation for an ideal gas, under Lam's partial viscosity hypothesis, as,

$$\mathbf{V}_j = -\sum_{i=1}^{Nc}\left[\widehat{K}_{ij}\right]^{-1}\left[\begin{array}{l}-\nabla X_i\cdot(-p\mathbf{I}+\mu\nabla\mathbf{u})-\\ \rho X_i\left(\dfrac{d\mathbf{u}}{dt}-\mathbf{f}\right)+\rho Y_i\left(\dfrac{d_i\mathbf{u}_i}{dt}-\mathbf{f}_i\right)\end{array}\right] \qquad (6.12)$$

$$= -\sum_{i=1}^{Nc}\left[\widehat{K}_{ij}\right]^{-1}\left[\nabla X_i\cdot\mathbf{T}-\rho\left(X_i\frac{d\mathbf{u}}{dt}-Y_i\frac{d_i\mathbf{u}_i}{dt}\right)+\rho(X_i\mathbf{f}-Y_i\mathbf{f}_i)\right]$$

This equation presents species and mixture variables. Since $\sum_{i=1}^{N_c} V_j = 0$, summing up the driving force vector over all species results in

$$\sum_{i=1}^{Nc}\left\{\begin{array}{l}\nabla X_i\cdot\mathbf{T}-\rho\left(X_i\dfrac{d\mathbf{u}}{dt}-Y_i\dfrac{d_i\mathbf{u}_i}{dt}\right)+\\ \rho(X_i\mathbf{f}-Y_i\mathbf{f}_i)\end{array}\right\} = -\rho\left(\frac{d\mathbf{u}}{dt}-\sum_{i=1}^{Nc}Y_i\frac{d_i\mathbf{u}_i}{dt}\right) \qquad (6.13)$$

This adds up to zero, as required, only when **Kerkhof's *homogeneous viscous mixture flow*** **(HVMF)** hypothesis (KERKHOF, 1996), leading to $\mathbf{u}_i = \mathbf{u}$, can be invoked. A similar hypothesis is advanced by Lam (2006) based on an asymptotic expansion analysis. The species material derivative can be expanded as

$$\frac{d_i\mathbf{u}_i}{dt} = \frac{d\mathbf{u}}{dt}+\frac{d_i\mathbf{V}_i}{dt}+\mathbf{V}_i\cdot\nabla(\mathbf{u}+\mathbf{V}_i) \qquad (6.14)$$

Lam (2006) argues that, in order to be consistent with the asymptotic analysis from the Boltzmann equation to arrive at the equation for the diffusive flux, the leading approximation in the small $\in$ limit is $\mathbf{V}_i = O(\in)$ where $\in$ is the ratio between the characteristic collision time (intra and interspecies) and the characteristic fluid dynamics time. Then, as a consequence

$$\frac{d_i\mathbf{u}_i}{dt} = \frac{d\mathbf{u}}{dt}\left[1+O(\in)\right] \qquad (6.15)$$

Thus, Lam´s hypothesis leads to $d_i\mathbf{u}_i/dt = d\mathbf{u}/dt$. With this hypothesis, one could write Eq. (6.12) as

$$\mathbf{V}_j = -\sum_{i=1}^{Nc}\left[\widehat{K}_{ij}\right]^{-1}\left[\nabla X_i\cdot\mathbf{T}-\rho\left(X_i-Y_i\right)\frac{d\mathbf{u}}{dt}+\rho(X_i\mathbf{f}-Y_i\mathbf{f}_i)\right] \qquad (6.16)$$

or

$$\mathbf{V}_j = -\sum_{i=1}^{Nc}\left[\widehat{K}_{ij}\right]^{-1}\begin{bmatrix} p\nabla X_i + \nabla X_i\cdot\mathbf{S} - \rho\left(X_i - Y_i\right)\dfrac{d\mathbf{u}}{dt} + \\ \rho(X_i\mathbf{f} - Y_i\mathbf{f}_i) \end{bmatrix} \tag{6.17}$$

In this form, shear stress appears as a source of diffusion even in the absence of acceleration. Acceleration only causes separation when the species have different molar weights

$$X_i - Y_i = X_i\left(1 - \frac{M_i}{M}\right) \tag{6.18}$$

Under static mechanical equilibrium, u = 0, and

$$\mathbf{V}_j = -\sum_{i=1}^{Nc}\left[\widehat{K}_{ij}\right]^{-1}\left[p\nabla X_i + \rho(X_i\mathbf{f} - Y_i\mathbf{f}_i)\right] \tag{6.19}$$

which suggests a driving force for diffusion in the form

$$\begin{aligned} cR_uT\mathrm{d}_i &= p\nabla X_i + \rho(X_i\mathbf{f} - Y_i\mathbf{f}_i) \\ &= \nabla p_i - \rho_i\mathbf{f}_i - X_i(\nabla p - \rho\mathbf{f}) \end{aligned} \tag{6.20}$$

This form clearly results in $\sum_{i=1}^{N_c} V_j = 0$ as required. This form is different than the final form adopted by Whitaker (1999), in his Eq. (49), under similar assumptions.

6.1.2 Reduction to Whitaker

To Arrive at Whitaker's equation, the partial viscosity should be modeled as (the simplest model compatible)

$$\hat{\eta}_i = Y_i\eta \tag{6.21}$$

and

$$\tau_i = -Y_i\eta\nabla\mathbf{u} \tag{6.22}$$

then,

$$\nabla\cdot(\hat{\eta}_i\nabla\mathrm{u}) = Y_i\nabla\cdot(\eta\nabla\mathrm{u}) + \eta\nabla\mathrm{u}\cdot\nabla Y_i \tag{6.23}$$

and, applying for an ideal gas, Eq. (6.1) becomes

$$\mathrm{V}_j = -\sum_{i=1}^{Nc}\left[\widehat{K}_{ij}\right]^{-1}\begin{bmatrix} p\nabla(X_i) + (X_i - Y_i)\nabla p - \rho_i(\mathbf{f}_i - \mathbf{f}) - \\ \mu\nabla\mathbf{u}\cdot\nabla Y_i + \rho_i\left(\dfrac{d_i\mathbf{u}_i}{dt} - \dfrac{d\mathbf{u}}{dt}\right) \end{bmatrix} \tag{6.24}$$

Using the HVMF hypothesis (KERKHOV, 1996),

$$\frac{d_i \mathbf{u}_i}{dt} = \frac{d\mathbf{u}}{dt} \tag{6.25}$$

one has

$$\mathbf{V}_j = -\sum_{i=1}^{Nc} \left[\widehat{K}_{ij} \right]^{-1} \left[\begin{array}{l} p\nabla(X_i) + (X_i - Y_i)\nabla p - \rho_i(\mathrm{f}_i - \mathrm{f}) - \\ \mu\nabla \mathrm{u} \cdot \nabla Y_i \end{array} \right] \tag{6.26}$$

Under static mechanical equilibrium, u = 0, and

$$\mathbf{V}_j = -\sum_{i=1}^{Nc} \left[\widehat{K}_{ij} \right]^{-1} \left[\begin{array}{l} p\nabla X_i + (X_i - Y_i)\nabla p - \\ \rho_i(\mathrm{f}_i - \mathrm{f}) \end{array} \right] \tag{6.27}$$

Rearranging, this becomes

$$\mathbf{V}_j = -\sum_{i=1}^{Nc} \left[\widehat{K}_{ij} \right]^{-1} \left[\nabla p_i - \rho_i \mathrm{f}_i - Y_i(\nabla p - \rho \mathrm{f}) \right] \tag{6.28}$$

Which is equivalent to **Whitaker's** Eq.(49)

6.1.3 Critique to the partial viscosity concept

Both hypothesis given by Eq. (6.6) or (6.21) are heuristic and not strongly supported by evidence. One of the earliest models for the *viscosity of mixtures of non-polar gases* is Wilke's equation (WILKEs, 1955) which may be expressed as

$$\eta = \sum_{i=1}^{Nc} \frac{X_j \eta_j^*}{\xi_j} \tag{6.29}$$

where

$$\xi_j = \sum_{i=1}^{Nc} X_j \Phi_{jk} \tag{6.30}$$

and

$$\Phi_{jk} = \frac{1}{\sqrt{8}} \left(1 + \frac{M_j}{M_k} \right)^{-1/2} \left[1 + \left(\frac{\eta_j^*}{\eta_k^*} \right)^{1/2} \left(\frac{M_k}{M_j} \right)^{1/4} \right]^2 \tag{6.31}$$

where η_j^* is the dynamic viscosity of the *j*-th species (pure).

Therefore, if we postulate

$$\eta = \sum_{i=1}^{Nc} \widehat{\eta}_i, \quad \widehat{\eta}_i = k_i \eta \tag{6.32}$$

then, from Wilke's model,

$$k_i = \frac{\eta_i^* X_i}{\xi_i}\left[\sum_{j=1}^{Nc}\frac{\eta_i^* X_j}{\xi_j}\right]^{-1} \tag{6.33}$$

where $\xi_j = \xi_j\left(X_k, M_k, \eta_k^*\right), k = 1,...,N_c$. Therefore, k_i is a complicated function of the mole fractions and viscosities of each species. In general,

$$k_i^{-1} = \sum_{j=1}^{N_c}\left(\frac{\eta_j^* X_j}{\eta_i^*}\frac{\sum_{k=1}^{Nc} X_k \Phi_{ik}}{\sum_{k=1}^{Nc} X_k \Phi_{jk}}\right) \tag{6.34}$$

For a single component fluid, when $\eta_i^* = \eta$ and $M_i = M$, then $k_i = X_i$ is recovered. Inverting the SLM equation resulted in

$$\mathbf{V}_j = -\sum_{i=1}^{Nc}\left[\widehat{K}_{ij}\right]^{-1}\left[\begin{array}{l}\nabla p_i - \rho_i \mathbf{f}_i + \nabla\cdot\mathbf{S}_i + \\ \left(\rho_i \dfrac{d_i \mathbf{u}_i}{dt} - \nabla\cdot\rho_i \mathbf{V}_i\mathbf{V}_i\right)\end{array}\right] \tag{6.35}$$

We note that the solution for the diffusion velocities in the presence of viscous flow become iterative, because of the species acceleration term and the "apparent stresses arising from diffusion" as named by Truesdell and Toupin (1960). The term within brackets could be identified to the driving force for diffusion $\mathbf{d_i}$,

$$cRT\mathbf{d}_i = \nabla p_i - \rho_i \mathbf{f}_i + \nabla\cdot\mathbf{S}_i + \left(\rho_i \frac{d_i \mathbf{u}_i}{dt} - \nabla\cdot\rho_i \mathbf{V}_i\mathbf{V}_i\right) \tag{6.36}$$

the term within parentheses satisfy the identity

$$\rho_i \frac{d_i \mathbf{u}_i}{dt} - \nabla\cdot\rho_i \mathbf{V}_i\mathbf{V}_i = \frac{\partial}{\partial t}\rho_i \mathrm{u}_i + \nabla\cdot\rho_i\left(\mathbf{u}_i\mathbf{u} + \mathbf{u}\mathbf{u}_i - \mathbf{u}\mathbf{u}\right) \tag{6.37}$$

then, the summation over *i* returns the mixture momentum equation

$$\sum_{i=1}^{N_c}\mathbf{d}_i = \nabla p - \rho\mathbf{f} + \nabla\cdot\mathbf{S} + \frac{\partial}{\partial t}\rho\mathbf{u} + \nabla\cdot\rho\mathbf{u}\mathbf{u} = 0 \tag{6.38}$$

This equation can also be written as

$$cRT\mathbf{d}_i = \nabla p_i - \rho_i \mathbf{f}_i + \nabla\cdot\boldsymbol{\tau}_i + \rho_i \frac{d_i \mathbf{u}_i}{dt} \tag{6.39}$$

where

$$\boldsymbol{\tau}_i = \mathbf{S}_i - \rho_i \mathbf{V}_i\mathbf{V}_i$$

There are other alternatives for the definition of the partial viscosities. For example, taking the partial viscosity as a combination of molecular and diffusion transfer of linear momentum, one can write

$$\nabla \cdot \boldsymbol{\tau}_i = \frac{\hat{\eta}_i}{\eta} \nabla \cdot \mathbf{S} = k_i \nabla \cdot \mathbf{S} \tag{6.40}$$

Assuming the HVMF hypothesis (KERKHOV, 1996),

$$\frac{d_i \mathbf{u}_i}{dt} = \frac{d\mathbf{u}}{dt} = \frac{1}{\rho}\left(-\nabla p + \rho \mathbf{f} - \nabla \cdot \mathbf{S}\right) \tag{6.41}$$

One can write

$$\begin{aligned} cRT\mathbf{d}_i &= \left(\nabla p_i - \rho_i \mathbf{f}\right) + \nabla \cdot \boldsymbol{\tau}_i + \rho_i \frac{d_i \mathbf{u}_i}{dt} \\ &= \left(\nabla p_i - \rho_i \mathbf{f}_i\right) + k_i \nabla \cdot \mathbf{S} + Y_i \left(-\nabla p + \rho \mathbf{f} - \nabla \cdot \mathbf{S}\right) \\ &= \left(\nabla p_i - \rho_i \mathbf{f}_i\right) - Y_i \left(\nabla p - \rho \mathbf{f}\right) - Y_i \nabla \cdot \mathbf{S} + k_i \nabla \cdot \mathbf{S} \\ &= \left(\nabla p_i - \rho_i \mathbf{f}_i\right) - Y_i \left(\nabla p - \rho \mathbf{f}\right) + \left(k_i - Y_i\right) \nabla \cdot \mathbf{S} \end{aligned} \tag{6.42}$$

This equation satisfy the requirement $\sum_{i=1}^{N_c} \mathbf{d}_i = 0$, since $\sum_{i=1}^{N_c} (k_i - Y_i) = 0$. The solution of Whitaker can be recovered by using $k_i = Y_i$ but with the limitations discussed above. This will be compared to the entropy dissipation function.

6.2 ANALYSIS OF THE FORMULATION FROM THE DISSIPATION FUNCTION

The classical approach from the dissipation function leads to the model by Lightfoot. This model is constrained by the enforcement of the mechanical equilibrium hypothesis.

To better appreciate the role of the assumption of faster mechanical static equilibrium, we can observe the application of the equation developed for the mass diffusion under the effect of body force.

First, the *diffusion under a centrifugal force field* is considered. The body force per unit mass applied on each species *i* is

$$\mathbf{f}_i = \Omega^2 \mathbf{r} \tag{6.43}$$

where Ω is the rotational speed (rad/s) and r is the position vector of the fluid particle in respect to the fixed axis of rotation. Then,

$$\mathbf{f} = \frac{1}{\rho}\sum_{j=1}^{N_c}\rho_j \mathbf{f}_j = \frac{1}{\rho}\sum_{j=1}^{N_c}\rho_j \Omega^2 \mathbf{r} = \Omega^2 \mathbf{r} \tag{6.44}$$

For *mechanical static equilibrium*, the pressure gradient caused by the centrifugal force is

$$\nabla p = \sum_{j=1}^{N_c}\rho_j \mathbf{f}_j = \rho\Omega^2 \tag{6.45}$$

Therefore, from Eq. (5.133), the driving force for diffusion is given by

$$\begin{aligned}\frac{cRT}{\rho_i}\mathbf{d}_i &= T\nabla\left(\frac{\mu_i}{T}\right) + h_i\frac{1}{T}\nabla T - \frac{1}{\rho}\nabla p - \mathbf{f}_i + \mathbf{f} \\ &= T\nabla\left(\frac{\mu_i}{T}\right) + h_i\frac{1}{T}\nabla T - \frac{1}{\rho}\rho\Omega^2\mathbf{r} - \Omega^2\mathbf{r} + \Omega^2\mathbf{r} \\ &= T\nabla\left(\frac{\mu_i}{T}\right) + h_i\frac{1}{T}\nabla T - \Omega^2\mathbf{r}\end{aligned} \tag{6.46}$$

Assuming thermal equilibrium, $\nabla T = 0$,

$$\frac{cRT}{\rho_i}\mathbf{d}_i = \nabla\mu_i - \Omega^2\mathbf{r} \tag{6.47}$$

Assuming, additionally, the existence of *chemical equilibrium*, $\mathbf{d}_i = 0$,

$$\nabla\mu_i = \Omega^2\mathbf{r} \tag{6.48}$$

and the species distribution will be such that the chemical potential gradient balances the centripetal acceleration. This indicates the possibility of separation of chemical species under the influence of a centrifugal force field. For example, for an ideal mixture

$$\nabla\mu_i = \frac{1}{M_i}\nabla\bar{\mu}_i = \frac{RT}{M_i}\nabla X_i \tag{6.49}$$

and

$$\nabla X_i = \frac{M_i\Omega^2}{RT}\mathbf{r} \tag{6.50}$$

The second example is the diffusion of charged species under the influence of an external electrical potential field. The body force per unit mass acting on species *i* is

$$\mathbf{f}_i = -\frac{z_i F}{M_i}\nabla\varphi \tag{6.51}$$

where φ is the electric potential, z_i is the charge of species *i* and *F* is Faraday's constant. Then,

$$\mathbf{f} = \frac{1}{\rho}\sum_{j=1}^{N_c}\rho_j\mathbf{f}_j = -\frac{1}{\rho}\sum_{j=1}^{N_c}\rho_j\frac{z_i F}{M_i}\nabla\varphi = -\frac{F\nabla\varphi}{\rho}\sum_{j=1}^{N_c}c_j z_j \tag{6.52}$$

Assuming the existence of electro-neutrality, i.e, for regions far from charged boundaries by more than the **Debye-Huckel** length,

$$\sum_{j=1}^{N_c}c_j z_j = 0 \Rightarrow \frac{1}{\rho}\sum_{j=1}^{N_c}\rho_j\mathbf{f}_i = 0 \tag{6.53}$$

For mechanical equilibrium, the pressure gradient caused by the electrical potential gradient is

$$\nabla p = \sum_{j=1}^{N_c}\rho_j\mathbf{f}_i = 0 \tag{6.54}$$

then

$$\begin{aligned}\frac{cRT}{\rho_i}\mathbf{d}_i &= T\nabla\left(\frac{\mu_i}{T}\right) + h_i\frac{1}{T}\nabla T - \frac{1}{\rho}\nabla p - \mathbf{f}_i + \frac{1}{\rho}\sum_{j=1}^{N_c}\rho_j\mathbf{f}_i \\ &= T\nabla\left(\frac{\mu_i}{T}\right) + h_i\frac{1}{T}\nabla T + \frac{z_i F}{M_i}\nabla\varphi\end{aligned} \tag{6.55}$$

Assuming thermal equilibrium, $\nabla T = 0$,

$$\frac{cRT}{\rho_i}\mathbf{d}_i = \nabla\mu_i - \frac{z_i F}{M_i}\nabla\varphi \tag{6.56}$$

Assuming, additionally, chemical equilibrium, $\mathbf{d}_i$=0,

$$\nabla\mu_i = -\frac{z_i F}{M_i}\nabla\varphi \tag{6.57}$$

and the species distribution will be such that the chemical potential gradient balances the electrical potential. For example, for an ideal mixture

$$\frac{RT}{M_i}\nabla X_i = -\frac{z_i F}{M_i}\nabla\varphi \tag{6.58}$$

$$\nabla X_i = -\frac{z_i F}{RT}\nabla\varphi \tag{6.59}$$

From the two cases analyzed above, we observe that the pressure gradient term in the driving force for diffusion is directly related, by the

mixture linear momentum equation, to an external body force, and not imposed by itself externally. *Should the pressure gradient be imposed by some external means to overcome drag or viscous losses, the static equilibrium would not be granted* (HAASE, 1969, pg. 231). Therefore, the static equilibrium hypothesis difficults the treatment of flow near walls, where the gradients in velocity become important and there is significant transport of linear momentum.

6.3 COMPARISON OF DF TO SLM

In order to compare the result from the ***dissipation function (DF)*** to the development from the species ***linear momentum equation (SLM)***, Eq. (5.136) is rewritten as

$$cR\mathbf{Td}_i^{DF} = \left(\rho_i \nabla_{T,p}\mu_i + \phi_i \nabla p - \rho_i \mathbf{f}_i\right) - Y_i\left(\nabla p - \rho \mathbf{f}\right) \tag{6.60}$$

For ideal gas,

$$cR\mathbf{Td}_i^{DF} = \left(\nabla p_i - \rho_i \mathbf{f}_i\right) - Y_i\left(\nabla p - \rho \mathbf{f}\right) \tag{6.61}$$

This can be compared directly to Eq. (6.42), that when cast in the same form becomes

$$cR\mathbf{Td}_i^{SLM} = \left(\nabla p_i - \rho_i \mathbf{f}_i\right) - Y_i\left(\nabla p - \rho \mathbf{f}\right) + \left(k_i - Y_i\right)\nabla \cdot \mathbf{S} \tag{6.62}$$

Equations (6.60) and (6.62) are different forms for the driving force for diffusion. The former generalizes for non-ideal solutions while the later seems to be adequate only for ideal gases, but in the presence of viscous effects. Also, even for a mixture of ideal gases, the equations become equal only when $k_i = Y_i$, a assumption that has been discussed above.

Therefore, the addition of the mixture momentum equation to the dissipation function (multiplication of $\left(\nabla p - \rho \mathbf{f}\right)$ by Y_i to obtain the Lightfoot formulation), although allowing for invariance in respect to reference system, does not allow for the treatment of externally imposed pressure gradients and has limited use for the transport in porous media.

One possible heuristic improvement for the driving force for diffusion obtained from the SLM would be to replace ∇p_i by the more general term that comes from DF $\rho_i \nabla_{T,p}\mu_i + \phi_i \nabla p$ obtaining

$$\begin{aligned} cR\mathbf{Td}_i^{SLM(2)} = \left(\rho_i \nabla_{T,p}\mu_i + \phi_i \nabla p - \rho_i \mathbf{f}_i\right) - Y_i\left(\nabla p - \rho \mathbf{f}\right) \\ - \left(k_i - Y_i\right)\nabla \cdot \mathbf{S} \end{aligned} \tag{6.63}$$

where k_i must satisfy $\sum_{i=1}^{N_c} k_i = 1$. The discussion of this equation will be finalized at the end of the chapter.

The critique developed above indicates the need to isolate the formulation that leads to the minimum number of hypothesis needed to formulate the mass transport problem. In the next section this formulation is isolated, to be used in the next chapters.

6.4 DEVELOPMENT AND ANALYSIS OF A FORMULATION VALID FOR GENERAL MECHANICAL NON EQUILIBRIUM

Here we propose to avoid the use of the hypothesis of mechanical equilibrium seeking a formulation with larger validity. The formulation obtained is compared to Kerkhof (1996) (and Whitaker (2009)) with the objective of identifying its limitations.

6.4.1 Formulation for general mechanical non-equilibrium

The starting point is

$$\frac{\partial}{\partial t}\left(\rho s\right) + \nabla \cdot \left(\rho \mathbf{u} s\right) = -\nabla \cdot \mathbf{j}_s + \sigma_s$$

here

$$\mathbf{j}_s = \frac{1}{T}\left(\mathbf{q} - \sum_{i=1}^{N_c} \mu_i \mathbf{j}_i\right)$$

and

$$T\sigma_s = -\mathbf{q} \cdot \frac{1}{T}\nabla T - \sum_{i=1}^{N_c} \mathbf{j}_i \cdot \left[T\nabla\left(\frac{\mu_i}{T}\right) - \mathbf{f}_i\right] - \left(\mathbf{S} : \nabla \mathbf{u}\right) - \sum_{i=1}^{N_R} \dot{w}_{r,i} A_i$$

Following Haase (1968), pg 240, develop the gradient of chemical potential as

$$T\nabla\left(\frac{\mu_i}{T}\right) = \nabla_T \mu_i - \frac{h_i}{T}\nabla T$$

where ∇T is taken at constant temperature.
Then,

$$\frac{\partial}{\partial t}(\rho s)+\boldsymbol{\nabla}\cdot\left[\sum_{i=1}^{N_c}\rho_i\mathbf{u}_i s_i\right]=-\boldsymbol{\nabla}\cdot\left[\frac{1}{T}\mathbf{q}+\sum_{i=1}^{N_c}\frac{h_i}{T}\mathbf{j}_i\right]-\mathbf{q}\cdot\frac{1}{T^2}\nabla T$$
$$-\frac{1}{T}\sum_{i=1}^{N_c}\mathbf{j}_i\cdot\left[\nabla_T\mu_i-\frac{h_i}{T}\nabla T-\mathbf{f}_i\right] \qquad (6.64)$$
$$-\frac{1}{T}(\mathbf{S}:\boldsymbol{\nabla}\mathbf{u})-\frac{1}{T}\sum_{j=1}^{N_R}\dot{w}_{r,j}A_j$$

and add the term proportional to ∇T to the heat transfer flux

$$\frac{\partial}{\partial t}(\rho s)+\boldsymbol{\nabla}\cdot\left[\sum_{i=1}^{N_c}\rho_i\mathbf{u}_i s_i\right]=-\boldsymbol{\nabla}\cdot\frac{1}{T}\left[\mathbf{q}-\sum_{i=1}^{N_c}h_i\mathbf{j}_i\right]-\left(\mathbf{q}-\sum_{i=1}^{N_c}h_i\mathbf{j}_i\right)\cdot\frac{1}{T^2}\nabla T$$
$$-\frac{1}{T}\sum_{i=1}^{N_c}\mathbf{j}_i\cdot\left[\nabla_T\mu_i-\mathbf{f}_i\right]-\frac{1}{T}(\mathbf{S}:\boldsymbol{\nabla}\mathbf{u}) \qquad (6.65)$$
$$-\frac{1}{T}\sum_{j=1}^{N_R}\dot{w}_{r,j}A_j$$

Then, we can write

$$\frac{\partial}{\partial t}(\rho s)+\boldsymbol{\nabla}\cdot\left[\sum_{i=1}^{N_c}\rho_i\mathbf{u}_i s_i\right]=-\nabla\cdot\mathrm{j}_s+\sigma_s \qquad (6.66)$$

where

$$\mathrm{j}_s=\frac{1}{T}\left(\mathbf{q}-\sum_{i=1}^{N_c}h_i\mathbf{j}_i\right) \qquad (6.67)$$

and

$$\sigma_s=-\left(\mathbf{q}-\sum_{i=1}^{N_c}h_i\mathbf{j}_i\right)\cdot\frac{1}{T^2}\nabla T-\frac{1}{T}\sum_{i=1}^{Nc}\mathbf{j}_i\cdot\left[\nabla_T\mu_i-\mathbf{f}_i\right]-\frac{1}{T}(\mathrm{S}:\nabla\mathrm{u})$$
$$-\frac{1}{T}\sum_{j=1}^{N_R}\dot{w}_{r,j}A_j \qquad (6.68)$$

With this choice,

$$\frac{cRT}{\rho_i}\mathbf{d}_i=\nabla_T\mu_i-\mathbf{f}_i \qquad (6.69)$$

and the *dissipation function* becomes (also, Kuiken (1996), pg. 131),

$$T\sigma_s=-\mathbf{q}_h\cdot\nabla\ln(T)-\left[\sum_{i=1}^{Nc}\mathbf{j}_i\cdot\frac{cRT}{\rho_i}\mathbf{d}_i\right]-(\mathrm{S}:\nabla\mathrm{u})-\sum_{i=1}^{N_R}\dot{w}_{r,i}A_i \qquad (6.70)$$

The advantage of writing the driving force as Eq. (6.69) is that conservative body forces may be written as the gradient of a potential function ψ as

$$\mathbf{f}_i = -\nabla \psi_i \tag{6.71}$$

Then, a total chemical potential

$$\tilde{\mu}_i = \mu_i + \psi_i \tag{6.72}$$

may be defined and the dissipation function becomes

$$T\sigma_s = -\mathbf{q}_h \cdot \nabla \ln(T) - \sum_{i=1}^{Nc} \mathbf{j}_i \cdot \nabla_T \tilde{\mu}_i - (\mathrm{S}:\nabla \mathrm{u}) - \sum_{i=1}^{N_R} \overline{w}_{r,i} A_i \tag{6.73}$$

This expression always applies to *stationary potential fields*, for example, constant gravity, electrostatic potential and potential originated from centrifugal field,

$$\mathbf{f}_i = g + \Omega^2 \mathbf{r} - \frac{z_i F}{M_i} \nabla \varphi \tag{6.74}$$

When the body force arises from a stationary electric potential field φ,

$$\tilde{\mu}_i = \mu_i + \frac{z_i F}{M_i} \nabla \varphi \tag{6.75}$$

is the *electrochemical potential of species i*.

With these choices, the driving force for *mass diffusion* is given by

$$\frac{cRT}{\rho_i} \mathbf{d}_i = \nabla_T \tilde{\mu}_i \tag{6.76}$$

Noting that

$$\nabla_T \mu_i = \nabla_{T,p} \mu_i + v_i \nabla p$$

this driving potential defined by Eq. (6.69) can also be expressed in two alternative forms as

$$\frac{cRT}{\rho_i} \mathbf{d}_i = T \nabla \left(\frac{\mu_i}{T} \right) + h_i \frac{1}{T} \nabla T - \mathbf{f}_i \tag{6.77}$$

or

$$\frac{cRT}{\rho_i} \mathbf{d}_i = \nabla_{T,p} \mu_i + v_i \nabla p - \mathbf{f}_i \tag{6.78}$$

Adding up the driving forces for all species,

$$\sum_{i=1}^{N_c}\mathbf{d}_i=\frac{1}{cRT}\sum_{i=1}^{N_C}\left(\rho_i\nabla_{T,p}\mu_i-\rho_i\mathbf{f}_i\right)=\frac{1}{cRT}\sum_{i=1}^{N_C}\left(\frac{\rho_i}{\rho}\nabla p-\rho_i\mathbf{f}_i\right)$$
$$=\frac{1}{cRT}\left(\nabla p-\rho\mathbf{f}\right) \tag{6.79}$$

Since,

$$-\boldsymbol{\nabla}p+\rho\mathbf{f}=\frac{\partial}{\partial t}\left(\rho\mathbf{u}\right)+\boldsymbol{\nabla}\cdot\left(\rho\mathbf{u}\mathbf{u}\right)+\boldsymbol{\nabla}\cdot\mathbf{S}$$
$$=\rho\frac{d\mathbf{u}}{dt}+\boldsymbol{\nabla}\cdot\mathbf{S}$$

when there is static mechanical equilibrium, $\sum_{i=1}^{N_c}\mathrm{d}_i=0$ Therefore, again, the driving force add up to zero only when mechanical equilibrium is enforced, as in **Lightfoot's** development (HAASE, 1969, pg. 68, pg 230). The driving force for heat transfer is the reduced heat flux $\mathbf{q}_h$ that becomes independent of the choice of reference velocity only when $\sum_{i=1}^{Nc}\mathbf{d}_i=0$ (HAASE, 1969, pg. 237).

Now, let us consider that there is creeping flow, in the sense that neglecting acceleration the momentum equation reduces to Stokes equation,

$$\boldsymbol{\nabla}p-\rho\mathbf{f}=-\boldsymbol{\nabla}\cdot\mathbf{S}$$

Then

$$\sum_{i=1}^{N_c}\mathbf{d}_i=\frac{1}{cRT}\left(\nabla p-\rho\mathbf{f}\right)$$
$$=-\frac{1}{cRT}\left(\nabla\cdot\mathbf{S}\right) \tag{6.80}$$

What formulation would take $\sum_{i=1}^{Nc}\mathbf{d}_i=0$ in the presence of creeping flow?

6.4.2 Development by Kherkof and Geboers (2005)

Kerkhof and Geboers (2005) use the heuristic choice

$$\nabla\cdot\mathbf{T}_i=\rho_i\nabla_T\mu_i+\nabla\cdot\boldsymbol{\tau}_i \tag{6.81}$$

Since,

$$\nabla_T\mu_i=\nabla_{T,p}\mu_i+v_i\nabla p \tag{6.82}$$

then

$$\nabla \cdot \mathbf{T}_i = \left(\rho_i \nabla_{T,p} \mu_i + \phi_i \nabla p \right) + \nabla \cdot \boldsymbol{\tau}_i \tag{6.83}$$

The term within parenthesis is found in the general driving force for diffusion from DF (before addition by **Lightfoot**). This form is equivalent to replacing ∇p_i by $\rho_i \nabla_{T,p} \mu_i + \phi_i \nabla p$ in the SLM form, as explicitly stated in Eq. (6.63). With this choice (neglecting the chemical reaction term for now),

$$\begin{aligned} \rho_i \frac{d_i \mathbf{u}_i}{dt} &= -\nabla \cdot \mathbf{T}_i + \rho_i \mathbf{f}_i + \sum_{j=1}^{N_c} \mathbf{P}_{ij} \\ &= -\left(\rho_i \nabla_{T,p} \mu_i + \phi_i \nabla p \right) - \nabla \cdot \boldsymbol{\tau}_i + \rho_i \mathbf{f}_i + \sum_{j=1}^{N_c} \mathbf{P}_{ij} \\ &= -\left(\rho_i \nabla_{T,p} \mu_i + \phi_i \nabla p - \rho_i \mathbf{f}_i \right) - \nabla \cdot \boldsymbol{\tau}_i + \sum_{j=1}^{N_c} \mathbf{P}_{ij} \end{aligned} \tag{6.84}$$

The term within parenthesis is the general driving force for diffusion (before addition by **Lightfoot**). When this is reorganized as

$$\rho_i \frac{d_i \mathbf{u}_i}{dt} = -\phi_i \nabla p + \rho_i \mathbf{f}_i - \nabla \cdot \tau_i + \left(-\rho_i \nabla_{T,p} \mu_i + \sum_{j=1}^{N_c} \mathbf{P}_{ij} \right) \tag{6.85}$$

and summed over *i*, recalling

$$\rho_i \mathbf{u}_i \mathbf{u}_i = \rho_i \left(\mathbf{u}_i \mathbf{u} + \mathbf{u} \mathbf{u}_i - \mathbf{u} \mathbf{u} \right) + \rho_i \left(\mathbf{u}_i - \mathbf{u} \right) \left(\mathbf{u}_i - \mathbf{u} \right)$$

the term within parenthesis is identically equal to zero *when at constant* T and we recover

$$\frac{\partial}{\partial t} \left(\rho \mathbf{u} \right) + \nabla \cdot \left(\rho \mathbf{u} \mathbf{u} \right) = -\nabla p + \rho \mathbf{f} - \nabla \cdot \mathbf{S} \tag{6.86}$$

when

$$\sum_{i=1}^{Nc} \phi_i = 1 \tag{6.87}$$

$$\rho \mathbf{f} = \sum_{i=1}^{Nc} \rho_i \mathbf{f}_i \tag{6.88}$$

$$\mathbf{S} = \sum_{i=1}^{N_c} \left[\boldsymbol{\tau}_i + \rho_i \left(\mathbf{u}_i - \mathbf{u} \right) \left(\mathbf{u}_i - \mathbf{u} \right) \right] = \sum_{i=1}^{N_c} \left(\boldsymbol{\tau}_i + \rho_i \mathbf{V}_i \mathbf{V}_i \right) = \sum_{i=1}^{N_c} \left(\boldsymbol{\tau}_i + \frac{1}{\rho_i} \mathbf{j}_i \mathbf{j}_i \right) \tag{6.89}$$

This development, when $d_i \mathbf{u}_i / dt$ is found negligible, suggests a form for Maxwell – Stefan as

$$\sum_{j=1}^{N_c} \mathbf{P}_{ij} = \rho_i \nabla_{T,p} \mu_i + \phi_i \nabla p - \rho_i \mathbf{f}_i + \nabla \cdot \boldsymbol{\tau}_i + \rho_i \frac{d_i \mathrm{u}_i}{dt} \tag{6.90}$$

Therefore, the extended driving force can be written as

$$cRT\mathbf{d}_i = \rho_i \nabla_{T,p} \mu_i + \phi_i \nabla p - \rho_i \mathbf{f}_i + \nabla \cdot \boldsymbol{\tau}_i + \rho_i \frac{d_i \mathrm{u}_i}{dt} \tag{6.91}$$

Enforcing the constitutive relation, from Eq. (6.40),

$$\nabla \cdot \boldsymbol{\tau}_i = k_i \nabla \cdot \mathrm{S} \tag{6.92}$$

and the HVMF approximation,

$$\frac{d_i \mathbf{u}_i}{dt} = \frac{d\mathbf{u}}{dt} = \frac{1}{\rho}\left(-\nabla p + \rho \mathrm{f} - \nabla \cdot \mathrm{S}\right) \tag{6.93}$$

we obtain

$$\begin{aligned} cRT\mathbf{d}_i = &\left(\rho_i \nabla_{T,p} \mu_i + \phi_i \nabla p - \rho_i \mathbf{f}_i\right) - Y_i\left(\nabla p - \rho \mathbf{f}\right) \\ &+ \left(k_i - Y_i\right) \nabla \cdot \mathbf{S} \end{aligned} \tag{6.94}$$

and Eq. (6.63) is recovered.

Under the assumption of creeping flow, when $-\nabla p + \rho \mathrm{f} - \nabla \cdot \mathrm{S} = 0$, the results is

$$cRT\mathbf{d}_i = \left(\rho_i \nabla_{T,p} \mu_i + \phi_i \nabla p - \rho_i \mathbf{f}_i\right) + k_i \nabla \cdot \mathbf{S} \tag{6.95}$$

6.4.3 Whitaker's equation for the diffusion velocity

Whitaker (2009), after obtaining the species linear momentum equation, derives a conservation equation for the diffusion velocity as a basis for his order of magnitude analysis. The diffusion velocity in respect to the barycentric velocity is written as

$$\mathbf{V}_i = \mathbf{u}_i - \mathbf{u}$$

Taking the species material derivative

$$\frac{d_i \mathbf{V}_i}{dt} = \frac{d_i \mathbf{u}_i}{dt} - \frac{d_i \mathbf{u}}{dt} \tag{6.96}$$

and multiplying by ρ_i we have

$$\rho_i \frac{d_i \mathbf{V}_i}{dt} = \rho_i \frac{d_i \mathbf{u}_i}{dt} - Y_i \left(\rho \frac{d_i \mathbf{u}}{dt} \right) \tag{6.97}$$

This suggests that a conservation equation for the diffusion velocity can be obtained from the subtraction of the species momentum

equation and the mixture momentum equation multiplied by Y*i*. First, we rewrite

$$\frac{d_i\mathbf{u}}{dt} = \frac{\partial \mathbf{u}}{\partial t} + \mathbf{u}_i \cdot \nabla \mathbf{u}$$
$$= \frac{\partial \mathbf{u}}{\partial t} + \mathbf{u} \cdot \nabla \mathbf{u} + \mathbf{V}_i \cdot \nabla \mathbf{u} \tag{6.98}$$
$$\frac{d_i\mathbf{u}}{dt} = \frac{d\mathbf{u}}{dt} + \mathbf{V}_i \cdot \nabla \mathbf{u}$$

Following this lead, considering

$$\rho_i \frac{d_i\mathbf{u}_i}{dt} = -\nabla p_i - \nabla \cdot \boldsymbol{\tau}_i + \rho_i \mathbf{f}_i + \sum_{j=1}^{N_c} \mathbf{P}_{ij} \tag{6.99}$$

$$\rho \frac{d\mathbf{u}}{dt} = -\nabla p + \rho \mathbf{f} - \nabla \cdot \mathbf{S} \tag{6.100}$$

where

$$p = \sum_{j=1}^{N_c} p_i \tag{6.101}$$

$$\rho \mathbf{f} = \sum_{j=1}^{N_c} \rho_i \mathbf{f}_i \tag{6.102}$$

$$\mathbf{S} = \sum_{j=1}^{N_c} \mathbf{S}_i \qquad \mathbf{S}_i = \boldsymbol{\tau}_i + \rho_i \mathbf{V}_i \mathbf{V}_i \tag{6.103}$$

we have

$$\rho_i \frac{d_i\mathbf{V}_i}{dt} + \rho_i \mathbf{V}_i \cdot \nabla \mathbf{u} = -\nabla p_i + Y_i \nabla p + \rho_i \left(\mathbf{f}_i - \mathbf{f}\right) - \nabla \cdot \boldsymbol{\tau}_i + Y_i \nabla \cdot \mathbf{S} + \sum_{j=1}^{N_c} \mathbf{P}_{ij} \tag{6.104}$$

This is the same as Eq. 46 of Whitaker (1999).

If the *momentum equation by Kerkhof (1996)* is used instead, we obtain

$$\rho_i \frac{d_i \mathbf{V}_i}{dt} + \rho_i \mathbf{V}_i \cdot \nabla \mathbf{u} = -\left(\rho_i \nabla_{T,p} \mu_i + \phi_i \nabla p\right) + Y_i \nabla p + \rho_i \left(\mathbf{f}_i - \mathbf{f}\right) - \nabla \cdot \boldsymbol{\tau}_i + Y_i \nabla \cdot \mathbf{S} + \sum_{j=1}^{N_c} \mathbf{P}_{ij} \quad (6.105)$$

$$= -\rho_i \nabla_{T,p} \mu_i + \left(Y_i - \phi_i\right) \nabla p + \rho_i \left(\mathbf{f}_i - \mathbf{f}\right) - \nabla \cdot \boldsymbol{\tau}_i + Y_i \nabla \cdot \mathbf{S} + \sum_{j=1}^{N_c} \mathbf{P}_{ij}$$

The first three terms are **Lightfoot's** terms. In this form, when the terms in the left-hand side are found negligible, we can write

$$\sum_{j=1}^{N_c} \mathbf{P}_{ij} = \rho_i \nabla_{T,p} \mu_i + \left(\phi_i - Y_i\right) \nabla p + \rho_i \left(\mathbf{f} - \mathbf{f}_i\right) + \nabla \cdot \boldsymbol{\tau}_i - Y_i \nabla \cdot \mathbf{S} \quad (6.106)$$

When Eq. (6.40) for the partial viscosity is used, this expression becomes also equal to Eq. (6.63),

$$cRT\mathbf{d}_i^{SLM(2)} = \left(\rho_i \nabla_{T,p} \mu_i + \phi_i \nabla p - \rho_i \mathbf{f}_i\right) - Y_i \left(\nabla p - \rho \mathbf{f}\right) + \left(k_i - Y_i\right) \nabla \cdot \mathbf{S}$$

6.5 DISCUSSION ON THE EXTENSIONS TO CREEPING FLOW AND SUMMARY

The discussion in this section can be summarized as follows. Starting from the species momentum equation, the driving force for diffusion can be written as

$$cRT\mathbf{d}_i = \rho_i \nabla . \mathbf{T}_i - \rho_i \mathbf{f}_i + \rho_i \frac{d_i \mathbf{u}_i}{dt} \quad (6.107)$$

Assuming :

I. The constitutive relations,

$$\nabla . \mathbf{T}_i = \rho_i \nabla_T \mu_i + \nabla \cdot \boldsymbol{\tau}_i = \left(\rho_i \nabla_{T,p} \mu_i + \phi_i \nabla p\right) + \nabla \cdot \boldsymbol{\tau}_i \quad (6.108)$$

$$\nabla \cdot \boldsymbol{\tau}_i = k_i \nabla . \mathbf{S}, \ \sum_{i=1}^{Nc} k_i = 1 \quad (6.109)$$

and

II. The HVMF approximation,

$$\frac{d_i \mathbf{u}_i}{dt} = \frac{d\mathbf{u}}{dt} = \frac{1}{\rho}\left(-\nabla p + \rho \mathbf{f} - \nabla \cdot \mathbf{S}\right) \tag{6.110}$$

or, equivalently,

$$\rho_i \frac{d_i \mathbf{V}_i}{dt} + \rho_i \mathbf{V}_i . \nabla \mathbf{u} = 0 \tag{6.111}$$

the extended driving force for diffusion can be written as,

$$cRT\mathbf{d}_i = \left(\rho_i \nabla_{T,p} \mu_i + \phi_i \nabla p - \rho_i \mathbf{f}_i\right) - Y_i\left(\nabla p - \rho \mathbf{f}\right) + (k_i - Y_i)\nabla \cdot \mathbf{S} \tag{6.112}$$

which satisfy $\sum_{i=1}^{Nc} \mathbf{d}_i = 0$, as required for invariance of reference system for the mixture velocity.

Enforcing *creeping flow*, when $-\nabla p + \rho \mathrm{f} - \nabla \cdot \mathbf{S} = 0$, the result is

$$cRT\mathbf{d}_i = \left(\rho_i \nabla_{T,p} + \phi_i \nabla p - \rho_i \mathbf{f}_i\right) + k_i\left(-\nabla p + \rho \mathbf{f}\right) \tag{6.113}$$

In this form, $\mathbf{d}_i$ is not completely expressed as a function of thermodynamic properties, since k_i is a transport property, related to the diffusion of species linear momentum.

For an ideal gas,

$$cRT\mathbf{d}_i = \nabla p_i - \rho_i \mathbf{f}_i + k_i\left(-\nabla p + \rho \mathbf{f}\right) \tag{6.114}$$

or, since $p_i = X_i p$,

$$cRT\mathbf{d}_i = p\nabla X_i + \left(X_i - k_i\right)\nabla p - \rho_i\left(\mathbf{f}_i - \frac{k_i}{Y_i}\mathbf{f}\right) \tag{6.115}$$

When $k_i = Y_i$, the classic form by **Lightfoot** is recovered.

To the author's knowledge, as matters rest right now, these relations have some important Limitations:

1. There is no experimental evidence that unbalance of shear stress causes mass diffusion, as suggested by Eq. (6.112).
2. There is no evidence that the constitutive relations presented above, Eqs. (6.108) and (6.109) are valid, or, under what circumstances they are valid.
3. The HVMF hypothesis, given by Eq. (6.110), although reasonable, has no direct evidence.

Therefore, in the developments that follow, Eq. (6.78),

$$\boxed{\frac{cRT\mathbf{d}_i}{\rho_i} = \nabla_{T,p}\mu_i + v_i \nabla p - \mathbf{f}_i}$$

will be used, knowing that, with all the consequences,

$$\sum_{i=1}^{N_c} \mathbf{d}_i = \frac{1}{cRT}(\nabla p - \rho \mathbf{f}) \tag{6.116}$$

For creeping flow, *du/dt = 0*, this results in

$$\sum_{i=1}^{N_c} \mathbf{d}_i = -\frac{1}{cRT}\nabla.\mathrm{S} \tag{6.117}$$

One of the important consequences is that Eq. (5.149) is no longer valid, since definition (5.148) can no longer be used. Therefore, the **derivation of the Maxwell-Stefan equation will become a purely mechanical derivation**, based only on drag arguments. Since heat transfer will not be addressed on the remaining, there is no need to discuss the implications in the definition of the heat transfer vector by diffusion.

In the following, the mass transport in multiphase porous media is reviewed with the aim of modeling mass transport in the MEA of fuel cells.

Part III

Multicomponent, multiphase modeling of heat and mass transfer in porous layers of PEM fuel cells

The objectives of this third part are to review the modeling of mass transport in porous media, to develop a general Maxwell-Stefan model for two phase flow and mass diffusion in porous media and to apply this model to the basic mass transfer processes that occur in the porous layers and membrane in PEM fuel cells.

Initially, the theories for mass transfer in porous media are reviewed, with emphasis on the theories derived from the Maxwell-Stefan approach. Then, from the general expression for the Maxwell-Stefan mass diffusion, a general model for two-phase flow in porous media is developed. Applications to simpler mass transfer processes are presented and used to elucidate the role of the bulk flow and the pressure gradient.

7 MODELING OF TRANSPORT IN POROUS MEDIA

Here the emphasis is on low Reynolds and low Peclet number. The low Reynolds number ensures that non-linear effects on the momentum equation for the flow in porous medium can be neglected. The low Peclet number ensures that dispersion effects become negligibly small when compared to diffusion effects

7.1 VOLUME –AVERAGE MODELS

The system under consideration is formed by three phases: a solid (phase σ) and two fluid phases (phases β and γ). In the fuel cell applications, the fluid phases are liquid and gas. The pore space is occupied by the liquid and gas phases. The porosity ε is the ratio of the volume of pore space divided by the total volume of the mixture,

$$\varepsilon = \frac{V_P}{V}. \tag{7.1}$$

The volume fraction ε_α of each phase α is defined as

$$\varepsilon_\alpha = \frac{V_\alpha}{V}. \tag{7.2}$$

For $\alpha = \beta, \gamma, \sigma,$ the volume fraction of each phase is related to the porosity ε and the liquid water saturation S by

$$\begin{aligned} \varepsilon_\sigma &= 1-\varepsilon \\ \varepsilon_\beta &= S\varepsilon \\ \varepsilon_\gamma &= (1-S)\varepsilon \end{aligned} \tag{7.3}$$

where the saturation S is defined as the ratio of the volume occupied by the liquid phase and the total volume of the pore space. The conservation of the total volume leads to $\varepsilon_\sigma + \varepsilon_\beta + \varepsilon_\gamma = 1$.

Within each phase α, each species i occupies a mass fraction $Y_{i,\alpha}$ and a mole fraction $X_{i,\alpha}$, following the common relation

$$X_{i,\alpha} = Y_{i,\alpha}\frac{M_\alpha}{M_i} \tag{7.4}$$

where M_i is the molar mass of species i (kg/kmol) and M_α is the molar mass of phase α. In general, the $b_{i,\alpha}$ averaged velocity of phase α, denoted $\mathbf{u}_\alpha^b$, is defined as

$$\mathrm{u}_\alpha^b = \sum_{i=1}^{N_\alpha} b_{i,\alpha}\mathrm{u}_{i,\alpha} \tag{7.5}$$

where $b_{i,\alpha}$ is the averaging weight. When $b_{i,\alpha} = Y_{i,\alpha}$ the mass averaged velocity u_α, or barycentric velocity, is recovered.

The *volume-averaged* of a property ψ_i^α for species i in phase α is defined as

$$\left\langle \psi_{i,\alpha} \right\rangle = \frac{1}{V}\int_V \psi_{i,\alpha} dV \tag{7.6}$$

and the phasic (or, intrinsic) volume-averaged is denoted as

$$\left\langle \psi_{i,\alpha} \right\rangle^\alpha = \frac{1}{V_\alpha}\int_V \psi_{i,\alpha} dV \tag{7.7}$$

Therefore, the relation between volume-averaged and phasic volume-averaged properties for phase α is

$$\left\langle \psi_{i,\alpha} \right\rangle = \varepsilon_\alpha \left\langle \psi_{i,\alpha} \right\rangle^\alpha \tag{7.8}$$

The phase property $\psi_{i,\alpha}$ may be decomposed into an average and a fluctuation following (GRAY, 1975)

$$\psi_{i,\alpha} = \left\langle \psi_{i,\alpha} \right\rangle^\alpha + \widetilde{\psi}_{i,\alpha} \tag{7.9}$$

The volume-averaging theory requires that

$$\left\langle \tilde{\psi}_{i,\alpha} \right\rangle = 0 \tag{7.10}$$

Two important theorems allow for the volume-averaging of the local point-wise conservation equations. The *volume-averaging theorem* applied to a property in phase β is

$$\left\langle \nabla \psi_{i,\beta} \right\rangle = \nabla \left\langle \psi_{i,\beta} \right\rangle + \frac{1}{V}\int_{A_{\beta\sigma}} \mathrm{n}_{\beta\sigma}\psi_{i,\beta} dA + \frac{1}{V}\int_{A_{\beta\gamma}} \mathrm{n}_{\beta\gamma}\psi_{i,\beta} dA \tag{7.11}$$

where n_{kl} is the normal unit vector in the interfacial area A_{kl} pointed from k to l. **The *general Reynolds transport theorem*** is

$$\left\langle \frac{\partial \psi_{i,\beta}}{\partial t} \right\rangle = \frac{\partial \left\langle \psi_{i,\beta} \right\rangle}{\partial t} - \frac{1}{V} \int_{A_{\beta\sigma}} \mathrm{n}_{\beta\sigma} \cdot \mathrm{w}_{\beta\sigma} \psi_{i,\beta} dA - \frac{1}{V} \int_{A_{\beta\gamma}} \mathrm{n}_{\beta\gamma} \cdot \mathrm{w}_{\beta\gamma} \psi_{i,\beta} dA \quad (7.12)$$

where w_{kl} is the velocity vector of the interfacial area A_{kl}. The integrals appearing above express the interfacial phenomena characteristic of transport in porous media. When the solid phase is assumed stationary, $\mathrm{w}_{\beta\sigma} = 0$. Applying the volume-averaged theorem Eq. (7.11) for $\psi_{i,\beta} = 1$ leads to the important result

$$\nabla \varepsilon_\beta = -\frac{1}{V} \int_{A_\beta} \mathrm{n}_\beta dA \quad (7.13)$$

where $A_\beta = A_{\beta\sigma} + A_{\beta\gamma}$ and n_β represents either $\mathrm{n}_{\beta\sigma}$ or $\mathrm{n}_{\beta\gamma}$.

The usual framework to obtain the volume-averaged equations is (WHITAKER, 1999):

1. Write the point-wise conservation equations and respective boundary conditions.
2. Apply the volume-averaged theorem Eq. (7.11) to the conservation equations and use the boundary conditions to transform the integrands in the area integrals.
3. Transform the volume-averaged variables appearing in the volume-averaged transport equations to intrinsic volume-averaged variables using relations (7.8).
4. Use Gray's decomposition, Eq. (7.9), and express the local variables remaining in the area integrals in terms of intrinsic averages and fluctuations.
5. Postulate transformations between the intrinsic volume-averaged variables and the fluctuations, usually in the form of linear combination of averages, difference of averages and gradient of averages. Higher order effects are usually neglected, since the problem can easily escalate and become intractable. The results are the volume- averaged equations and the definitions of the effective coefficients.
6. Define closure problems and obtain the closure equations from the point-wise and volume-averaged conservation equations. The closure equations are usually stationary.
7. Solve the closure equations in deterministic, usually periodic, simple structures, in order to obtain the values of the effective coefficients.

8. Solve the volume-averaged equations to a problem of interest and compare to measurements, or detailed (**DNS**) solutions.

This general framework has been very successful in dealing with problems progressively more complicated, as shown mainly by the works of Whitaker (1999), Quintard (2006) and co-workers. Here, only general results pertaining to volume-averaged models are reviewed. For developments the reader can consult the references cited.

7.1.1 Single-phase, multicomponent flow

Here, the medium is composed of a solid phase σ and a single component fluid phase β. The solid is assumed stationary. In the absence of chemical reaction, the formulation for a single-phase flow of a multi-component mixture within a porous medium becomes: *Conservation of mass of mixture*

$$\frac{\partial \varepsilon_\beta \left\langle \rho_\beta \right\rangle^\beta}{\partial t} + \nabla \cdot \left(\varepsilon_\beta \left\langle \rho_\beta \right\rangle^\beta \left\langle \mathbf{u}_\beta \right\rangle^\beta \right) = 0 \tag{7.14}$$

Conservation of mass specie i

$$\frac{\partial \varepsilon_\beta \left\langle \rho_\beta \right\rangle^\beta \left\langle Y_{i,\beta} \right\rangle^\beta}{\partial t} + \nabla \cdot \left(\varepsilon_\beta \left\langle \rho_\beta \right\rangle^\beta \left\langle Y_{i,\beta} \right\rangle^\beta \left\langle \mathbf{u}_\beta \right\rangle^\beta \right) = -\nabla \cdot \left\langle \mathbf{j}_{i,\beta} \right\rangle^\beta \tag{7.15}$$

Mixture momentum equation

$$\varepsilon_\beta \left\langle \mathbf{u}_\beta \right\rangle^\beta = -\frac{\mathbf{K}}{\mu} \cdot \left(\nabla \left\langle p_\beta \right\rangle^\beta - \left\langle \rho_\beta \right\rangle^\beta \mathbf{g} \right) \tag{7.16}$$

where $\mathbf{K}$ is the permeability tensor.

The treatment of the diffusion flux follows two lines. A generalized Fick formulation provides

$$\left\langle \mathbf{j}_{i,\beta} \right\rangle^\beta = -\sum_{j=1}^{N-1} \varepsilon_\beta \left\langle \rho_\beta \right\rangle^\beta \left\langle D_{eff,ij} \right\rangle^\beta \nabla \left\langle Y_{j,\beta} \right\rangle^\beta \tag{7.17}$$

constrained to

$$\sum_{i=1}^{N} \left\langle \mathbf{j}_{i,\beta} \right\rangle^\beta = \sum_{i=1}^{N} \nabla \left\langle Y_{i,\beta} \right\rangle^\beta = 0 \tag{7.18}$$

The effective Fick diffusion coefficients $\left\langle D_{eff,ij} \right\rangle^\beta$ are either modeled, an instance in which the summation of diffusion fluxes may not be exactly zero, or obtained from the Stefan-Maxwell equations (QUINTARD et al., 2006)

7.1.1.1 Quintard et al. (2006)

The work by Quintard et al. (2006) allows an appreciation of the dispersion effects on diffusion. Quintard et al. (2006) start from a Maxwell-Stefan formulation for the pore level, invert the equations to obtain a generalized Fick formulation and then volume-average the resulting conservation of mass of the species, obtaining volume-averaged equations:

Conservation of mass of mixture in phase β

$$\frac{\partial \varepsilon_\beta \left\langle \rho_\beta \right\rangle^\beta}{\partial t} + \nabla \cdot \varepsilon_\beta \left\langle \rho_\beta \right\rangle^\beta \left\langle \mathbf{u}_\beta \right\rangle^\beta = 0 \tag{7.19}$$

Conservation of mass of species i

$$\frac{\partial}{\partial t}\left(\varepsilon_\beta \left\langle \rho_\beta \right\rangle^\beta \left\langle Y_{i,\beta} \right\rangle^\beta\right) + \nabla \cdot \left(\varepsilon_\beta \left\langle \rho_\beta \right\rangle^\beta \left\langle Y_{i,\beta} \right\rangle^\beta \left\langle \mathbf{u}_\beta \right\rangle^\beta\right) = \nabla \cdot \left(\varepsilon_\beta \left\langle \rho_\beta \right\rangle^\beta \left(\left[\mathbf{D}_{eff}\right] + \left[\mathbf{D}^m\right]\right) \cdot \left(\nabla \left\langle Y_\beta \right\rangle^\beta\right)\right) \tag{7.20}$$

Mixture momentum equation

$$\varepsilon_\beta \left\langle \mathbf{u}_\beta \right\rangle^\beta = -\frac{\mathbf{K}_\beta}{\mu_\beta} \cdot \left(\nabla \left\langle p_\beta \right\rangle^\beta - \left\langle \rho_\beta \right\rangle^\beta \mathbf{g}\right) \tag{7.21}$$

In the conservation of mass equation $\left[\mathbf{D}_{eff}\right]$ and $\left[\mathbf{D}^m\right]$ are, respectively, the (N − 1)×(N − 1) effective diffusivity and dispersion matrices and $\left(\nabla \left\langle Y_{i,\beta} \right\rangle^\beta\right)$ is the grandient of mass fraction column vector.

For diluted mixtures, the convective effect becomes negligible and Quintard et al. (2006) show that $\left[\mathbf{D}^m\right] = 0$ and

$$\left[\mathrm{D}_{eff}\right] = \left[D_\beta\right]\frac{\mathrm{I}}{\tau} \tag{7.22}$$

where τ is the classical tortuosity. In this case, a single value of tortuosity applies to all chemical species.

They show also that in the linear dispersion regime, i.e., when the dispersion depends linearly on the Peclet number, for isotropic media, a simple dispersion term may be added to the diagonal of the effective diffusivity matrix. This longitudinal dispersion term has the form

$$\left[\mathbf{D}^m\right] = \alpha_L \left\langle \mathbf{u}_\beta \right\rangle^\beta \mathbf{I}$$

where α_L is a constant.

Outside this linear regime, however, the calculation of the dispersion matrix becomes complicated, and no general conclusions are obtained. The authors do show, however, that for high Peclet number the solution of the full closure problem becomes necessary.

7.1.1.2 Stockie et al. (2001)

They considered low Reynolds and low Peclet number single phase, ternary flow in the cathode of a PEM fuel cell and postulated in an *ad-hoc* manner:

Conservation of mass of mixture

$$\frac{\partial \rho}{\partial t} + \nabla \cdot \rho \langle \mathbf{u} \rangle = 0 \tag{7.23}$$

Conservation of mass of species i

$$\frac{\partial \langle c_i \rangle}{\partial t} + \nabla \cdot \langle c_i \rangle \langle \mathbf{u} \rangle = -\nabla \cdot \langle \overline{\mathbf{j}_i} \rangle \tag{7.24}$$

Mixture momentum equation

$$\langle \mathbf{u} \rangle = -\frac{\mathbf{K}}{\mu} \cdot \nabla \langle p \rangle \tag{7.25}$$

where $\mathbf{K}$ is the permeability tensor.

In their formulation, $\langle \mathbf{u} \rangle$ is the barycentric velocity,

$$\rho \langle \mathbf{u} \rangle = \sum_{i=1}^{3} \rho_i \langle \mathbf{u}_i \rangle \tag{7.26}$$

and $\langle \overline{\mathbf{j}_i} \rangle$ is the molar diffusion flux in respect to the barycentric velocity,

$$\langle \overline{\mathbf{j}_i} \rangle = \langle c_i \rangle \left(\langle \mathbf{u}_i \rangle - \langle \mathbf{u} \rangle \right) \tag{7.27}$$

The molar diffusion flux in respect to the molar averaged velocity

$$c \langle \overline{\mathbf{u}} \rangle = \sum_{i=1}^{3} \langle c_i \rangle \langle \mathbf{u}_i \rangle \tag{7.28}$$

is

$$\langle \overline{\mathbf{J}_i} \rangle = \langle c_i \rangle \left(\langle \mathbf{u}_i \rangle - \langle \overline{\mathbf{u}} \rangle \right). \tag{7.29}$$

They are transformed according to:

$$\left\langle \overline{\mathbf{j}_i} \right\rangle = \left[B_{ij} \right] \left\langle \overline{\mathbf{J}_i} \right\rangle . \tag{7.30}$$

Stockie et al. (2001) obtain the Fick diffusion flux from the Maxwell-Stefan fluxes. In matrix form, this gives.

$$\left(\left\langle \overline{\mathbf{j}_i} \right\rangle \right) = -c \left[B_{ij} \right] \left[D_{ij} \right] \left(\boldsymbol{\nabla} \left\langle X_i \right\rangle \right) \tag{7.31}$$

Then, for a ternary mixture, the two equations for the conservation of mass of species 1 and 2 are

$$\frac{\partial c \left\langle X_1 \right\rangle}{\partial t} + \boldsymbol{\nabla} \cdot c \left\langle X_1 \right\rangle \left\langle \mathbf{u} \right\rangle = \boldsymbol{\nabla} \cdot c \left(\breve{D}_{11} \boldsymbol{\nabla} \left\langle X_1 \right\rangle + \breve{D}_{12} \boldsymbol{\nabla} \left\langle X_2 \right\rangle \right) \tag{7.32}$$

$$\frac{\partial c \left\langle X_2 \right\rangle}{\partial t} + \boldsymbol{\nabla} \cdot c \left\langle X_2 \right\rangle \left\langle \mathbf{u} \right\rangle = \boldsymbol{\nabla} \cdot c \left(\breve{D}_{21} \boldsymbol{\nabla} \left\langle X_1 \right\rangle + \breve{D}_{22} \boldsymbol{\nabla} \left\langle X_2 \right\rangle \right) \tag{7.33}$$

the mole fraction of species 3 is given by

$$\left\langle X_3 \right\rangle = 1 - \left\langle X_1 \right\rangle - \left\langle X_2 \right\rangle \tag{7.34}$$

and from the ideal gas law

$$\left\langle p \right\rangle = cRT \tag{7.35}$$

Equations (7.23), (7.25), (7.32), (7.33), (7.34) and (7.35) form a closed system of 6 equations for 6 unknowns, $\left\langle X_1 \right\rangle$, $\left\langle X_2 \right\rangle$, c, $\left\langle \rho \right\rangle$, $\left\langle p \right\rangle$ and $\left\langle \mathbf{u} \right\rangle$.

Stockie et al. (2001) continued assuming an isothermal ideal-gas mixture and writing

$$\boldsymbol{\nabla} \left\langle p \right\rangle = RT \boldsymbol{\nabla} c . \tag{7.36}$$

Then, using

$$\frac{\left\langle \rho \right\rangle}{\left\langle c \right\rangle} = \sum_{i=1}^{3} M_i \left\langle X_i \right\rangle = M_3 \left[1 - \left(1 - \frac{M_1}{M_3} \right) \left\langle X_1 \right\rangle - \left(1 - \frac{M_2}{M_3} \right) \left\langle X_2 \right\rangle \right]$$

the momentum equation becomes

$$\left\langle \mathbf{u} \right\rangle = -\frac{RT\mathbf{K}}{\mu} \cdot \left[\xi_1 \boldsymbol{\nabla} \left\langle X_1 \right\rangle + \xi_2 \boldsymbol{\nabla} \left\langle X_2 \right\rangle + \xi_\rho \boldsymbol{\nabla} \left\langle \rho \right\rangle \right] \tag{7.37}$$

Therefore, substituting in the conservation of mass of species i, term expressing diffusion as a function of pressure appears, besides the convective flow driven by $\boldsymbol{\nabla} \left\langle \rho \right\rangle$. For ideal gases, the dynamic

viscosity is independent of pressure and proportional to a power of the temperature, ranging from 1/2 to 1. Therefore, the magnitude of the Darcy diffusion term is proportional to pressure and inversely proportional to temperature.

7.1.2 Two-phase, immiscible, single component flow

Whitaker (1986) uses the volume-averaging of the local flow equations to arrive at the upscaled macroscopic equations. The local flow is modeled as an incompressible viscous, i.e., Stokes, flow of immiscible fluids and the interfaces are assumed in local mechanical equilibrium. The fluid phases are denoted as β and γ, let's say, gas and liquid, while the solid phase is denoted as σ. The volume fractions are constrained by

$$\varepsilon_\beta + \varepsilon_\gamma + \varepsilon_\sigma = 1 \tag{7.38}$$

The solid is stationary $\left(\langle \mu_\sigma \rangle = 0\right)$ He arrives at:

Conservation of mass of phase β

$$\frac{\partial \varepsilon_\beta}{\partial t} + \nabla \cdot \langle \mathbf{u}_\beta \rangle = 0 . \tag{7.39}$$

Conservation of mass of phase γ

$$\frac{\partial \varepsilon_\gamma}{\partial t} + \nabla \cdot \langle \mathbf{u}_\gamma \rangle = 0 . \tag{7.40}$$

Flow velocity for phase β

$$\langle \mathbf{u}_\beta \rangle = -\frac{\mathbf{K}_\beta}{\mu_\beta} \cdot \left(\nabla \langle p_\beta \rangle^\beta - \rho_\beta \mathbf{g} \right) + \mathbf{K}_{\beta\gamma} \cdot \langle \mathbf{u}_\gamma \rangle , \tag{7.41}$$

where $\mathbf{K}_\beta$ is the permeability tensor for *phase β.*

Flow velocity for phase γ

$$\langle \mathbf{u}_\gamma \rangle = -\frac{\mathbf{K}_\gamma}{\mu_\gamma} \cdot \left(\nabla \langle p_\gamma \rangle^\gamma - \rho_\gamma \mathbf{g} \right) + \mathbf{K}_{\gamma\beta} \cdot \langle \mathbf{u}_\beta \rangle , \tag{7.42}$$

where $\mathbf{K}_\gamma$ is the permeability tensor for *phase γ*

The volume-averaged *capillary pressure* across the interfaces is modeled as

$$\langle p_C \rangle = \langle p_\beta \rangle^\beta - \langle p_\gamma \rangle^\gamma = 2\sigma \langle H \rangle_{\beta\gamma} , \tag{7.43}$$

where $\langle H \rangle_{\beta\gamma}$ is the area-averaged curvature of the menisci. The sign of $\langle p_C \rangle$ depends on the relative wettability of the β and γ phases. This relation is shown to be an approximation valid for

$$\frac{\mu_\alpha \langle \mathbf{u}_\alpha \rangle^\alpha}{\sigma \langle H \rangle_{\beta\gamma} l_\alpha} \ll 1 \tag{7.44}$$

where α represents the fluid with the largest number defined above. This restriction is equivalent to assuming small capillary numbers.

The tensors $\mathbf{K}_{\gamma\beta}$ and $\mathbf{K}_{\beta\gamma}$ account for the effect of the viscous drag among the γ and β phases. They become important when μ_γ approaches μ_β. For gas and liquid phases, $\mu_\gamma \ll \mu_\beta$ and they can probably be neglected. However, an order of magnitude analysis shows that for thin films of gas, $l_\beta \ll l_\gamma$ where l_α is a characteristic film thickness for phase α, this term may become important. This occurs near the threshold for gas phase percolation, i.e., at the irreducible saturation for the gas phase.

For single-phase, we have

$$\langle \mathbf{u}_\beta \rangle = -\frac{\mathbf{K}_\beta}{\mu_\beta} \cdot \left(\nabla \langle p_\beta \rangle^\beta - \rho_\beta \mathbf{g} \right) \tag{7.45}$$

For one-dimensional flow, we usually write

$$K_\beta = k_{r,\beta} K \tag{7.46}$$

where $k_{r,\beta}$ is the relative permeability. There is no guarantee that this applies equally to multidimensional flow in anisotropic media, i.e., $\mathbf{K}_\beta \overset{?}{=} k_{r,\beta}\mathbf{K}$ proposed (Kaviany, 1995).

The equations including phase change are obtained by extending the above equations to include a volumetric source term. (WANG and BECKERMAN, 1993; STOCKIE et al., 2001). For *two incompressible phases*, the equations can be written as:

Conservation of mass of phase β

$$\rho_\beta \left(\frac{\partial \varepsilon_\beta}{\partial t} + \nabla \cdot \langle \mathbf{u}_\beta \rangle \right) = \langle \dot{m}_{\beta\gamma} \rangle \tag{7.47}$$

where $\langle \dot{m}_{\beta\gamma} \rangle$ is the volume-averaged β phase change or chemical reaction.

Conservation of mass of phase γ

$$\rho_\gamma \left(\frac{\partial \varepsilon_\gamma}{\partial t} + \nabla \cdot \langle \mathbf{u}_\gamma \rangle \right) = \langle \dot{m}_{\gamma\beta} \rangle \tag{7.48}$$

where $\langle \dot{m}_{\gamma\beta} \rangle$ is the volume-averaged γ phase change or chemical reaction, $\langle \dot{m}_{\beta\gamma} \rangle = -\langle \dot{m}_{\gamma\beta} \rangle$.

Wang and Beckerman (1993) neglect the cross effects, $\mathbf{K}_{\beta\gamma} = \mathbf{K}_{\gamma\beta} = 0$ and assume isotropic medium:

Flow velocity for phase β

$$\langle \mathbf{u}_\beta \rangle = -\frac{k_{r,\beta} K}{\mu_\beta} \left(\nabla \langle p_\beta \rangle^\beta - \rho_\beta \mathbf{g} \right) \tag{7.49}$$

Flow velocity for phase γ

$$\langle \mathbf{u}_\gamma \rangle = -\frac{k_{r,\gamma} K}{\mu_\gamma} \cdot \left(\nabla \langle p_\gamma \rangle^\gamma - \rho_\gamma \mathbf{g} \right) \tag{7.50}$$

They also assume

$$\langle p_C \rangle = \langle p_\beta \rangle^\beta - \langle p_\gamma \rangle^\gamma = 2\sigma \langle H \rangle_{\beta\gamma} \tag{7.51}$$

where $\langle H \rangle_{\beta\gamma} = f(\varepsilon_\gamma)$. Since they are interested in liquid-gas flows,

$$\varepsilon_\beta = \varepsilon S, \qquad \varepsilon_\gamma = \varepsilon (1 - S) \tag{7.52}$$

where S is the liquid saturation and ε is the porosity of the porous medium. Conservation of volume requires $\varepsilon_\beta + \varepsilon_\gamma = \varepsilon$. When ε is constant, S becomes the variable that defines the phase distribution.

The *total fluid mass flux*, i.e., the flow rate of the multiphase flow per unit area of porous medium, is given as

$$G = \rho \langle \mathbf{u} \rangle = \rho_\beta \langle \mathbf{u}_\beta \rangle + \rho_\gamma \langle \mathbf{u}_\gamma \rangle \tag{7.53}$$

where the averaged fluid density is

$$\varepsilon \rho = \varepsilon_\beta \rho_\beta + \varepsilon_\gamma \rho_\gamma \tag{7.54}$$

or

$$\rho = \rho_\beta S + \rho_\gamma (1 - S) \tag{7.55}$$

The equations above, once $\langle \dot{m}_{\beta\gamma} \rangle$ and the two-phase functions $\langle H \rangle_{\beta\gamma}$, $k_{r,\beta}$ and $k_{r,\gamma}$ are known from modeling, form a system of 5 equations for the unknown $\langle p_\beta \rangle^\beta$, $\langle p_\gamma \rangle^\gamma$, $\langle \mathbf{u}_\gamma \rangle$, $\langle \mathbf{u}_\beta \rangle$ and *S*.

7.1.2.1 Wang and Beckerman (1993)

Wang and Beckerman (1993) proceeded to transform this into a system of three only equations.

The *conservation of mass* of fluid is obtained by adding the equations of conservation of mass for each phase, resulting in

$$\varepsilon \frac{\partial \rho}{\partial t} + \nabla \cdot \rho \langle \mathbf{u} \rangle = 0 \tag{7.56}$$

where the porosity ε is assumed constant. This equation can be used to solve for ρ once the averaged velocity is known.

They then proceed to develop a single transport equation for the liquid saturation. For that, they write an expression for the total flow rate, in the absence of gravity, in terms of equivalent pressure $\langle p \rangle$ and effective kinematic viscosity ν defined by the mixture Darcy equation.

$$\rho \langle \mathbf{u} \rangle = -\frac{K}{\nu} \nabla \langle p \rangle . \tag{7.57}$$

From the phase velocities, this equality implies that

$$\frac{1}{\nu} \nabla \langle p \rangle = \frac{k_{r,\beta}}{\nu_\beta} \nabla \langle p_\beta \rangle^\beta + \frac{k_{r,\gamma}}{\nu_\gamma} \nabla \langle p_\gamma \rangle^\gamma \tag{7.58}$$

Relative mobilities are defined as

$$\lambda_\beta = \nu \frac{k_{r,\beta}}{\nu_\beta}, \qquad \lambda_\gamma = \nu \frac{k_{r,\gamma}}{\nu_\gamma} \tag{7.59}$$

such that the gradient of total pressure becomes

$$\nabla \langle p \rangle = \lambda_\beta \nabla \langle p_\beta \rangle^\beta + \lambda_\gamma \nabla \langle p_\gamma \rangle^\gamma \tag{7.60}$$

From the definition of capillary pressure, and assuming that $\lambda_\beta + \lambda_\gamma = 1$, or,

$$\frac{1}{\nu} = \frac{k_{r,\beta}}{\nu_\beta} + \frac{k_{r,\gamma}}{\nu_\gamma} \tag{7.61}$$

two equivalent relations are obtained

$$\nabla\langle p\rangle = \nabla\langle p_\beta\rangle^\beta - \lambda_\gamma \nabla\langle p_c\rangle \tag{7.62}$$

$$\nabla\langle p\rangle = \nabla\langle p_\gamma\rangle^\gamma - \lambda_\beta \nabla\langle p_c\rangle \tag{7.63}$$

Neglecting the possibility of hysteresis, they argue that

$$d\langle p\rangle = \frac{\partial\langle p\rangle}{\partial\langle p_\gamma\rangle^\gamma} d\langle p_\gamma\rangle^\gamma + \frac{\partial\langle p\rangle}{\partial\langle p_\beta\rangle^\beta} d\langle p_\beta\rangle^\beta \tag{7.64}$$

From the relations above,

$$d\langle p\rangle = \left[\left(\frac{\partial\langle p\rangle}{\partial\langle p_c\rangle}\right)_{\langle p_\gamma\rangle^\gamma} - \left(\frac{\partial\langle p\rangle}{\partial\langle p_c\rangle}\right)_{\langle p_\beta\rangle^\beta}\right] d\langle p_c\rangle = (\lambda_\gamma - \lambda_\beta) d\langle p_c\rangle \tag{7.65}$$

Integration along $\langle p_c\rangle$ from $\langle p_c\rangle(S=1)=0$ to $\langle p_c\rangle(S)$, gives

$$\langle p\rangle = \langle p\rangle_0 + \int_0^{\langle p_c\rangle(S)} (\lambda_\gamma - \lambda_\beta) d\xi \tag{7.66}$$

This equation must satisfy:

$$\begin{aligned} S \to 1 &\Rightarrow k_{r,\beta} \to 0 \Rightarrow \langle p\rangle \to \langle p_\gamma\rangle^\gamma \\ S \to 1 &\Rightarrow k_{r,\gamma} \to 0 \Rightarrow \langle p\rangle \to \langle p_\beta\rangle^\beta \end{aligned} \tag{7.67}$$

This is satisfied when

$$\langle p\rangle = \frac{\langle p_\gamma\rangle^\gamma + \langle p_\beta\rangle^\beta}{2} + \frac{1}{2}\int_0^{\langle p_c\rangle(S)} (\lambda_\gamma - \lambda_\beta) d\xi \tag{7.68}$$

Using these concepts they arrive at a multiphase mixture equation that describes the total flow as a convection-diffusion transport problem. Starting from the conservation of the liquid phase, substituting $\langle \mathbf{u}_\gamma\rangle$, the relation between $\nabla\langle p_\beta\rangle^\beta$ and $\nabla\langle p\rangle$, and using $\varepsilon_\gamma = \varepsilon S$, they find,

$$\rho_\gamma \varepsilon \frac{\partial S}{\partial t} + \nabla\cdot\lambda_\gamma \rho\langle \mathbf{u}\rangle = -\nabla\cdot\mathbf{j} + \langle \dot{m}_{\gamma\beta}\rangle \tag{7.69}$$

where $\mathbf{j}$ is a diffusive flux given by

$$\mathbf{j} = -D_S \nabla S + \rho\mathbf{f} \tag{7.70}$$

with

$$Ds = -\frac{K\lambda_\gamma(1-\lambda_\gamma)}{\nu}\frac{\partial\langle p_c\rangle}{\partial S} \tag{7.71}$$

$$\rho \mathbf{f} = \frac{\lambda_\gamma \rho_\gamma K}{\nu} \mathbf{g} \tag{7.72}$$

This becomes a convective-diffusive equation for the saturation S, which replaces the conservation of the mass of liquid. The body force appears as a driving force for diffusion, as part of the mass diffusion flux. The convective term is scaled by a mobility parameter which depends on a ratio of permeabilities. The form of equation (7.69) is amenable for solution using computer codes written for the conservative form of the species transport equation.

A *total momentum equation* is also obtained along the same lines. Adding up the phase momentum equations, one obtains

$$\rho \langle \mathbf{u} \rangle = -\frac{K}{\nu} \left[\nabla \langle p_c \rangle - \left(\lambda_\gamma \rho_\gamma + \lambda_\beta \rho_\beta \right) \mathbf{g} \right] \tag{7.73}$$

which is essentially an equation for $\rho \langle \mathbf{u} \rangle$.

Equations (7.56), (7.69) and (7.73) form a system of 3 equations for the unknowns S, $\rho \langle \mathbf{u} \rangle$ and $\langle p \rangle$. During this homogenization process, the phase information is not lost. The phase velocities can be recovered from

$$\rho_\gamma \langle \mathbf{u}_\gamma \rangle = \lambda_\gamma \rho \langle \mathbf{u} \rangle + \mathbf{j} \tag{7.74}$$

$$\rho_\beta \langle \mathbf{u}_\beta \rangle = \lambda_\beta \rho \langle \mathbf{u} \rangle + \mathbf{j} \tag{7.75}$$

and the phase pressures can be calculated from the respective phase-momentum equations. The authors proceed to develop a mixture energy equation, but this is beyond the objective of this section. They claim that the important advantages of their model is the reduction of the number of equations to be solved by almost half and the transformation of the formulation into equations the behavior if which can be easily interpreted and solved using well known algorithms. The explicit representation of the capillary driven flow as a diffusive transport, as noted before by several authors in the context of moisture movement in porous media, is also an advantage in terms of comparison to older models (PHILLIP and DE VRIES, 1957).

7.1.3 Two-phase, miscible, multi-component flow

Soulaine et al. (2011) derive equations for the multicomponent mass transport in two- phase flow in porous media. They start from the

conservation of mass of species applied to the pore level assuming a mixture Fick model and incompressible viscous, i.e., low Reynolds, flow. Chemical reaction is neglected. At the phase interfaces, a linear relation among the molar fractions, as in **Raoult´s and Henry´s laws**, describing chemical equilibrium is used. This equilibrium relation is expressed in mass fractions in the form

$$Y_{i,\beta} = H_i Y_{i,\gamma}.$$

The equations for the conservation of mass and momentum of both phases remain the same as in the single-component two-phase flow. The equation for the conservation of mass of species i in phases β and γ assumes a complicated form that requires the solution of transient closure problems. The final form of the closure problems depend on the phase interface velocity and its interaction with the velocity and mass fraction fluctuations, becoming rather complicated. A simpler form of the final equation is obtained when the closure problem is formulated under the assumption of incompressible fluids and stationary interface.

In this situation, they obtain the *conservation of mass* of species i in phase β as

$$\begin{aligned}
&\frac{\partial}{\partial t}\left(\varepsilon_\beta \langle \rho_\beta \rangle^\beta \langle Y_{i,\beta} \rangle^\beta\right) + \\
&\nabla\cdot\left(\varepsilon_\beta \langle \rho_\beta \rangle^\beta \langle Y_{i,\beta} \rangle^\beta \langle \mathbf{u}_\beta \rangle^\beta\right) + \\
&\nabla\cdot\left[\varepsilon_\beta \langle \rho_\beta \rangle^\beta \mathbf{E}_\beta\left(H_i \langle Y_{i,\gamma} \rangle^\gamma - \langle Y_{i,\beta} \rangle^\beta\right)\right] = \\
&\nabla\cdot\left[\varepsilon_\beta \langle \rho_\beta \rangle^\beta [D_{\beta\beta}]\cdot\left(\nabla \langle Y_\beta \rangle^\beta\right)\right] + \nabla\cdot\left[\varepsilon_\beta \langle \rho_\beta \rangle^\beta [D_{\beta\gamma}]\cdot\left(\nabla \langle Y_{i,\gamma} \rangle^\gamma\right)\right] - \langle \dot{m}_{i,\beta\lambda} \rangle
\end{aligned} \tag{7.76}$$

In the third term on the left-hand side, the velocity-like coefficient E_β arises from the mass fraction fluctuation across the phase interface dependence on the volume-averaged mass fraction. The dispersion coefficient $[D_{\beta\beta}]$ retains the usual definition while the dispersion correction coefficient $[D_{\beta\gamma}]$ arises from the mass fraction fluctuation across the phase interface dependence on the volume-averaged mass fraction gradient. These coefficients are evaluated from the solution of stationary, periodic closure problems, formulated in the absence of interfacial mass transport. This still captures the influence of a phase distribution into the mass transfer in the other phase. These simplifications are possible since the closure problem must only capture characteristics of the most

decisive transport mechanism present, in this case, inter-phase mass diffusion.

For phase γ, a similar equation is obtained. An important result for the interfacial mass flux, under the assumptions used, is

$$\left\langle \dot{m}_{i,\beta\lambda} \right\rangle = -\mathbf{u}_{\gamma\beta} \cdot \nabla \left\langle Y_{i,\beta} \right\rangle^{\beta} + \mathbf{u}_{\beta\gamma} \cdot \nabla \left\langle Y_{i,\gamma} \right\rangle^{\gamma} + \alpha_i \left(H_i \left\langle Y_{i,\gamma} \right\rangle^{\gamma} - \left\langle Y_{i,\beta} \right\rangle^{\beta} \right)$$

where $\mathbf{u}_{\gamma\beta}$ and $\mathbf{u}_{\beta\gamma}$ are effective velocities related to the interface flux of species i and α_i is a typical interface (surface convection) mass transfer coefficient, all of them obtained from the closure problem. This shows that the interfacial mass transfer is not only a local effect at the interface, dependent on a local mass transfer coefficient (later term), but also depends (in a complicated way) on the whole β and γ velocity and concentration fields (first two terms).

The authors apply their model to a simple stratified flow in a straight two-dimensional capillary with height L. The geometrical simplicity allows for obtaining closed form analytical solutions for all the effective parameters in the limit $\varepsilon_\beta \ll \varepsilon_\gamma$. In special way, the interface transfer coefficient becomes

$$\frac{1}{\alpha_i} = \frac{L}{3}\left(\frac{H_i \varepsilon_\gamma L}{\rho_\gamma D_{i,\gamma}} + \frac{\varepsilon_\beta L}{\rho_\beta D_{i,\beta}} \right)$$

This relation is equivalent to a classical film theory and defines the characteristic film thicknesses as $L\varepsilon_\beta$ and $L\varepsilon_\gamma$ where L is a characteristic pore length.

7.2 MAXWELL-STEFAN MODELS

Several models, based on a Maxwell-Stefan framework, have been proposed to solve for the transport across membranes. These have broad applications in membrane science, from adsorption to fluid separation, including ultrafiltration and diafiltration. The models are developed to work from molecular (low Knudsen number) to continuum flow (high Knudsen number), using the minimum possible number of adjustable parameters. The starting points are usually **Lightfoot's** development and the dusty gas model of Mason and co-workers (MASON and MALINAUSKAS, 1983). Taylor and Krishna (1993), Kuiken (1994), Kerkhof (1996) and Krishna and Wesselingh (1997)

present thorough reviews of these models. The following review is mostly based on Kerkhof (1996) and Krishna and Wesselingh (1997).

7.2.1 Lightfoot's model

The derivation presented in Kerkhof (1996) is used. The starting point of Lightfoot's model is the Maxwell-Stefan equation. From the dissipation function, without the static mechanical assumption, the Maxwell-Stefan formulation becomes

$$\sum_{k=1,k\neq i}^{N_c} \frac{1}{cD_{ik}}\left(X_i\dot{\mathbf{n}}_k - X_k\dot{\mathbf{n}}_i\right) = \frac{1}{cRT}\left(c_i\nabla_{T,p}\overline{\mu}_i + \phi_i\nabla p - \rho_i\mathbf{f}_i\right) \qquad (7.77)$$

where $\dot{\mathbf{n}}_i = c_i\mathbf{u}_i$ is the molar flux in respect to a stationary reference system (total molar flux).

When the flow within the porous medium is considered, the authors assume that all the fluxes and driving forces are taken as volume-averaged quantities and the concentrations as intrinsic volume-averaged concentrations. The porous medium is assumed as the $N_c + 1$ component denoted *m*. The left-hand side is extended to include this membrane species and the membrane is assumed stationary. Then, we obtain

$$\sum_{k=1,k\neq i}^{N_c} R_{ik}\left(X_i\dot{\mathbf{n}}_k - X_k\dot{\mathbf{n}}_i\right) - R_{i,m}\dot{\mathbf{n}}_i = \frac{1}{cRT}\left(c_i\nabla_{T,p}\overline{\mu}_i + \phi_i\nabla p - \rho_i\mathbf{f}_i\right) \qquad (7.78)$$

where the interspecies and the membrane resistances are $R_{m,i} = X_m/\left(cD_{im}\right) = \beta_{i,m}/c_i$ and $R_{ik} = 1/\left(cD_{ik}\right)$.

7.2.2 Dusty-gas model

The Dusty-Gas applied to a mixture of ideal gases superposes Darcy flow to a generalized form of the Maxwell-Stefan equations to include Knudsen flow. In this model, the walls of the pores are modeled as giant "dust" particles homogeneously dispersed in the fluid continuum. As diffusion occurs, the fluid particles of species *i* experience drag with the remaining species j and with the dust particles. The interspecies drag is modeled using the Stefan-Maxwell diffusivities while the drag with the dust particles is modeled as a Knudsen flow. When the characteristic pore size length d_p is large, i.e., in the limit of small Knudsen number,

$$K_n = \frac{\lambda_m}{d_p} \ll 1 \qquad (7.79)$$

where λ_m is the molecular mean free path, the effect of the dust particles become negligible. The basic hypothesis for the formulation is that the species molar flux can be split in a diffusion contribution and a convective contribution,

$$\dot{\mathbf{n}}_i = \overline{\mathbf{j}}_i + \dot{\mathbf{n}}_{i,v} \tag{7.80}$$

The convective contribution is associated to the bulk pressure-driven flow described by a Darcy relation,

$$\dot{\mathbf{n}}_{i,v} = -\frac{c}{R_m}\left(\nabla p - \rho \mathbf{f}\right) \tag{7.81}$$

where $R_m = \eta / K$ and K is the permeability. In the work of Mason and Malinauskas (1983), all species moved with the same average velocity (a form of HVMF hypothesis) and therefore

$$\dot{\mathbf{n}}_{i,v} = X_i \dot{\mathbf{n}}_v = -\frac{c_i}{R_m}\left(\nabla p - \rho \mathbf{f}\right) \tag{7.82}$$

Later work (MASON and DEL CASTILLO, 1985; MASON and LONSDALE, 1990), writing equations for larger molecules, used a viscous selectivity factor α_i that accounted for the contribution of species i to the total viscous flow. Larger species tend to congregate near the center of the pore, then result in $\alpha_i > 1$, while species that tend to stick at the pore walls result in $\alpha_i < 1$. With this simple model, the relation between the species viscous flow and the mixture viscous flow is assumed as

$$\dot{\mathbf{n}}_{i,v} = \alpha_i X_i \dot{\mathbf{n}}_v = -\alpha_i \frac{c_i}{R_m}\left(\nabla p - \rho \mathbf{f}\right) \tag{7.83}$$

therefore,

$$\dot{\mathbf{n}}_i = \overline{\mathbf{j}}_i + \dot{\mathbf{n}}_{i,v} = \overline{\mathbf{j}}_i - \alpha_i \frac{c_i}{R_m}\left(\nabla p - \rho \mathbf{f}\right) \tag{7.84}$$

The Maxwell-Stefan including Knudsen flow in the pore space is written as an equation for the diffusion flux,

$$\sum_{k=1,k\neq i}^{N-1} \frac{X_i \overline{\mathbf{j}}_k - X_k \overline{\mathbf{j}}_i}{c D_{ik}^e} - \frac{\overline{\mathbf{j}}_i}{c D_{im}^e} = \mathbf{d}_i \tag{7.85}$$

where $\overline{\mathbf{j}}_i$ is the molar diffusion flux in respect to the molar averaged velocity, D_{ik}^e is the Maxwell-Stefan effective diffusivity of species i in k species and D_{im}^e is the Knudsen effective diffusivity of species i in the

dust particles, which are assumed motionless. For ideal gases, the gradient of partial pressure is taken as the correct driving force for diffusion. The Maxwell-Stefan diffusivities are related to the molecular values by a single tortuosity τ.

$$D_{ik}^e = \frac{\varepsilon}{\tau} D_{ik}, \qquad D_{im}^e = \frac{\varepsilon}{\tau} D_{im} \tag{7.86}$$

where ε is the porosity.

Substituting the expression for the total molar flux, Eq. (7.84), into the Maxwell-Stefan equation, Eq. (7.85), they obtain

$$\sum_{k=1,k\neq i}^{N-1} \frac{X_i \dot{\mathbf{n}}_K - X_k \dot{\mathbf{n}}_i}{cD_{ik}^e} - \sum_{k=1,k\neq i}^{N-1} \frac{X_i \dot{\mathbf{n}}_{K,v} - X_k \dot{\mathbf{n}}_{i,v}}{cD_{ik}^e} - \frac{\dot{\mathbf{n}}_i - \dot{\mathbf{n}}_{i,v}}{cD_{im}^e} = \mathbf{d}_i \tag{7.87}$$

Using the expression for $\dot{\mathbf{n}}_{i,v}$, and rewriting the second and third terms,

$$\sum_{k=1,k\neq i}^{N-1} \frac{X_i \dot{\mathbf{n}}_K - X_k \dot{\mathbf{n}}_i}{cD_{ik}^e} - \frac{\dot{\mathbf{n}}_i}{cD_{im}^e} = \mathbf{d}_i + \frac{\alpha_i' X_i}{D_{ik}^e R_m}\left(\nabla p - \rho \mathbf{f}\right) \tag{7.88}$$

where

$$\alpha_i' = \alpha_i + \sum_{k=1,k\neq i}^{N-1} X_k \left(\alpha_i + \alpha_k\right) \frac{D_{im}^e}{D_{ik}^e} \tag{7.89}$$

The driving force for diffusion is obtained from the dissipation function as

$$\mathbf{d}_i = \frac{1}{cRT}\left(c_i \nabla_{T,p} \overline{\mu}_i + \phi_i \nabla p - \rho_i \mathbf{f}_i\right) \tag{7.90}$$

The viscous selectivity appears important for nanofiltration, but can usually be neglected otherwise (BUNGAY and BRENNER, 1973; KRISHNA and WESSELINGH, 1997). For a mixture of ideal gases, neglecting body force,

$$\sum_{k=1,k\neq i}^{N-1} \frac{X_i \dot{\mathbf{n}}_K - X_k \dot{\mathbf{n}}_i}{cD_{ik}^e} - \frac{\dot{\mathbf{n}}_i}{cD_{im}^e} = \nabla X_i + \left(1 + \frac{cRT}{D_{im}^e R_m}\right) \frac{X_i}{cRT} \nabla p \tag{7.91}$$

For a single component fluid,

$$\dot{\mathbf{n}} = -\left(\frac{D_{im}^e}{RT} + \frac{c}{R_m}\right) \nabla p \tag{7.92}$$

The Knudsen term accounts for a slip flux superposed to the viscous flux. When $K_n \ll 1$, $D_{im}^e \to 0$.

7.2.3 Binary friction model

The binary friction model (KERKHOF, 1996) was developed as an alternative to the Dusty Gas Model. He started from the Lightfoot model and modeled the membrane drag resistance as

$$R_{i,m} = \alpha_m \frac{\kappa_i \phi_i}{c_i} = \alpha_m \kappa_i \overline{v}_i \tag{7.93}$$

where α_m depends only on the porous matrix and κ_i is the "*fractional viscosity coefficient*".

Then, the Maxwell-Stefan formulation becomes,

$$\sum_{k=1,k\neq i}^{N_c} \frac{1}{cD_{ik}} \left(X_i \dot{\mathbf{n}}_k - X_k \dot{\mathbf{n}}_i \right) - \alpha_m \kappa_i \phi_i \mathbf{u}_i = \frac{1}{cRT} \left(c_i \nabla_{T,p} \overline{\mu}_i + \phi_i \nabla p - \rho_i \mathbf{f}_i \right) \tag{7.94}$$

Adding up over all species, we obtain

$$-\alpha_m \sum_{i=1}^{N_c} \kappa_i \phi_i \mathbf{u}_i = \frac{1}{cRT} \left(\nabla p - \rho \mathbf{f} \right) \tag{7.95}$$

As above, Darcy's law is written as

$$\dot{\mathbf{n}} = c\mathbf{u} = -\frac{c}{R_m} \left(\nabla p - \rho \mathbf{f} \right) \tag{7.96}$$

where $R_m = \eta / K$ and K is the permeability.

Comparing both equations, we obtain

$$\alpha_m \sum_{i=1}^{N_c} \kappa_i \phi_i \mathbf{u}_i = \frac{R_m}{cRT} \mathbf{u} \tag{7.97}$$

He then uses the homogeneous viscous mixture flow (HVMF) hypothesis and assumes $\mathbf{u} = \mathbf{u}_i$. Then,

$$\eta = \alpha_m K c R T \sum_{i=1}^{N_c} \kappa_i \phi_i \tag{7.98}$$

Taking $\alpha_m = 1/K$, an equation for the mixture viscosity is found as

$$\eta = cRT \sum_{i=1}^{N_c} \kappa_i \phi_i \tag{7.99}$$

Finally, with the understanding that the mixture viscosity has the formula above, we can write

$$\sum_{k=1,k\neq i}^{N_c} \frac{1}{cD_{ik}} \left(X_i \dot{\mathbf{n}}_k - X_k \dot{\mathbf{n}}_i \right) - \frac{\kappa_i \phi_i}{K} \mathbf{u}_i = \frac{1}{cRT} \left(c_i \nabla_{T,p} \overline{\mu}_i + \phi_i \nabla p - \rho_i \mathbf{f}_i \right) \tag{7.100}$$

Adding up over all species returns Darcy's law.

7.2.4 Analysis

We can compare the models presented above attempting to formulate the *binary Stefan tube problem*. In the classic analysis, a liquid (species 1), contained in a capillary, evaporates in a gas (species 2). The liquid surface is kept stationary. Species 1 vapor diffuses along the mixture of 1 and 2. Assumed a one-dimensional problem, the total flow is

$$\dot{n} = \dot{n}_1 + \dot{n}_2$$

Assuming that the liquid is impermeable to the gas (species 2), $\dot{n}_2 = 0$. Both species in the gas phase are assumed ideal. Body force is neglected.

From Lightfoot's model,

$$\sum_{k=1,k\neq i}^{N_c} \frac{1}{cD_{ik}}\left(X_i\dot{n}_k - X_k\dot{n}_i\right) - \frac{\beta_{im}}{c_i}\dot{n}_i = \frac{dX_i}{dz} + \frac{X_i}{cRT}\frac{dp}{dz} \tag{7.101}$$

For $i = 1$, and using $\dot{n}_2 = 0$,

$$\begin{aligned} -\frac{X_2}{cD_{12}}\dot{n}_1 - \frac{\beta_{1m}}{c_1}\dot{n}_1 &= \frac{dX_1}{dz} + \frac{X_1}{cRT}\frac{dp}{dz} \\ -\frac{X_2}{cD_{12}}\dot{n}_1 - \frac{dX_1}{dz} &= \frac{\beta_{1m}}{c_1}\dot{n}_1 + \frac{X_1}{cRT}\frac{dp}{dz} \end{aligned} \tag{7.102}$$

For $i = 2$, and using again $\dot{n}_2 = 0$,

$$\begin{aligned} \frac{X_2}{cD_{12}}\dot{n}_1 &= \frac{dX_2}{dz} + \frac{X_2}{cRT}\frac{dp}{dz} \\ \frac{X_2}{cD_{12}}\dot{n}_1 + \frac{dX_1}{dz} &= \frac{X_2}{cRT}\frac{dp}{dz} \end{aligned} \tag{7.103}$$

Adding up the equations above,

$$\dot{n}_1 = -\frac{c_1}{\beta_{1m}cRT}\frac{dp}{dz} \tag{7.104}$$

For the binary mixture,

$$\begin{aligned} \dot{n} = cu = \frac{c}{\rho}\dot{m} &= \frac{c}{\rho}\left(\dot{m}_1 + \dot{m}_2\right) \\ &= \frac{c}{\rho}\left(\frac{\rho_1}{c_1}\dot{n}_1 + \frac{\rho_2}{c_2}\dot{n}_2\right) \end{aligned} \tag{7.105}$$

For $\dot{n}_2 = 0$,

$$\dot{n} = \frac{c}{\rho}\dot{m} = \frac{M_1}{M}\dot{n}_1 \tag{7.106}$$

Then, from Darcy´s Law, for $\dot{n}_2 = 0$, the total flux is given by

$$\dot{n} = \frac{M_1}{M}\dot{n}_1 = cu = -\frac{c}{R_m}\frac{dp}{dz} \tag{7.107}$$

and we can associate β_{1m} with

$$\beta_{1m} = \frac{M_1}{M}\frac{X_1 R_m}{cRT} \tag{7.108}$$

When $R_m \to 0$, $dp/dz \to 0$ and

$$\dot{n}_1 = -\frac{cD_{12}}{X_2}\frac{dX_1}{dz} \tag{7.109}$$

a well known result. Therefore, Lightfoot's formulation provides a reasonable answer.

From the DGM,

$$\sum_{k=1,k\neq i}^{N-1}\frac{X_i\dot{n}_k - X_k\dot{n}_i}{cD_{ik}^e} - \frac{\dot{n}_i}{cD_{im}^e} = \frac{dX_i}{dz} + \left(1 + \frac{cRT}{D_{im}^e R_m}\right)\frac{X_i}{cRT}\frac{dp}{dz} \tag{7.110}$$

For $i = 1$, $\dot{n}_2 = 0$,

$$\begin{aligned} -\left(\frac{X_2}{cD_{12}^e} + \frac{1}{cD_{1m}^e}\right)\dot{n}_1 &= \frac{dX_1}{dz} + \left(1 + \frac{cRT}{D_{1m}^e R_m}\right)\frac{X_1}{cRT}\frac{dp}{dz} \\ -\frac{X_2}{cD_{12}^e}\dot{n}_1 + \frac{dX_2}{dz} &= \frac{1}{cD_{1m}^e}\dot{n}_1 + \left(1 + \frac{cRT}{D_{1m}^e R_m}\right)\frac{X_1}{cRT}\frac{dp}{dz} \end{aligned} \tag{7.111}$$

For $i = 2$, $\dot{n}_2 = 0$,

$$\frac{X_2}{cD_{12}^e}\dot{n}_1 - \frac{dX_2}{dz} = \left(1 + \frac{cRT}{D_{2m}^e R_m}\right)\frac{X_2}{cRT}\frac{dp}{dz} \tag{7.112}$$

Adding both equations,

$$\dot{n}_1 = -cD_{1m}^e\left[\frac{1}{cRT} + \left(\frac{X_1}{D_{1m}^e} + \frac{X_2}{D_{2m}^e}\right)\frac{1}{R_m}\right]\frac{dp}{dz} \tag{7.113}$$

As above, the total flux, from Darcy´s Law, is

$$\dot{n}_1 = \frac{M}{M_1}\dot{n} = -\frac{M}{M_1}\frac{c}{R_m}\frac{dp}{dz} \tag{7.114}$$

Then, comparing both equations,

$$\frac{R_m D_{1m}^e}{cRT} = \frac{M}{M_1} - \left[1 - X_2\left(1 + \frac{D_{1m}^e}{D_{2m}^e}\right)\right] \tag{7.115}$$

Since species 2 is stationary, it is surprising that D_{2m}^e remains in the equation. This is not a reasonable result.

From the BFM,

$$\sum_{k=1,k\neq i}^{N_c} \frac{1}{cD_{ik}}\left(X_i\dot{n}_k - X_k\dot{n}_i\right) - \frac{\kappa_i\phi_i}{K}u_i = \frac{dX_i}{dz} + \frac{X_i}{cRT}\frac{dp}{dz} \tag{7.116}$$

For $i = 1$, $\dot{n}_2 = 0$,

$$\begin{aligned} -\frac{X_2}{cD_{12}}\dot{n}_1 - \frac{\kappa_1\phi_1}{K}u_1 &= \frac{dX_1}{dz} + \frac{X_1}{cRT}\frac{dp}{dz} \\ -\frac{X_2}{cD_{12}}\dot{n}_1 - \frac{dX_1}{dz} &= \frac{\kappa_1\phi_1}{K}u_1 + \frac{X_1}{cRT}\frac{dp}{dz} \end{aligned} \tag{7.117}$$

For $i = 2$, $\dot{n}_2 = 0$,

$$\begin{aligned} \frac{X_2}{cD_{12}}\dot{n}_1 &= \frac{dX_2}{dz} + \frac{X_2}{cRT}\frac{dp}{dz} \\ \frac{X_2}{cD_{12}}\dot{n}_1 + \frac{dX_1}{dz} &= \frac{X_2}{cRT}\frac{dp}{dz} \end{aligned} \tag{7.118}$$

Adding both equations, provides

$$u_1 = -\frac{K}{cRT\kappa_1\phi_1}\frac{dp}{dz} = -\frac{K}{\eta}\frac{dp}{dz} \tag{7.119}$$

which is Darcy's law under the HVMF hypothesis ($u = u_1$). Also, Darcy's law is not affected by the partial viscosity of species 2, which is good. When the HVMF hypothesis does not hold, we must remember that $u = Y_1 u_1$.

Both the Lightfoot model and the BFM return reasonable answers for the Stefan tube problem. The DGM returns a complicated answer.

In the next chapter, due to its higher simplicity in concept, **Lightfoot's model will be the base for the model developed here**.

8 DEVELOPMENT OF A GENERAL ONE COMPONENT MODEL FOR MULTIPHASE, MULTICOMPONENT MIXTURE

The system under consideration is formed by three phases, solid, liquid and gas and the solid is stationary, i.e., a porous medium. The pore space is occupied by the liquid and gas phases. The porosity ε is the ratio of the volume of pore space divided by the total volume of the mixture

$$\varepsilon = \frac{V_p}{V}. \tag{8.1}$$

The volume fraction ε_α of each phase α is defined as

$$\varepsilon_\alpha = \frac{V_\alpha}{V}. \tag{8.2}$$

For $\alpha = g, l, s,$ the volume fraction of each phase is related to the porosity ε and the liquid water saturation S by

$$\begin{aligned} \varepsilon_S &= 1-\varepsilon \\ \varepsilon_l &= S_\varepsilon \\ \varepsilon_g &= (1-S)\varepsilon \end{aligned} \tag{8.3}$$

where the saturation S is defined as the ratio of the volume occupied by the liquid phase and the total volume of the pore space. The conservation of the total volume leads to $\varepsilon_g + \varepsilon_l + \varepsilon_S = 1$.

Each species occupies a volume fraction of the total volume of phase α corresponding to $\varepsilon_{i,\alpha}$. A volume relation can be written as

$$\varepsilon_\alpha = \sum_{i=1}^{N_\alpha} \varepsilon_{i,\alpha} \tag{8.4}$$

where N_α is the number of species in phase α. This rule applies directly for immiscible species and ideal gases. For nonindeal mixtures, a proper definition of volume fraction $\varepsilon_{i,\alpha}$, as shown below, is needed.

For the gas phase formed by N_g species,

$$\varepsilon_g = \sum_{i=1}^{N_g} \varepsilon_{i,g} \ . \tag{8.5}$$

For the liquid phase, a similar reasoning leads to

$$\varepsilon_l = \sum_{i=1}^{N_l} \varepsilon_{i,l} \ . \tag{8.6}$$

for the moment, a single solid phase is assumed.

Within phase α, each species occupies a volume fraction $\phi_{i,\alpha}$ a mass fraction $Y_{i,\alpha}$ and a mole fraction $X_{i,\alpha}$, following the common relations

$$\phi_{i,\alpha} = c_{i,\alpha}\overline{v}_{i,\alpha} = c_\alpha X_{i,\alpha}\overline{v}_{i,\alpha} = \rho_\alpha Y_{i,\alpha} v_{i,\alpha}; \quad X_{i,\alpha} = Y_{i,\alpha}\frac{M_\alpha}{M_i} \tag{8.7}$$

where $\overline{v}_{i,\alpha}$ is the partial molar volume of species *i* in phase α (with units m^3/kmol), $v_{i,\alpha} = \overline{v}_{i,\alpha} / M_i$ is the partial specific volume (m^3/kg), $v_{i,\beta}$ is the partial mass volume of species *i* (in m^3/kg).

The transformation of concentration measures from the mixture reference to the α-phase reference is accomplished by

$$\varepsilon_{i,\alpha} = \varepsilon_\alpha \phi_{i,\alpha} \tag{8.8}$$

Particularizing for the gas and liquid phases, this relation becomes

$$\varepsilon_{i,g} = \varepsilon_g \phi_{i,g} = \varepsilon\left(1-S\right)\phi_{i,g} \qquad \varepsilon_{i,l} = \varepsilon_l \phi_{i,l} = \varepsilon S \phi_{i,l} \tag{8.9}$$

In general, the $b_{i,\alpha}$ averaged velocity of phase α, denoted $\mathbf{u}_\alpha^b$, is defined as

$$\mathbf{u}_\alpha^b = \sum_{i=1}^{N_\alpha} b_{i,\alpha}\mathbf{u}_{i,\alpha} \tag{8.10}$$

where $b_{i,\alpha}$ is the averaging weight. When $b_{i,\alpha} = Y_{i,\alpha}$, the mass averaged velocity $\mathbf{u}_\alpha$, or barycentric velocity, is recovered.

The *volume-averaged* of a property ψ_i^α for species *i* in phase α is defined as

$$\left\langle \psi_{i,\alpha} \right\rangle = \frac{1}{V}\int_V \psi_{i,\alpha} dV \tag{8.11}$$

The *phasic, or, intrinsic*, *volume-averaged* is denoted as

$$\left\langle \psi_{i,\alpha} \right\rangle^{\alpha} = \frac{1}{V_\alpha} \int_V \psi_{i,\alpha} dV \tag{8.12}$$

Therefore, the relation between phasic-volume and volume averaged properties is

$$\left\langle \psi_{i,\alpha} \right\rangle = \varepsilon_\alpha \left\langle \psi_{i,\alpha} \right\rangle^{\alpha} \tag{8.13}$$

8.1 CONSERVATION OF MASS OF SPECIES I

The volume-averaged equation for the conservation of mass of species i in phase β is written as

$$\frac{\partial \varepsilon_\beta \left\langle \rho_{i,\beta} \right\rangle^{\beta}}{\partial t} + \nabla \cdot \left(\varepsilon_\beta \left\langle \rho_{i,\beta} \right\rangle^{\beta} \left\langle \mathbf{u}_{i,\beta} \right\rangle^{\beta} \right) = \varepsilon_\beta \left\langle \dot{w}_{i,\beta} \right\rangle^{\beta} + \varepsilon_\beta \left\langle \dot{w}_{i,\beta\gamma} \right\rangle^{\beta} \tag{8.14}$$

where $\left\langle \dot{w}_{i,\beta} \right\rangle^{\beta}$ is the volumetric reaction rate and $\left\langle \dot{w}_{i,\beta\gamma} \right\rangle^{\beta}$ is the volumetric phase change rate of species i. We note that

$$\left\langle \rho_{i,\beta} \right\rangle^{\beta} = \left\langle \rho_\beta \right\rangle^{\beta} \left\langle Y_{i,\beta} \right\rangle^{\beta} \tag{8.15}$$

The homogeneous reaction rate $\dot{w}_{i,\beta}$ is the net effect of the reaction rates of the individual reactions, i.e.,

$$\varepsilon_\beta \left\langle \dot{w}_{i,\beta} \right\rangle^{\beta} \equiv \frac{1}{V} \int_{V_\beta} \left(\sum_{j=1}^{N_R} \nu_{ij} M_i r_j \right) dV \,, \tag{8.16}$$

where N_R is the number of independent chemical reactions, $\nu_{ij} = \nu''_{ij} - \nu'_{ij}$ is the stoichiometric coefficient of species i in reaction j (ν'_{ij} as a reactant and ν''_{ij} as a product), and $r_j > 0$ is the reaction speed, calculated from the *Law of Mass Action*, of reaction j. Summing up the reaction rates over all the species, we have

$$\sum_{i=1}^{N_c} \varepsilon_\beta \left\langle \dot{w}_{i,\beta} \right\rangle^{\beta} \equiv \frac{1}{V} \int_{V_\beta} \left(\sum_{i=1}^{N_c} \sum_{j=1}^{N_R} \nu_{ij} M_i r_j \right) dV = 0 \tag{8.17}$$

The volumetric phase change rate of species i depends on a local model for the interfacial transport of species i. In general

$$\varepsilon_\beta \left\langle \dot{w}_{i,\beta} \right\rangle^{\beta} = -\frac{1}{V} \int_{A_{\beta\gamma}} \rho_{i,\beta} \left(\mathbf{u}_{i,\beta} - \mathbf{w}_{\beta\gamma} \right) \cdot \mathbf{n}_{\beta\gamma} dA \tag{8.18}$$

where $\mathbf{w}_{\beta\gamma}$ is the interface velocity between phases β and γ and $\mathbf{n}_{\beta\gamma}$ is the unit normal vector pointing from phase β to phase γ at the $A_{\beta\gamma}$ interface. When phase γ is impermeable to species i, $\langle \dot{w}_{i,\beta} \rangle^{\beta} = 0$. Using $\langle \dot{w}_{i,\beta} \rangle^{\beta}$ other interfacial phenomena can be taken into account, such as absorption, adsorption and surface reaction.

8.1.1 Maxwell-Stefan formulation

Following a Maxwell-Stefan framework, the conservation of linear momentum over a control volume that surrounds species 1 in phase β under fully developed flow states that the drag among species plus the interfacial drag among the gas, liquid and solid phases is balanced by the net driving force $\mathbf{d}'_{1,\beta}$. For example, for a system composed of 3 chemical species (i = 1, 2, 3) in the gas phase (β), a liquid phase (γ) and a solid phase (σ), the volume- averaged dynamic equilibrium for a fluid particle of species i in phase β can be expressed as

$$\begin{aligned} &\left\langle \tilde{C}_{12} \right\rangle \left(\left\langle \mathbf{u}_{1,\beta} \right\rangle - \left\langle \mathbf{u}_{2,\beta} \right\rangle \right) + \left\langle \tilde{C}_{13} \right\rangle \left(\left\langle \mathbf{u}_{1,\beta} \right\rangle - \left\langle \mathbf{u}_{3,\beta} \right\rangle \right) + \\ &\left\langle \tilde{C}_{1\gamma} \right\rangle_{\beta\gamma} \left(\left\langle \mathbf{u}_{1,\beta} \right\rangle - \left\langle \mathbf{u}_{\gamma} \right\rangle \right) + \left\langle \tilde{C}_{1\sigma} \right\rangle_{\beta\sigma} \left(\left\langle \mathbf{u}_{1,\beta} \right\rangle - \left\langle \mathbf{u}_{\sigma} \right\rangle \right) = -\left\langle \tilde{\mathbf{d}}_{1,\beta} \right\rangle \end{aligned} \tag{8.19}$$

where $\left\langle \tilde{C}_{ij} \right\rangle$ is the volume-averaged drag coefficient among species in the same phase, $\left\langle \tilde{C}_{1\sigma} \right\rangle_{\beta\sigma}$ and $\left\langle \tilde{C}_{1\gamma} \right\rangle_{\beta\gamma}$ are the area-averaged boundary drags with the σ and γ phases. The driving force, $\left\langle \tilde{\mathbf{d}}_{1,\beta} \right\rangle$, has units of N/m^3.

In this section, all variables are taken as volume-averaged, not intrinsic volume-averaged, and the notation $\langle\ \rangle$ will be droped for simplicity. We will then write

$$\begin{aligned} &\tilde{C}_{12} \left(\mathbf{u}_{1,\beta} - \mathbf{u}_{2,\beta} \right) + \tilde{C}_{13} \left(\mathbf{u}_{1,\beta} - \mathbf{u}_{3,\beta} \right) + \\ &\tilde{C}_{1\gamma} \left(\mathbf{u}_{1,\beta} - \mathbf{u}_{\gamma} \right) + \tilde{C}_{1\sigma} \left(\mathbf{u}_{1,\beta} - \mathbf{u}_{\sigma} \right) = -\tilde{\mathbf{d}}_{1,\beta} \end{aligned} \tag{8.20}$$

A few properties of this linear relation are:

- This form assumes that

$$\left| \mathrm{u}_{i,\alpha} - \mathrm{u}_{j,\alpha} \right| \ll \mathrm{u}_{\alpha}^{b} \tag{8.21}$$

where $\mathbf{u}_{\alpha}^{b}$ is a characteristic *b*-averaged velocity of the flow of the mixture, such that the drag among components can be modeled by linear relations. Then, the $\tilde{C}_{ij}$ does not depend directly on the velocities themselves, but only on the species concentrations. Therefore, this allows for the development of a first-order theory, and excludes, for example, second-order effects like pore-level inertia effects. Implicit in this condition is the concept that the flow of the mixture can be appropriately modeled by one equation of motion, which is basically a one-component model of a multicomponent system.

- Since the drag force among species acts both ways,

$$\tilde{C}_{ij} = \tilde{C}_{ji} \tag{8.22}$$

- Finally, it is noticed that Eq. (8.20) is independent of the frame of reference, i.e., the choice of the b_i weight factors, to be adopted for the diffusion fluxes.

Eq.() can be expressed in general form as

$$\sum_{k=1,k\neq i}^{N_\beta} \tilde{C}_{ik}\left(\mathbf{u}_{i,\beta}-\mathbf{u}_{k,\beta}\right)+\tilde{C}_{1\gamma}\left(\mathbf{u}_{i,\beta}-\mathbf{u}_{\gamma}\right)+ \tilde{C}_{1\sigma}\left(\mathbf{u}_{i,\beta}-\mathbf{u}_{\sigma}\right)=-\tilde{\mathbf{d}}_{i,\beta} \tag{8.23}$$

where N_β is the number of species in phase β.

Now, the drag coefficient among species is modeled as

$$\tilde{C}_{ik} = \xi_{ik}\varepsilon_{k,\beta} = \xi_{ik}\varepsilon_{\beta}\phi_{k,\beta} \tag{8.24}$$

where the definition for the volumetric fraction in phase β, $\varepsilon_{i,\beta} = \varepsilon_{\beta}\phi_{i,\beta}$,was used. In this representation, ξ_{ik} is the drag coefficient per unit-volume of species *i* in phase β, i.e., an *intrinsic volume-averaged quantity*. This representation is convenient for treating mixtures with widely different molar masses, as discussed below. The driving force is also expressed now as an intrinsic quantity, i.e., per unit-volume of phase β, and then transformed to a mass basis, becoming

$$\tilde{\mathbf{d}}_{i,\beta} = \frac{\varepsilon_{\beta}}{\nu_{i,\beta}}\mathbf{d}_{i,\beta}\,. \tag{8.25}$$

where $\mathbf{d}_{i,\beta}$ is the net force applied over species i per unit mass of phase β.

Using this representation

$$\sum_{k=1,k\neq i}^{N_\beta} \xi_{ik}\varepsilon_\beta\phi_{k,\beta}\left(\mathbf{u}_{i,\beta}-\mathbf{u}_{k,\beta}\right)+ \\ \xi_{i\gamma}\varepsilon_\gamma\left(\mathbf{u}_{i,\beta}-\mathbf{u}_\gamma\right)+\xi_{i\sigma}\varepsilon_\sigma\left(\mathbf{u}_{i,\beta}-\mathbf{u}_\sigma\right)=-\frac{\varepsilon_\beta}{v_{i,\beta}}\mathbf{d}_{i,\beta} \tag{8.26}$$

This expression indicates that when the phase disappears, the related drag term also disappears. Multiplying both sides by $\phi_{i,\beta}$ one obtains

$$\varepsilon_\beta\sum_{k=1,k\neq i}^{N_\beta} \xi_{ik}\phi_{i,\beta}\phi_{k,\beta}\left(\mathbf{u}_{i,\beta}-\mathbf{u}_{k,\beta}\right)+ \\ \varepsilon_\gamma\xi_{i\gamma}\phi_{i,\beta}\left(\mathbf{u}_{i,\beta}-\mathbf{u}_\gamma\right)+\varepsilon_\sigma\xi_{i\sigma}\phi_{i,\beta}\left(\mathbf{u}_{i,\beta}-\mathbf{u}_\sigma\right)=-\varepsilon_\beta\rho_{i,\beta}\mathbf{d}_{i,\beta} \tag{8.27}$$

Since $\xi_{ik}=\xi_{ki}$, the first term is symmetric, i.e.,

$$\sum_{i=1}^{N_\beta}\sum_{k=1,k\neq i}^{N_\beta} \xi_{ik}\phi_{i,\beta}\phi_{k,\beta}\left(\mathbf{u}_{i,\beta}-\mathbf{u}_{k,\beta}\right)=0 \tag{8.28}$$

The net driving force over species i is given from thermodynamics as

$$\mathbf{d}_{i,\beta}=\nabla_{T,p}\mu_{i,\beta}+v_{i,\beta}\nabla p_\beta-\mathbf{f}_{i,\beta} \tag{8.29}$$

Gravity does not play an important role here and the body force of interest is due to electric potential fields,

$$\mathbf{f}_{i,\beta}=-z_{i,\beta}F\nabla\varphi_\beta \tag{8.30}$$

The right-hand side of Eq. (8.27) is written as

$$\varepsilon_\beta\rho_{i,\beta}\mathbf{d}_{i,\beta}=\varepsilon_\beta\rho_{i,\beta}\left(\nabla_{T,p}\mu_{i,\beta}+v_{i,\beta}\nabla p_\beta-\mathbf{f}_{i,\beta}\right) \tag{8.31}$$

Adding up over all species and using Gibbs-Duhem, we obtain

$$\varepsilon_\gamma\rho_\beta\sum_{i=1}^{N_\beta}\xi_{i,\gamma}v_{i,\beta}Y_{i,\beta}\left(\mathbf{u}_{i,\beta}-\mathbf{u}_\gamma\right)+ \\ \varepsilon_\sigma\rho_\beta\sum_{i=1}^{N_\beta}\xi_{i,\sigma}v_{i,\beta}Y_{i,\beta}\left(\mathbf{u}_{i,\beta}-\mathbf{u}_\sigma\right)=-\varepsilon_\beta\left(\nabla p_\beta-\rho_\beta\mathbf{f}\right) \tag{8.32}$$

This result must recover Darcy's Law. Associating

$$\xi_{i\gamma}=\xi_{\gamma i}=\frac{\mu_{\beta\gamma}}{\rho_\beta v_{i,\beta}K_{\beta\gamma}}=\frac{\mu_{\gamma\beta}}{\rho_\beta v_{i,\beta}K_{\gamma\beta}} \tag{8.33}$$

and

$$\xi_{i\sigma} = \frac{\mu_\beta}{\rho_\beta v_{i,\beta} K_\beta} \tag{8.34}$$

we have

$$\frac{\varepsilon_\gamma \mu_{\beta\gamma}}{K_{\beta\gamma}}\left(\mathbf{u}_\beta - \mathbf{u}_\gamma\right) + \frac{\varepsilon_\sigma \mu_\beta}{K_\beta}\left(\mathbf{u}_\beta - \mathbf{u}_\sigma\right) = -\varepsilon_\beta\left(\nabla p_\beta - \rho_\beta \mathbf{f}\right) \tag{8.35}$$

When $\mathbf{u}_\sigma = 0$,

$$\frac{\varepsilon_\gamma \mu_{\beta\gamma}}{K_{\beta\gamma}}\left(\mathbf{u}_\beta - \mathbf{u}_\gamma\right) + \frac{\varepsilon_\sigma \mu_\beta}{K_\beta}\mathbf{u}_\beta = -\varepsilon_\beta\left(\nabla p_\beta - \rho_\beta \mathbf{f}\right) \tag{8.36}$$

which is the v*olume-averaged linear momentum equation for two-phase flow in porous media* in a first-order approximation (i.e., Darcy's law is valid for the flow of the β and γ phases).

This equation can be recast in the form developed by Whitaker (1986),

$$\left(\frac{\varepsilon_\gamma \mu_{\beta\gamma}}{K_{\beta\gamma}} + \frac{\varepsilon_\sigma \mu_\beta}{K_\beta}\right)\mathbf{u}_\beta - \left(\frac{\varepsilon_\gamma \mu_{\beta\gamma}}{K_{\beta\gamma}}\right)\mathbf{u}_\gamma = -\varepsilon_\beta\left(\nabla p_\beta - \rho_\beta \mathbf{f}\right) \tag{8.37}$$

Comparing to Whitaker's form, repeated here for *isotropi*c media, where $\bar{K}$ are Whitaker's permeabilities, as

$$\frac{\varepsilon_\beta \mu_\beta}{\bar{K}_\beta}\left\langle \mathbf{u}_\beta \right\rangle - \frac{\varepsilon_\beta \mu_\beta \bar{K}_{\beta\gamma}}{\bar{K}_\beta}\left\langle \mathbf{u}_\gamma \right\rangle = -\varepsilon_\beta\left(\nabla \left\langle p_\beta \right\rangle^\beta - \rho_\beta \mathbf{g}\right) \tag{8.38}$$

We note that the permeability coefficients may be easily transformed by

$$\bar{K}_\beta \equiv \frac{\varepsilon_\beta \mu_\beta}{\varepsilon_\gamma \mu_{\beta\gamma} / K_{\beta\gamma} + \varepsilon_\sigma \mu_\beta / K_\beta} \tag{8.39}$$

$$\bar{K}_{\beta\gamma} \equiv \frac{\varepsilon_\gamma \mu_{\beta\gamma} / K_{\beta\gamma}}{\varepsilon_\gamma \mu_{\beta\gamma} / K_{\beta\gamma} + \varepsilon_\sigma \mu_\beta / K_\beta} \tag{8.40}$$

Using Equations (8.31), (8.33) and (8.34) the model becomes

$$\begin{aligned} &\varepsilon_\beta \sum_{k=1,k\neq i}^{N_\beta} \xi_{ik} \phi_{i,\beta} \phi_{k,\beta}\left(\mathbf{u}_{i,\beta} - \mathbf{u}_{k,\beta}\right) + \\ &\frac{\varepsilon_\gamma \mu_{\beta\gamma}}{K_{\beta\gamma}} Y_{i,\beta}\left(\mathbf{u}_{i,\beta} - \mathbf{u}_\gamma\right) + \frac{\varepsilon_\sigma \mu_\beta}{K_\beta} Y_{i,\beta}\left(\mathbf{u}_{i,\beta} - \mathbf{u}_\sigma\right) = \\ &\qquad -\varepsilon_\beta \rho_\beta Y_{i,\beta}\left(\nabla_{T,p} \mu_{i,\beta} + v_{i,\beta} \nabla p_\beta - \mathbf{f}_{i,\beta}\right) \end{aligned} \tag{8.41}$$

The drag coefficients can also be expressed as Maxwell-Stefan diffusion coefficients in the form:

$$D_{ik} = \frac{c_\beta RT}{\xi_{ik}} \tag{8.42}$$

$$D_{i\gamma} = K_{\beta\gamma} \frac{\rho_\beta v_{i,\beta} p_\beta}{\mu_{\beta\gamma}} \tag{8.43}$$

$$D_{i\sigma} = K_\beta \frac{\rho_\beta v_{i,\beta} p_\beta}{\mu_\beta} \tag{8.44}$$

The Maxwell-Stefan diffusivities in respect to the liquid and solid phases are therefore proportional to the relative permeabilities and inversely proportional to the phase viscosity.

8.1.2 Frame of reference

Now we must decide on an appropriate frame of reference. Here, a **Hittorf frame** of reference is used, for which the velocity of the solid phase is taken as the reference velocity for diffusion. Then

$$\mathbf{V}_{i,\beta} = \mathbf{u}_{i,\beta} - \mathbf{u}_\sigma \tag{8.45}$$

$$\mathbf{V}_\gamma = \mathbf{u}_\gamma - \mathbf{u}_\sigma \tag{8.46}$$

Eq.(8.41) may be rewritten as

$$\begin{aligned} &\varepsilon_\beta \sum_{k=1,k\neq i}^{N_\beta} \xi_{ik} \phi_{i,\beta} \phi_{k,\beta} \left(\mathbf{V}_{i,\beta} - \mathbf{V}_{k,\beta} \right) + \\ &\frac{\varepsilon_\gamma \mu_{\beta\gamma}}{K_{\beta\gamma}} Y_{i,\beta} \left(\mathbf{V}_{i,\beta} - \mathbf{V}_\gamma \right) + \frac{\varepsilon_\sigma \mu_\beta}{K_\beta} Y_{i,\beta} \mathbf{V}_{i,\beta} = \\ &\qquad - \varepsilon_\beta \rho_\beta Y_{i,\beta} \left(\nabla_{T,p} \mu_{i,\beta} + v_{i,\beta} \nabla p_\beta - \mathbf{f}_{i,\beta} \right) \end{aligned} \tag{8.47}$$

The mass diffusion fluxes in the **Hittorf frame** of reference become

$$\mathbf{j}_{i,\beta} = \rho_{i,\beta} \mathbf{V}_{i,\beta} \tag{8.48}$$

$$\mathbf{j}_\gamma = \rho_\gamma \mathbf{V}_\gamma \tag{8.49}$$

and then,

$$\varepsilon_\beta \sum_{k=1,k\neq i}^{N_\beta} \xi_{ik} v_{i,\beta} v_{k,\beta} \left(\rho_{k,\beta} \mathbf{j}_{i,\beta} - \rho_{i,\beta} \mathbf{j}_{k,\beta} \right) +$$

$$\frac{\varepsilon_\gamma \mu_{\beta\gamma}}{K_{\beta\gamma} \rho_\gamma \rho_\beta} \left(\rho_\gamma \mathbf{j}_{i,\beta} - \rho_{i,\beta} \mathbf{j}_\gamma \right) + \frac{\varepsilon_\sigma \mu_\beta}{K_\beta \rho_\beta} \mathbf{j}_{i,\beta} = \tag{8.50}$$

$$- \varepsilon_\beta \rho_{i,\beta} \left(\nabla_{T,p} \mu_{i,\beta} + v_{i,\beta} \nabla p_\beta - \mathbf{f}_{i,\beta} \right)$$

This expressed in *matrix form* becomes

$$R_{i,\beta} \mathbf{j}_{i,\beta} + \sum_{k=1,k\neq i}^{N_\beta} R_{ik,\beta} \mathbf{j}_{k,\beta} + R_{i,\gamma} \mathbf{j}_\gamma = \mathbf{b}_{i,\beta} \tag{8.51}$$

where the effective resistances are

$$R_{i,\beta} = \varepsilon_\beta v_{i,\beta} \left(\sum_{k=1,k\neq i}^{N_\beta} \xi_{ik} \phi_{k,\beta} \right) + \frac{\varepsilon_\gamma \mu_{\beta\gamma}}{K_{\beta\gamma} \rho_\beta} + \frac{\varepsilon_\sigma \mu_\beta}{K_\beta \rho_\beta} \tag{8.52}$$

$$R_{ik,\beta} = -\varepsilon_\beta v_{k,\beta} \xi_{ik} \phi_{i,\beta} \tag{8.53}$$

$$R_{i,\gamma} = -\frac{\varepsilon_\gamma \mu_{\beta\gamma}}{K_{\beta\gamma} \rho_\gamma} Y_{i,\beta} \tag{8.54}$$

and the driving force per unit volume of phase β is

$$\mathbf{b}_{i,\beta} = -\varepsilon_\beta \rho_{i,\beta} \left(\nabla_{T,p} \mu_{i,\beta} + v_{i,\beta} \nabla p_\beta - \mathbf{f}_{i,\beta} \right) \tag{8.55}$$

8.2 PHASE MOMENTUM EQUATIONS

Summing up for phase β, we obtain

$$\frac{\varepsilon_\gamma \mu_{\beta\gamma}}{K_{\beta\gamma} \rho_\beta \rho_\gamma} \left(\rho_\gamma \mathbf{j}_\beta - \rho_\beta \mathbf{j}_\gamma \right) + \frac{\varepsilon_\sigma \mu_\beta}{K_\beta \rho_\beta} \mathbf{j}_\beta = -\varepsilon_\beta \left(\nabla p_\beta - \rho_\beta \mathbf{f} \right) \tag{8.56}$$

where

$$\mathbf{j}_\beta = \sum_{i=1}^{N_\beta} \mathbf{j}_{i,\beta} \ . \tag{8.57}$$

In matrix form,

$$R_{\beta\beta} = \left(\sum_{i=1}^{N_\beta} \mathbf{j}_{i,\beta} \right) + R_{\beta\gamma} \mathbf{j}_\gamma = \mathbf{b}_\beta \ , \tag{8.58}$$

where

$$R_{\beta\beta} = \frac{1}{\rho_\beta}\left(\frac{\varepsilon_\gamma \mu_{\beta\gamma}}{K_{\beta\gamma}} + \frac{\varepsilon_\sigma \mu_\beta}{K_\beta}\right) \tag{8.59}$$

$$R_{\beta\gamma} = \frac{1}{\rho_\gamma}\left(\frac{\varepsilon_\gamma \mu_{\beta\gamma}}{K_{\beta\gamma}}\right) \tag{8.60}$$

$$\mathbf{b}_\beta = -\varepsilon_\beta\left(\nabla p_\beta - \rho_\beta \mathbf{f}\right). \tag{8.61}$$

For *phase γ*, we obtain

$$\frac{\varepsilon_\beta \mu_{\gamma\beta}}{K_{\gamma\beta}\rho_\beta\rho_\gamma}\left(\rho_\beta \mathbf{j}_\gamma - \rho_\gamma \mathbf{j}_\beta\right) + \frac{\varepsilon_\sigma \mu_\gamma}{K_\gamma \rho_\gamma}\mathbf{j}_\gamma = -\varepsilon_\gamma\left(\nabla p_\gamma - \rho_\gamma \mathbf{f}\right) \tag{8.62}$$

where

$$\mathbf{j}_\beta = \sum_{i=1}^{N_\beta} \mathbf{j}_{i,\beta}\ . \tag{8.63}$$

In matrix form,

$$R_{\gamma\gamma}\mathbf{j}_\gamma + R_{\gamma\beta}\left(\sum_{i=1}^{N_\beta} \mathbf{j}_{i,\beta}\right) = \mathbf{b}_\gamma \tag{8.64}$$

where

$$R_{\gamma\gamma} = \frac{1}{\rho_\gamma}\left(\frac{\varepsilon_\beta \mu_{\gamma\beta}}{K_{\gamma\beta}} + \frac{\varepsilon_\sigma \mu_\gamma}{K_\gamma}\right) \tag{8.65}$$

$$R_{\gamma\beta} = -\frac{1}{\rho_\beta}\left(\frac{\varepsilon_\beta \mu_{\gamma\beta}}{K_{\gamma\beta}}\right) \tag{8.66}$$

$$\mathbf{b}_\gamma = -\varepsilon_\gamma\left(\nabla p_\gamma - \rho_\gamma \mathbf{f}\right). \tag{8.67}$$

For the *two-phase flow*, the phase pressures are related by

$$p_\beta - p_\gamma = 2\sigma H\left(S\right) \tag{8.68}$$

which depends on a *volume-averaged capillary pressure model* for $H\left(S\right)$. In this expression, σ is the surface tension.

8.3 REDUCTION TO THE BINARY FRICTION MODEL

As a special case, consider the particularization for a multicomponent gas phase and a single component liquid phase. The phasic volume fractions are:

$$\varepsilon_g = \varepsilon\left(1-S\right)$$
$$\varepsilon_l = \varepsilon S \tag{8.69}$$
$$\varepsilon_s = \left(1-\varepsilon\right)$$

Dropping the subscript β for gas and using $\gamma = l$ and $\sigma = s$, the equation for the diffusion fluxes becomes,

$$\varepsilon\left(1-S\right)\sum_{k=1,k\neq i}^{N_g}\xi_{ik}\phi_k\phi_i\left(\mathbf{u}_i-\mathbf{u}_k\right)+$$
$$\varepsilon S\frac{\mu_{gl}}{K_{gl}}Y_i\left(\mathbf{u}_i-\mathbf{u}_l\right)+\left(1-\varepsilon\right)\frac{\mu_g}{K_g}Y_i\left(\mathbf{u}_i-\mathbf{u}_s\right)= \tag{8.70}$$
$$-\varepsilon\left(1-S\right)\left(\rho_i\nabla_{T,p}\mu_i+\phi_i\nabla p_g-\mathbf{f}_i\right)$$

As a further simplification, in the absence of a liquid phase, S = 0, and then

$$\varepsilon\sum_{k=1,k\neq i}^{N_g}\xi_{ik}\phi_k\phi_i\left(\mathbf{u}_i-\mathbf{u}_k\right)+$$
$$\left(1-\varepsilon\right)\frac{\mu_g}{K_g}Y_i\left(\mathbf{u}_i-\mathbf{u}_s\right)=-\varepsilon\left(\rho_i\nabla_{T,p}\mu_i+\phi_i\nabla p_g-\mathbf{f}_i\right) \tag{8.71}$$

Considering a **Hittorf frame** of reference,

$$\varepsilon\sum_{k=1,k\neq i}^{N_g}\xi_{ik}\phi_k\phi_i\left(\mathbf{V}_i-\mathbf{V}_k\right)+$$
$$\left(1-\varepsilon\right)\frac{\mu_g}{K_g}Y_i\mathbf{V}_i=-\varepsilon\left(\rho_i\nabla_{T,p}\mu_i+\phi_i\nabla p_g-\mathbf{f}_i\right) \tag{8.72}$$

For convenience, we divide by $p_g = c_g R_u T$,

$$\varepsilon\sum_{k=1,k\neq i}^{N_g}\frac{\xi_{ik}\phi_k\phi_i}{c_g RT}\left(\mathbf{V}_i-\mathbf{V}_k\right)+$$
$$\frac{\left(1-\varepsilon\right)}{c_g RT}\frac{\mu_g}{K_g}Y_i\mathbf{V}_i=-\varepsilon\frac{\rho_i}{c_g RT}\left(\nabla_{T,p}\mu_i+v_i\nabla p_g-\mathbf{f}_i\right) \tag{8.73}$$

For $f_i = 0$, and using $Y_i M_g = X_i M_i$,

$$\varepsilon \sum_{k=1,k\neq i}^{N_g} \frac{\xi_{ik}\phi_k\phi_i}{c_g RT}\left(\mathbf{V}_i - \mathbf{V}_k\right) + \frac{\left(1-\varepsilon\right)}{c_g RT}\frac{\mu_g}{K_g}\frac{\phi_i}{\rho_g v_i}\mathbf{V}_i = -\varepsilon\left(\frac{X_i}{RT}\nabla_{T,p}\overline{\mu}_i + \frac{X_i\overline{v}_i}{RT}\nabla p_g\right) \tag{8.74}$$

Now we use the relation

$$D_{ik} = \frac{c_g RT}{\xi_{ik}} \tag{8.75}$$

to write (inverting the signs)

$$\sum_{k=1,k\neq i}^{N_g} \frac{\phi_k\phi_i}{D_{ik}}\left(\mathbf{V}_k - \mathbf{V}_i\right) - \frac{1-\varepsilon}{\varepsilon}\frac{1}{c_g RT}\frac{\mu_g}{K_g}\frac{1}{\rho_g v_i}\phi_i\mathbf{V}_i = \frac{X_i}{RT}\nabla_{T,p}\overline{\mu}_i + \frac{X_i\overline{v}_i}{RT}\nabla p_g \tag{8.76}$$

The *Binary Friction Model* (**BFM**) (KERKHOF, 1996, Eq. 78) is

$$\sum_{k=1,k\neq i}^{N_g} \frac{X_i X_k}{D_{ik}^K}\left(\mathbf{V}_k - \mathbf{V}_i\right) - \frac{1}{B_o}\kappa_i\phi_i\mathbf{V}_i = \frac{X_i}{RT}\nabla_{T,p}\overline{\mu}_i + \frac{X_i\overline{v}_i}{RT}\nabla p_g \tag{8.77}$$

where κ_i is the "*fractional viscosity coefficient*". In order to recover the mixture conservation of momentum for the mixture with the BFM, it is required that

$$\mu_g = c_g RT\sum_{i=1}^{N_g}\kappa_i\phi_i \tag{8.78}$$

Comparing both models, the following identities are found:
For the inter-species drag term,

$$D_{ik} = c_g^2\overline{v}_i\overline{v}_k D_{ik}^K \tag{8.79}$$

and for the *gas-solid drag* term

$$\frac{1-\varepsilon}{\varepsilon}\frac{1}{c_g RT}\frac{\mu_g}{K_g}\frac{1}{\rho_g v_i} = \frac{1}{B_o}\kappa_i \tag{8.80}$$

Separating species-dependent from phase-dependent variables in the gas-solid drag term we obtain

$$c_g RT\kappa_i = \frac{\mu_g}{\rho_g v_i} = \frac{Y_i}{\phi_i}\mu_g \tag{8.81}$$

$$B_o = \frac{\varepsilon K_g}{1-\varepsilon}, \tag{8.82}$$

where, as required,

$$\mu_g = c_g RT \sum_{i=1}^{N_g} \kappa_i \phi_i = \frac{\mu_g}{\rho_g} \sum_{i=1}^{N_g} \frac{\phi_i}{v_i} = \frac{\mu_g}{\rho_g} \sum_{i=1}^{N_g} \rho_i = \mu_g \tag{8.83}$$

Therefore, the model developed is compatible with the BFM. In particular, Eq. (8.81) provides a simple model for the fractional viscosity coefficient κ_i. In this model, from equation (8.78) and (8.81),

$$\frac{\partial \ln(\mu_g)}{\partial \ln(\phi_i)} = Y_i + \frac{\kappa_i \phi_i}{\sum_{i=1}^{N_g} \kappa_i \phi_i} \frac{\partial \ln(\kappa_i)}{\partial \ln(\phi_i)} \tag{8.84}$$

which provides an additional relation among μ_g and κ_i.

The model developed here is formed by Eqs. (8.41) or (8.50), for the species velocity or the species diffusion flux in the Hittorf frame of reference, respectively, Eqs. (8.56) for phase β and (8.62) for phase γ.

In the next chapter, these equations are applied to a few basic problems relevant for the modeling of the MEA of PEM fuel cells.

8.4 FORMULATION OF SIMPLE MASS DIFFUSION PROBLEMS

The model developed in the preceeding section is now applied to the prediction of simple mass diffusion problems in order to elucidate the modeling of the effect of pressure and of bulk flow. The problems adressed are assumed isothermal. The formulation for a problem with *N* species in *M* dimensions, in molar variables, requires:

Equations	Variables	Dimension
Maxwell-Stefan	$\overline{\mathrm{J}}_i$ or $\boldsymbol{n}_i$	M x N
Conservation of mass of species	X_i	N
Conservation of mass	c	1
Conservation of momentum	$\overline{\mathrm{u}}$	M
Equation of state	p	1
Total		$(M \times N) + N + M + 2$

When M = 1, i.e, a one-dimensional problem, there are $2N + 3$ equations and variables. A few one-dimensonal forms are explored in the next sections.

8.4.1 Constant pressure, zero convective flow mass diffusion

The two bulb diffusion is a simple device that can be used to measure the diffusion coefficient in gas mixtures (Taylor and Krishna, 1993). Both bulbs are filled with different gases and are connected by a capillary tube with a stopcock. At t = 0, the valve is open and the gases are allowed to diffuse. Concentration measurements are taken in the two bulbs at different times. This bulb set up was used by Duncan and Toor (1962) with a ternary mixture of hydrogen, nitrogen and carbon dioxide in order to examine diffusion in an ideal ternary gas mixture. The experiments evidenced the occurrence of diffusion fluxes of a species *i* contrary to their own gradient of concentration. Figure 46 presents the solution of the Maxwell-Stefan equations by Krishna and Wesselingh (1997) compared to the measurements of Duncan and Toor (1962). The insert on top of the figure provides the initial concentrations of hydrogen (1), nitrogen (2) and carbon dioxide (3). The horizontal axis represents the time after the valve is opened and the vertical axis is the transient molar concentrations of (1) hydrogen and (2) nitrogen in bulbs A and B. In spite of the equal concentrations (no driving force), there is an initial nitrogen diffusion flux from bulb A to bulb B, contrary to a Fickian model. This diffusion flux continues increasing the composition of bulb A at the expense of bulb B, in an up-hill direction (reverse diffusion) until both concentrations reach a plateau. This plateau is an evidence of null flux despite the large gradient of nitrogen concentration that has been generated. Beyond this elapsed time the driving force is large enough to overcome the reverse diffusion effect and nitrogen diffuses down its own concentration gradient. This curious nitrogen behavior is due to the *diffusional interaction effects* with the other chemical species. This behavior is well reproduced by the Maxwell Stefan equations, as shown by TAYLOR and KRISHNA (1993), KRISHNA and WESSENLINGH (1997) and AMUNDSON and PAULSEN (2003).

Figure 46 - Comparison of the result of the Maxwell-Stefan equations (Krishna and Wesselingh, 1997) with the experiments of Duncan and Toor (1962).

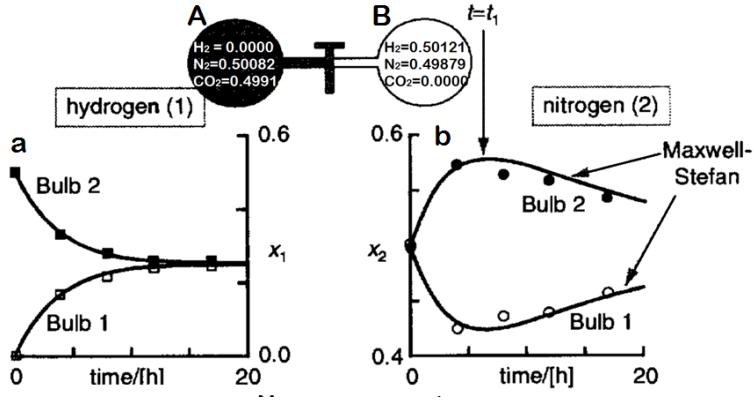

In this problem, the two bulbs and the connecting capillar form a constant volume vessel and the fluid is isothermal. The mixture velocity at the vessel walls is zero and diffusion takes place primarily in a single direction. As a result, since the initial pressure is uniform everywhere, $\overline{u}\left(t,z\right)=0$. Therefore, the *mixture molar concentration is constant* and a description based on the *molar center of reference* makes the formulation simpler.

Using a molar basis, the conservation of mass of a species *i* becomes

$$\frac{\partial}{\partial t}\left(cX_i\right)+\nabla\cdot\left(cX_i\overline{\mathbf{u}}+\overline{\mathbf{J}}_i\right)=0\,. \tag{8.85}$$

This equation is solved for species $i = 1, \ldots, N-1$. The molar fraction for species N is obtained from

$$\sum_{i=1}^{N}X_i=0 \tag{8. 86}$$

Considering that the $\overline{J}_i$ and $\overline{u}_i$ are known, this set of N equations are used to find X_i, $i = 1, 2, \ldots, N$.

For single-phase $\left(\varepsilon_\beta=1\right)$ the Maxwell-Stefan system, becomes

$$\sum_{k=1,k\neq i}^{N_\beta}\frac{cRT}{D_{ik}}\phi_i\phi_k\left(\mathbf{u}_i-\mathbf{u}_k\right)=-\rho Y_i\left(\nabla_{T,p}\mu_i+v_i\nabla p-\mathbf{f}_i\right) \tag{8. 87}$$

Using a *molar center of reference*, the diffusion fluxes are defined as

$$\overline{\mathbf{J}}_i = c_i \overline{\mathbf{V}}_i = c_i \left(\mathbf{u}_i - \overline{\mathbf{u}} \right), \quad \sum_{i=1}^{N_g} \overline{\mathbf{J}}_i = 0 \tag{8. 88}$$

Using the ideal gas realtions,

$$\phi_i = X_i, \qquad M_i \mu_i = \overline{\mu}_i = \overline{\mu}_i^o + RT \ln X_i \tag{8. 89}$$

we obtain

$$\sum_{k=1,k\neq i}^{N_\beta} \frac{X_k X_i}{D_{ik}} \left(\overline{\mathbf{V}}_i - \overline{\mathbf{V}}_k \right) = -\nabla_{T,p} X_i - \frac{X_i}{cRT} \nabla p + \frac{X_i M_i}{RT} \mathbf{f}_i \tag{8. 90}$$

or

$$\sum_{k=1,k\neq i}^{N_\beta} \frac{1}{D_{ik}} \left(X_k \overline{\mathbf{J}}_i - X_i \overline{\mathbf{J}}_k \right) = -c \nabla_{T,p} X_i - \frac{X_i}{RT} \nabla p + \frac{c X_i M_i}{RT} \mathbf{f}_i \tag{8. 91}$$

Considering uniform pressure and absense of body force, in the molar center of reference, the one-dimensional formulation reduces to the classic Maxwell-Stefan form,

$$\sum_{k=1,k\neq i}^{N_\beta} \frac{1}{D_{ik}} \left(X_k \overline{\mathbf{J}}_i - X_i \overline{\mathbf{J}}_k \right) = -c \nabla_{T,p} X_i \tag{8.92}$$

This equation is solved for species i = 1,…, N-1. The molar diffusion flux for species N is obtained from

$$\sum_{i=1}^{N} \overline{\mathbf{J}}_i = 0 \tag{8.93}$$

Considering that p and X_i are know, this set of N equations are used to find $\overline{\mathbf{J}}_i$, i = 1, 2,…, N. The mathematical problem resumes to a matrix inversion problem.

For the ternary (N = 3) mixture, the Maxwell-Stefan form system becomes

$$\begin{aligned}
&\left(\frac{X_2}{D_{12}} + \frac{X_3}{D_{13}} \right) \overline{\mathbf{J}}_1 \; - \; \frac{X_1}{D_{12}} \overline{\mathbf{J}}_2 \; - \frac{X_1}{D_{13}} \overline{\mathbf{J}}_3 = -c \frac{\partial X_1}{\partial z} \\
&- \frac{X_2}{D_{21}} \overline{\mathbf{J}}_1 \; + \left(\frac{X_1}{D_{21}} + \frac{X_3}{D_{23}} \right) \overline{\mathbf{J}}_2 \; - \frac{X_2}{D_{23}} \overline{\mathbf{J}}_3 = -c \frac{\partial X_2}{\partial z} \\
&\overline{\mathbf{J}}_1 \; + \; \overline{\mathbf{J}}_2 \; + \; \overline{\mathbf{J}}_3 = 0
\end{aligned} \tag{8. 94}$$

The last equation could substitute any of the three species equation. Species 3 was chosen to be left out of the system.

The conservation of mass os species i = 1, 2 in the capillar in the absense of bulk flow, becomes

$$\frac{\partial}{\partial t}\left(cX_i\right) = -\frac{\partial \overline{\mathbf{J}}_i}{\partial z} \tag{8.95}$$

The mole fraction of species 3 may be obtained simply from

$$X_3 = 1 - X_1 - X_2 \tag{8.96}$$

Finally, the conservation of mass of species i = 1, 2 for the two bulbs, A and B, is

$$\frac{\partial}{\partial t}\left(c_{i,A}V_A\right) = -\overline{\mathbf{J}}_i\Big|_{z=0} \quad A_u\,, \qquad i=1,\,2, \tag{8.97}$$

$$\frac{\partial}{\partial t}\left(c_{i,B}V_B\right) = \overline{\mathbf{J}}_i\Big|_{z=L} \quad A_u\,, \; i=1,\,2,\,3 \tag{8.98}$$

where V_A and V_B are the volume of the bulbs and A_u is the transversal area of the capillary (constants).

In Eqs (8.95) to (8.98), the ideal gas law and the boundary conditions form a closed system for the solution of the $c_{i,A}$, $c_{i,B}$, X_i and $\overline{\mathbf{J}}_i$. The solution could be numerically obtained implementing a Gaussian elimination subroutine for the solution of the Maxwell-Stefan system and a Backward-Euler finite volume subroutine for the solution of the equations for the conservation of mass. A staggered grid could be used for the treatment of the coupling between the fluxes and the mole fractions.

8.4.2 Constant pressure, prescribed convective flow mass diffusion

The classic Stefan-tube problem or Arnold cell problem presents a diffusion induced bulk fluid flow. When the capillary has a large diameter, the pressure may be assumed constant, even though there is a bulk fluid flow. There are several analyses available in the literature. Among them, we refer to Bird et.al. (1962), Taylor and Krishna (1993), Whitaker (1999) and Kerkhof (1997). A careful experiment was performed by Carty and Schrodt (1975).

In the traditional configuration, a pool of quiescent liquid, which can be a pure substance (forming a binary gas mixture) or a convenient mixture (forming a multicomponent gas mixture), remains at constant level and concentration in the bottom of the tube. Vapor of this liquid diffuses up-ward towards the open end in the top of the tube. At the top, a stream of gas flows across the opening and sweeps away the vapor, approximating a condition of constant concentration. The mole fraction

of the vapor at the vapor-liquid interface is its equilibrium value at the liquid surface temperature. This device is sometimes used for measuring diffusion coefficient in binary vapor mixtures.

A simple solution is available when the problem is isothermal, the pressure is constant, the liquid pool surface is kept stationary, phase equilibrium prevails and the liquid is impermeable to air. The surface mole fraction is obtained from the ratio of the saturation and total Assuming that the gas is ideal, the formulation of the model becomes the same as above (which is repeated here for clarity),

$$\sum_{k=1,k\neq i}^{N_\beta} \frac{1}{D_{ik}}\left(X_k\bar{\mathbf{J}}_i - X_i\bar{\mathbf{J}}_k\right) = -c\frac{\partial X_i}{\partial z} \tag{8.99}$$

For the binary problem, they become

$$\begin{aligned} \frac{X_2}{D_{12}}\bar{J}_1 - \frac{X_1}{D_{12}}\bar{J}_2 &= -c\frac{\partial X_1}{\partial z} \\ \bar{J}_1 + \quad \bar{J}_2 &= 0 \end{aligned} \tag{8.100}$$

The conservation of mass for species 1 becomes

$$\frac{\partial}{\partial t}\left(cX_1\right) + \frac{\partial}{\partial z}\left(c\bar{u}X_1\right) = -\frac{\partial \bar{J}_1}{\partial z} \tag{8. 101}$$

The boundary conditions are:

$$\begin{aligned} &z = 0,\ X_1 = X_{1,o} = \frac{p_{sat,1}(T)}{p},\ X_2 = 1 - X_{1,o}, \\ &z = L,\ X_1 = X_{1,L}, \qquad\qquad X_2 = 1 - X_{1,L} \end{aligned} \tag{8.102}$$

The bulk flow velocity at steady-state is easily obtained from the mass balance at the liquid surface. For the bulk mixture, at steady-state,

$$\frac{\partial}{\partial z}\left(c\bar{u}\right) = 0 \tag{8.103}$$

and, therefore,

$$\bar{u} = \frac{1}{c\left(1 - X_{1,o}\right)}\bar{\mathbf{J}}_1\Big|_{z=0} \tag{8.104}$$

This condition may be generalized as follows. From the definition of molar averaged velocity,

$$c\bar{u} = \sum_{k=1}^{N} c_i u_i \tag{8.105}$$

but, $\dot{n}_N = c_N u_N = 0$, then

$$
\begin{aligned}
c\overline{u} &= \sum_{k=1}^{N-1} c_i u_i = \sum_{k=1}^{N-1} \left(c_i \overline{u} + \overline{J}_i \right) \\
\left(c - \sum_{k=1}^{N-1} c_i \right) \overline{u} &= c_N \overline{u} = \sum_{k=1}^{N-1} \overline{J}_i \\
\overline{u} &= \frac{1}{c_N} \sum_{k=1}^{N-1} \overline{J}_i
\end{aligned}
\tag{8.106}
$$

Again, the problem is solved using the full numerical subroutine and the results are compared to analytical solutions.

To arrive at the analytical solution, the solution for $\overline{\mathbf{J}}_1$ in Eq.(8.100) gives

$$\overline{J}_1 = -c_{12} \frac{\partial X_1}{\partial z} \tag{8.107}$$

From the assumption that the liquid surface is stationary and impermeable to species 2, species 2 become stagnant $\left(\overline{N}_2 = 0 \right)$ and the total mole flux of 1 at the surface becomes

$$\overline{N}_1 = -\frac{c_{12}}{1 - X_{1,o}} \frac{\partial X_1}{\partial z} \bigg|_{z=0} \tag{8.108}$$

Solving for the conservation of mass Eq.(8. 101) the mole fraction distribution becomes

$$\frac{1 - X_1}{1 - X_{1,o}} = \left(\frac{1 - X_{1,L}}{1 - X_{1,o}} \right)^{z/L} \tag{8.109}$$

the total molar flux at $z = 0$ becomes

$$\overline{N}_1 = \frac{c_{12}}{L} \ln \left(\frac{1 - X_{1,L}}{1 - X_{1,o}} \right) \tag{8.110}$$

The ternary diffusion problem, under the same assumptions as above, was studied experimentally by Carty and Schrodt (1975).

The formulation for the ternary 1-D problem is

$$
\begin{aligned}
\left(\frac{X_2}{D_{12}} + \frac{X_3}{D_{13}} \right) \overline{\mathbf{J}}_1 - & \quad \frac{X_1}{D_{12}} \overline{\mathbf{J}}_2 - \frac{X_1}{D_{13}} \overline{\mathbf{J}}_3 = -c \frac{\partial X_1}{\partial z} \\
-\frac{X_2}{D_{21}} \overline{\mathbf{J}}_1 + & \left(\frac{X_1}{D_{21}} + \frac{X_3}{D_{23}} \right) \overline{\mathbf{J}}_2 - \frac{X_2}{D_{23}} \overline{\mathbf{J}}_3 = -c \frac{\partial X_2}{\partial z} \\
\overline{\mathbf{J}}_1 + & \quad \overline{\mathbf{J}}_2 + \quad \overline{\mathbf{J}}_3 = 0
\end{aligned}
\tag{8.111}
$$

The conservation of mass for species 1 and 2 becomes

$$\frac{\partial}{\partial t}\left(cX_i\right)+\frac{\partial}{\partial z}\left(c\bar{u}X_i\right)=-\frac{\partial \bar{J}_i}{\partial z} \tag{8.112}$$

The boundary conditions are:

$$\begin{aligned} z&=0 \qquad X_i=X_{i,o} \\ z&=L \qquad X_i=X_{i,L} \end{aligned}. \tag{8.113}$$

The bulk flow velocity at steady-state is obtained from the mass balance at the liquid surface,

$$\bar{u}=\frac{1}{cX_{3,o}}\bar{J}_1+\bar{J}_2\Big|_{z=0} \tag{8.114}$$

An analytical solution is developed in AMUNDSON and PAULSEN (2003) but it will not be reported here.

8.4.3 Variable pressure, prescribed convective flow mass diffusion

The same problem of Carty and Schrodt (1975) may be extended to capillaries of smaller diameters, resembling a porous medium. The effect of the pressure variation affects the boundary condition at the liquid surface, lowering the magnitude of the binary diffusivities and originating a driving force for diffusion.

The effect of pressure becomes important as the diameter of the Stefan tube decreases. The bulk flow induced by diffusion is subjected to a pressure drop as the mixture flows down the tube. The bulk velocity distribution, under the no-slip condition at the tube walls (large Knudsen approximation), is two dimensional and obtained from the solution of the Conservation of Momentum equation, i.e., the Navier-Stokes equation. The velocity profile, in turn, will induce radial variations of the mole fraction (HEINZELMANN et al., 1965; RAO and BENNET, 1966; MEYER and KOSTIN, 1975). Here, we intend to keep a strictly one-dimensional problem. With this objective, the bulk flow will be assumed fully developed, laminar and with constant properties. In this *Poiseuille flow*, the mass averaged velocity is related to the pressure drop as

$$u=-\frac{d^2}{32\mu}\frac{dp}{dz} \tag{8.115}$$

where d is the tube diameter. This relation can be modeled as a Darcy flow with permeability $K = d^2/32$. This relation is integrated into the solution of the Maxwell-Stefan equations as follows.

In order to model the pressure effect on diffusion, we start from the basic formulation. The general model (repeated here for easy of reference),

$$\sum_{k=1,k\neq i}^{N_\beta} \frac{cRT}{D_{ik}} \phi_i \phi_k \left(\mathbf{u}_i - \mathbf{u}_k\right) + \frac{\eta}{K} Y_i u_i = -\rho_i \left(\frac{d\mu_i}{dz} + v_i \frac{dp}{dz} - f_i \right) \quad (8.116)$$

becomes exactly equal to Lighfoot´s formulation,

$$\sum_{k=1,k\neq i}^{N_\beta} \frac{1}{cD_{ik}} \left(X_i \dot{n}_k - X_k \dot{n}_i \right) - \frac{R_m}{c^2 RT} \frac{M_i}{M} \dot{n}_i = \frac{1}{cRT} \left(c \nabla_{T,p} \overline{\mu}_i + \phi_i \nabla p - \rho_i \mathrm{f}_i \right)$$

since, $\beta_{im} = (M_i X_i R_m)/(M_c RT)$.

Assuming ideal gas and f_i =0, the M.-S. equation becomes

$$\sum_{k=1,k\neq i}^{N_\beta} \frac{X_i X_k}{D_{ik}} \left(u_i - u_k \right) + \frac{R_m}{cRT} Y_i u_i = -\frac{dX_i}{dz} - \frac{X_i}{cRT} \frac{dp}{dz} \quad (8.117)$$

where

$$R_m = \frac{\eta}{K} \quad (8.118)$$

Writing for molar fluxes, $\dot{n}_i = c_i u_i$,

$$\sum_{k=1,k\neq i}^{N_\beta} \frac{1}{D_{ik}} \left(X_k \dot{n}_i - X_i \dot{n}_k \right) + \frac{R_m}{cRT} \frac{M_i}{M} \dot{n}_i = -c \frac{dX_i}{dz} - \frac{X_i}{RT} \frac{dp}{dz} \quad (8.119)$$

For a binary mixture, the mass flux becomes

$$\dot{m} = \dot{m}_1 + \dot{m}_2 = M_1 \dot{n}_1 + M_2 \dot{n}_2 = \text{ contant}, \quad (8.120)$$

For $\dot{m} = 0$, then

$$\begin{aligned} \dot{m} = \dot{m}_o = \left(M_1 \dot{n}_1 \right)\Big|_{z=0} = M_1 \dot{n}_{1,o} = \text{ contant}, \\ \dot{n}_1 = \dot{n}_{1,o} = \text{ contant}, \end{aligned} \quad (8.121)$$

From Darcy´s law,

$$u = \frac{M_1 \dot{n}_{1,o}}{cM} = -\frac{1}{R_m} \frac{dp}{dz}$$

or,

$$\dot{n}_1 = -\frac{cM}{R_m M_1} \frac{dp}{dz}, \qquad \frac{dp}{dz} = -\frac{R_m M_1}{cM} \dot{n}_1 \quad (8.122)$$

For N=2

$$\frac{1}{D_{12}}\left(X_2\dot{n}_1 - X_1\dot{n}_2\right) + \frac{R_m}{cRT}\frac{M_1}{M}\dot{n}_1 = -c\frac{dX_1}{dz} - \frac{X_1}{RT}\frac{dp}{dz}$$
$$\frac{1}{D_{21}}\left(X_1\dot{n}_2 - X_2\dot{n}_1\right) + \frac{R_m}{cRT}\frac{M_1}{M}\dot{n}_2 = -c\frac{dX_2}{dz} - \frac{X_2}{RT}\frac{dp}{dz} \tag{8.123}$$

The sum of the two equations recovers Darcy's law. This relation substitutes the last equation of the system to be solved (this was done above with the term $\sum_{k=1}^{N}\bar{J}_k = 0$)

$$\frac{1}{D_{12}}\left(X_2\dot{n}_1 - X_1\dot{n}_2\right) + \frac{R_m}{cRT}\frac{M_1}{M}\dot{n}_1 = -c\frac{dX_1}{dz} - \frac{X_1}{RT}\frac{dp}{dz}$$
$$\frac{R_m}{cRT}\frac{M_1}{M}\dot{n}_1 + \frac{R_m}{cRT}\frac{M_2}{M}\dot{n}_2 = -\frac{1}{RT}\frac{dp}{dz} \tag{8.124}$$

To obtain an analytical solution, from $\dot{n}_2 = 0$

$$\left(\frac{X_2}{D_{12}} + \frac{R_m}{cRT}\frac{M_1}{M}\right)\dot{n}_1 = -c\frac{dX_1}{dz} - \frac{X_1}{RT}\frac{dp}{dz}$$
$$-\frac{X_2}{D_{21}}\dot{n}_1 = -c\frac{dX_2}{dz} - \frac{X_2}{RT}\frac{dp}{dz} \tag{8.125}$$

From Darcy, substituting for dp/dz ,

$$\dot{n}_1 = \frac{c}{X_2\left(\frac{1}{D_{12}} + \frac{1}{RT}\frac{R_m M_1}{M}\right)} - \frac{dX_1}{dz} \tag{8.126}$$

This is the same as to consider

$$\frac{1}{D_1} = \frac{1}{D_{12}} + \frac{1}{RT}\frac{R_m M_1}{cM} \tag{8.127}$$

and

$$\dot{n}_1 = -\frac{cD_1}{X_2}\frac{dX_1}{dz} \tag{8.128}$$

As before, the conservation of mass for species 1 becomes

$$\frac{d}{dz}\left(M_1\dot{n}_1\right) = 0 \tag{8. 129}$$

The boundary condition are:

$$\begin{aligned} z=0, \quad & X_1 = X_{1,o} = \frac{p_{sat\_i}(T)}{p_o}, \quad X_2 = 1 - X_{1,o} \\ z=L, \quad & X_1 = X_{1,L}, \qquad\qquad X_2 = 1 - X_{1,L} \end{aligned} \tag{8.130}$$

where p_o is unknown, since it depends on the pressure drop along the tube.

A direct solution is obtained when the diffusion is equimolal, i.e. $M_1=M_2=M$. This leads to a constant D_1 and the mole fraction distribution becomes

$$\frac{1-X_1}{1-X_{1,o}} = \left(\frac{1-X_{1,L}}{1-X_{1,o}}\right)^{z/L} \tag{8.131}$$

The total molar flux at z = 0 becomes

$$\dot{n}_1 = -\frac{c}{L\left(\frac{1}{D_{21}} + \frac{R_m}{p}\frac{M_i}{M}\right)} \ln\left(\frac{1-X_{1,L}}{1-X_{1,o}}\right) \tag{8.132}$$

When $R_m \to \infty, \dot{n}_1 = 0$. When $R_m \to 0, or\ p \gg R_m M_1/M$, we recover the previous Stefan-tube solution.

The value of $p_{o,}$, the total pressure at the liquid surface, is obtained from the integration of Darcy's Law as

$$\frac{dp}{dz} = -\frac{R_m M_1}{cM}\dot{n}_1 . \tag{8.133}$$

Assuming $M_1=M_2=M$, and integrating form $p=p_L$ at z=L

$$p = p_L + \frac{R_m D_1 M_1}{LM} \ln\left(\frac{1-X_{1,L}}{1-X_{1,o}}\right)\left(L-z\right) \tag{8.134}$$

Since $\dot{n}_1 / \left(cM\right)$ is assumed constant, the pressure variations is linear. The pressure at z=0 is

$$p_o = p_L + \frac{R_m D_1 M_1}{LM} \ln\left(\frac{1-X_{1,L}}{1-X_{1,o}}\right), \qquad X_{1,o} = \frac{p_{1,sat}(T)}{p_o} \tag{8.135}$$

From the solution for p_o, $X_{1,o}$, may be obtained. When $p_{1,sat}(T) \ll p_o$, $p_o \to p_L$ as expected.

These simple problems elucidate the roles of the bulk convective flow and the pressure gradient. The general model developed can be

reduced to the simpler known formulations and capture the pressure effects.

Here a direct validation will not be attempted. The literature provides a vast amount of information that could be used to develop and validate a general computer code. This development is deferred for future work.

9 CONCLUSION

In the present work, a model for the mass transport in the MEA of PEM fuel cells, based on the fundamentals of the multicomponent, multiphase mass transport in porous media, was developed. The model integrates the transport in the gas diffusion layer, micro-porous layer, catalytic layer and membrane into a single Maxwell-Stefan framework.

This work was divided into three parts.

In the first part, the behavior of PEM fuel cells based on current thermodynamics and electrochemical models is reviewed. A thorough description of the characteristics and typical length scales of the different components of the fuel cell was presented in order to obtain fundamental information to help the development of phenomenological models. The models available in the literature were classified and reviewed. The experimental analysis of a 200 W fuel cell stack, using the polarization curve method, allowed to study the basic behavior and magnitude of the variables involved in the fuel cell design and operation. The fuel cell in this work operated exclusively in the activation and ohmic losses regime. The measured polarization curve was analyzed and reproduced using a lumped-component model. Initially, since the measurements did not cover the mass transfer limited regime, the lumped-component model was validated using data from the literature, employing a one-dimensional mass transfer treatment. This model was then applied to reproduce the measurements in this work, obtaining the correspondent set of constants that characterizes the present fuel cell stack.

In the second part of the work, in order to progress towards more comprehensive models, the conservation equations for mass and linear momentum transport in multicomponent fluids were derived based on thermodynamics and continuum mechanics. The focus was on determining the correct form for the driving forces for diffusion for a mixture in creeping flow. Traditional models have assumed local mechanical equilibrium, and the extension for nonequilibrium is thoroughly discussed. After obtaining a general form for the driving force, the Maxwell-Stefan equations were derived from purely mechanical arguments.

Finally, in the third part the models reviewed in part II provided the basis for the development of a general homogeneous model for the transport of liquid, gas and chemical species in a porous medium, under

the action of pressure and electrical potentials. This model is completely expressed in a single matrix form, allowing for the solution of the species, liquid and gas fluxes in and out of the MEA. A few simplified problems were addressed in order to clarify the roles of the bulk convective flow and the pressure gradient.

The main conclusions of this work are presented in the following.

The available models for fuel cells have been developed focusing one of the following purposes: To help to understand the internal physics and chemistry of fuel cells; to focus experimental development efforts; to support system design and optimization; to support or form the basis of control algorithms; to evaluate the technical and economic suitability of fuel cell applications. Models also help with the understanding of the effect of parameters on the fuel cells performance.

The literature review revealed the vast amount of information that exists in PEM fuel cell modeling and simulation. Most of the recent works are improvements of the earlier models and implementations known as Computational Fuel Cell Dynamics –CFCD. They explore multidimensional and multiphysics effects. The higher computational capacity available today allows to use more refined grids, explore more detailed geometries and to develop optimization routines aimed at optimizing certain design or operation features. The basic phenomenology, however, has remained unchanged, based on the classical mass and charge transport models.

Rarely the fuel cell models focus on specific behavior of fuel cell components on attempts to better understand the role of micro and nano phenomena on the macroscopic output. The major difficulty in using the available detailed models and interpreting their results is that the large superposition and interrelation of different modeling principles, with different requirements, produces a very rich macroscopic picture with sometimes over-simplified local features and, in this sense, they lose their generality.

The application of a simple lumped model was able to reproduce the data from the literature for different reactants temperatures and pressures. It provided the parameters needed to predict the polarization curve for the entire range of temperatures and pressures with a single set of constants. Using order of magnitude arguments, these values presented good qualitative agreement to estimates from known mass transfer relations. The modeling with an overall model allowed the understanding of basic fuel cell behavior as well as, to estimate the typical magnitudes of fluxes, potentials and global transport parameters.

This basic footwork established the need for developing a more basic mass transport modeling of the MEA.

The treatment used here consisted in developing the constitutive relations for mass transfer in the context of the Maxwell-Stefan formulation for a general concentration, pressure, temperature and body force (e.g., electrical) driving potential. The traditional derivations based on the dissipation function and the species linear momentum equation lead to basically different formulations that can be brought together only under very restrictive assumptions. The common formulations for the diffusion flux as a result of unbalanced shear stress, constitutive relations for the species diffusion flux of linear momentum and the equality of mixture and species velocities find no direct evidence. This lead to the conclusion that, in a general framework, only the basic driving force for diffusion,

$$\frac{cRT\mathbf{d}_i}{\rho_i} = \nabla_{T,p}\mu_i + v_i\nabla p - \mathbf{f}_i$$

can be safely used, knowing that, with all the consequences,

$$\sum_{i=1}^{N_c}\mathbf{d}_i = \frac{1}{cRT}(\nabla p - \rho\mathbf{f})$$

For creeping flow, *du/dt = 0*, and

$$\sum_{i=1}^{N_c}\mathbf{d}_i = -\frac{1}{cRT}\nabla.\mathbf{S}$$

One of the important consequences is that the well-known Lightfoot formulation is no longer valid. In this context, therefore, the derivation of the Maxwell-Stefan equation becomes a purely mechanical derivation, based only on drag arguments.

The general model for two-phase, multicomponent flow in porous media was developed limited for low Reynolds and low Peclet number. The low Reynolds number ensures that non-linear effects on the momentum equation for the flow in porous medium can be neglected. The low Peclet number ensures that dispersion effects become negligibly small when compared to diffusion effects. Following a Maxwell-Stefan framework, for a system composed of N_β chemical species in the gas phase (β), a liquid phase (γ) and a solid phase (σ), the volume- averaged dynamic equilibrium for a fluid particle of species i in phase β can be expressed as

$$\varepsilon_\beta \sum_{k=1,k\neq i}^{N_\beta} \xi_{ik}\phi_{i,\beta}\phi_{k,\beta}\left(\mathbf{u}_{i,\beta}-\mathbf{u}_{k,\beta}\right)+$$

$$\frac{\varepsilon_\gamma \mu_{\beta\gamma}}{K_{\beta\gamma}} Y_{i,\beta}\left(\mathbf{u}_{i,\beta}-\mathbf{u}_{\gamma}\right)+ \frac{\varepsilon_\sigma \mu_{\beta\sigma}}{K_{\beta\sigma}} Y_{i,\beta}\left(\mathbf{u}_{i,\beta}-\mathbf{u}_{\sigma}\right)=$$

$$-\varepsilon_\beta \rho_\beta Y_{i,\beta}\left(\nabla_{T,p}\mu_{i,\beta}+v_{i,\beta}\nabla p_\beta-\mathbf{f}_{i,\beta}\right)$$

The model captured the interactions among species and phases. Adding up the velocity fields for the species within each phase, the phase momentum equations were recovered, where $K_{\beta\gamma}$ and $K_{\beta\sigma}$ are phase permeabilities. All the equations could be set in a single matrix formulation, allowing for a fully coupled solution.

The general model developed reduced to the well-known forms of Darcy´s law for single phase flow in porous media and the extended forms of Darcy´s law for two-phase flow in porous media. The treatment of the effect of the pressure gradient arose naturally from the equations, without the need to create additional bulk flow terms. Once the correct simplifications are applied the model reduces to the known simple solutions for the Stefan tube and the two-bulb diffusion problems.

The general formulation could be reduced to other models from the literature, as the binary friction model, evidencing the meaning of the transport parameters. The application to simpler mass diffusion problems, as the two-bulb and the Stefan problem, recovered, under the correct assumptions, the simpler well known solutions. These simple problems elucidated the roles of the bulk convective flow and the pressure gradient. The general model developed can capture the pressure effects without resorting to additional *ad-hoc* terms.

Here a direct validation was not attempted. The literature provides a vast amount of information that could be used to develop and validate a general computer code. This development is deferred for future work.

The following suggestions for future work are listed:

1. Program and perform a full validation of the computational code against analytical solutions, solutions from the literature and measurements for binary and ternary mass diffusion problems, in gas and liquid phases.

2. Extend the simulations to PEM fuel cell systems in order to compare the predictions to measurements and models from the literature.
3. Apply the general framework to analyze the operation of PEM fuel cells with multicomponent gas mixtures, simulating the operation with syngas and biogas, and to direct alcohol fuel cells.
4. Analyze the role of heat transfer within the fuel cell components, focusing the operation of larger fuel cell stacks.
5. Formulate two and three dimensional problems and analyze the computational issues involved.
6. Extend the model to account for Knudsen flow in porous media to allow the modeling of high temperature fuel cells, as the SOFC fuel cells.

REFERENCES

ACEVEDO, L. E. G. Simulação e análise de um reator de reforma de metano para a produção de hidrogênio. 2006. 183 p. (Mestre em Engenharia Mecânica). Departamento de Engenharia Mecânica, Universidade Federal de Santa Catarina, Florianópolis.

ALBERTI, G.; CASCIOLA, M. Solid state protonic conductors, present main application and future prospects. Solid States Ionics, v. 145, n. 1-4, p. 3-16, 2001.

ALBERTAZZI, G. Jr. A., SOUSA, A. R. Fundamentos de emtrologia cientifica e industrial. Barueri, SP: Ed. Manole 2008

AMPHLETT, J. C.; BAUMERT, R. M.; MANN, R. F.; PEPPLEY, B. A.; ROBERGE, P. R.; HARRIS, T. J. Performance modeling of the Ballard Mark IV solid polymer electrolyte fuel cell: I. Mechanistic model development. Journal of the Electrochemical Society, v. 142, n. 1, p. 1-8, 1995a.

_____. Performance modeling of the Ballard Mark IV solid polymer electrolyte fuel cell: II. Empirical model development. Journal of the Electrochemical Society, v. 142, n. 1, p. 9-15, 1995b.

AMPHLETT, J. C.; MANN, R. F.; PEPPLEY, B. A.; ROBERGE, P. R.; RODRIGUES, A. A model predicting transient responses of proton exchange membrane fuel cells. Journal of Power Sources, v. 61, n. 1-2, p. 183-188, 1996.

AMUNDSON, N. R.; PAN, T.-W.; PAULSEN, V. I. Diffusing with Stefan and Maxwell. Fluid Mechanics and Transport Phenomena. AIChE Journal, v. 49, n. 4, p. 813-830, 2003.

ANL. General Computational Toolkit (GcTool) Documentation Argonne National Laboratory: disponível em: www.transportation.anl.gov/modeling Acesso em 2008.

ARATO, E.; COSTA, P. Gas-phase mass-transfer resistance at PEMFC electrodes: Part 1. Diffusive and forced migration through a

porous medium. Journal of Power Sources, v. 158, n. 1, p. 200-205, 2006a.

_____. Transport mechanisms and voltage losses in PEMFC membranes and at electrodes: a discussion of open-circuit irreversibility. Journal of Power Sources, v. 159, n. 2, p. 861-868, 2006b.

ARATO, E.; PINNA, M.; COSTA, P. Gas-phase mass-transfer resistance at PEMFC electrodes: Part 2. Effects of the flow geometry and the related pressure field. Journal of Power Sources, v. 158, n. 1, p. 206-212, 2006.

ATKINS, P. W. Physical Chemistry. 6 ed. Oxford University Press, 1998. 997 p.

BARBIR, F. PEM Fuel Cells. In: SAMMES, N. (Ed.). Fuel Cell Technology - Reaching Towards Commercialization Germany: Springer-Verlag London Limited, 2006. p.27-50.

_____. PEM Fuel Cells: Theory and Practice. Elsevier Science & Technology, 2011.

BARD, A. J.; FAULKNER, L. R. Electrochemical Methods - Fundamentals and Application. John Wiley & Sons, 1980.

BASCHUK, J. J. Comprehensive, consistent and systematic approach to the mathematical modeling of PEM fuel cells. 2006. 240 p. (Doctor of Phylosophy in Mechanical Engineering). Mechanical Engineering, University of Waterloo, Canadá.

BASCHUK, J. J.; LI, X. Modeling of polymer electrolyte membrane fuel cells with variable degrees of water flooding. Journal of Power Sources, v. 86, n. 1-2, p. 181-196, 2000.

_____. A general formulation for a mathematical PEM fuel cell model. Journal of Power Sources, v. 142, p. 134-153, 2004.

BEN. Balanço energético nacional 2011. (Brasil)- ano base 2010. Ministério de Minas e Energia . Rio de Janeiro: Empresa de Pesquisa Energética 2011

BEN. Balanço energético nacional 2012. (Brasil)- ano base 2011. Ministério de Minas e Energia. Rio de Janeiro: Empresa de Pesquisa Energética 2012

BERNARDI, D.; VERBRUGGE, M. A mathematical model of a gas diffusion electrode bonded to a polymer electrolyte. AIChE Journal, v. 37, n. 8, p. 1151-1163, 1991.

_____. A mathematical model of the solid-polymer electrolyte fuel cell. Journal of the Electrochemical Society, v. 139, n. 9, p. 2477-2491, 1992.

BERNING, T.; LU, D. M.; DJILALI, N. Three-dimensional computational analysis of transport phenomena in a PEM fuel cell. Journal of Power Sources, v. 106, n. 1-2, p. 284-294, 2002.

BERNING, T.; DJILALI, N. A 3D, A 3D, Multiphase, Multicomponent Model of the Cathode and Anode of a PEM Fuel Cell. Journal of the electrochemical society, v.150 n.12 p. A1589-A1598, 2003a

BERNING, T.; DJILALI, N. Three-dimensional computational analysis of transport phenomena in a PEM fuel cell – a parametric study. Journal of power sources. V. 124 p. 440-452, 2003b

BICAKOVA, O., STRAKA, P., Production of hydrogen from renewable resources and its effectiveness. Review. International Journal of hydrogen Energy. V37 p. 11563 2012

BIRD, R. B.; STEWART, W. E.; LIGHTFOOT, E. N. Transport Phenomena. New York: John Wiley & Sons, 2002.(2nd) 780 p.

BIYIKOGLU, A. A review of proton exchange membrane fuel cell models. International Journal of Hydrogen Energy, v. 30, n. 11, p. 1181-1212, 2005.

BLOMEN, L. J. M. J.; MUGERWA, M. N. Fuel Cell Systems. Plenum Press, 1993. 614 p.

BOTHE, D. On multicomponent two-phase flows with mass transfer. Waseda University: International Workshop on Mathematical Fluid Dynamics 2010.

_____. On the Maxwell-Stefan approach to multicomponent diffusion. In: ESCHER, J., et al (Ed.). Parabolic Problems - Progress in Nonlinear Differential Equations and Their Applications Springer Basel AG, v.80, 2011. p.81-93.

BREITER, M. W. Electrochemical Process in Fuel Cell. Springer-Verlag, 1969. 274 p.

BUNGAY, P. M.; BRENNER, H. Pressure drop due to the motion of a sphere near the wall bounding a poiseuille flow. Journal Fluid Mechanics, v. 60, p. 81-96, 1973.

CANDUSSO, D.; HAREL, F.; DE BERNARDINIS, A.; FRANÇOIS, X.; PÉRA, M. C.; HISSEL, D.; SCHOTT, P.; COQUERY, G.; KAUFFMANN, J.-M. Characterisation and modelling of a 5 kW PEMFC for transportation applications. International Journal of Hydrogen Energy, v. 31, n. 8, p. 1019-1030, 2006.

CAPPADONIA, M.; ERNING, J. W.; STIMMING, U. Proton conduction of Nafion® 117 membrane between 140 K and room temperature. Journal of Electroanalytical Chemistry, v. 376, n. 1-2, p. 189-193, 1994.

CARTY, R.; SCHRODT, T. Concentration profiles in ternary gaseous diffusion. Ind. Eng. Chem. Fundam., v. 14, n. 3, p. 276-278, 1975.

CD-ADAPCO. Star-CD Documentation CD-Adapco Group: Disponível em: www.cd-adapco.com Acesso em 2008.

CENGEL, Y. A.; BOLES, M. A. Thermodynamics - an Engineering Approach. 5 ed. Mc Graw Hill, 2005. 881 p.

CHAPMAN, S.; COWLING, T. G. The mathematical theory of non-uniform gases. 3 ed. Cambridge Mathematical Library, 1970.

_____. The Mathematical Theory of Non-uniform Gases: An Account of the Kinetic Theory of Viscosity, Thermal Conduction and Diffusion in Gases. 3 ed. Cambridge University, 1991.

CHEN, K. S.; EVANS, G. H.; LARSON, R. S.; NOBLE, D. R.; HOUF, W. G. Final report on LDRD project: A phenomenological model for multicomponent transport with simultaneous electrochemical reaction in concentrated solutions. Sandia National Laboratories. Albquerque. 2000

CHEN, N. H.; OTHMER, D. F. New generalized equation for gas diffusion coefficient. Journal of Chemical Engineering Data, v. 7, n. 1, p. 37-41, 1962.

COMSOL. Chemical Engineering Model - Femlab Documentation Comsol: Disponível em: www.comsol.com/products/chem Acesso em 2008.

COSTAMAGNA, P. Transport phenomena in polymeric membrane fuel cells. Chemical Engineering Science, v. 56, n. 2, p. 323-332, 2001.

CROW, D. R. Principles and Application of Electrochemistry. Black Academic & Professional, 1994. 282 p.

CURTISS, C. F.; BIRD, R. B. Milticomponent diffusion in polymeric liquids. Proceedings of the National Academy of Sciences of USA, v. 93, n. 15, p. 7440-7445, 1996.

DE GROOT, S. R.; MAZUR, P. Non-Equilibrium Thermodynamics. New York: Dover Publications, 1984. 510 p.

DEMOND, A. H.; ROBERTS, P. V. Effect of interfacial forces on two-phase capillary pressure-saturation relationships. Water Resources Research, v. 27, n. 3, p. 423-437, 1991.

DHATHATHREYAN, K. S.; RAJALAKSHMI, N. Polymer electrolyte membrane fuel cell In: BASU, S. (Ed.). Recent trends in fuel cell science and technology. New Delhi, India: Anamaya Publishers, 2007. p.40-115.

DIAT, O.; GEBEL, G. Fuel cell proton channels. Nature Materials, v. 7, p. 13-14, 2008.

DJILALI, N. Computational modelling of polymer electrolyte membrane (PEM) fuel cells: challenges and opportunities. Energy, v. 32, p. 269-280, 2007.

DUNCAN, J. B.; TOOR, H. L. An experimental study of three component gas diffusion. AIChE Journal, v. 8, n. 1, p. 38-41, 1962.

DUTTA, S.; SHIMPALEE, S.; VAN ZEE, J. W. Three-dimensional numerical simulation of straight channel PEM fuel cells. Journal of Applied Electrochemistry, v. 30, p. 135-146, 2000.

_____. Numerical prediction of mass-exchange between cathode and anode channels in a PEM fuel cell. International Journal of Heat and Mass Transfer, v. 44, p. 2029-2042, 2001.

ELLIOT, J. A.; WU, D.; PADDISON, S. J.; MOORE, R. B. A unified morphological description of Nafion membranes from SAXS and mesoscale simulations. Soft Matter, v. 7, n. 15, p. 6820-6827, 2011.

ELLIOT, J. R.; LIRA, C. Introductory Chemical Engineering Thermodynamics. Prentice-Hall. International Series in the Physical and Chemical Engineering Sciences, 2000.

ENERDATA, Global Energy Statistical Yearbook 2012. Total primary production. Available in :< http://yearbook.enerdata.net/#/energy-primary-production.html> Accessed on October 2012.

FIMRITE, J. A. Transport phenomena in polymer electrolyte membranes. 2002. 139 p. (Master of Applied Science). Department of Mechanical Engineering, University of Victoria, Canadá.

FLUENT. Fluent Documentation Disponível em: www.fluent.com Acesso em 2008.

FULLER, E. N.; SCHETTLER, P. D.; GIDDINGS, J. C. A new method for prediction of binary gas-phase diffusion coefficients. Industrial and Engineering Chemistry, v. 58, n. 5, p. 19-27, 1966.

FULLER, T.; NEWMAN, J. Water and thermal management in solid-polymer electrolyte fuel cells. Journal of the Electrochemical Society, v. 140, n. 5, p. 1218-1225, 1993.

FURRY, W. H. On the elementary explanation of diffusion phenomena in gases. American Journal of Physics, v. 16, n. 2, p. 63-78, 1948.

GARCIA-ACEVEDO, L. E.; FIGUEROA, R. F.; OLIVEIRA, A. A. M.; BAZZO, E. Analysis of mass and charge transfer in a PEM fuel cell. Proceeding of COBEM, 2007.

GIERKE, T. D.; MUNN, G. E.; WILSON, F. C. The morphology in nafion perfluorinated membrane products as determined by wide- and small-angle x-ray studies. Journal of Polymer Science: Polymer Physics Edition, v. 19, n. 11, p. 1687-1704, 1981.

GOSTICK, J. T.; FOWLER, M. W.; LOANNIDIS, M. A.; PRITZKER, M. D.; VOLFKOVICH, Y. M.; SAKARS, A. Capillary pressure and hydrophilic porosity in gas diffusion layers for polymer electrolyte fuel cells. Journal of Power Sources, v. 156, n. 2, p. 375-387, 2006.

GRANIER, J.; SALAS, J.-F.; RIVA, R.; POIROT-CROUVEZIER, J.-P. The hydrogen pathway - Innovative concepts for bipolar plates: CLEFS CEA Winter 2004/2005.

GRAY, W. G., A derivation of the equations for multiphase transport. Chem. Engng. Sci. 30, p.229-2331975

GURAU, V.; BARBIR, F.; LIU, H. An analytical solution of a half-cell model for PEM fuel cells. Journal of the Electrochemical Society, v. 147, n. 7, p. 2468-2477, 2000.

GURAU, V.; BLUEMLE, M. J.; CASTRO, E. S.; TSOU, Y.-M.; MANN JR., A.; ZAWODZINSKI, T. A. Characterization of transport properties in GDL for PEMFC 1. Wetability - International contact angle to water and surface energy of GDL fibers. Journal of Power Sources, v. 160, p. 1156-1162, 2006.

GURAU, V.; BLUEMLE, M. J.; DE CASTRO, E. S.; TSOU, Y.-M.; ZAWODSINSKI JR., T.; MANN JR, J. A. Characterization of transport properties in GDL for PEMFC 2. Absolute permeability. Journal of Power Sources, v. 165, n. 793-802, 2007.

GURAU, V.; LIU, H.; KAKAÇ, S. Two-dimensional model for proton exchange membrane fuel cells. AIChE Journal, v. 44, n. 11, p. 2410-2422, 1998.

HAASE, R. Thermodynamics of irreversible processes. London: Addison-Wesley, 1969.

HAMANN, C. H.; HAMNETT, A.; VIELSTICH, W. Electrochemistry. Wiley-VCH, 1998.

HARALDSSON, K.; WIPKE, K. Evaluating PEM fuel cell system models. Journal of Power Sources, v. 126, n. 1-2, p. 88-97, 2004.

HAULBOLD, H.-G.; VAD, T.; JUNGBLUTH, H.; HILLER, P. Nano struture of NAFION: a SAXS study. Electrochimica Acta, v. 46, n. 10-11, p. 1559-1563, 2001.

HEINZELMANN, F. J.; WASAN, D. T.; WILKE, C. R. Concentration profiles in stefan diffusion tube. Ind. Eng. Chem. Fundamen., v. 4, n. 1, p. 55-61, 1965.

HEITNER-WIRGUIN, C. Recent advances in perfluorinated ionomer membranes: struture, properties and applications. Journal of Membrane Science, v. 120, n. 1, p. 1-33, 1996.

HIRSCHFELDER, J. O.; CURTISS, C. F.; BIRD, R. B. Molecular Theory of Gases and Liquids. New York: John Wiley, 1954.

HONTAÑÓN, E.; ESCUDERO, M. J.; BAUTISTA, C.; GARCÍA-YBARRA, P. L.; DAZA, L. Optimisation of flow-field in polymer electrolyte membrane fuel cells using computational fluid dynamics techniques. Journal of Power Sources, v. 86, n. 1-2, p. 363-368, 2000.

HOOGERS, G. Fuel cell Technology Handbook. CRC Press, 2003.

HSU, W. Y.; GIERKE, T. D. Elastic theory for ionic clustering in perfluorinated ionomers. Macromolecules, v. 15, n. 1, p. 101-105, 1982.

_____. Ion transport and clustering in nafion perfluorinated membranes. Journal of Membrane Science, v. 13, n. 3, p. 307-326, 1983.

HURLEY, P. Build your own fuel cells. Wheelock mountain publication, 2002.

INZELT, G.; PINERI, M.; SCHULTZE, J. W.; VOROTYNTSEV, M. A. Electron and proton conducting polymers: recent developments and prospects. Electrochimica Acta, v. 45, n. 15-16, p. 2403-2421, 2000.

JANG, S. S.; MOLINERO, V.; ÇAGIN, T.; GODDARD III, W. A. Effect of monomeric sequence on nanostructure and water dynamics in Nafion 117. Solid States Ionics, v. 175, p. 805-808, 2004.

JESUS, J. R. Obtenção e avaliação das propriedades físico-químicas de membranas poliméricas SPEEK/PANI de condução mista. 2005. 105 p. (Doutor em Química). Centro de Ciências Físicas e Matemáticas, Universidade Federal de Santa Catarina, Florianópolis.

JIAO, K.; LI, X. Water transport in polymer electrolyte membrane fuel cells. Progress in energy and combustion science, v. 37, p. 221-291, 2011.

KÄFER, K. A. Obtenção e caracterização de compósits de poli(éter-éter-cetona) sulfonado/níquel-fósforo com condução protônica e

elétrica. 2010. 74 p. (Mestre em Ciências e Engenharia de Materiais). Ciências e Engenharia de Materiais, Universidade Federal de Santa Catarina, Florianópolis.

KAST, W.; HOHENTHANNER, C.-R. Mass transfer within the gas-phase of porous media. International Journal of Heat and Mass Transfer, v. 43, n. 5, p. 807-823, 2000.

KAVIANY, M. Principles of heat transfer in porous media. 2nd ed. New York: Springer, 1995. 708 p.

_____. Principles of Convective Heat Transfer. 2nd ed. New York: Springer, 2001a.

_____. Principles of Heat Transfer. New York: Wiley, 2001b.

KAZIM, A.; LIU, H.; FORGES, P. Modelling of performance of PEM fuel cells with conventional and interdigitated flow fields. Journal of Applied Electrochemistry, v. 29, n. 12, p. 1409-1416, 1999.

KERKHOF, P. J. A. M., GEBOERS, M. A. M. Analysis and extension of the theory of multicomponent fluid diffusion, Chemical Engineering Science, V. 60, Issue 12, June 2005, Pages 3129–3167

KERKHOF, P. J. A. M. A modified Maxwell-Stefan model for transport through inert membranes: the binary friction model. The Chemical Engineering Journal v. 64, n. 3, p. 319-343, 1996.

_____. New light on some old problems: revisiting the Stefan Tube, Graham's Law, and the Bosanquet Equation. Ind. Eng. Chem. Res., v. 36, n. 3, p. 915-922, 1997.

KIM, J.-S.; PARK, J.-B.; KIM, Y.-M.; AHN, S.-H.; SUN, H.-Y.; KIM, K.-H.; SONG, T.-W. Fuel cell end plates: a review. International Journal of Precision Engineering and Manufacturing, v. 9, n. 1, p. 39-46, 2008.

KIM, J.; LEE, S.-M.; SRINIVASAN, S.; CHAMBERLIN, C. E. Modeling of proton exchange membrane fuel cell performance

with an empirical equation. Journal of Electrochemical Society, v. 142, n. 8, p. 2670-2674, 1995.

KIM, M.-H.; GLINKA, C. J.; GROT, S. A.; GROT, W. G. SANS study of the effects of water vapor sorption on the nanoscale structure of perfluorinated sulfoni acid (NAFION) membranes. Macromolecules, v. 39, p. 4775-4787, 2006.

KIRILLIN, V. A.; SICHEV, V. V.; SHEINDLIN, A. E. Termodinámica Técnica. 2 ed. Ed. Moscú, 1986.

KONDEPUDI, D.; PRIGOGINE, I. Modern Thermodynamics - From Heat Engines to Dissipative Structures. Chichester: Wiley, 1998.

KORDESCH, K.; SIMADER, G. Fuel Cells and Their Applications. VCH, 1996.

KRISHNA, R. Steady-state mass transport in multicomponent liquid mixtures. Letters In Heat and Mass Transfer, v. 3, p. 153-162, 1976.

KRISHNA, R.; WESSELINGH, J. A. The Maxwell-Stefan-Maxwell approach to mass transfer - Review article number 50. Chemical Engineering Science, v. 52, n. 6, p. 861-911, 1997.

KUIKEN, G. D. C. Thermodynamics of Irreversible Processes. Chichester: Wiley & Sons, 1994.

KULIKOVSKY, A. A. The voltage current curve of a PEM fuel cell: analytical and numerical modeling. Nanotech, v. 3, p. 467-470, 2003a.

KULIKOVSKY, A. A. Quasi-3D modeling of water transport in polymer electrolyte fuel cells. Journal of the Electrochemical Society, v. 150, n. 11, p. 1432-1439, 2003b.

LAM, S. H. Multicomponent diffusion revisited. Physics of Fluids, v. 18, p. 1-8, 2006.

LARMINIE, J.; DICKS, A. Fuel Cell System Explained. John Wiley & Sons Ltd., 2003.

LAURENCELLE, F.; CHAHINE, R.; HAMELIN, J.; AGBOSSOU, K.; FOURNIER, M.; BOSE, T. K.; LAPERRIÈRE, A. Characterization of a ballard MK5-E proton exchange membrane fuel cell stack. Fuel cells, v. 1, n. 1, p. 66-71, 2001.

LEONARDI E., ANGELI C. On Maxwell-Stefan approach to diffusion: A general resolution in the transient regime for one-dimensional systems. Journal of physical chemistry, 2010 v.114 p. 1511-164

LI, P.-W.; SCHAEFER, L.; WANG, Q.-M.; ZHANG, T.; CHYU, M. K. Multi-gas transportation and electrochemical performance of a polymer electrolyte fuel cell with complex flow channels. Journal of Power Sources, v. 115, n. 1, p. 90-100, 2003.

LI, S.; BECKER, U. A three-dimensional CFD model for PEMFC - Proceedings of the 2004 Fuel Cell Science. Engineering and Technology Conference, 2004. American Society of Mechanical Engineers. p.157-164.

LI, X.; SABIR, I. Review of bipolar plates in PEM fuel cells: flow-field designs. International Journal of Hydrogen Energy, v. 30, n. 4, p. 359-371, 2005.

LIGHTFOOT, E. N. Transport Phenomena and Living Systems: Biomedical Aspects of Momentum and Mass Transport. New York: Wiley-Interscience, 1974.

LINARDI, M. Introdução à ciência e tecnologia de células a combustível São Paulo: ArtLiber Editora Ltda, 2010.

LITSTER, S.; PHAROAH, J. G.; MCLEAN, G.; DJILALI, N. Computational analysis of heat and mass transfer in a micro-structured PEMFC cathode. Journal of Power Sources, v. 156, n. 2, p. 334-344, 2006.

LMS. Emmeskay Documentation LMS - International Acquires Emmeskay: Disponível em: www.emmeskay.com Acesso em 2008.

LUGG, G. A. Diffusion coefficients of some organic and other vapors in air. Analytical Chemistry, v. 40, n. 7, p. 1072-1077, 1968.

MARIÑO, D. L.; FIGUEROA, R. F.; GARCIA-ACEVEDO, L. E.; PORRAS, G. O.; OLIVEIRA, A. A. M. Thermal and electrical characterization and modeling of a proton exchange membrane fuel cell (PEMFC). Summited to Hydrogen Power, 2012.

MARIÑO, D. L. M. Thermal and electrical characterization and modeling of a proton exchange membrane fuel cell (PEMFC). 2011. (Final course project). Mechanical Engineering Department, Universidade Federal de Santa Catarina, Florianópolis.

MASON, E. A.; DEL CASTILLO, L. F. The role of viscous flow in theories of membrane transport. Journal of Membrane Science, v. 23, n. 2, p. 199-220, 1985.

MASON, E. A.; LONSDALE, H. K. Statistical-mechanical theory of membrane transport. Journal of Membrane Science, v. 51, n. 1-2, p. 1-81, 1990.

MASON, E. A.; MALINAUKAS, A. P. Gas Transport in Porous Media: The Dusty-gas Model. Amsterdam: Elsevier, 1983.

MATELLI, J. A. Sistemas de cogeração baseados em células-combustíveis aplicados em hospitais. 2001. 116 p. (Mestre em Engenharia Mecânica). Departamento de Engenharia Mecânica, Universidade Federal de Santa Catarina, Florianópolis.

MATHIAS, M.; ROTH, J.; FLEMING, J.; LEHNERT, W. Diffusion media materials and characterization. In: VIELSTICH, W., et al (Ed.). Handbook of Fuel Cells: Fundamentals, Technology, Applications: John Wiley & Sons, v.4, 2003. p.517-537.

MATHUR, V. K.; CRAWFORD, J. Fundamentals of Gas Diffusion Layers in PEM Fuel Cells. In: BASU, S. (Ed.). Recent Trends in Fuel Cell Science and Technology. New Delhi, India: Springer, 2007. p.116-128.

MAURITZ, K. A.; MOORE, R. B. State of understanding of Nafion. Chemical Reviews, v. 104, p. 4535-4585, 2004.

MEYER, J. P.; KOSTIN, M. D. Circulation phenomena in stefan diffusion. International Journal of Heat and Mass Transfer, v. 18, n. 11, p. 1293-1297, 1975.

MIKKOLA, M. Laboratory of Advanced Energy Systems. New & Renewable Energy System Group. Helsinki University of Technology: Available in : http://tfy.tkk.fi/aes/AES/projects/renew/fc.html Accessed on 2007.

NAM, J. H.; KAVIANY, M. Effective diffusivity and water-saturation distribution in single- and two-layer PEMFC diffusion medium. International Journal of Heat and Mass Transfer, v. 46, n. 24, p. 4595-4611, 2003.

NATARAJAN, D.; NGUYEN, T. A two-dimensional, two-phase, multicomponent, transient model for the cathode of a proton exchange membrane fuel cell using conventional gas distributors. Journal of The Electrochemical Society, v. 148, n. 12, p. 1324-1335, 2001.

NATARAJAN, D.; VAN NGUYEN, T. Three-dimensional effects of liquid water flooding in the cathode of a PEM fuel cell. Journal of Power Sources, v. 115, n. 1, p. 66-80, 2003.

NGUYEN, T.; WHITE, R. A water and heat management model for proton exchange membrane fuel cells. Journal of The Electrochemical Society, v. 140, n. 8, p. 2178-2186, 1993.

NGUYEN, T. P.; BERNING, T.; DJILALI, N. Computational model of a PEM fuel cell with serpentine gas flow channels. Journal of Power Sources, v. 130, n. 1-2, p. 149-157, 2004.

NITTA, I. Inhomogeneous compression of PEMFC gas diffusion layers. 2008. 89 p. (Doctor of Science in Technology). Department of Engineering Physics, Helsinki University of Technology, Espoo, Finland.

NUNES, N. T. K. Implementação de uma bancada e caracterização experimental de uma célula a combustível tipo PEM de 200 w. 2011. (Projeto final de curso). Departamento de Engenharia Mecânica, Universidade Federal de Santa Catarina, Florianóplis.

PHILIP, J. R.; DE VRIES, D. A. Moisture movement in porous materials under temperature gradients. Tran. Am. Geophysical Union, v. 38, n. 2, p. 222-232, 1957.

PIÑA, R. F. F. Análise e desenvolvimento de reformador compacto de etanol para obtenção de hidrogênio. 2006. 173 p. (Mestre em Engenharia Mecânica). Departamento de Engenharia Mecânica, Universidade Federal de Santa Catarina, Florianópolis.

PRIGOGINE, I. Introduction to thermodynamics of irreversible processes. 3rd ed. New York: Interscience Publishers, 1968.

QUINTARD, M.; BLETZACKER, L.; CHENU, D.; WHITAKER, S. Nonlinear, multicomponent, mass trasnsport in porous media. Chemical Engineering Science, v. 61, n. 8, p. 2643-2669, 2006.

RAO, S. S.; BENNETT, C. O. Radial effects in a Stefan diffusion tube. Ind. Eng. Chem. Fundam., v. 5, n. 4, p. 573-575, 1966.

RABEY K.and VERSTRAETE, W., Microbial fuel cell: Novel biotechnology for energy generation. Review. Trends in biotechnology. V.23 n.6 p.291-298, 2005

REN, G. P.; YU, L. J.; JIANG, X. M.; YUAN, J. Q. A three dimensional, gas-liquid two-phase flow and transport model for PEM fuel cell with interdigitated flow field. 2007

RESHETENKO, T. V., BETHUNE, K.,ROCHELEAU, R. Spatial proton exchange membrane fuel cell performance under carbon monoxide poisoning at a low concentration using a segmented cell system, Journal of Power Sources, Volume 218, 15, p.412-423, 2012.

ROLLET, A. L.; DIAT, O.; GEBEL, G. A new insight into Nafion structure. The Journal of Physical Chemistry B, v. 106, n. 12, p. 3033-3036, 2002.

ROSNER, D. E. Transport Processes in Chemically Reacting Flow Systems. Butterworths, Boston: 1986.

_____. Transport Processes in Chemically Reacting Flow Systems. Canada: General Publishing Company, 2000.

ROWE, A.; LI, X. Mathematical modeling of proton exchange membrane fuel cells. Journal of Power Sources, v. 102, n. 1-2, p. 82-96, 2001.

RUBATAT, L.; ALLEGRAUD, J. J.; GEBEL, G.; VAN DER HEIJDEN, P.; ROSA, A.; DIAT, O. Large scale structure in perfluorinated ionomer membranes (Nafion): CEA-Grenoble, Groupe Polymères Conducteurs Ioniques, DRFMC/SI3M 2004.

RUBATAT, L.; GEBEL, G.; DIAT, O. Fibrillar structure of Nafion: matching fourier and real space studies of corresponding films and solutions. Macromolecules, v. 37, n. 20, p. 7772-7783, 2004.

RUBATAT, L.; ROLLET, A. L.; GEBEL, G.; DIAT, O. Evidence of elongated polymeric aggregates in Naftion Macromolecules, v. 35, n. 10, p. 4050-4055, 2002.

SAITO, M.; HAYAMIZU, K.; OKADA, T. Temperature dependence of ion and water transport in perfluorinated ionomer membranes for fuel cells. J. Phys. Chem. B., v. 109, n. 8, p. 3112-3119, 2005.

SCHMIDT-ROHR, K.; CHEN, Q. V.N.5 Water nanochannels in Nafion®: quantitative scattering analysis and NMR. DOE Hydrogen Program - FY 2007 Annual Progress Report, p.975-978. 2007

_____. Parallel cylindrical water nanochannels in Nafion flel-cell membranes. Nature Materials, v. 7, p. 75-83, 2008a.

_____. Supplementary Material for "Parallel cylindrical water nanochannels in the Nafion fuel cell membrane". Nature Materials Group, 2008b.

SCHUSTER et al., 2010

SHIMPALEE, S.; DUTTA, S. Numerical prediction of temperature distribution in PEM fuel cells. Numerical Heat Transfer. Part A: Applications, v. 38, n. 2, p. 111-128, 2000.

SHIMPALEE, S.; DUTTA, S.; LEE, W.; ZEE, J. V. Effect of humidity on PEM fuel cell performance Part II - Numerical simulation American Society of Mechanical Engineers, Heat Transfer Division - HTD, v. 364, n. 1, p. 367-374, 1999.

SHIMPALEE, S.; GREENWAY, S.; SPUCKLER, D.; VAN ZEE, J. W. Predicting water and current distributions in a commercial-size PEMFC. Journal of Power Sources, v. 135, n. 1-2, p. 79-87, 2004.

SHIMPALEE, S.; LEE, W.-K.; ZEE, J. V.; NASERI-NESHAT, H. Predicting the transient response of a serpentine flow-field PEMFC: I. Excess to normal fuel and air. Journal of Power Sources, v. 156, n. 2, p. 355-368, 2006a.

SHIMPALEE, S.; LEE, W.; ZEE, J. V.; NASERI-NESHAT, H. Predicting the transient response of a serpentine flow-field PEMFC: II.Normal to minimal fuel and air. Journal of Power Sources, v. 156, n. 2, p. 369-374, 2006b.

SIEGEL, C. Review of computational and mass transfer modeling in polymer-electrolyte-membrane (PEM) fuel cells. Energy, v. 33, p. 1331-1352, 2008.

SIEGEL, N. P.; ELLIS, M. W.; NELSON, D. J.; VON SPAKOVSKY, M. R. Single domain PEMFC model based on agglomerate catalyst geometry. Journal of Power Sources, v. 115, n. 1, p. 81-89, 2003.

_____. A two-dimensional computational model of a PEMFC with liquid water transport. Journal of Power Sources, v. 128, n. 2, p. 173-184, 2004.

SILVA, A. P. Comportamento térmico de sistemas bifásicos para arrefecimento de células a combustível tipo PEM. 2010. 130 p. (Mestre em Engenharia Mecânica). Departamento de Engenharia Mecânica, Universidade Federal de Santa Catarina, Florianópolis.

SINGH, D.; LU, D.; DJILALI, N. A two-dimensional analysis of mass transport in proton exchange membrane fuel cells. International Journal of engineering Science, v. 37, n. 4, p. 431-452, 1999.

SIVERTSEN, B. R.; DJILALI, N. CFD-based modelling of proton exchange membrane fuel cells. Journal of Power Sources, v. 141, n. 1, p. 65-78, 2005.

SLATERRY, J. C. Momentum, Energy and Mass Transfer in Continua. Huntington, N.Y.: R. E. Krieger Pub. Co., 1981.

SONG, S., TSIAKARAS P. Recent progress in direct ethanol exchange membrane fuel cells (DE-PEMFCs). Applied Catalysis, Vol. 63. p. 187-193, 2006.

SOULAINE, C.; DEBENEST, G.; QUINTARD, M. Upscaling multi-component two-phase flow in porous media with partitioning coefficient. Chemical Engineering Science, v. 66, n. 23, p. 6180-6192, 2011.

SOUSA JR., R.; GONZALES, E. R. Mathematical modeling of polymer electrolyte fuel cells. Journal of Power Sources, v. 147, n. 1-2, p. 32-45, 2005.

SOUZY, R.; AMEDURI, B. Functional fluoropolymers for fuel cell membranes. Progress in Polymer Science, v. 30, n. 6, p. 644-687, 2005.

SPIEGEL, C. PEM Fuel Cell - Modeling and Simulation using Matlab. Academic Press, 2008.

SPRINGER, T.; WILSON, M.; GOTTESFELD, S. Modeling and experimental diagnostics in polymer electrolyte fuel cells. Journal of the Electrochemical Society, v. 140, n. 12, p. 3513-3526, 1993.

SPRINGER, T.; ZAWODZINSKI, T.; GOTTESFELD, S. Polymer electrolyte fuel cell model. Journal of the Electrochemical Society, v. 138, n. 8, p. 2334-2342, 1991.

STANDART, G. L.; TAYLOR, R.; KRISHNA, R. The Maxwell-Stefan formulation of irreversible thermodynamics for simultaneous heat and mass transfer. Chem. Eng. Commun., v. 3, p. 277-289, 1979.

STEIDEL, P. S. Estudo teórico e experimental de célula-combustível tipo PEM e perspectivas de aplicação em sistemas de geração distribuída. 2005. 86 p. (Mestre em Engenharia Mecânica). Departamento de Engenharia Mecânica, Universidade Federal de Santa Catarina, Florianópolis.

STOCKIE, J. M.; PROMISLOW, K.; WETTON, B. R. A finite volume method for multicomponent gas transport in a porous fuel cell electrode. International Journal for Numerical Methods in Fluids, v. 0, p. 1-35, 2001.

TASAKA, M.; SUZUKI, S.; OGAWA, Y.; KAMAYA, M. Freezing and nonfreezing water in charged membranes. Journal of Membrane Science, v. 38, n. 2, p. 175-183, 1988.

TAYLOR, R.; KRISHNA, R. Milticomponent Mass Transfer. New York: John Wiley & Sons, Inc., 1993.

THOMPSON, E. L.; CAPEHART, T. W.; FULLER, T. J.; JORNE, J. Investigation of low-temperature proton transport in Nafion using direct current conductivity and Differential Scanning Calorimetry. J. Electrochem. Soc., v. 153, n. A2351, 2006.

TICIANELLI, E. A.; GONZALES, E. R. Células a combustível: uma alternativa promissora para a geração de eletricidade. Química Nova, v. 12, n. 3, p. 268-272, 1989.

TRUESDELL, C. A.; TOUPIN, R. A. The Classical Field Theories - Handbuch der Physik 3/1. Berlin: Springer-Verlag, 1960.

UM, S.; WANG, C.-Y. Three dimensional analysis of transport and reaction in proton exchange membrane fuel cells. The ASME International Mechanical Engineering Congress & Exposition, 2000. Walt Disney World Dolphin - Orlando. Proceedings of The ASME Fuel Cell Division.

_____. Three-dimensional analysis of transport and electrochemical reactions in polymer electrolyte fuel cells. Journal of Power Sources, v. 125, n. 1, p. 40-51, 2004.

UM, S.; WANG, C.-Y.; CHEN, K. S. Computational fluid dynamics modeling of proton exchange membrane fuel cells. Journal of The Electrochemical Society, v. 147, n. 12, p. 4485-4493, 2000.

USA. Department of Energy (DOE). DOE'S National Energy Technology Laboratory: HYSIS, GCTool (Argonne National Laboratory) and Chem CAD 2004a.

_____. Fuel Cell Handbook. 7 ed. USA: EG&G Technical Service, Inc., 2004b. 427 p

_____. Energy efficiency and renewable energy. Hydrogen Fuel Cells & Infrastructure Technologies Program: Disponível em: http://www.eere.energy.gov/hydrogenandfuelcells/fuelcells/fc_ parts.html Acesso em 2006.

VAN DER HEIJDEN, P. C.; BOUZENAD, F.; DIAT, O. Birefringence study of drawn Nafion films. Journal of Polymer Science Part B: Polymer Physics, v. 42, n. 15, p. 2857-2870, 2004.

VAN DER HEIJDEN, P. C.; RUBATAT, L.; DIAT, O. Orientation of drawn Nafion at molecular and mesoscopic scales. Macromolecules, v. 37, n. 14, p. 5327-5336, 2004.

VAN DER STEGEN, J. H. G.; VAN DER VEEN , A. J.; WEERDENBURG, H.; HOGENDOORN, J. A.; VERSTEEG, G. F. Application of the Maxwell-Stefan theory to the transport

in ion-selective membranes used in the chloralkali slectrolysis process. Chemical Engineering Science, v. 54, n. 13-14, p. 2501-2511, 1999.

VAN DER STEGEN, J. H. G.; WEERDENBURG, H.; VAN DER VEEN , A. J.; HOGENDOORN, J. A.; VERSTEEG, G. F. Application of the Pitzer model for the stimulation of activity coefficients of electrolytes in ion selective membranes. Fluid Phase Equilibria, v. 157, p. 181-196, 1999.

VINCENTI, W. G.; KRUGER, C. H. Introduction to Physical Gas Dynamics. New York: John Wiley, 1965.

WANG, C.-Y.; BECKERMANN, C. A two-phase mixture model of liquid-gas flow and heat transfer in capillary porous media - I. Formulation. International Journal of Heat and Mass Transfer, v. 36, n. 11, p. 2747-2758, 1993.

WANG, C.Y. Fundamental model for fuel cell engineering. Chem. Rev. 2004. v. 104. p.4727-4766

WANG, C.Y.; WANG, Z.; PAN, Y. Two-phase transport in proton exchange membrane fuel cells. American Society of Mechanical Engineers, Heat Transfer Division - HTD, v. 364, n. 1, p. 351-357, 1999.

WANG, C. Y.; CHENG, P. Multiphase flow and heat transfer in porous media. Advances in Heat Transfer, v. 30, p. 93-182, 1997.

WANG, M. Q. Development and use of GREET 1.6 fuel-cycle model for transportation fuels and vehicle technologies. Argonne National Laboratory - Center for Transportation Research. Chicago, p.39. 2001

WANG, Y.; WANG, C.-Y. Ultra large-scale simulation of polymer electrolyte fuel cells. Journal of Power Sources, v. 153, n. 1, p. 130-135, 2006.

WANG, Z. H.; WANG, C.-Y.; CHEN, K. S. Two-phase flow and transport in the air cathode of proton exchange membrane fuel cells. Journal of Power Sources, v. 94, n. 1, p. 40-50, 2001.

WEBER, A. W.; NEWMAN, J. Transport in polyer-electrolyte membranes. I. Physical model. Journal of The Electrochemical Society, v. 150, n. 7A, p. 1008-1015, 2003.

WENDT, H.; GÖTZ, M.; LINARDI, M. Tecnologia de células a combustível. Química Nova, v. 23, n. 4, p. 538-546, 2000.

WESSELINGH, J. A.; VONK, P.; KRAAIJEVELD, G. Exploring the Maxwell-Stefan description of ion exchange. The Chemical Engineering Journal and The Biochemical Engineering Journal, v. 57, n. 2, p. 75-89, 1995.

WHITAKER, S. Flow in porous media II: the governing equations for immiscible, two-phase flow. Transport in Porous Media, v. 1, n. 2, p. 105-125, 1986.

_____. The closure problem for two-phase flow in homogeneous porous media. Chemical Engineering Science, v. 49, n. 5, p. 765-780, 1994.

_____. The Method of Volume Averaging, Theory and Applications of Transport in Porous Media. Kluwer Academic Publishers, 1999.

_____. Derivation and application of the Stefan-Maxwell equation. Revista Mexicana de Ingeniería Química, v. 8, n. 3, p. 213-243, 2009.

WILKE, C. R.; LEE, C. Y. Estimation of diffusion coefficients for gases and vapors. Ind. Eng. Chem., v. 47, n. 6, p. 1253-1257, 1955.

WILLIAMS, F. A. Elementary derivation of the multicomponent diffusion equation Reprinted from American Journal of Physics, v. 26, n. 7, p. 467-469, 1958.

WISHART, J. D. Modelling, simulation, testing and optimization of advanced hybrid vehicle powertrains. 2008. 308 p. (Doctor of Philosophy in Mechanical Engineering). Department of Mechanical Engineering, University of Victoria, Canada.

WOOD, D. L.; YI, J. S.; NGUYEN, T. V. Effect of direct water injection and interdigitated flow field on the performance of proton exchange membrane fuel cell Electrochimica Acta, v. 43, n. 24, p. 3795-3809, 1998.

YAN, W.-M.; CHEN, F.; WU, H.-Y.; SOONG, C.-Y.; CHU, H.-S. Analysis of thermal and water management with temperature dependent diffusion effects in membrane of proton exchange membrane fuel cells. Journal of Power Sources, v. 129, n. 2, p. 127-137, 2004.

YANG, F.; PITCHUMANI, R. Transport and Electrochemical Phenomena. In: SAMMES, N. (Ed.). Fuel Cell Technology - Reaching Towards Commercialization Germany: Springer-Verlag London Limited, 2006. p.69-163.

YEAGER, H. L.; STECK, A. Cation and water diffusion in Nafion ion exchange membranes: influence of polymer structure. Journal of the Electrochemical Society, v. 128, n. 9, p. 1880-1884, 1981.

YI, J. S.; NGUYEN, T. V. An along-the-channel model for proton exchange membrane fuel cells. Journal of The Electrochemical Society, v. 145, n. 4, p. 1149-1159, 1998.

_____. Multicomponent transport in porous electrodes of proton exchange membrane fuel cells using interdigitated gas distributors. Journal of The Electrochemical Society, v. 146, n. 1, p. 38-45, 1999.

ZIEGLER, C. Modeling and simulation of the dynamic behavior of portable proton exchange membrane fuel cell. 2005. 179 (Doctor). Fraunhofer Institut Für Solare Energiesysteme Freiburg Im Breisgau.